CRANFIELD UNIVERSITY

GIUSEPPE TRAPANI

The Design of High Lift Aircraft Configurations Through Multi-Objective Optimisation

SCHOOL OF ENGINEERING

EngD Thesis
Academic Year: 2009 - 2014

Academic Supervisors:	Prof. A. Mark Savill
	Dr. Timoleon Kipouros
SoM Supervisor:	Dr. Saghiri Soorosh
Industrial Supervisor:	Dr. Stefano Tursi

March 2014

CRANFIELD UNIVERSITY

SCHOOL OF ENGINEERING

EngD Thesis

Academic Year: 2009 - 2014

GIUSEPPE TRAPANI

The Design of High Lift Aircraft Configurations Through Multi-Objective Optimisation

Academic Supervisors:	Prof. A. Mark Savill
	Dr. Timoleon Kipouros
SoM Supervisor:	Dr. Saghiri Soorosh
Industrial Supervisor:	Dr. Stefano Tursi

March 2014

This thesis is submitted in partial fulfilment of the requirements for the degree of Engineering Doctorate

"To Marta, my niña...
As you wish!"

Abstract

An approach is proposed in this work to support the preliminary design of High-Lift aircraft configurations through the use of Multi-Objective optimisation techniques. For this purpose a framework is developed which collates a Free-Form Deformation parametrisation technique, a number of Computational Fluid Dynamics suites of different fidelity levels, a rapid aero-structure coupling procedure and two multi-objective optimisation techniques, namely Multi-Objective Tabu Search and Non-dominated Sorting Genetic Algorithm-II.

The proposed optimisation framework is used for the execution of several design studies. Firstly, the deployment settings and elements' shape of the 2D multi-element GARTEUR A310 test case are optimised for take-off conditions. Considerable performance improvements are achieved using both the optimisation algorithms, though the sensitivity of the optimum designs to changes in operating conditions is highlighted. Therefore, a new optimisation set-up is proposed which successfully identifies operational robust designs. Secondly, the framework is extended to the optimisation of 3D geometries, using a Quasi-three-dimensional approach for the evaluation of the aerodynamic performance. The application to the deployment settings optimisation of the (DLF F11) KH3Y configuration illustrates that the method can be applied to more complicated real-world design cases. In particular, the deployment settings of slat and flaps (inboard and outboard segments) are successfully optimised for landing conditions. Finally, a rapid aero-structure coupling procedure is implemented, in order to perform static aero-elastic analysis within the optimisation process. The KH3Y optimisation study is repeated including, this time, the effects of structural deformations. Different optima deployment settings are identified compared to the rigid case, illustrating that, despite being of reduced magnitude, wing deformations influence the optimum high-lift system settings.

Furthermore, an industrial development and application of multi-objective optimisation techniques is also presented. In the proposed approach, a reduced order model based on Proper Orthogonal Decomposition methods is used in an offline-online optimisation strategy. The results of the optimisation process for the RAE2822 single-element aerofoil and for the GARTEUR A310 multi-element aerofoil illustrate the potential of the method, as well as its limitations. The technical analysis is completed with a description of the Agile project management approach used to run the project. Finally, future work directions have been identified and recommended.

Acknowledgement

The Engineering Doctorate has been an incredible professional and personal journey, and I would like to thank everyone who made it possible. First of all, I am extremely grateful to my supervisors, Prof. A. Mark Savill and Dr. Timoleon Kipouros, for their constant guidance and support throughout the research programme. Their advices and insights into the topic of multi-objective optimisation have continuously motivated and encouraged me to keep exploring this challenging and extremely interesting research topic.

Also, I would like to express my gratitude to Airbus Operations Ltd., and especially to Murray Cross, for the given opportunity and for the countless occasions in which he has supported me personally or in my research activities. I wish to extend my thanks to the entire Methods and Tools department in Filton (UK), and to the friends I have made there. A special thanks goes to Abdul Rampurawala, who has always fostered a cooperative and supporting working environment, and whose positivism is so contagious.

My sincere thanks go to Stefano Tursi, my industrial supervisor, for providing me with opportunities to blend the academic research within an industrial context. I also wish to express my gratitude to Dr. Thomas Rendall, for his invaluable support on the aero-structure coupling work of this thesis, and Ilya Tolchinsky for sharing with me his extensive experience in software development.

Special thanks go to my colleagues at Cranfield University, with whom I have shared a big chunk of this journey, and to the PhDs and EngDs involved in the CFMS academic engagement. Amongst all, my dear friend and colleague Christian Agostinelli, for the work we have done together but, most of all, for the experiences we have shared.

I cannot thank enough Diego and Lara, mainly for still being my friends after all I have put them through during my stay in Cranfield for the writing-up period of this thesis.

No part of this journey would have been possible without the continuous support and love of my family, to whom I thank with all my heart. Thank you papá, Andrea and I wish mamma could be here to share this with us.

Marta deserves a special place! I cannot even attempt to express in words how thankful I am of having you by my side. Your strength has been my own and I consider myself lucky to have found you, my niña.

This research has been conducted under an Airbus Operations Ltd./ Engineering and Physical Sciences Research Council (EPSRC) EngD studentship and the financial support of both institutions is here gratefully acknowledged.

The source codes and data related to the 2D GARTEUR A310 optimisation are stored at Cranfield University, in the Department of Power and Propulsion cluster Pareto: *pareto.soe.cranfield.ac.uk*, accessible from Cranfield's scp gateway *hpcgate.cranfield.ac.uk*. The remaining data are stored in a shared drive at Airbus Operations Ltd., Filton (UK), and access can be requested to Murray Cross (murray.cross@airbus.com).

Contents

List of Figures

List of Tables

Nomenclature

Acronyms

AM	Agile Modelling
ANOVA	Analysis of Variance
BSM	Beam Stick Model
CAD	Computer Aided Design
CBL	Confluent Boundary Layer
CE	Concurrent Engineering
CFD	Computational Fluid Dynamics
CSM	Computational Structure Mechanics
CST	Class/Shape functions Transformation parameterisation method
DOC	Direct Operating Costs
DRMOGA	Divided Range Multi-Objective Genetic Algorithm
EA	Evolutionary Algorithm
FDD	Feature Driven Development
FEM	Finite Element Method
FFD	Free-Form Deformation parameterisation algorithm
FSI	Fluid Structure Interaction
GA	Genetic Algorithm
H&J	Hooke and Jeeves move
HPC	High Performance Computing
IBL	Interactive Boundary Layer
ICAO	International Civil Aviation Organization
IM	Intensification Memory
JAR	Joint Aviation Requirements
KLD	Karhunen-Loeve Decomposition
LTM	Long Term Memory
MOGA	Multi-Objective Genetic Algorithm
MOTS	Multi-Objective Tabu Search
MTM	Medium Term Memory

NSGA-II	Non-dominated Sorting Genetic Algorithm II
NURBS	Non-Uniform Rational B-Spline
PARSEC	PARSEC parameterisation method
PCA	Principal Component Analysis
PDE	Partial Differential Equation
RANS	Reynolds Averaged Navier-Stokes
RBF	Radial Basis Functions
ROM	Reduced Order Model
SD	Search Diversification strategy for MOTS algorithm
SI	Search Intensification strategy for MOTS algorithm
SSR	Step Size Reduction strategy for MOTS algorithm
STM	Short Term Memory
SVD	Singular Value Decomposition
TE	Airfoil or Element Trailing Edge
TS	Tabu Search
URANS	Unsteady Reynolds Averaged Navier-Stokes
XP	Extreme Programming

Greek Symbols

α	Angle of attack
α_i	Induced angle of attack
α_m	Wing section absolute incidence
α_{eff}	Effective angle of attack
$\alpha_{L=0}$	Angle of attack of zero lift
β_m	Wing section geometric twist
Δx	Normalised x-axis deployment parameter
δx	x-axis deployment parameter
Δz	Normalised z-axis deployment parameter
δz	z-axis deployment parameter
δ	Boundary layer height
δ^*	Boundary layer displacement thickness
Γ	Circulation
$\gamma(s)$	Vortex strength per unit length
κ_i	Hicks-Henne function bump maximum point
Λ	Wing aspect ratio
μ	Kinematic viscosity
ν	Dynamic viscosity
Ω_i	Set of RBF coefficients

Φ	Basis function
ϕ	Velocity potential
ψ	Angle of cylindrical coordinates
ρ	Density
τ_w	Wall shear stress
Θ	Deflection angle deployment parameter
θ	Boundary layer momentum thickness
φ_{25}	Quarter chord sweep
ζ	Damping factor
θ^*	Kinetic energy thickness

Roman Symbols

A	Wing reference area
ac	PARSEC aerofoil camber parameter 1
$b/2$	Wing semi-span
b_i	Hicks-Henne functions
bc	PARSEC aerofoil camber parameter 2
c_Δ	Dissipation coefficiend
c_a	Tangent force coefficient
c_i	Set of constraints to which $f(\overline{x})$ is subjected
c_n	Normal force coefficient
c_x	Force coefficient along x-axis
c_y	Force coefficient along y-axis
c_z	Force coefficient along z-axis
c_{geom}	Geometric mean Chord
c_{ref}	Aerodynamic mean Chord
cd	Drag coefficient
cf	Friction coefficient
cl	Lift coefficient
cl_α	Lift curve slope
cl_{appr}	Approach lift coefficient
cl_{max}	Maximum lift coefficient
cm	Aerodynamic moment coefficient
cm_x	Moment coefficient along x-axis
cm_y	Moment coefficient along y-axis
cm_z	Moment coefficient along z-axis
cp	Pressure coefficient
D_i	Induced drag

$f(\overline{x})$	Objective function
F_x	x component of aerodynamic Force vector
F_y	y component of aerodynamic Force vector
F_z	z component of aerodynamic Force vector
gap	Gap deployment parameter
$\mathbf{H}$	Coupling matrix
H	Boundary layer shape factor
i_local	MOTS local counter
$\mathbf{K}$	Stiffness matrix
L	Lift force
L/D	Lift to Drag ratio
L/D_{appr}	Lift to Drag ratio at approach angle of attack
M	Number of sections along span
M_x	x component of aerodynamic Moment vector
M_y	y component of aerodynamic Moment vector
M_z	z component of aerodynamic Moment vector
M_∞	Freestream Mach number
Ma	Mach number
$\hat{n}$	Surface normal
N	Number of flight incidence in the database
N_a	Number of aerodynamic nodes
N_s	Number of structural nodes
n_sample	Number of sample in modified H&J move
n_var	Number of design variables
ovl	Overlap deployment parameter
p	Pressure
p_∞	Freestream pressure
P_c	GA crossover probability
p_e	Pressure at the edge of the boundary layer
P_m	GA mutation probability
p_{tot}	Total pressure
q_∞	Freestream dynamic pressure
R	Number of RBFs centres
r	Radius of cylindrical coordinates
Re	Reynolds number
Re_θ	Momentum thickness Reynolds number
rle	PARSEC leading edge radius parameter

$\mathbf{S}$	Flexibility matrix
S	Wing Surface
s	Distance along the vortex sheet
t	Hicks-Henne function bump width
t_{tot}	Total temperature
teq	PARSEC trailing edge angle parameter
$\acute{u}$	Perturbation of velocity component u
$\mathbf{u}$	Displacements array
u	x-component of Velocity vector
U_∞	x-component of freestream velocity
U_e	Velocity at the edge of the boundary layer
u_*	Friction velocity
$\acute{v}$	Perturbation of velocity component v
$\vec{V}$	Velocity vector
V	Velocity module
v	y-component of Velocity vector
V_n	Normal component of Velocity
V_∞	Freestream Velocity
V_{LOF}	Lift-off speed
V_{MU}	Minimum unstick speed
Vs_{appr}	Approach speed
Vs_{min}	Dynamic stall speed
$\acute{w}$	Perturbation of velocity component w
w	z-component of Velocity vector
$\overline{x}$	Design variables vector
$\mathbf{x}_a$	Aerodynamic surface position vector along x
$\mathbf{x}_i$	Location of the R RBFs centres
$\mathbf{X}_s$	Extended structural position vector along x
x_{Mi}	Hicks-Henne function bump maximum point
$\mathbf{y}_a$	Aerodynamic surface position vector along y
$\mathbf{Y}_s$	Extended structural position vector along y
y^+	Dimensionless wall distance
ytc	PARSEC aerofoil camber parameter 3
Z	Forces and moments array
$\mathbf{z}_a$	Aerodynamic surface position vector along z
$\mathbf{Z}_s$	Extended structural position vector along z

Chapter 1

The Research Project

1.1 Aims and Objectives

The aim of the research project is the analysis of High-Lift aircraft configurations using parametric geometrical descriptions, sensitivity analysis and different performance simulation capabilities. Such analysis has been carried out in the context of the multidisciplinary/multiobjective design optimisation environment based on the Industrial Sponsor tool-chain expanded with several tool-kits developed at Cranfield University.

In order to successfully achieve the above described goal the listed objectives have been identified:

- Set-up and perform different 2D Multi-Objective optimisation processes using high-fidelity Computational Fluid Dynamics (CFD) simulations. Gain knowledge and better understanding of the high-lift aerodynamics in relation with slat and flap shape and deployment settings
- Exploit the possible speed-up offered by Reduced Order Models (ROMs), assessing their accuracy and range of validity. Compare the outcomes of similar optimisation problems to the *"CFD in the loop"* ones
- Use the findings of the research to guide the development of an R&T tool

within the high-lift design process of the Industrial Sponsor. Focus on both the technical challenges as well as the project management ones

- Extend the analysis to 3D geometries, identifying appropriate techniques to rapidly and accurately simulate high-lift wing aerodynamic performance. Develop a flexible and efficient framework to assess different optimisation algorithms
- Include constraints and requirements from different disciplines, with initial focus on structural coupling.

1.2 Approach

The author's research methodology required the implementation of an optimisation framework into a work-flow management system to produce an automated toolkit for the multidisciplinary design of high-lift configurations. The chosen work-flow management system had to be flexible, reliable and efficient in order to allow a successful implementation and execution of the optimisation process. Multi-Objective optimisation algorithms have been used throughout the research project to tackle challenging industrial and academic design problems. Specifically, the innovative Multi-Objective Tabu Search (MOTS) and the well-known Non-dominated Sorting Genetic Algorithm-II (NSGA-II) have been extensively utilised, and their performance compared. Finally, different level of fidelity simulation tools have been implemented, according to the computational demand of the optimisation process and the requirements defined for the specific optimisation task.

1.3 Context

The ACARE initiative [7] has posed a series of challenging goals for the aeronautical industry, calling for a drastic reduction in both noise and pollution levels of future

aircraft. In order to achieve such improvement in aircraft performance, a paradigm shift in the capability of simulation-based design processes is needed. Moreover, many organisations realise that the need for more advanced design processes is not restricted to the aerospace industry. That is why in January 2008 a not-for-profit company, CFMS Ltd, was formed by six major parties.

In order to deliver the step changes embedded in the *"CFMS vision"*, a co-ordinated, sustainable programme of research and capability demonstration was launched. The largest research project within the CFMS Framework to date has been the CFMS Core Programme, launched in early 2007. At its peak, the project involved 15 industrial participants and 12 universities.

As of today, the engagement with the wide research community is still one of the main focus of CFMS Ltd. The EngD research project of the author is part of such engagement. Conducted within the CFMS context, the research is aimed at providing a contribution towards the development of innovative methodologies and simulation capability.

1.4 Thesis Contents Outline

This thesis is structured as follows:

Chapter 1 has described the aims and objectives of the research, the approach used and has also given an overview of the context in which the research has been carried out.

Chapter 2 introduces the typical high lift design process. Firstly, the purpose of such systems and the current trend in the aeronautical industry is discussed. Secondly, the most common high lift devices are introduced, focusing on both leading edge and trailing edge elements. Then, the main aerodynamic effects of slots (gaps between elements) in the design of multi-element airfoils are described. Finally, a survey of work related to numerical optimisation applied to high lift design is

presented.

Chapter 3 provides a detailed technical description of the optimisation framework for the design of multi-element airfoils. The main modules that make up the automated process are presented and discussed. Moreover, the chapter illustrates the parametrisation technique used to represent the shape of the high lift elements and their deployment settings.

In **Chapter 4** the application of the previously described optimisation frameworks to an industrial 2D test case is presented. Firstly, a validation and verification study of the suite for aerodynamic performance simulation is performed. Then, two different optimisation problems are set-up and executed. The first case focuses on improving the configuration for the nominal design point conditions, whereas the second case introduces robust design considerations within the design. The results are analysed and discussed, and a comparison of two different optimisation algorithms is performed.

Chapter 5 focuses on the development of a design tool included within the Industrial Sponsor's R&T programme. The technical description of the tool and of the ROM approach used is accompanied by an analysis of the project management aspects of the development. Techniques from the Agile Software Development and Concurrent Engineering approaches have been used to reduce development time and cost, and to maximise the quality of the deliverables. Also, a *"Pilot Study"* is presented, which illustrates the user testing phase and the designers' feedback.

Chapter 6 switches the focus of the research from 2D to *"quasi-three-dimensional"*, an approximate method to simulate 3D wing aerodynamics. The background literature on the specific method is presented, together with a description of its implementation. A validation study is performed before including the method within the optimisation framework introduced in Chapter 3. In addition, the application of the proposed methodology to the optimisation of the KH3Y test case is also presented. Both MOTS and NSGA-II are used to drive he optimisation process, and

their performance are later compared and assessed.

Chapter 7 considers the coupling of the quasi-three-dimensional approach, described in the previous chapter, with a reduced structural model. The implemented rapid coupling procedure allows to include static aero-elastic effects early in the design phase, with a fraction of the cost of an high fidelity coupling procedure. A validation of the deformation results obtained applying this methodology to the KH3Y test case is performed. Finally, the same optimisation problem introduced in the previous chapter is performed, this time considering the effects of structural deformation.

Finally, **Chapter 8** summarises the results of this work and identifies future development directions to improve the effectiveness of numerical optimisation within the high-lift design process. Moreover, considerations are made on the challenges posed by the introduction of such methodologies within an industrial environment.

Chapter 2

High-Lift Design, a Literature Survey

2.1 Introduction

In the highly competitive commercial aviation market of today the definition of the layout of a transport aircraft is driven by effort of minimising its Direct Operating Costs (DOC). In fact, the close link of airline performance to passenger volumes, and the constant increase in fuel costs, have emphasised the crucial importance of reducing DOC for airlines to be able to transform revenues into profit. Indeed, the low profit margins that airlines continue to face is a major challenge for the civil aircraft sector [8]. As a consequence, the aircraft manufacturers have aimed at simplifying the aircraft systems, reducing their production and operational costs. This trend is clearly identifiable in the design of the latest aircraft's high-lift system, where *"simpler"* but more optimised designs have replaced complex and heavy ones.

The main purpose of the high-lift system is to reduce the stall speed of an aircraft, increasing the generated lift, for takeoff and landing purposes. The design of such systems for civil aircraft has become increasingly important within the aerospace industry. Efficient high-lift configurations are, nowadays, fundamental to fulfil the increasing requirements in terms of aerodynamic efficiency and noise levels in near

airport regions imposed by ICAO (Chapter 4 of Annex 16) [7]. Although deployed only for short segments of an aircraft typical mission profile, relatively small changes in the aerodynamic performance of the high-lift systems can produce large pay-off in aircraft's weight and performance [9]. Furthermore, these systems have a significant impact on the cost of a typical jet transport: they are time consuming and expensive to design and test; their flows, geometry, and actuation and support systems are complex; they are heavy and maintenance intensive [9].

Besides, the design of the high-lift system is a highly constrained and multi-disciplinary problem. Strong interrelations exist between the wing layout and the high-lift system efficiency, making the final design a compromise between cruise efficiency and acceptable airfield performance [2]. Indeed, the specification of the cruise aerodynamic requirements determines many of the design parameters that define the wing layout: sweep angle, span loading, wing area, aspect ratio, thickness, chord and twist distributions. Hence, only few parameters are left to the high-lift designer to develop a solution which will meet the required airfield performance. The type of high-lift devices, the shape, the spanwise extension and the settings can be varied during the design process. Also, several structural and manufacturing constraints have to be taken into consideration, limiting even further the freedom of the designer. For example, the location of the front and rear spars (designed to provide the required wing structural stiffness and internal fuel volume) usually limits the chordwise extension of the high-lift devices.

2.2 Type of High-Lift Systems

A broad range of different high-lift systems has been developed over the years, although the most widely used in civil aircraft is the multi-element wing. This configuration is typically composed of a leading-edge device that increases the stall angle of attack, and a trailing-edge device that produces an upward shift in the lift

curve, see Figure 2.1. A review of the available high-lift devices, as described by Rudolph [1] and Niu [10], is presented in the following paragraphs, with particular focus on the most common solutions.

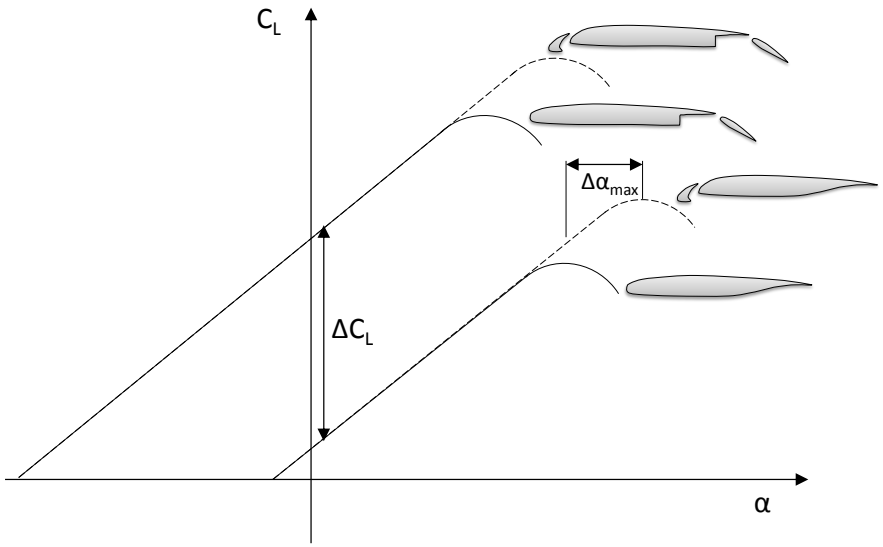

Figure 2.1: Effects of leading edge (increase of stall angle of attack) and trailing edge devices (upward shift) on lift curve.

2.2.1 Leading-edge Devices

The following list identifies the main leading-edge devices in use on modern aircraft:

- Hinged leading edge (droop nose)
- Variable-Camber (VC) leading edge
- Fixed slot
- Simple Krüger flap
- Folding, bull-nose Krüger flap
- VC Krüger flap

- Two-position slat
- Three-position slat

Amongst the above mentioned list, actively controlled slats and Krüger flaps are the most frequently used leading-edge devices on modern civil transport jets.

Slats are usually divided in several panels which, as illustrated in Figure 2.2, form the wing leading edge during cruise (devices stowed). Although earlier designs used two-position slats, current aircraft adopt three-position slats, allowing optimised positions for the entire aeroplane mission. During takeoff the slat is deployed at a shallow angle in an intermediate position, usually forming a small slot with the fixed leading edge (as in the Airbus A320) or sealing this slot with its trailing edge (as in the Boeing 777). A gapped configuration is, instead, used during landing, with the slat fully deployed at higher angles.

Krüger flaps are simpler than slats, but usually present only two positions (stowed and deployed), with a consequent reduction in takeoff performance. Despite the improvements in aerofoil shapes offered by the variable camber variant, Krügers present limited ability to accommodate varying angle of attack. Nonetheless, those devices are used in current aircraft as leading edge devices over the entire wing span (as in the Boeing 747) or on the inboard wing sections between the fuselage and the engine pylon (as in the Boeing 737). Furthermore, Krügers are the candidate leading edge devices for hybrid laminar flow wing designs. Since they stow in the lower surface of the wing, the cruise aerofoil presents a smooth upper surface without any gaps or steps. In fact, the lack of surface discontinuities is one of the mandatory requirements for laminar flow to develop. Also, they act as insect shields protecting the fixed-wing leading edge from contamination at low-altitude flying (during takeoff and landing).

Leading-edge devices typically cover the whole span of the wing, forming a continuous device but for the gates at the pylons locations. They can be classified as constant-chord or tapered slats, according to the variation of the elements' chord

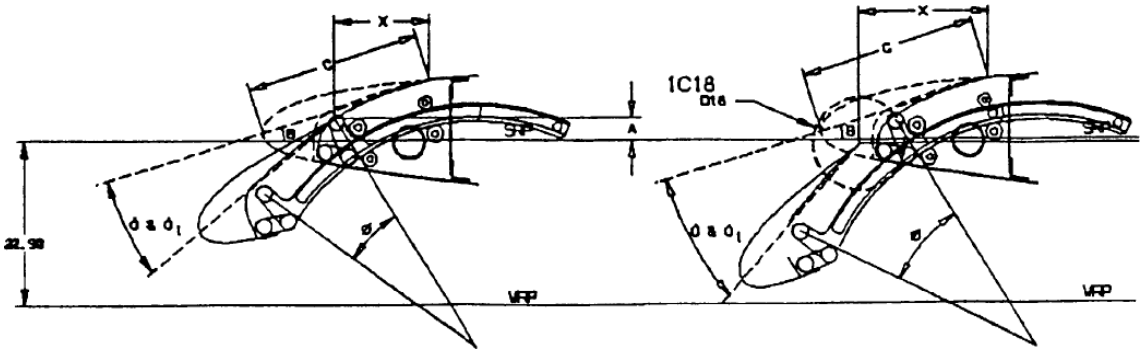

Figure 2.2: Example of a three-position slat, with sealed takeoff configuration and gapped landing deployment, [1] p.9.

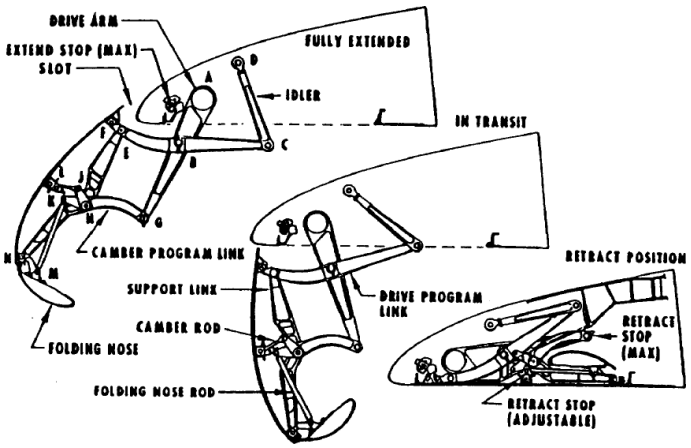

Figure 2.3: Example of Folding, bull-nose Krüger, with gapped deployment, [1] p.8.

along the span. On the one hand, the constant chord type has the advantage that the same mechanism can be used to deploy the slat from wing root to tip. However, aerodynamically the tip elements will usually be oversized, in contrast to the inboard ones which will be under-sized. On the other hand, more targeted aerodynamics can be achieved with the tapered design, although the deployment system will result in a more complex and expensive solution.

2.2.2 Trailing-edge Devices

With regard to the trailing-edge devices, a variety of flap configurations can be found in modern airliners. These include:

- Split flap

- Plain flap
- Simple slotted flap
- Single-slotted Fowler flap
- Fixed vane/main double-slotted flap
- Articulating vane/main double-slotted flap
- Main/aft double-slotted flap
- Triple-slotted flap

The split flap, see Figure 2.4, is the simplest trailing-edge device. It is used only as a glide-slope and attitude control device, due to the fact that it does not produce any considerable lift increase. If used as speed brake it is a more efficient solution than the spoiler, since it produces drag without losing lift.

Next, the plain flap, see Figure 2.5, is a sealed device deployed by rotating a rounded leading edge panel downward. It presents modest lift generating capabilities, limited by the occurrence of flow separation on the profile suction side for deployment angles above 20°. Together with the simple slotted flap, they are mainly used as inboard or outboard flaperons, that is ailerons deployed at low speed.

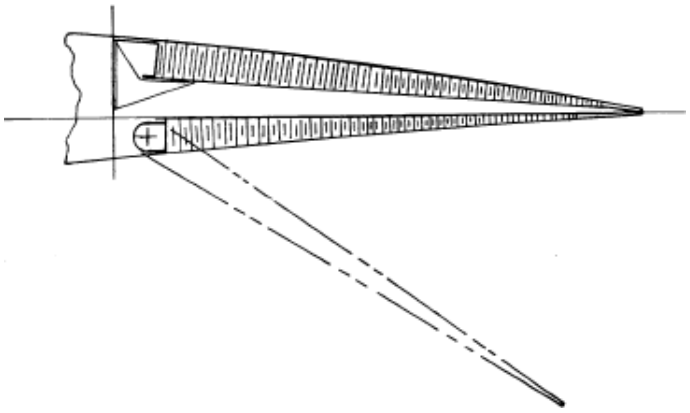

Figure 2.4: Example of split flap, [1] p.11.

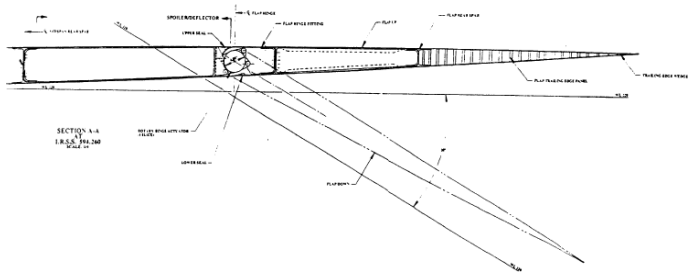

Figure 2.5: Example of plain flap, [1] p.12.

The remaining trailing edge devices exploit the aerodynamic benefits of slots between elements to generate considerable sectional lift increases. Moreover, an increase in wing area is also achieved through the use of Fowler motion: the conversion of the overlap between flap and spoilers when stowed into an aft travel of the flap element. The single-slotted flap, see Figure 2.6, is the simplest of all Fowler flaps. It has been extensively used in the early days of the jet age and it is now making a comeback thanks to its attractiveness from a weight and cost point of view. Moving towards more complex configurations, as for example double and triple slotted flaps, an increase in generated lift is attained. However, this is usually accompanied by a substantial step-up in weight, due to both the increased complexity of the deployment systems and the structural requirements of the flap supports. Probably, the most complex trailing-edge system currently used in a civil aircraft is the triple-slotted flap of the Boeing 747, see Figure 2.7. Very high Fowler motion and deflections of up to 80°are allowed without incurring in extensive flow separation.

Slotted Fowler flaps are the standard trailing-edge devices used on modern commercial aircraft. For the landing phase the devices are deployed to their maximum extension (or close to it). The optimum deployments for takeoff, instead, depend heavily on the aircraft wing loading and thrust-to-weight ratio. Nonetheless, to achieve the high-lift to drag ratio (L/D) required at takeoff it is desirable that as much of the available Fowler motion as possible is developed, and only one of the slot is open. Both requirements deeply influence the design of the flap deployment mechanisms.

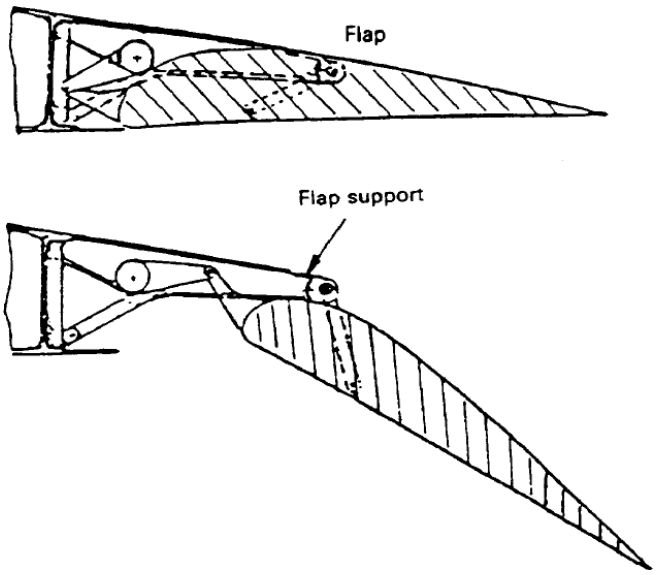

Figure 2.6: Example of single slotted flap, [1] p.14.

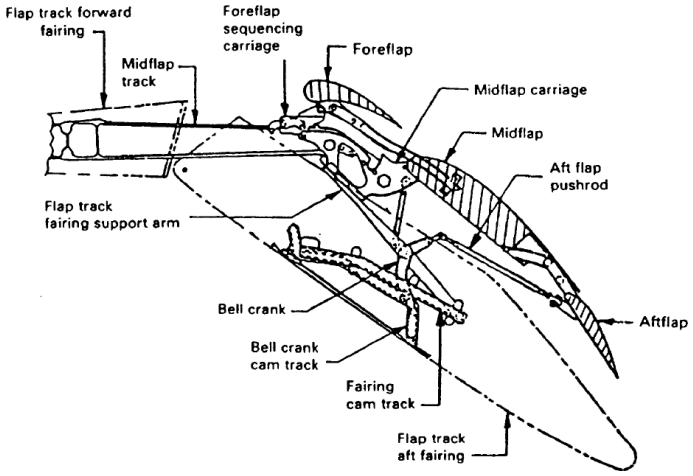

Figure 2.7: Triple slotted flap as installed on the Boeing 747 aircraft, [1] p.18.

2.3 Airfield Performance Requirements

The primary requirements that dictate the design of the high-lift system are identified by Flaig [2] as: the approach speed, the takeoff field length and the climb rate. As discussed later on in this chapter, those requirements are in conflict with one another, so that usually a trade-off is necessary to obtain a satisfactory design. Moreover, flight safety considerations have to be included in the design process: moderate approach speed, good handling qualities and *"normal"* stall characteristics have to be guaranteed.

In particular, the last two requirements are directly related to the flow separation pattern of the wing at maximum lift condition. In fact, in order to maintain aileron efficiency at high angle of attack, the high-lift system should be designed to protect the outboard wing sections from stall. This is achieved by confining the maximum lift limiting separation to the inboard region of the wing, thus influencing the designer's choices.

Due to the different requirements on the aerodynamic performance of the high-lift system, the takeoff and landing phases will be discussed separately in the next sections.

2.3.1 Takeoff

The main driver for the design of the high-lift system at takeoff is the minimisation of the required *"takeoff field length"*. This is defined, in the Joint Aviation Requirements (JAR), as the sum of the total ground roll distance and the airborne distance to overfly a 35-foot obstacle, see Figure 2.8. Hence, both contributions have to be reduced if a minimum value wants to be achieved.

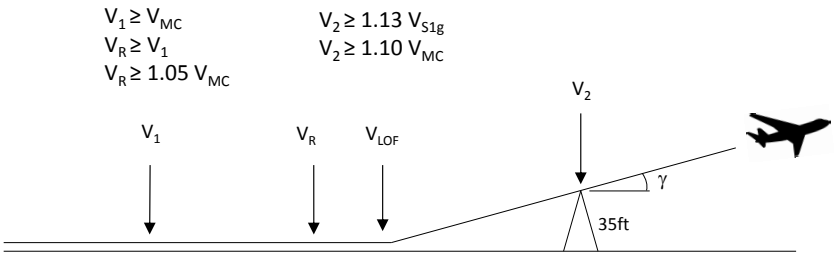

Figure 2.8: Takeoff procedure for civil jet-propelled transport aeroplanes.

The acceleration distance on ground is inversely proportional to the lift-off speed V_{LOF}, which is required by the airworthiness regulations to be equal to or greater than 1.1 times (1.05 with one engine out) the minimum unstick speed, V_{MU}. The V_{MU} indicates the minimum speed at which the aeroplane can safely take off in the

event of an engine failure. It is function of the maximum usable lift coefficient, namely cl_{max}, when no limitations on rotations are imposed due to tailstrike. An increase in cl_{max} will, therefore, directly translate into a reduced takeoff field length.

With regard to the airborne distance, the JAR rules require a minimum climb rate to be maintained, even with one engine inoperative (2 engine configurations: 2.4°, 4 engine configurations: 3.0°). For a given thrust-to-weight ratio the climb rate is proportional to $-D/L$ for the given flap configuration. It is thus clear the conflicting requirement of an increase in maximum lift performance, and associated high level of aerodynamic drag, and a concurrent high values of L/D.

2.3.2 Landing

The landing manoeuvre for civil transport aeroplane is illustrated in Figure 2.9. During the final approach the aeroplane, with the high-lift system deployed in landing configuration, descends on a 3°glide slope (the minimum required by JAR rules). The approach speed of the aeroplane, Vs_{appr}, is required, by airworthiness rules, to be at least 1.3 times the dynamic stall speed Vs_{min}. This translates into an approach lift coefficient, cl_{appr}, of about $cl_{max}/1.54$, as by Equation. 6.4.2:

$$\begin{aligned} \frac{1}{2}\rho \mathsf{S} {Vs_{appr}}^2 cl_{appr} &= \frac{1}{2}\rho \mathsf{S} {Vs_{1g}}^2 cl_{max} \\ {Vs_{appr}}^2 cl_{appr} &= \left(1.05\,\frac{Vs_{appr}}{1.3}\right)^2 cl_{max} \\ cl_{appr} &= \frac{cl_{max}}{1.54} \end{aligned} \tag{2.1}$$

where $Vs_{1g} = 1.05 Vs_{min}$ and $Vs_{min} = Vs_{appr}/1.3$.

A low approach speed is generally desirable for many reasons: it reduces the *"landing field length"*; it alleviates the stresses induced on the aeroplane structure during landing; and, principally, reduces the possibilities of accidents. Consequently,

high-lift systems are designed to provide high value of the maximum lift coefficient when deployed in landing configuration. The aircraft approach angle is determined from the lift polar curve, at a cl corresponding to the cl_{appr}. However, safety considerations such as pilot visibility or available rotation for the landing flare, may influence or limit its value.

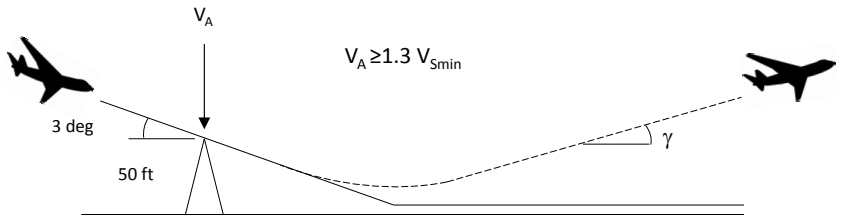

Figure 2.9: Landing procedure for civil jet-propelled transport aeroplanes.

In contrast to the takeoff configuration, the requirement on the approach angle during landing demands the L/D ratio to be low. High values of drag can, thus, be expected due to the high-lift generated. However, this is in conflict with the JAR requirement for the go-around or balked landing case, where a climb gradient of 3.2°with all engines operative must be guaranteed.

2.4 High-Lift Aerodynamics

The aerodynamic performance of a multi-element wing is strongly dependent on the interactions between the different elements. Leading-edge devices have to be properly matched with trailing-edge flaps (and vice-versa) to be effective and maximise performance. Compared with a single element aerofoil, additional complexity can be identified in the flowfield that develops around such configurations, as illustrated in Figure 2.10. In particular, recirculation areas develop in the cove regions of slat and main element, together with the mixing of the shear layers of the different elements. The complexity of the underlying aerodynamics, and the sensitivity of the

aerofoil performance to the values of gap and overlap, make the determination of the optimum positions of the elements a challenging task.

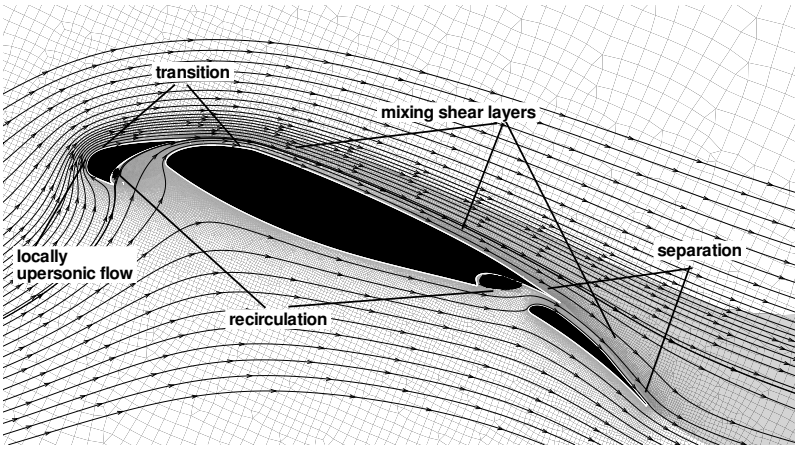

Figure 2.10: Visualisation of flow-field around a multi-element wing.

The positive effects of slotted flaps in increasing aerofoil aerodynamic performance have been known for more than a century. But it was not until the 1970s that a theoretical basis for high-lift aerodynamics was made. This was a result of the insight into the underlying physics of the highly complex flows involved provided by A.M.O. Smith [11]. Five primary effects of *"slots"* (gaps between the elements) in properly designing a multi-element aerofoil have been identified and analysed:

1. the *"slat effect"*. It is due to the circulation on the upstream element that modifies the flow region near the downstream element, reducing the pressure peaks of the aerofoil. This effect results in a decreased lift coefficient for the downstream element but an overall increase in the aerofoil *cl*.

2. the *"circulation effect"*. This effect is similar to the previous one but, this time, it is the downstream element that modifies the flow, placing effectively the trailing edge of the upstream element at a higher angle of attack. The main consequence is an increase of the circulation of the upstream element, in order to satisfy the Kutta condition.

3. the *"dumping effect"*. The influence of the downstream element can also in-

crease the tangential velocity at the trailing edge of the upstream element leading to a reduction on the pressure-recovery demands. As a consequence, the likelihood of boundary layer separation is consistently decreased.

4. the *"off-the surface pressure recovery"*. The boundary layer of multi-element aerofoils can meet high pressure-rise demand due to the fact that the fluid is moving towards regions of higher pressure but without the contact of any wall (e.g. wakes of forward element flowing in the nose region of the next element). The off-the surface pressure recovery is much more effective than the best possible deceleration in contact with a wall [11].

5. the *"fresh-boundary-layer effect"*. This effect describes the characteristic of properly designed multi-element aerofoils, where a fresh boundary layer is formed upon each element. A delay in separation is achieved due to the better response of such thin boundary layers to adverse pressure gradients. Nonetheless, the wake of a leading element can, depending on the values of the slots, merge with the boundary layer of a following element. This condition is usually defined as *"Confluent Boundary Layer (CBL)"* flow, and leads to an increase in the likelihood of separation.

The five primary effects enumerated above illustrate how both inviscid and viscous effects characterise the flow-field around multi-element aerofoils. As a consequence, the aerodynamic performance of such aerofoils is very sensitive to small variations in the gap and the overlap between the various elements. On the one hand, smaller slots are favourable for the inviscid effects, due to the stronger influence of an element's circulation on the others. On the other, wider slots reduce the percentage of CBL flow (viscous effects), increasing the boundary layer ability to withstand separation. Furthermore, it must be noticed that the effective slot between the elements is determined by the thickness of the shear layers, so that viscous effects play a paramount role in high-lift aerodynamics.

2.5 Numerical Optimisation

The fine tuning required in the design of high-lift system elements has been traditionally achieved through careful wind tunnel testing. However, the high cost associated with such tests have increasingly encouraged the development and consequent use of alternative CFD tools within the design process. For example, Interactive Boundary Layer (IBL) approaches, which employ separate inviscid and viscous flow solvers coupled in an interactive manner, have traditionally been used to simulate the flow of multi-element aerofoils. More recently, RANS (Reynolds Averaged Navier-Stokes) methods, although still a subject of research, have been found to be reasonably reliable in predicting the aerodynamic performance of high-lift configurations. The use of RANS solvers in simulating the complex flow field around multi-element aerofoils has been validated in the past for 2D test cases [12, 13, 14, 15]. This validation process has enabled the application of numerical optimisation methods to the design of high-lift aerofoils, making it an active area of research.

An initial optimisation study of a multi-element aerofoil was presented in 1998 by Besnard et al. [16]. The deployment settings of leading and trailing edge elements are optimised in order to increase the L/D performance at takeoff. A Modified Feasible Directions (gradient based) optimisation algorithm from the commercial DOT package [17] is used in conjunction with an Interactive Boundary Layer approach. The framework led to considerable improvements in the objective function within a few iterations. Eyi et al. [18] prefer an higher fidelity level aerodynamic model, coupling the same DOT optimisation suite with a RANS solver. A chimera overlaid grid system is generated for each new design, reducing the complexity of the grid generation task. The optimisation process proved successful in improving the aerodynamic performance of the configuration, although the authors recognised that the global optimum was not found, and the process became stagnant at a local minimum.

The difficulty of deterministic algorithms in identifying the global optimum is

highlighted by Wild [19], who performs a comparison of different optimisation strategies including gradient based, gradient free and stochastic. The Domain Decay Simulated Annealing (stochastic algorithm) of Siclari [20] is found to be superior in achieving a global optimum, although an order of magnitude more evaluations is needed compared to the deterministic approaches. As a consequence, the faster SUBPLEX [21] algorithm is subsequently used by the author for the optimisation of a multi-element aerofoil. Wang and Periaux [22] tackle the high computational demand of the Genetic Algorithm (GA) used in their framework replacing the global optimisation by decentralised local sub-optimisations using Game Theory. A multipoint optimisation of an high-lift aerofoil for takeoff and landing is performed, coupling the optimisation strategy with an IBL solver.

In the context of gradient-based optimisations, the Adjoint method has been used by Kim et al. [23] to obtain the gradient information used in a Steepest Descent optimisation algorithm. Compared to finite difference, the adjoint method substantially reduces the computational cost associated with the evaluation of the gradient. Several optimisation problems are set up and executed for a single and a multi-element aerofoil, considering, in all cases, a single objective formulation. Significant improvements are achieved for the single element case, while lower performance increment is found for the high-lift aerofoil. A similar approach has been used by Nemec et al. [24], where the gradient information from the adjoint formulation is used in a quasi-Newton method. Multi-objective and multi-point optimisations are executed using a weighted function approach.

An alternative method to reduce the CPU time of an optimisation process is to use Reduced Order Models (ROMs). Kanazaki et al. [25] use Kriging models in conjunction with Divided Range Multi-Objective Genetic Algorithm (DRMOGA) for the optimisation of the slat and flap deployment settings at two design points (alpha 8°and alpha 20°). The Analysis of Variance (ANOVA), performed a-posteriori on the optimisation results, highlights the importance of both leading and trailing

edge device settings in achieving good performance at near stall conditions. On the same line of thoughts, a more recent study is presented by Carrese et al. [26], where a surrogate-driven (Kriging) multi-objective Swarm optimisation algorithm is used. To further lower the computational demand, a reference point distance metric is used to drive the optimisation towards a sector of special interest on the Pareto front and, thus, reduce the scale of the design space.

The promising results shown by the application of numerical optimisation to aerodynamic design led to the creation of various European collaborative research projects involving academia and industry. Those projects favoured the implementation and usage of optimisation framework within an industrial context. For example, Kroll et al. [27] present the development of an optimisation framework within the Megadesign project, and its application to the design of a multi-element aerofoil in landing configuration. Two design points are considered combined in a weighted function: alpha 10°and alpha at maximum cl. The determination of the angle of attack of maximum lift implies several consecutive flow-field calculations and is, thus, a computational costly task. To reduce the number of iterations to convergence of the optimisation process a gradient-free Downhill Simplex optimisation algorithm is used. Also, Wild [28] presents another practical high-lift design case. A new Fowler flap is designed and optimised for both takeoff and landing conditions, imposing a fixed hinge fowler flap kinematic. Shape and deployment settings of the element are varied, and five design points (2 for landing, 2 for takeoff and 1 clean) are considered in an aggregated weighted function.

A more recent European project, EUROLIFT II [29], has promoted the assessment and comparison of several optimisation strategies (gradient based, gradient-free and stochastic methods) combined with different RANS solvers. A common design problem was defined for a 2D test case in landing configuration. All the involved partners approached the multi-objective problem using a single objective weighted function formulation. The only exception was CIRA, which used a multi-objective

genetic algorithm (MOGA) combined with the well-known Euler coupled boundary layer code MSES [30]. The outcome of the study shows some improvements on the landing performance, although a dependency of the optimum solution on the specific solver used is identified.

More recently Benini et al. [31] use an optimisation framework including MOGA and MSES for the optimisation of slat and flap shape and setting for the British National High Lift Programme's three-element airfoil NHLP-2D. A Bezier curve representation is used to parametrise the cut-outs of slat and flap, and two different sets of deployment settings are used for takeoff and landing configurations. The optimisation results are validated with the RANS solver ANSYS Fluent, confirming the obtained improvements. The deployments settings and the flap shape are found to be more important in the fine tuning of the configuration than the slat shape.

When considering 3D geometries, RANS solutions tend to be less robust and less accurate in predicting the aerodynamic performance of high-lift configurations. The increased complexity of both the geometry and the flow features make such simulations a real challenge. An assessment of the numerical prediction capability of current-generation CFD technology for high-lift configurations has been conducted in the High-Lift Prediction Workshops (I and II) [32]. The outcomes of the assessment clearly shows that improvements in today's methods are needed to reliably simulate takeoff and landing performance. Nevertheless, some examples of the application of numerical optimisation to a complex 3D large civil aircraft research test case are presented by Brezillon et al. [33] and, more recently, by Minervino et al. [34]. The results of those studies have shown the ability to successfully settting up and runnning computationally expensive optimisation frameworks for high-lift design. However, the aerodynamic performance improvements obtained by Minervino [34] using the full 3D geometry were limited when compared to similar results obtained from a previous 2D optimisation. Moreover, a substantial increase in effort and computational time is needed to set up and run such optimisations.

2.6 High-Lift Design Process

The high-lift design process, as presented by Flaig and Hilbig in [2], is illustrated in Figure 2.11. Three distinct phases are identified: *"pre-development"*, *"development"* and *"pre-flight"*. The work presented in this thesis focuses on the pre-development stage, where several alternative concepts are developed and analysed using a variety of methods. It is, therefore, a computationally intensive phase, characterised by a high number of design iterations. The requirement for a quick turn around time dictates the accuracy/speed trade-off of the methods employed for the aerodynamic predictions. Some wind tunnel testing is still present, performed to validate the performance of the most promising concepts identified, although it is increasingly being replaced by high fidelity CFD (e.g. RANS and URANS).

Indeed, it is crucial to address the design of high-lift systems even at this early stages, in order to meet the required aerodynamic performance at the lowest development cost. In fact, as described by Bhimani [35], between 70% and 90% of total product development costs are committed in the first 10% of the product design cycle. This is particularly true for new aircraft development, where the cost percentage easily reaches the higher limit of the range (Davis P. in [36], pag. 1076). That is why, the next chapters focus on the introduction of numerical optimisation techniques at the preliminary phase of the design process, as a mean for the designer to achieve better solutions within the given timeframe.

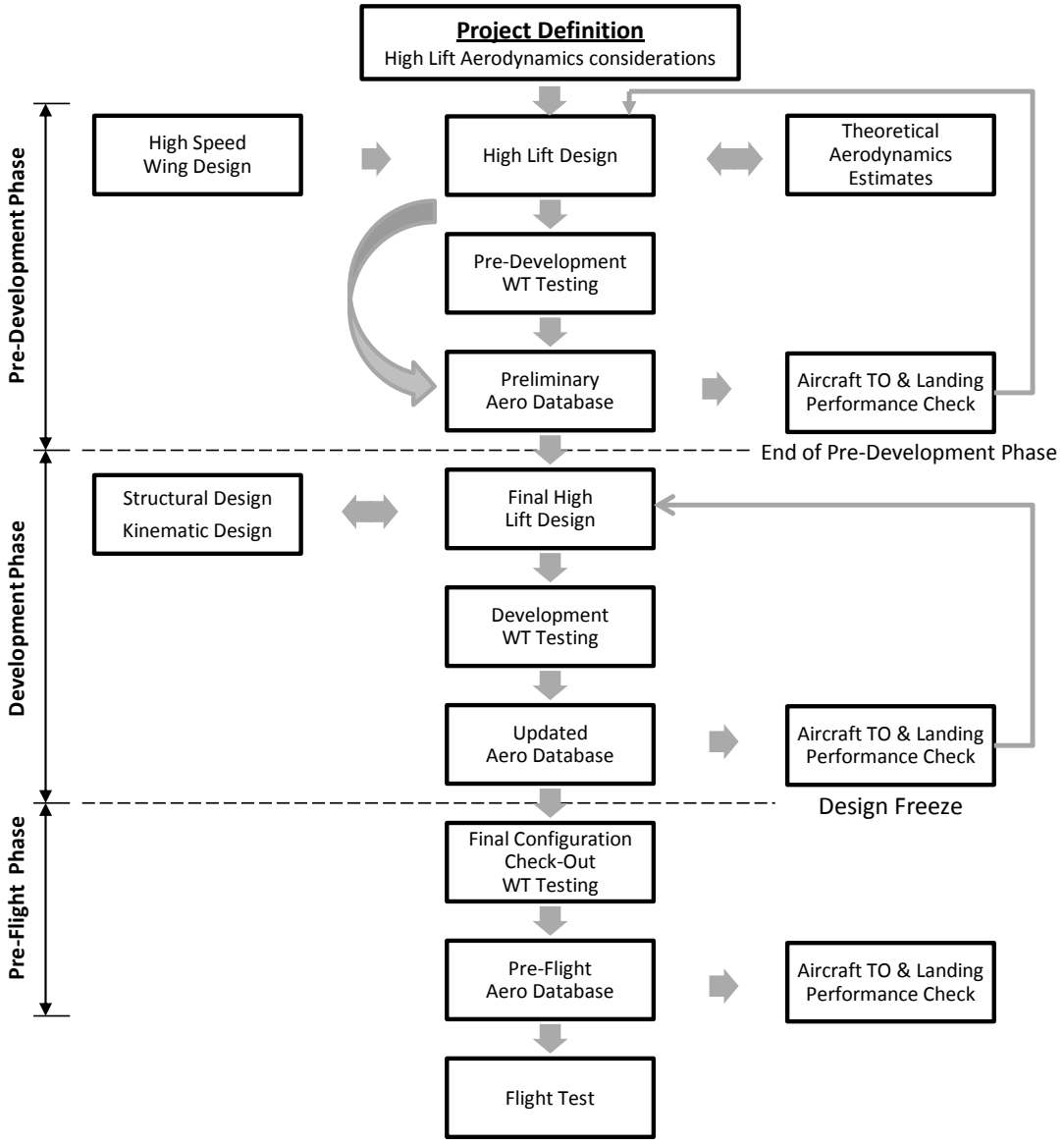

Figure 2.11: The three phases of the High-Lift design process: *"pre-development"*, *"development"* and *"pre-flight"*. Adapted from [2]

Chapter 3

Optimisation Methodology and Framework Description

3.1 Introduction

The optimisation framework used throughout this work for the design of high-lift configurations is here introduced and described. The system comprises of both commercial suites and in-house libraries, collated together using a series of codes in C++, and exploiting the journalling capabilities of the commercial packages. Several modules constitute the framework, as illustrated by the flow diagram of Figure 3.1.

The first step in the optimisation process is the parameterisation of the initial high-lift geometry. Depending on the chosen techniques a fitting process is executed to match the datum shape. The elements' shape is then modified and the high-lift devices are positioned corresponding to their relative deployment settings. Either the direct or the incremental deployment parameters can be used, depending on the configuration of the imported input file. In fact, both stowed and pre-deployed configurations can be analysed within the same framework. Following the deployment of the configuration, one of the implemented method for the evaluation of the aerodynamic performance is used. In the case of RANS, a mesh is generated

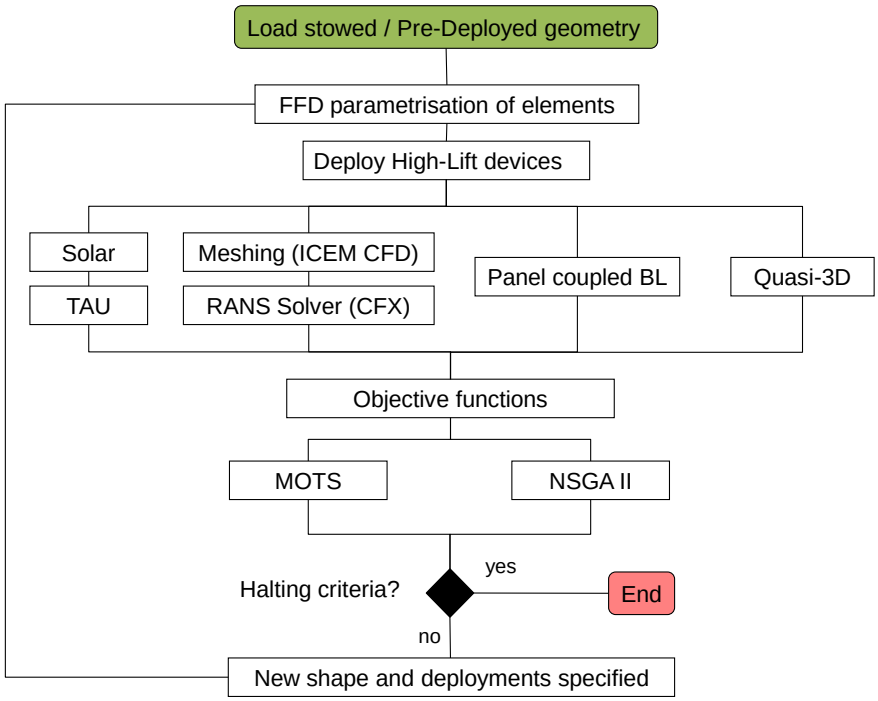

Figure 3.1: Proposed Multi-Objective Optimisation framework for the design of high-lift configurations.

in an automated fashion around the aerofoil using either the commercial software Ansys®ICEM CFD or Solar. Feasibility checks are carried out to exclude geometry intersections and low mesh quality from the process. The mesh is, then, transferred to the CFD solver, either Ansys®CFX v5.0 or TAU, for the evaluation of the performance. The metrics of interest are extracted from the aerodynamic simulation, combined to evaluate the objective functions, and sent to the optimisation algorithm together with the design variables values. Based on this evaluation the optimisation toolkit suggests a new configuration that is subsequently analysed. The described loop continues until a stopping criterion is reached, e.g. evaluation time, number of iterations or residual increase in performance.

With regard to the implementation of the framework, the whole optimisation process is controller within the optimiser's code, i.e. either MOTS or NSGA-II. An interface function is coded within the optimisation algorithm's implementation,

which handles the calls to the external functions (implemented in separate files) and the execution of the different simulation methods. This modular approach has guaranteed both an easy debugging of the code and the flexibility to personalise the optimisation process depending on the analysed case. In addition, this architecture allows the execution of the same evaluation chain defined within the optimisation set-up for single analysis case. This *"out of the optimisation loop"* execution is particular useful for post-optimisation analyses, when detailed information regarding the flowfield of the identified optimum designs is needed.

As a general rule tasks such are the preparation of input files or the extraction of the metrics of interest from the simulations' output files are performed within coded functions (see A for a detailed description of the framework's architecture). Also the FFD parameterisation of the elements' shape and their deployment are executed through functions. The simulation methods are, instead, run through executables. The reasons behind this distinction are twofold: firstly no access is granted to the source code of commercial software (e.g. ICEMCFD), so that no alternative execution is possible for such simulations; secondly, the use of compiled executables guarantees the tracking and monitoring of the software version used. The latest is of paramount importance in an industrial context, where only tested and approved software can be run in the company's IT infrastructure, and where it must be possible to reproduce the exact output data in any moment using the same input files and software version.

Additionally, the simulation methods are divided into locally and remotely executed ones. The first class contains the Panel Coupled Boundary Layer method and the meshing software (ICEMCFD and Solar), which are executed on the local machine where the optimisation process is run. The remotely executed ones are the RANS solvers (cfx5solve and TAU) and the Quasi-three-dimensional code, which are submitted to a scheduling system and executed on an HPC cluster. In either cases the metrics of interest are extracted from the simulations' output files and fed

back to the optimiser, restarting in this way the analysis cycle.

A more detailed description of the methodology used for each stage executed during the optimisation process (as presented in Figure 3.1) is presented in the next sections, together with the background literature relevant for each method used.

3.2 High-Lift Devices Deployment Settings

The optimisation of multi-element aerofoils requires the relative position of the different elements as well as their shape to be varied. Therefore, not only a suitable parameterisation technique must be identified to represent the profile geometry, but also a set of parameters have to be defined that uniquely describe the positioning of each element. Various solutions have been proposed in literature, although the most commonly used parameters are either the *"Cartesian coordinates"* or the *"gap-overlap definition"*.

The Cartesian coordinate system, illustrated in Figure 3.2, is the most convenient of the two for mathematical modelling. Three variables are used to define the deployment settings of each element, namely δx, δz and Θ. The first two variables express the distance between the trailing edge of an element and the leading edge of the following, along the two Cartesian axis x and z. Following their definition, the δ values are defined positive when the trailing edge (TE) of the leading element is located above and aft the nose of the following element. This is the case for the flap element, illustrated in Figure 3.2(b). Moreover, the third parameter Θ, defines the angle between the clean profile chord and the rotated chord fixed relative to the deployed element (slat or flap). A positive deflection Θ is associated to a clockwise rotation of the element.

In addition, Cartesian coordinates are a convenient system in which to express the elements positioning relatively to a reference pre-deployed configuration. In fact, although a stowed profile is usually the initial geometry used for the high-lift design

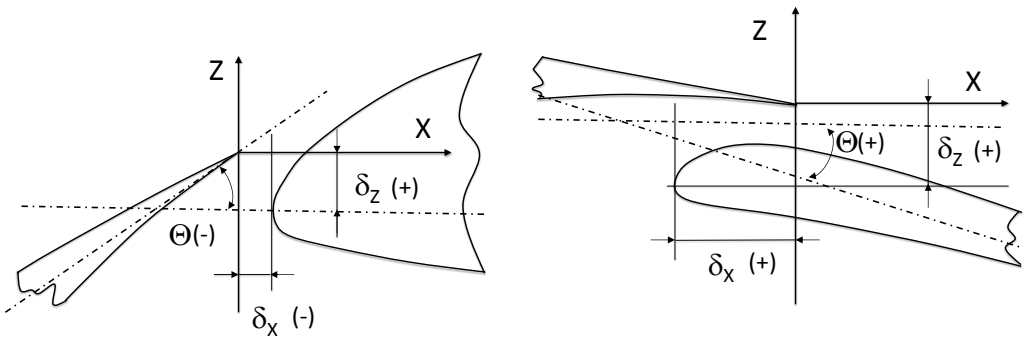

(a) Slat (b) Flap

Figure 3.2: Cartesian coordinate systems for high-lift device deployments.

process, in some cases a pre-deployed reference geometry is used instead. Therefore, the deployment settings must be expressed as increments of the reference ones. This task is easily performed using the Cartesian system, while it might be less straight forward when different methods are applied.

The gap-lap definition is, instead, more related to the physical sensitivities of the flow to geometrical changes. Just like the previous method, three variables are used for the definition of the deployment positions: *"gap"*, *"overlap"* and *"deflection angle"*. The gap is defined as the radius of the circle centred at the trailing edge of the preceding element, and tangent to the following one (see Figure 3.3). It is, by definition, always a positive value. The overlap is, as the name suggests, a measure of the elements overlapping, measured along the stowed configuration chord line. It is defined positive when the elements do overlap, whereas a negative value indicates increased separation of the elements. Furthermore, the overlap coincides, in absolute values, to the δx Cartesian parameter earlier introduced when the x-axis is chosen parallel to the stowed chord line. Finally, the deflection angle is, as for the Cartesian system, the angle between the clean profile chord and the rotated chord fixed relative to the deployed element (slat or flap). However, in this case a positive Θ is associated with an increase in the deflection angle of the elements, which corresponds to a clockwise rotation for the flap element, and a counter-clockwise rotation for the

slat.

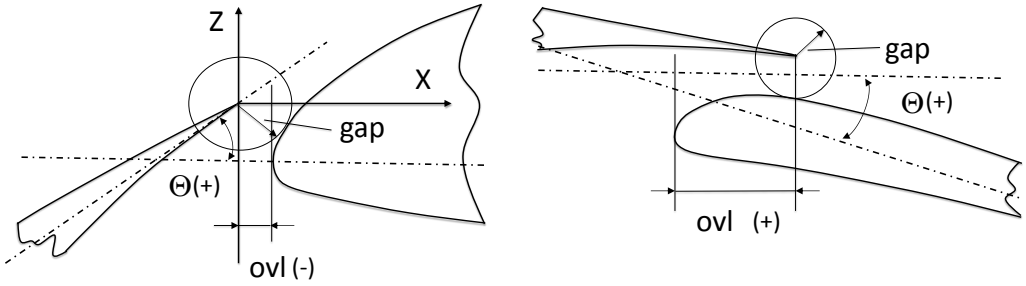

(a) Slat (b) Flap

Figure 3.3: Gap-lap definition for high-lift device deployments.

Within the optimisation framework here presented both approaches are implemented, so that the choice of using one or the other is based on the specified design problem.

3.3 Parametrisation Techniques

The deployment parameters introduced in the previous section allow the optimisation of the high-lift aerofoil in terms of element positioning. However, if also the shape of the elements is to be modified, a parametric model of the geometry must be generated using an appropriate parameterisation technique. Usually, the parameterisation step represents one of the key inhibitors of the development of an automated optimisation system. This is due to the contrasting requirements for the parameterisation technique to provide an accurate representation of the geometry using, in doing so, the minimum number of design variables. In addition, the selected strategy must be flexible enough to allow an extensive exploration of the design space and, at the same time, robust in generating feasible geometries for subsequent analyses.

The choice of a parameterisation method has a substantial impact on the effectiveness of the entire optimisation framework. Therefore, particular attention must be posed in the selection of an approach that suite the design problem tackled.

A survey and assessment of the most commonly used parameterisation techniques is presented by Samareh [37]. In his work the author identifies eight main categories into which the shape parameterisation approaches can be classified, providing a summary of strengths and weaknesses for each one of them. Amongst the analysed approaches, the Partial Differential Equation (PDE) [38] is identified as a promising technique. The PDE method transforms the parameterisation procedure to a boundary-value problem, where the surface of interest is generated as a solution to an elliptic partial differential equation. Only a small number of parameters are needed to represent even complex three-dimensional geometries, making it an attractive method for numerical optimisation problems. This approach has been used, firstly by Harvey et al. [39] and then by Kipouros [4], for the parameterisation of the blade within a compressor stage optimisation study. The drawback of the method is that the design parameters do not directly represent engineering quantities, and are not intuitive for the geometrical and physical understanding of the geometry being designed.

More intuitive parameters are obtained when using polynomial or spline representations methods. In particular, Bézier and NURBS (Non-Uniform Rational B-Spline) representations are extensively used methods in aerodynamic design, since they allow to considerably reduce the number of design variables required. These techniques are well suited for two-dimensional and simple three-dimensional models [37]. For example, a NURBS-based parameterisation tool for the representation of Formula One's rear aerofoils is developed by Garnesson [40]. The same tool is, later, adapted to high-lift wing configurations by Trapani [41] and used within a preliminary optimisation design. More recently, a NURBS parameterisation is used by Diwakar et al. [42] for the optimisation of aerofoils in unsteady flow, whereas Bézier polynomials are used by Benini et al. [31] to represent the cut-out regions of a multi-element aerofoil.

With the development of gradient-based and adjoint optimisation techniques,

the ability of calculating design variables sensitivities during the optimisation process has become increasingly important. That is why analytical parameterisation methods have recently attracted renewed interest from the research community. The advantage of expressing the geometry parameterisation problem using analytical functions resides in the possibility of analytically differentiate those describing functions. As a result, design variables sensitivities can easily and accurately be calculated, avoiding highly computational heavy finite differences approaches. Examples of such parameterisation techniques are presented by Sobieczky [43], who describes the development of an intuitive parameterisation technique that uses 11 aerodynamically related geometrical parameters, the so defined PARSEC method (see Figure 3.4). Lian et al. [44] apply this parameterisation method together with data mining techniques to the design optimisation of a generic aerofoil. Moreover, an extension of the PARSEC method is presented by Zhu and Qin [45]. In their work the authors add further 16 variables for a more accurate representation of the geometry, later mapping the entire set of variables into the coefficients of a Class/Shape function Transformation (CST) [46].

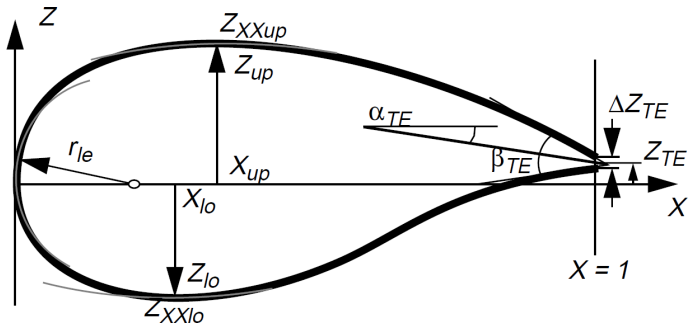

Figure 3.4: Visualisation of the 11 design parameters used in the PARSEC parameterisation technique.

The parameterisation methods described so far aim at representing the initial geometry as accurately as possible using the minimum number of design parameters. A different approach can, however, be considered which implies the parameterisation of the changes in the geometry relative to the datum, rather than the geometry itself. The formulation of this technique was first made by Hicks and Henne [47], and it

was based on superimposing analytical functions defined as *"shape functions"* to the baseline geometry. These shape functions assume the form of *"bumps"*, and are defined as

$$b_i(x) = sin^t(\pi x^{ln(0.5)/ln(x_{Mi})}) \tag{3.1}$$

where t controls the width of the bump, while x_{Mi} is the position of the maximum point of the bump. The contribution of each parameter is determined by the value of the participating coefficients, α_i associated with a shape function, so that the total perturbation is iven by

$$\sum_{i=1}^{N} \kappa_i \, b_i(x) = \sum_{i=1}^{N} \kappa_i \, sin^t(\pi x^{ln(0.5)/ln(x_{Mi})}) \tag{3.2}$$

Similarly, the Free-Form Deformation (FFD), introduced by Sederberg and Parry [48], is known to be a powerful method for deforming an object independently of its representation. The FFD algorithm has its root in computer graphics, in particular in the soft object animation field, where it is used for deforming models and morphing images [37]. This technique enables the deformation of objects by modifying the space around them. For this purpose a control volume is defined around the geometry to parametrise, and a number of control points on each direction, $l \times m \times n$, is specified. Those control points have coordinates (i, j, k), while (s, t, u) represent the local curvilinear coordinates mapped into the control box, which range between 0 and 1. Then, the displacement vector tensor product of trivariate Bernstein polynomial is evaluated for any of the node point $x(s, t, u)$ in the control box:

$$x(s,t,u) + \Delta x(s,t,u) = \sum_{i=1}^{l} \sum_{j=1}^{m} \sum_{k=1}^{n} \left[B_{l-1}^{i-1}(s) B_{m-1}^{j-1}(t) B_{n-1}^{k-1}(u) \right] [Pi, j, k + \Delta Pi, j, k] \tag{3.3}$$

where $B_{l-1}^{i-1}(s)$ is the $(i-1)-$th Bernstein polynomial of degree $l-1$ defined as follows

$$B_{l-1}^{i-1}(s) = \frac{(l-1)!}{(i-1)!(l-1)!} s^{(i-1)}(1-s)^{(l-1)} \tag{3.4}$$

The above described equations introduce a link between each control point and the geometrical points contained inside the volume. Therefore, the modification of any of the control point is transferred to the geometry proportionally to the previously defined tensor. This formulation allows, on the one hand, the method to work with surfaces of any formulation or degree, whereas on the other hand, it results in difficulties in controlling the shape of an object under complex deformations.

In this work, the FFD algorithm has been preferred to other parameterisation strategies for its efficient manipulation of very complex geometries using only a limited number of control points. Thus, this parameterisation technique has been implemented into the optimisation framework.

3.4 Aerodynamic Performance Evaluation

The successive step in the optimisation process of Figure 3.1 is the aerodynamic simulation of the newly generated designs. Several evaluation tools have been implemented within the framework, thus providing different level of fidelity and computational overheads. In particular, for the design of 2D multi-element aerofoils, either a panel coupled boundary layer or a Reynolds-Averaged Navier-Stokes (RANS) simulation can be performed. Clearly, different physics are resolved by the two approaches, with the RANS simulations providing the higher-fidelity resolution of the flow-field. Nevertheless, the panel coupled boundary layer method has shown more than satisfactory level of accuracy, especially for the use of such optimisations at the preliminary design stage. For the analysis of 3D high-lift configurations a quasi-three-dimensional approach has been implemented, as described in detail in

Chapter 6.

The panel coupled boundary layer presents a much lower computational cost compared to RANS, and it has been extensively used for the preliminary set-up of the optimisation problems later described. Moreover, it is the method used to evaluate the sectional performance in the quasi-three-dimensional formulation. However, the final results obtained for the 2D optimisations presented in Chapter 4 have all been obtained using RANS simulations. Therefore, a description of the settings and the automation process used for the RANS simulations follows.

3.5 Reynolds-Averaged Navier-Stokes Methods

As illustrated in Figure 3.1, two equivalent RANS simulation suites are implemented within the framework. However, only the settings of the commercial package Ansys®will be presented in the following sections. In fact, the alternative RANS suite Solar-TAU has been set-up so to resemble, as closely as possible, the settings of the Ansys®tools. In particular, a similar meshing strategy has been used in both suites as well as similar solver settings and solution fidelity requirements.

3.5.1 Meshing Strategies

In a computational fluid dynamics context, mesh generation is as important as the effective solution of the governing equations of the physical problem. Indeed, the quality of the mesh influences the final results of the CFD simulation, as well as the computational time required to obtain a solution. Moreover, mesh generation, usually, represents the most challenging and time consuming task from a user point of view. In fact, as Thompson [49] states *"there is both art and science in the design of the mathematics for mesh generation systems"*. Nevertheless, the developments that the mesh generation process has seen throughout the last years, both in mathematical methodologies and in software capabilities, have enabled the execution of

this process in a completely automatic fashion. This is true, at least, for relatively simple geometries, e.g. 2D aerofoils and simple 3D wing-body configurations.

A hybrid mesh approach has been selected for the automated meshing procedure, combining structured meshes in near wall regions and unstructured meshes in the remaining parts of the domain. Therefore, full advantage is taken from both the meshing strategies, with an accurate solution of the boundary layer and a more flexible and robust meshing strategy for complex regions such as the slat and flap coves. Furthermore, a quad-dominant mesh has been preferred to a pure triangular unstructured one, due to the various advantages offered by this approach. Firstly, a reduction in mesh points can be obtained due to the geometrical definition (or shape) of the mesh elements, especially in the far-field region, where coarser mesh can be used. Consequently, it is possible to either reduce the simulation computational time (reduced mesh size) or increase the accuracy of the simulation, refining regions where the flow presents more complex phenomena to be resolved. Additionally, the obtained quad mesh presents a higher number of cells aligned with the main flow direction, reducing the numerical error of the solution.

Within the optimisation framework presented the mesh *"re-generation"* approach is used, meaning that a new mesh is generated for the flowfield evaluation of each new design identified. Therefore, the implemented meshing process has to be automatically performed, requiring no input from the user. Moreover, it has to be robust and able to produce a high quality mesh around a continuous changing geometry. For this purpose, either the Solar mesher or the commercial suite Ansys®ICEM CFD are used. In the latter case, the tool's native scripting language and journalling capabilities are exploited to create a customised meshing procedure. In addition, geometrical checks are also performed to exclude from the analysis any infeasible design. Finally, in order to guarantee the accuracy of the RANS simulation, quality checks are automatically performed on the generated mesh before the flow-field evaluation step is executed. These checks ensure that the produced mesh presents no

element with a value of *determinant* ≥ 0.3, *skewness angle* $\leq 18°$and *circumsphere ratio* ≥ 0.05. Meshes that present any of the quality indicators below the predefined thresholds are excluded from the evaluation and the correspondent design is marked as infeasible. If on the one hand this approach guarantees accurate flowfield solutions, it excludes from the optimisation process designs which might improve the performance of the initial configuration. This limitations on the automatic mesh generation process is here accepted, though more sofisticated and flexible meshing algorithms could be developed to tackle the problem.

The steps involved in the automated meshing process are presented below:

- the geometry, parameterised by FFD, is imported within Ansys®ICEM CFD as a point-cloud;
- the correspondent aerofoil curves are generated;
- intersection checks of the deployed elements are carried out;
- far-field boundaries are created all around the aerofoil elements at a distance equal to 50 times the chord;
- mesh seeding is distributed to all the edges, defining the mean Δ between two consecutive points and the appropriate (if any) bunching laws;
- a *"wake region"* is created downstream the flap trailing edge;
- a structured *"boundary layer"* mesh is generated all around each element, satisfying the *"low-Reynolds model"* requirements of $y^+ \leq 1$, and placing at least 20 grid points within the boundary layer region;
- a surface mesh on the symmetry plane is generated using the far-field boundaries and the outer surface of the structured mesh just created;
- the so obtained 2D mesh is extruded by 1 unit in the y-direction, since a 3D solver (Ansys®CFX v5) is used;

- finally, the 3D mesh is checked for minimum quality requirements and, if satisfactory, it is output for further analysis.

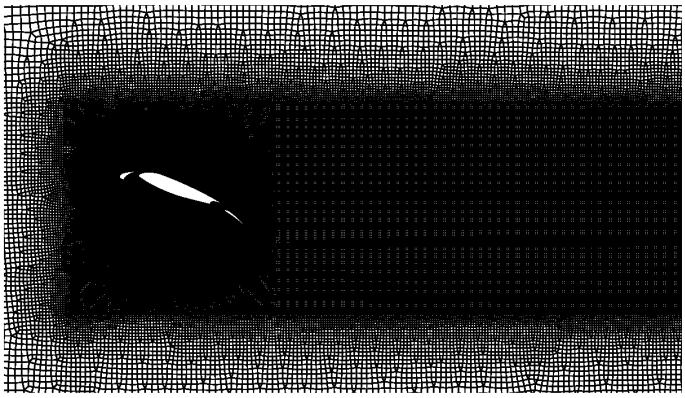

(a) Near-Field

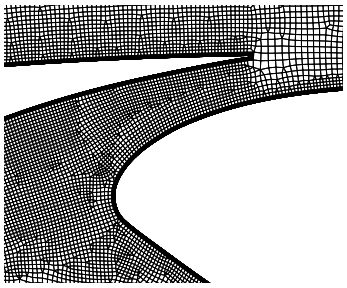

(b) Slat Slot Region

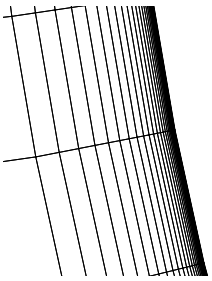

(c) Boundary Layer

Figure 3.5: Details of the quad-dominant mesh around a multi-element aerofoil. The refined near-field and slot regions are illustrated together with the boundary layer prisma layers.

This automated procedure allows the generation of high quality mesh around high-lift configurations when the relative positions of the elements, as well as their shape, is varying. An example of the resultant mesh is illustrated in Figure 3.5, which also shows a close-up of the structured boundary layer region. The height of the first cell layer is set accordingly to obtain a dimensionless wall distance y^+, as defined in eq. 3.6, less or equal to unity all along the airfoil walls.

$$y^+ = \frac{u_* y}{\nu} \tag{3.5}$$

$$u_* = \sqrt{\frac{\tau_w}{\rho}} \tag{3.6}$$

In order to better control the mesh points distribution, the computational domain has been divided into three sub-regions: near-field, wake and far-field. In this way, a finer mesh can be used in the boundary layer and elements' wake regions to better resolve the underlying physics. The described approach generates a mesh with a total of approximately $260,000$ points.

3.5.2 RANS Solver

The CFD solver represents the most computational and time demanding phase of the whole optimisation process. The outcome of the aerodynamic simulation will provide the performance criteria on which the objective functions value are evaluated, so that it is important to accurately predict the behaviour of the fluid around the newly generated designs. In particular, the CFD simulation has to be able to correctly capture the physics expected to be of importance for the specific problem analysed (e.g. flow separation if considering maximum lift conditions). At the same time, the the computational cost of the simulations (either time or resources) must be kept at a minimum. Therefore, a trade-off analysis between accuracy and cost must be performed before the setup of the optimisation, identifying the level of accuracy that most efficiently capture the changes in performance. In fact, the optimisation process will be successful as long as the correct trend in performance improvement is identified. More refined (and therefore costly) simulations can be executed a posteriori on the identified optima in order to precisely assess the performance improvements of these designs.

In the case of high-lift configurations, the flow that develops around the multi-element aerofoils represents a challenging numerical simulation, even when considering 2D configurations. The numerical solution must be able to accurately capture the mixing of boundary layers and wakes of preceding elements, the development of recirculation areas in the cut-outs, but also the occurrence of flow separation. This last requirement, in particular, is fundamental if optimisations are to be performed for maximum lift conditions. For 2D flows the maturity level that steady RANS methods have reached allows a reliable prediction of maximum lift conditions. However, this is not the case for 3D configurations, where the increased geometrical and flow features complexities represent a challenge for a robust and reliable prediction of flow separation. Finally, although the free-stream Mach number M_∞ is relatively low, the flow can easily become transonic due to the high curvature imposed on the suction side by the slat element. Therefore, a compressible CFD solver is strongly recommended [28].

The commercial software selected in this work, namely Ansys®CFX v5, integrates the compressible unsteady RANS equations using a time-marching Second-Order Backward Euler scheme until a steady state solution is reached. The *"High Resolution Scheme"* is used for the discretisation of the governing equations, where a *"blend factor"* is used to combine first and second order level of accuracy. In this specific scheme the value of the blend factor is not fixed over the whole domain but is calculated locally by the software to be as close to 1 as possible without resulting in non-physical values. This results in both high accuracy and stability of the solution. The turbulence equations are solved using a first order method using the Menter Shear Stress Transport (SST) k-ω turbulence model, due to its superiority in capturing the occurrence of flow separation [50]. To benefit from this model the boundary layer has to be well resolved, dictating the requirement for the dimensionless wall distance $y+$ value to be lower than unit on the aerofoil's walls. The physical modelling and solver settings of the analysis are summarised in Table 3.1.

Furthermore, the flow is here considered to be fully turbulent on both lower and upper surfaces of the aerofoil. Indeed, this simplification will affect the resultant lift and drag coefficients of the analysed configurations, as illustrated by Rumsey et al. [51]. In their work the authors have shown the importance of specifying transition location correctly to accurately computation boundary layer's velocity profiles, although no method is developed to estimate the transition location itself. Similar results have been shown for 3D configuration by Fares and Nolting [52] and Eliasson et al. [53, 54], where laminar conditions have been imposed on some regions of the RANS domain. However, in the work here presented laminar to turbulent transition is neglected in the view of achieving a more consistent solution within the optimisation process. In fact, although recent applications of transition prediction techniques (e.g. laminar boundary layer method and e^N-database method [55], or the correlation-based $\gamma - Re_\theta$ transition model [56]) to both 2D test cases [55] and 3D ones [56, 57] have shown promising results, the dependence of such methods on the mesh resolution and test case geometry might result in incorrect transition locations for some of the analysed designs. This inconsistency within an optimisation process might mislead the optimisation algorithm toward unreal optimum regions. An example of such a case is presented by Steed [56], where the transition model predicts early separation of the high-lift configuration analysed, but the fully turbulent case continues to follow the wind tunnel data.

The final result of the simulation is achieved through the solution of the unsteady equations using a fictitious time-step. In order to avoid divergence behaviours and, hence, increase the robustness of the simulation, an increasing step function for the time-step has been used. Computational time has been reduced exploiting the built-in parallelisation capability of Ansys®CFX v5, executing each flow simulation on a four-processor node. Convergence checks are carried out at the end of each simulation in order to exclude any solution that presents oscillating or not converged behaviour.

Table 3.1: CFD physical modelling and solver settings

Material:	Air Ideal Gas
Heat Transfer Model:	Total energy (compressible flow)
Turbulence Model:	SST k-ω
Advection Scheme (state variables):	High Resolution
Advection Scheme (turbulence):	First Order
Timescale Control:	Auto time-scale
Time Integration Scheme:	Second order Backward Euler
Maximum number of iteration:	250
Residual target:	1×10^{-06}

With regard to the boundary conditions, velocity has been specified at the inlet of the domain, whereas static pressure has been imposed at the outlet. Moreover, since Ansys®CFX solves exclusively 3D problems, additional conditions must be imposed on the domain in order to simulate 2D flow-field using a 3D mesh. As a consequence, translational symmetry condition was imposed on the side boundaries.

3.6 Optimisation Algorithms

The selection of the optimisation algorithm to implement within the framework has been driven by two main factors: the computational time required by a single flow evaluation, and the characteristics of the considered design space. On the one hand, the first criterion implies that efficient algorithms, which minimise the number of objective functions evaluations, have to be used for time-consuming simulations. On the other, the presence of multiple local minima drives the need of an optimisation algorithm that can widely explore the design space and identify the so defined *"global optimum"*. It is obvious the contrasting nature of such requirements.

Local search algorithms, and especially gradient-based methods, represent highly efficient optimisation strategies. However, they present a major drawback, which is the tendency to be trapped in local minima, providing sub-optima solutions. On the contrary, stochastic algorithms (e.g. Genetic Algorithm, Simulated Annealing,

Tabu Search) are able to identify global optima, but represent a heavier and less efficient optimisation strategy.

The Tabu Search algorithm is here chosen as primary optimisation strategy, due to its *"intelligent"* approach to the optimisation process. In particular, the specific Multi-Objective Tabu Search (MOTS) software used in this work has been developed by Jaeggi et al. [3], adapting the single-objective TS software implemented by Connor and Tilley [58]. More details on MOTS are given in Section 3.6.2, together with a description of the main strategies adopted by the method to extensively and efficiently explore the design space. Furthermore, the optimisation framework is extended with the implementation of the well-known NSGA-II (Non-dominated Sorting Genetic Algorithm II) [59] optimisation algorithm. These implementations have provided the opportunity of performing comparison studies between the two algorithms, as well as assessing the performance of MOTS on real engineering design cases.

3.6.1 Multi-Objective Optimisation

The classical set-up of an optimisation process involves the definition of a unique objective function to be improved which depends on several design variables. This single-objective formulation aims at obtaining the best possible solution available, defined as the Global Optimum of the problem. However, due to the strong dependence of real-world problems upon different objectives, usually conflicting, the single-objective formulation has proved not to be suitable in achieving realistic solutions. That is the reason why multi-objective approaches must be considered if reliable computational design is to be performed.

The simplest approach adopted to tackle the multi-objective problem is the definition of a *"composite objective"* function, which represents a weighted sum of the objectives. In this way, the problem is transformed back into a single-objective one, which does not require any special formulation to be solved. However, the weighted

composite function approach presents a few drawbacks. Firstly, the weights of the different objectives considered must be pre-set, so introducing implicitly the user designer's pre-conceptions into the problem formulation. Also, only a partial solution of the problem, i.e. a single optimum design, is found using this approach. In fact, as it will be shown later, the solution of a multi-objective optimisation consists of a set of optima. Consequently, it can be stated that *"performing real multi-objective optimisation and finding a Pareto front is the only effective way to find a set of designs satisfying performance criteria in an industrial context"* [60].

In order to introduce the concept of *"Pareto front"* let's express an optimisation problem in general mathematical terms as:

$$\begin{array}{ll} \text{minimise} & f(\overline{x}),\ \overline{x} \in R^n \\ \text{Subject to} & c_i = 0, i = 1, 2, ..., m^{'}; \\ & c_i \geq 0, i = m^{'} + 1, ..., m \end{array}$$

where $f(\overline{x})$ is defined as the objective function, $\overline{x}$ is the vector containing the *"design variables"* and c_i is the set of constraints to which $f(\overline{x})$ is subjected.

To find a solution to this problem means to determine a set of design variables that minimise the value of the objective function satisfying, at the same time, the constraints. Throughout this work the minimisation of the objective function will be associated to the improvements of the design, and will, thus, represent the target of the optimisation process. Considering a point $\overline{x}_1$ of the design space, it will be "better" than another point $\overline{x}_2$ if $f(\overline{x}_1) < f(\overline{x}_2)$. This problem, as stated earlier, admits a unique optimum value of the objective function. However, in multi-objective optimisation the aim is to minimise not only one but n objective functions $f_1(\overline{x}), ..., f_n(\overline{x})$, where $n \geq 2$. This problem, instead, is characterised by a family of alternative solutions rather than a single absolute optimum, and the concept of *"Pareto-optimality"* must be introduced.

Originally postulated by Ysidro Edgeworth in 1881 [61] and generalised afterwards by Vilfredo Pareto [62] the Pareto-optimality concept states that a solution

is *"Pareto optimal"* if no other feasible solution exists which would simultaneously improve all of the objective functions. The set of all the solutions that satisfy this requirement is defined as *"Pareto optimal set"*, and consists of all the non-dominated solutions. The concept of inferiority or dominance is explained considering an objective function vector $\overline{F}(\overline{x}) = \{f_1(\overline{x}), ..., f_n(\overline{x})\}$. If no component of the objective function vector $\overline{F}_1$ evaluated in $\overline{x}_1$ is greater than its correspondent element in $\overline{F}_2$ (objective function vector evaluated in $\overline{x}_2$) and at least one is smaller, then $\overline{x}_1$ *"dominates"* $\overline{x}_2$. In the same way, if some components of $\overline{F}_1$ are bigger than $\overline{F}_2$ and some smaller, $\overline{x}_1$ is defined as *"Pareto-equivalent"* to $\overline{x}_2$ [63].

The final goal in multi-objective optimisation is the identification of the Pareto-optimal set, which represents the trade-off between the competing objective functions. In this way the designer is presented with the complete solution to the problem, and a more informed decision on the choice of the final design can be made. In conclusion, an example of Pareto front is illustrated in Figure 3.6 for a two objective problem in which the first objective function is to be maximised (hence the negative sign), whereas the second objective is to be minimised.

3.6.2 Multi-Objective Tabu Search

The Tabu Search algorithm can be seen as a further development and enhancement of a local search method. Its main characteristic is the use of an adaptive memory to explore the entire design space in an efficient way, avoiding unfruitful moves. It is, therefore, a gradient-free method, that has at its core the Hooke and Jeeves (H&J) [64] local search algorithm. In more details, the optimiser generates $2n\_var$ new designs at each iteration, where n_var is the number of design variables, using a predefined step to decrease $x_i - \delta_i$ and increase $x_i + \delta_i$ the variable value. Next, the objective functions are evaluated for the $2n\_var$ new designs (or a reduced subset $n\_sample < 2n\_var$), and the "best" one is selected as the next base point in the search. This selection process is based on the dominance or Pareto-equivalence

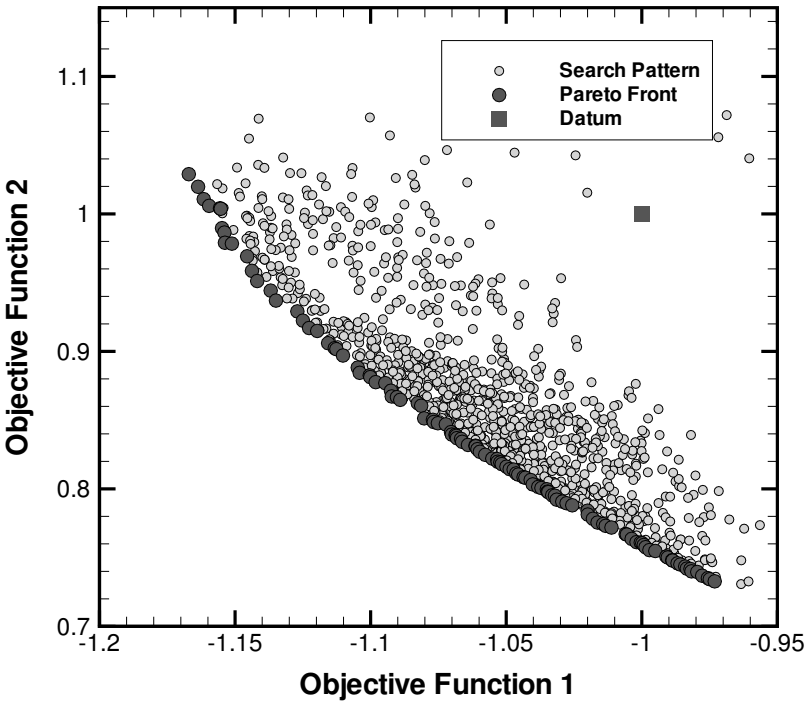

Figure 3.6: Example of a Multi-Objective Optimisation search pattern and Pareto front.

concepts earlier described. In addition, if more than one non-dominated design is identified at this stage, a random selection is performed and the remaining designs are stored in the *"Intensification Memory"*. Those designs will be used later on during the search procedure, as prescribed by Glover and Laguna [65].

The performance of TS can be effectively improved by repeating a previous successful H&J move and, if the new design found dominates the previous one, accepting it as current optimum. This technique is usually referred to as *"pattern move"*, and has the effect of leading the algorithm towards optimal regions of the design space. In the case in which the pattern move fails to find a non-dominated design a normal H&J move is performed.

Three main stages characterise the MOTS algorithm, each of which is associated with a particular memory allocation. Recently visited points are recorded in the *"Short Term Memory"* (STM), creating in such a way a Tabu list of points that will

not be revisited. A *"Medium Term Memory"* (MTM) is used to store the optimal or near-optimal points which are used to perform the *"Search Intensification"* (SI) strategy. This consists in returning to a region that seems attractive and perform a more intense search, but without revisiting the same solutions found. Search intensification occurs if there have been no successful moves for a defined number of local search iterations. While the SI intensifies the search of the optimum in one zone of the design space, the *"Search Diversification"* (SD) strategy moves the search to unvisited regions. A *"Long Term Memory"* (LTM) is used for this purpose, storing the areas which have been extensively searched by the optimiser. In order to perform such a move, the design domain is divided in N sub-domains and the number of points visited in each sub-domain represent its visited index. When SD occurs the search is moved to a random sub-domain with a low visited index. Figure 3.7 illustrates in a simple example the different memory categories of TS. The final stage of the algorithm is the *"Step Size Reduction"* (SSR) and occurs after a continued lack of successful moves. This strategy is performed to ensure an intensive search in the neighbourhood of the current optimal solutions. The step sizes of each design variable are reduced and the search returns to a randomly selected point from the MTM.

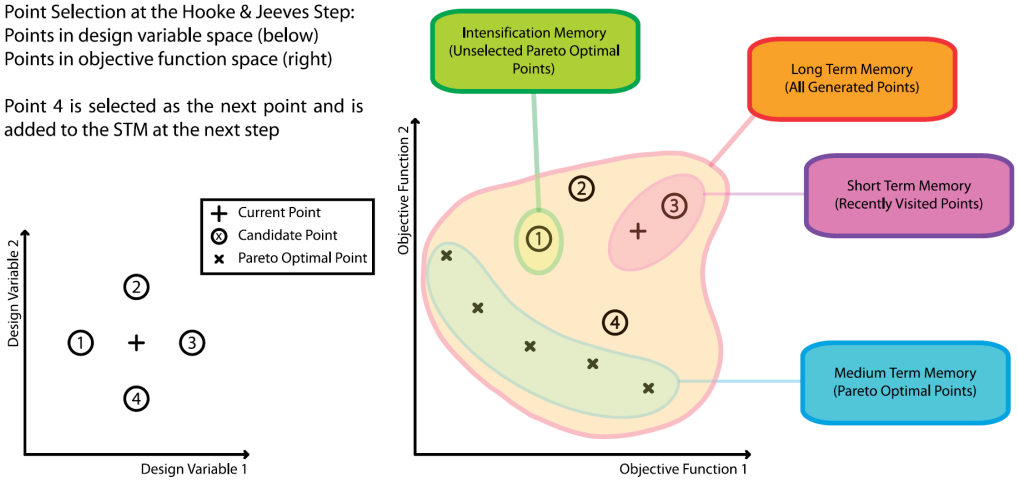

Figure 3.7: Point selection for the Hooke & Jeeves move and Tabu Search memories. Adapted from [3].

3.6.3 MOTS Software Description

The flow diagram of the MOTS algorithm is illustrated in Figure 3.8. The sequential iterative process of the algorithm is performed using a local counter *i_local*, which is reset every time the MTM is successfully updated. Moreover, when *i_local* reaches some user-specified values, the different strategies described in the previous section (Intensification, Diversification and Step Size Reduction) will be executed. Finally, the optimisation process is halted when a stopping criteria is reached, i. e. maximum number of iterations or evaluations, or when the defined wall-clock time has elapsed. In both cases, the final Pareto-optimal set will be output, together with a history of the optimisation process.

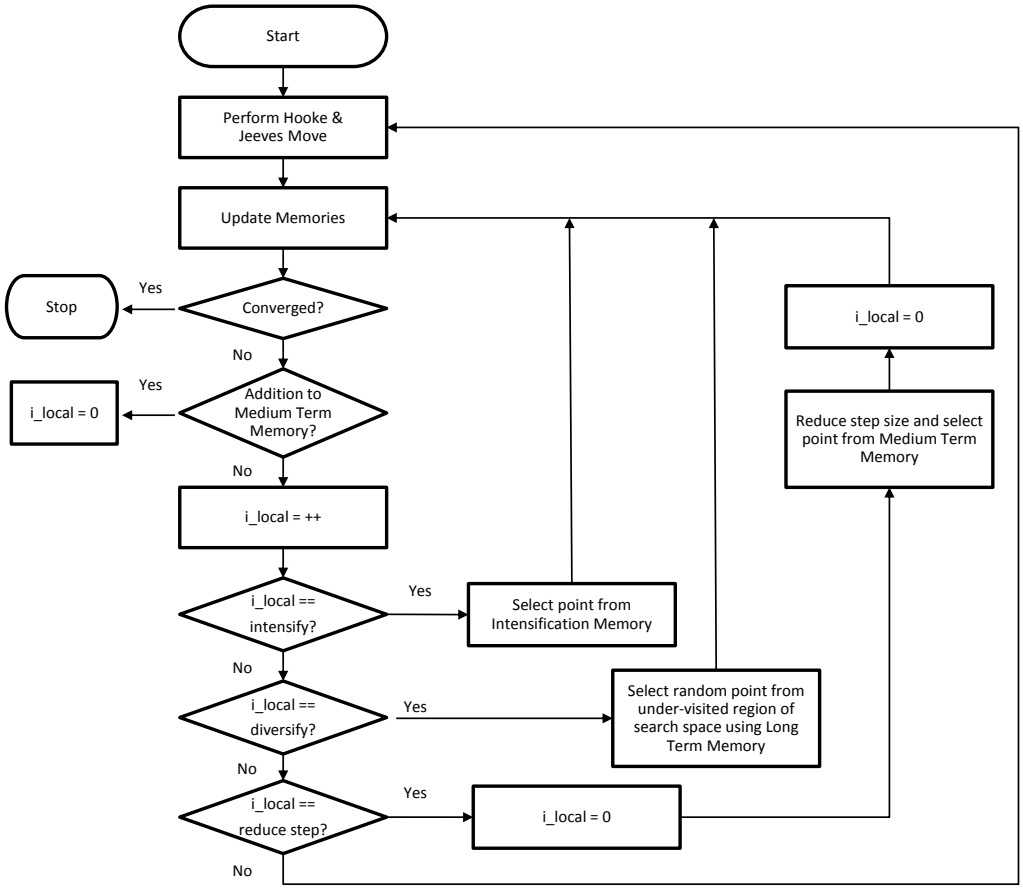

Figure 3.8: Flow diagram of the multi-objective Tabu Search algorithm. Source: [4].

An additional advantage of MOTS over other optimisation algorithm is repre-

sented by the ease with which *"binary"* constraints are handled. In fact, this class of constraints does not require the quantification of the extent of the violation, so that if any point is identified as infeasible it can easily be flagged as Tabu and will not be visited again. Nonetheless, as a result of the specification of many binary constraints within an optimisation process, the design space can be divided into many disjoint feasible and infeasible regions. As a result, the complexity of the optimisation problem is considerably increased.

The *"penalty function"* class of constraints represents, instead, a less intrusive specification of design infeasibility. In this case, a quantification of the constraint violation is needed to move the search into feasible regions. The advantage of this method is the increased freedom of the optimisation algorithm in changing the design variable values allowing small constraint violation in order to see the behaviour of the objective functions in these regions of the design space. On this basis, the constraint assigned using penalty function approach can also be defined as soft constraint, while hard constraints are those which, when violated, deem the design to be infeasible.

From a more technical point of view, the algorithm has been coded using MPI (message passing interface) standards, in a *"Master and Slaves"* configuration. This allows the process to be performed in a parallel environment, and the n_sample generated designs can, thus, be evaluated in parallel. In particular, the core of the optimiser is located in the master, whereas the slave processes manage the evaluation of the objective functions of a particular design vector provided by the master. This parallel execution, namely *"Functional Decomposition"*, is coupled to the parallel execution of the CFD analysis or *"Domain Decomposition"*, providing a multi-level parallelisation capability which allows a drastic reduction of the time to completion.

Finally, MOTS has been developed and proved to be particularly effective on aerodynamic problems [66]. In [58] the MOTS algorithm has been compared with a leading multi-objective genetic algorithm, NSGA-II [59], showing that the two algorithms perform comparably. Moreover, the tool has successfully been used by

Kipouros and Ghisu [4, 3, 63, 67, 68] in the multi-objective optimisation of axial compressors.

3.6.4 Evolutionary Algorithms and NSGA-II

Evolutionary Algorithms (EAs) have received in the last years considerable attention from the research community. Their capability to extensively explore the design space, as well as their inherent parallelism have established them as methods for exploring the Pareto front of multi-objective optimisation problems. Moreover, EAs have been shown to be effective methods for handling complex and multimodal design spaces that presents discontinuities and disjoint feasible spaces [69]. These algorithms attempt to solve optimisation problems by mimicking the processes of Darwinian evolution. In their general formulation a number of artificial individuals is defined which searches over the design space, competing continually with each other. It is hoped that over time some of these individuals will evolve and identify the optimal solution of the problem. Typically, the individuals are represented by fixed length strings of real or binary variables.

Many independent implementation instances of EAs can be found in literature [70], amongst which the three main are: Genetic Algorithms (GAs); Evolution Strategies (ESs); and Evolutionary Programming (EP). In this work the focus is posed on GAs, which have proved to be the most popular of the three EAs.

Canonical Genetic Algorithms are started with the generation of ξ random individuals (obtained setting each value in every string using a random number generator) which form the *"initial generation"*. This initial set of individuals is then evaluated to obtain the relative objective functions value and assigned a fitness value indicating the quality of the solution in terms of pareto-optimality, as proposed by Goldberg [71]. Therefore, individuals with high fitness scores represent better solutions to the problem than population members with lower fitness scores. After this initial phase the main loop of the algorithm begins. The selection of $\xi/2$

pairs of parent from the initial population is performed using a stochastic approach in which the probability of choosing an individual is proportional to its fitness. An intermediate population is so created (fittest individuals can feature more than once), from where each pair of individuals is then recombined with probability P_C using the *"crossover"* operator to produce a pair of children. This process involves the random selection of a cross point in the parents' string of variables and the recombination of the obtained four chunks to form the offspring. A new population of ξ individuals is formed. Following crossover, a *"mutation"* operator which invert each bit in every string with probability P_m (usually lower than 1%) is applied to the entire population. Finally, this newly evaluated population is set as the current population and the iterative cycle is repeated until some halting criteria (e.g. maximum number of iterations, convergence, wall-clock time) is reached.

However, the pareto-optimality sorting mechanism just described does not guarantee that the Pareto set be uniformly sampled. In fact, when multiple equivalent optima are identified EAs have shown the tendency to converge to a single solution and often lose identified optimal solutions [72]. This phenomenon is caused by the stochastic errors in the selection process and is usually known as *"genetic drift"* [69]. The development of first-generation EAs has, therefore, focused on overcoming this problem by preserving diversity in the population, thus trying to also prevent premature convergence. The use of some kind of niching technique was proposed by Goldberg [71] to keep the EAs from converging to a single point on the pareto. Though no practical implementation is presented, it posed the initial idea of niches which has been used in many recent EAs implementations.

The *"fitness sharing"* is, for example, a frequently used niching technique based on the idea that individuals in a particular niche have to share the available resources. Practically, this is achieved trough the definition of a neighbour region around each individual and the degradation of the individual's fitness value according to the number of population members located inside this region. A *"niche radius"* defined

by the user is used to identify the neighbourhood, making the method case specific.

A second-generation EAs has also been developed, this time with focus on efficiency. The concept of *"elitism"* was then introduced as a method to guarantee that the final solutions of the optimisation process are non-dominated with respect to every other solution that the EA has produced. Also, the use of elitism techniques enhances the convergence properties of a EAs, ensuring that the search is directed toward the non-dominated solutions. Usually an external or secondary population is used to retain the non-dominated individuals found along the evolutionary process, as shown in the work of Zitzler and Thiele [72]. However, this strategy introduces some complication in the memory management and increases the computational costs of the algorithm (comparison of an higher number of solutions to establish ranking). A more efficient way of guarantee both elitism and spread of solutions on the pareto front is presented by Deb et al. [59], with the implementation of a Non-dominated Sorting Genetic Algorithm-II (NSGA-II).

The NSGA-II is a more efficient version (in term of computational time) of the previously developed NSGA, with an improved algorithm for the non-dominated sorting of the individuals. In particular, for each solution two entities are calculated: the number of solutions that dominate it or *"domination count"*, and a set of solutions that it dominates. For each solution of the first non-dominated front (i.e. domination count equal zero) each member of the relative dominated set is visited and its domination count reduced by one. If after this operation any of the dominated members present a domination count equal to zero, it is moved on the second non-dominated front. The process is then continued for all the members of this newly generated front, so that the third front is identified. Finally, the process is executed until all the fronts are identified. This technique allows a reduction of the required time for the sorting process of the solutions, although it increases the memory requirements (less restrictive penalty considering modern resources).

In addition, to preserve diversity of the solutions a *"crowding distance"* is also

calculated for each individual and used as a secondary criteria during selection. If two solutions are identified which have the same rank, the one with a lower crowding distance is selected. The estimation of the density of solutions around a particular individual is based on the average distance of two points on either side of the individual along each objective. These values are then normalised and summed up to obtain the overall crowding-distance value.

Finally, the elitist characteristic of the algorithm is guaranteed using a simple systematic comparison of individuals from parent and offspring populations. In particular, the non-dominated solutions of the offspring population are compared with that of the parent, forming an overall non-dominated set. This set becomes the parent population for the next generation, and if its size is less that the initial population size it is completed with individuals from the offspring population.

Thanks to the above described characteristics (intrinsic elitism, fast sorting and evenly spread solutions), the NSGA-II has become a landmark against which other multi-objective evolutionary algorithms have to be compared [70]. Thus, NSGA-II features as a secondary optimisation algorithm within the optimisation framework used throughout this work.

Chapter 4

2D Optimisation Applications

The optimisation framework introduced in Chapter 3 is here used for the aerodynamic optimisation studies of a 2D multi-element aerofoil. The high-fidelity RANS simulation is preferred to the panel coupled boundary layer code as evaluation method, due to the higher accuracy of the method and the affordable computational cost for 2D problems. In particular, both the Ansys®suite and the Solar-TAU chains are used, as described in more detail later in the chapter. Two different optimisation set-ups are executed to tackle the design problem of increasing the aerofoil lift capabilities and, concurrently, reduce its drag levels.

The first set-up presented, indicated as *"single-point"*, aims at improving the aerodynamic performance of the configuration varying only the deployment settings of the high-lift devices. Using the MOTS algorithm, the trade-off between lift and drag performance is identified and the Pareto front revealed. A detailed post-processing of the outcomes of the optimisation is performed in order to illustrate the link between geometrical changes and aerodynamic improvements. Moreover, a comparison between MOTS and NSGA-II is performed, after the same optimisation case is executed using the evolutionary algorithm and the Solar-TAU chain.

From the analysis of the single-point optimisation results, the sensitivity of the optimised configuration to changes in the operating conditions is highlighted. There-

fore, a second optimisation study is proposed, which includes the design's sensitivity to changes in angle of attack within the optimisation process. The set-up of this second optimisation includes also flap shape modifications, since it is recognised that these variables considerably affect the stall behaviour of the configuration. Despite the increased complexity and computational cost of the optimisation, MOTS is once again able to identify a Pareto front and increase the performance of the datum aerofoil.

4.1 Test Case Description

The high-lift configuration selected as test case for the numerical-assisted design study is the GARTEUR A310 aerofoil [73]. The configuration has been derived from the 3D swept wing of the A310 aircraft, corrected applying a local normalisation. The aerofoil comprises a slat, a main element, and a single-slotted flap, as shown in Figure 4.1. Two different rigging settings are possible for the high-lift devices, to reproduce landing and take-off conditions. Here, the moderate deployment settings are chosen, which are characteristic of a take-off case. Reference wind tunnel tests, carried out in the ONERA F1 wind tunnel, are available at a Reynolds number of $Re = 4.1 \times 10^6$ and $M_\infty = 0.2$ [74].

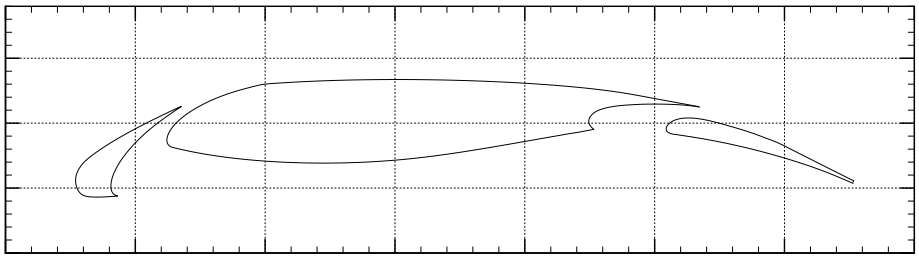

Figure 4.1: GARTEUR A310 aerofoil.

Prior to the execution of the optimisation process a validation and verification study is performed. For this purpose, the available experimental data are compared

with numerical simulations, performed at the same onset conditions. The obtained results are presented in the next section.

4.2 Validation and Verification

For the validation study here presented the flowfield around the datum configuration is evaluated using Ansys®CFX v5.0 on a similar mesh to the one presented in Section 3.5.1. The onset conditions used are specified in Table 4.1. Due to the confidentiality of the data the absolute values of the obtained results cannot be presented here.

Table 4.1: ONERA F1 wind tunnel onset conditions.

Mach number	Ma	0.2
Reynolds number	Re	4.1×10^6
Angle of attack	α	12.2° and 20.4°

A comparison of the pressure coefficient distribution (cp) over the aerofoil is presented in Figure 4.2 for the specified angles of attack $\alpha = 12.2°$ and $\alpha = 20.4°$. For both conditions, the numerical solution shows a good agreement with the wind tunnel data, with only a slight mismatch on the slat element at the higher angle of attack. At this condition, the wind tunnel data show the presence of a separation bubble on the suction side of the slat element, which cannot be captured by the numerical simulation, due to the assumption of fully turbulent flow.

Moreover, a comparison of numerically evaluated and experimental polars is shown in Figure 4.3. The CFD simulation satisfactorily predicts the aerodynamic performance of the aerofoil for angle of attack up to maximum lift. However, the numerical solution slightly under-predicts both the cl_{max} and the α_{clmax} values. This phenomena can be related to the chosen turbulence model, namely k-ω SST, which tends to overestimate flow separation. However, the earlier break-down of the flow is conservative in term of design of the configuration, and does not considerably affect the results of the optimisation. Also, the predicted α_{clmax} is indicated in the

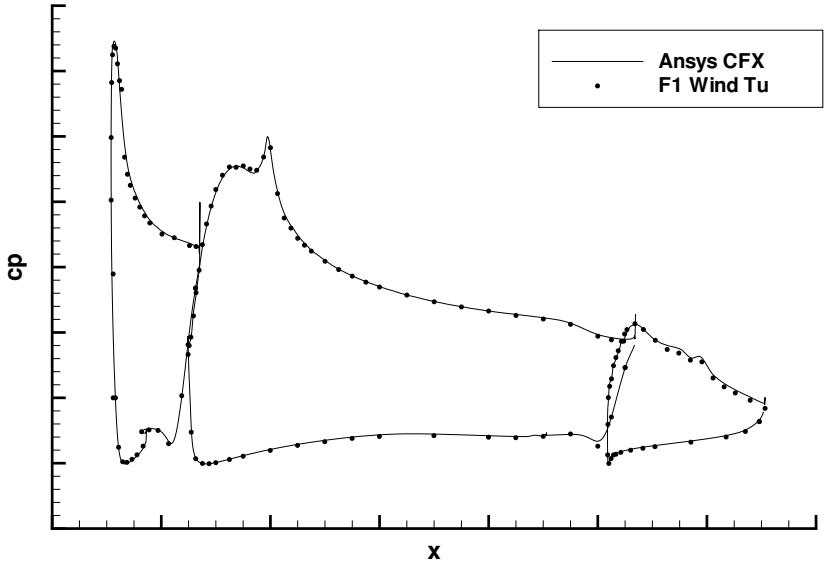

(a) Angle of attack $\alpha = 12.2^{\circ}$

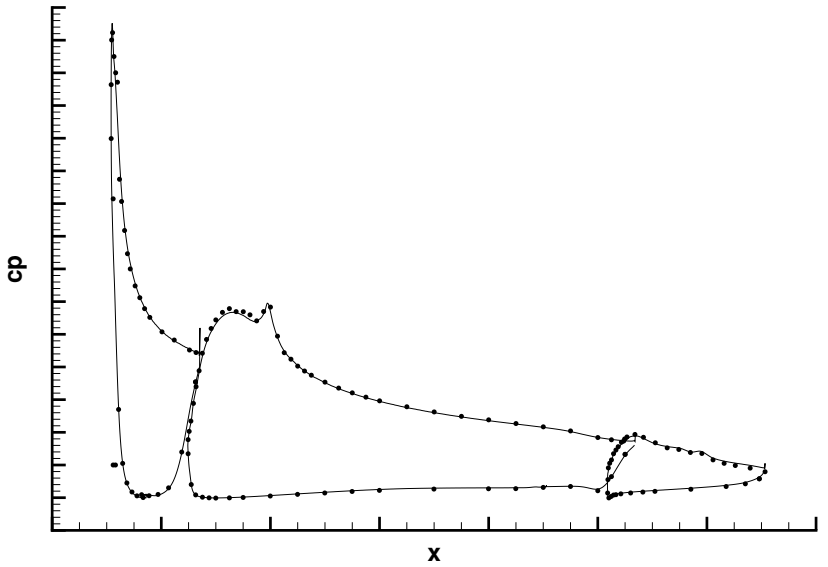

(b) Angle of attack $\alpha = 20.4^{\circ}$

Figure 4.2: Pressure coefficient distribution on the GARTEUR A310 aerofoil at $\alpha = 12.2^{\circ}$ (a) and $\alpha = 20.4^{\circ}$ (b). Ansys®CFX simulation results (solid line) are compared with wind tunnel data (dots).

plot as α_1, and it represents the condition at which the optimisation processes are performed. A direct comparison of the drag coefficient cannot be made, due to the inconsistency of the experimental data (pressure tabs measurement versus wake survey). Nonetheless, the numerical solution predicts *cd* values that fall between the two experimental curves.

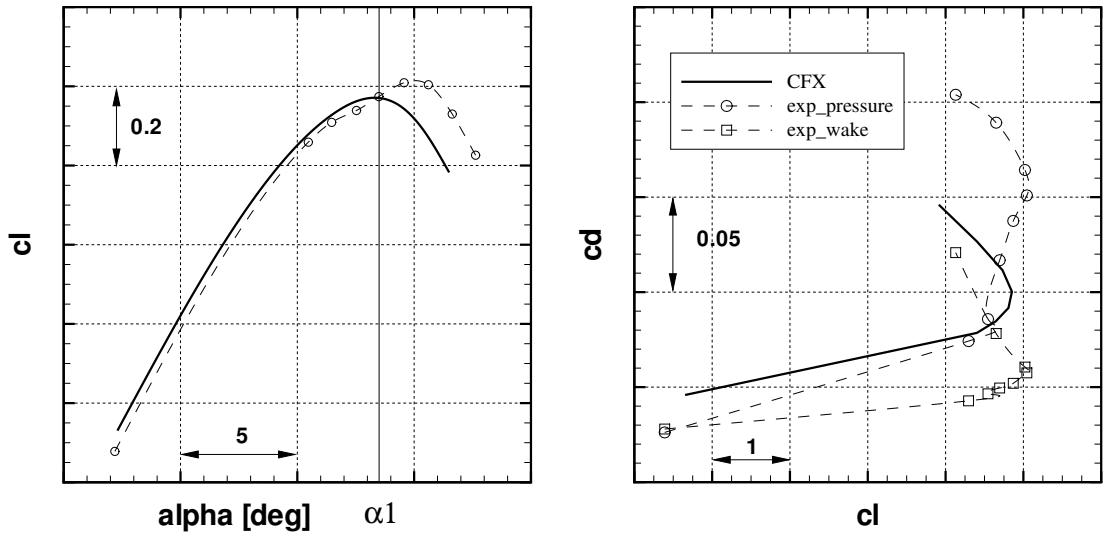

(a) $cl - \alpha$ (b) $cd - cl$

Figure 4.3: Comparison of $cl - \alpha$ and $cd - cl$ polars for numerical simulations (solid line) and wind tunnel data (line with circles). Both pressure tabs and wake survey measurements are plotted for the $cd - cl$ polar.

The validation and verification study is completed with a grid convergence analysis. Three different meshes with increasing number of grid points are generated coarsening and refining the standard mesh used so far in the validation study. A RANS solution is then obtained for each mesh for a fixed angle of attack. The so obtained lift and drag coefficients are compared against wind tunnel tests (the cd evaluated using pressure data is used) for the same flow settings, allowing the quantification of the numerical error. Figure 4.4 shows the percentage error plotted as a function of the spacing on the airfoil surface. Clearly, the trend for both the lift and drag coefficients shows that the numerical error reduces with increasing mesh size. However, despite the more accurate solution achieved with the fine mesh, the

medium one is selected for the subsequent optimisation problems due to its better trade-off accuracy/computational cost.

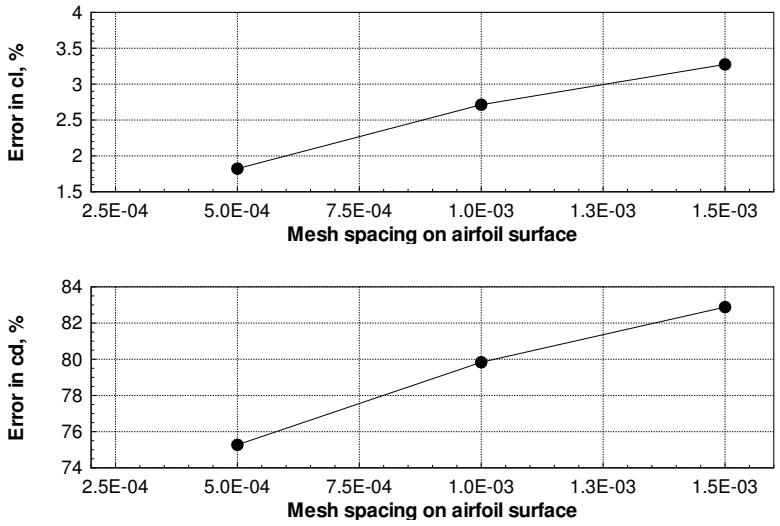

Figure 4.4: Mesh convergence study at $\alpha = 12.2°$ for the GARTEUR A310 aerofoil. The standard medium grid (260×10^6 nodes) obtained with airfoil surface spacing $= 1.0e^{-3}$, is coarsened using spacing $= 1.5e^{-3}$ (230×10^6 nodes) and refined using spacing $= 5e^{-4}$ (385×10^6 nodes).

Finally, the convergence behaviour of the numerical solution is analysed, in order to identify the minimum number of iterations required to achieve a converged solution. Figure 4.5 shows the history of the averaged density and momentum residuals, together with the aerodynamic coefficients, during the simulation at the numerical maximum angle of attack condition α_1. After 160 iterations the residuals of the solution converged to the selected threshold of 10^{-6}, and both the aerodynamic coefficients present converged behaviour. However, to allow the optimizer the exploration of configurations with harder convergence behaviour, the maximum number of iterations is set to 250 time-steps, after which the simulation is stopped even if the residuals are above the set threshold. Clearly this approach does not guarantee the same level of convergence if the maximum number of iterations is reached, but it is considered sufficient for the application within an optimisation process. Moreover, *cl* and *cd* mean values and standard deviations are evaluated using the last 50 iteration and a warning flag is issued if the analysed design presents a mean to

stdandard deviation ratio greater than $5e-2$ on either coefficient.

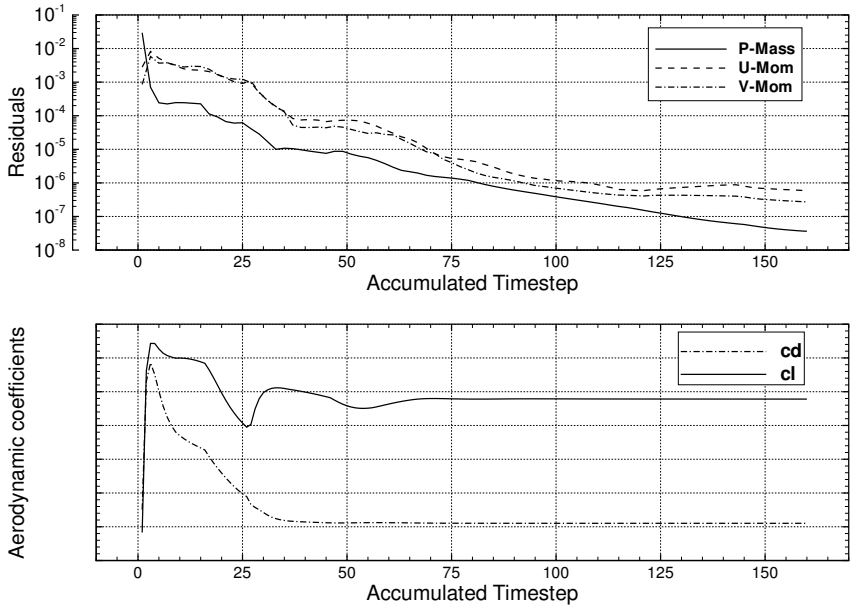

Figure 4.5: Datum design convergence monitor for the numerical solution at α_1

4.3 Single-point Optimisation

The first optimisation set-up here described aims at increasing the lift performance of the GARTEUR A310 configuration, reducing, at the same time, the generated drag. The RANS solution obtained in the validation study using the medium density grid is considered as baseline. In particular, the aerodynamic coefficients are evaluated at the angle of attack at which the datum configuration achieves its numerical maximum lift, indicated as α_1 (see Figure 4.3). Therefore, the optimisation is performed at a fixed angle of attack.

The multi-objective definition of the above stated design problem is expressed by the minimisation of the two objective functions:

$$\text{obj1} = -\frac{cl}{cl_0} \quad ; \quad \text{obj2} = \frac{cd}{cd_0} \tag{4.1}$$

where the subscript 0 indicates datum design values.

The deployment settings of slat and flap elements, expressed in the Cartesian coordinate system, are considered as design variables. Thus, a total of six variables are used to describe the problem (3 per element). Hard constraints are applied on the values of the design variables to exclude zero gap configurations from the optimisation process. In addition, element intersection checks are performed within the meshing tool, as described in Section 3.5.1.

The MOTS algorithm is chosen for this optimisation study, in conjunction with the Ansys®suite. The range of variations of each variable, and its correspondent initial step size used within MOTS, are summarised in Table 4.2. In the practical parametrization process the translational parameters δ are normalised with the aerofoil chord c_{ref}, introducing the variables $\Delta = \delta/c_{ref}$. The deflection angle is, instead, defined as incremental value over the datum deflection Θ_0.

Table 4.2: Range of variation and initial step size for the single-point optimisation set-up.

Parameter	**Description**	**Step**	**Range**
$\Delta x_S = \delta x_S/c_{ref}$	Slat Translation along x	0.02	$[-0.06; 0.14]$
$\Delta z_S = \delta z_S/c_{ref}$	Slat Translation along z	0.01	$[-0.05; 0.09]$
Θ_S	Incremental slat rotation	1°	$[-10.0°; 10.0°]$
$\Delta x_F = \delta x_F/c_{ref}$	Flap Translation along x	0.02	$[-0.09; 0.17]$
$\Delta z_F = \delta z_F/c_{ref}$	Flap Translation along z	0.01	$[0.00; 0.06]$
Θ_F	Incremental flap rotation	1°	$[-10.0°; 10.0°]$

In order to define the design space, i.e. the range of variability of the design variables, many different constraints should be considered. One of the most important class of constraints is represented by the kinematics used to deploy the high-lift devices. This aspect has an important influence on limiting the relative positions of slats and flaps in respect of the main element. Although, in the current study this class of constraints is not taken into account, the design space is defined, for both slat and flap, keeping these limitations in mind (see Table 4.2).

Finally, the settings of the MOTS optimisation algorithms are summarised in

Table 4.3: MOTS optimization algorithm settings for the single-point optimisation of the GARTEUR A310 aerofoil.

Parameter	Value	Description
n_stm	15	Short Term Memory (STM) size
n_ltm	4	Long Term Memory (LTM) size
intensify	15	Intensify search after *"intensify"* iterations without adding to the (MTM)
diversify	25	Diversify search after *"diversify"* iterations without adding to the (MTM)
reduce_ss	45	Reduce step sizes and restart after *"reduce_ss"* iterations without adding to the (MTM)
n_sample	4	Number of points randomly selected at each Hooke and Jeeves move
n_regions	4	In the LTM each variable is divided into n_regions to determine which regions of the design space have been under-explored
max_evals	2000	Max Evaluations halting criteria

Table 4.3 (a more detailed explanation of the parameters is presented by Jaeggi et al. [3]). These same settings are used throughout the work presented in this thesis, and will, therefore, be referred to when presenting further optimisation problems (e. g. Chapter 6).

4.3.1 Results and Discussion

The numerical results of the single-point optimisation process are presented in this section. The data are extracted from the optimisation framework after 164 MOTS iterations, corresponding to 1217 objective functions evaluations. The time required for a single candidate CFD simulation is about 40 minutes, and an average of 8.5 objective functions evaluations (up to 11) per iteration are required. To reduce wall-clock run-time the optimisation is run on a eight-node parallel PC cluster of 3.0 GHz Intel 5160 Xeon dual-core machines, exploiting the multi-level parallelisation capability of the tool. In more detail, two slave processes are concurrently executed and controlled by a master process. Moreover, within each of the slave process the CFD simulation is performed in parallel on 4 CPU nodes. Finally, the residual

improvement in the objective functions is selected as halting criteria, resulting in a 450 hours, or 20 days, turn around time.

Figure 4.6 shows the revealed Pareto front, together with the optimisation search pattern. The trade-off between the competing objective functions is clearly captured, with many identified designs which improve both objective functions. To gain a better understanding of the physics that lead to the performance improvements, three optimum solutions from the Pareto front are analysed in more detail and compared with the datum aerofoil. In particular, the two extreme optima, representing maximum (normalized) lift coefficient and minimum (normalized) drag coefficient and a compromise solution are selected. These designs are highlighted in Figure 4.6, whereas a summary of the objective functions values is provided in Table 4.4.

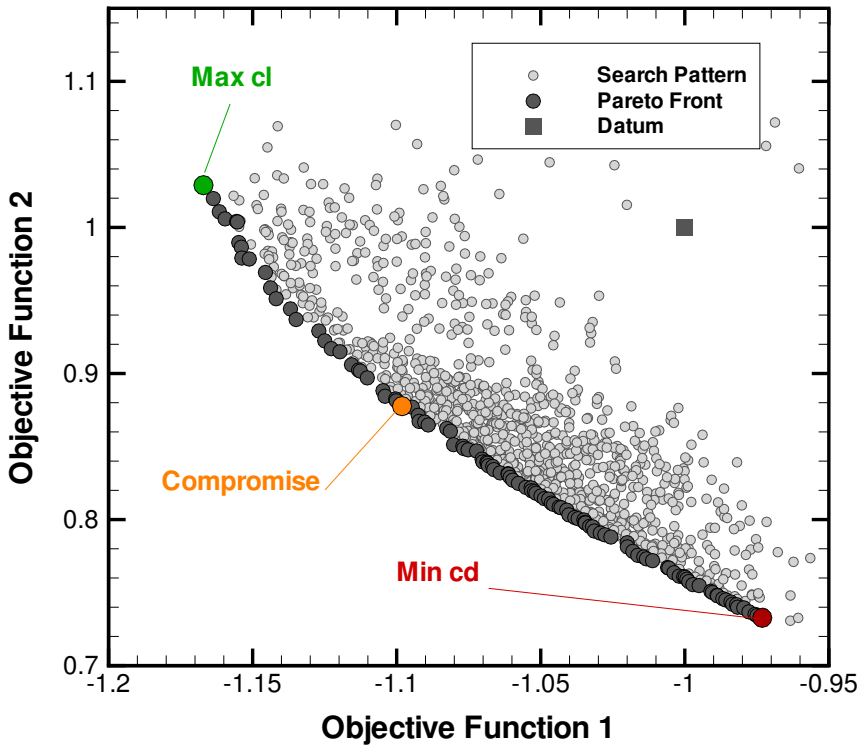

Figure 4.6: Pareto front and Search Pattern revealed using MOTS after 164 iterations for the single-point optimisation.

The identified optimum designs are illustrated in Figure 4.7 together with the da-

Table 4.4: Design variables and objective functions improvement for the three optimum designs max_cl, compromise and min_cd, single-point optimisation.

	Max_cl	**Compromise**	**Min_cd**
Δobj1	-16.7%	-9.6%	1.2%
Δobj2	$+2.9\%$	-11.6%	-24.7%
Δx_S	-0.0178	-0.0178	-0.0178
Δz_S	-0.033	-0.023	-0.023
Θ_S	4°	9°	10°
Δx_F	-0.009	0.011	0.011
Δz_F	0.045	0.045	0.045
Θ_F	4°	-1°	-9°

tum aerofoil. Although each configuration presents peculiar features, some common trends can be identified from the plots. Firstly, all the optimum solutions increase the gap and lap values of both slat and flap elements, compared with the datum design. This characteristic is especially true for the max_cl configuration, which presents the higher separation between the aerofoil elements. It must be highlighted that the optimisation process does not consider structural constraints on the flap deployments, which might be affected by the increased load associated with the higher deployment. However, it is usually the landing and not the take-off configuration (here considered) which sizes the flap tracks. Secondly, the deflection angle of the slat is consistently increased amongst all the optima. On the contrary, a contrasting trend is observed for the flap deflection angle, which is reduced for both the min_cd and compromise designs, while it is increased max_cl solutions.

The changes in deployment settings are reflected in the elements pressure coefficient distribution, shown in Figure 4.8. For all the optima, the increased spatial separation between slat and main wing leads to a reduction of slat effectiveness and a consequent reduction in its aerodynamic load. The opposite trend is, instead, observed for the flap element, whose effectiveness is increased. As a result, both the flap and main wing aerodynamic loads are higher than the datum configuration ones.

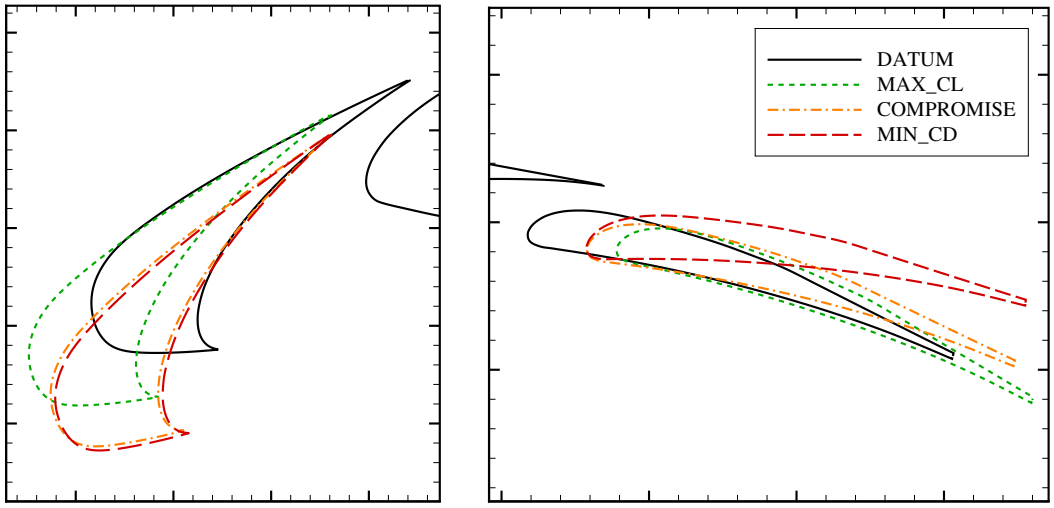

Figure 4.7: Geometry comparison for datum (black solid line), max_cl (green dotted line), compromise (orange dash-dot line) and min_cd design (red dashed line), single-point optimisation.

As shown in Table 4.4, the max_cl design achieves a 16.7% increase in the lift coefficient with a drag increase that leads to a penalty on the objective function definition as low as 2.9%. This considerable performance gain is achieved increasing the deflection angle of both slat and flap by 4 degrees. The resulting lift polar, illustrated in Figure 4.9, presents a slightly higher value for the angle of attack of maximum lift (slat effect) and an upward shift (flap effect) compared to the datum. The drag performance is similar to the datum design in the range of angle of attack near α_1. However, for lower angle of attack the drag coefficient is higher than the datum. As a result of these trends the lift to drag ratio of the max_cl design is generally higher than the datum, becoming lower only at moderate angles of attack.

On the contrary, the min_cd design reduces the deflection angle of the flap element by 9 degrees and increases the slat deflection by 10 degrees. The result is a 24.7% decrease in the drag coefficient and only a 1.2% penalty in the lift performance. Again, the flap and slat effects are visible in the lift polar (Figure 4.9). A downward shift of the polar is shown together with an increase in the angle of maximum lift. The low drag coefficient values drive the lift over drag performance of the design,

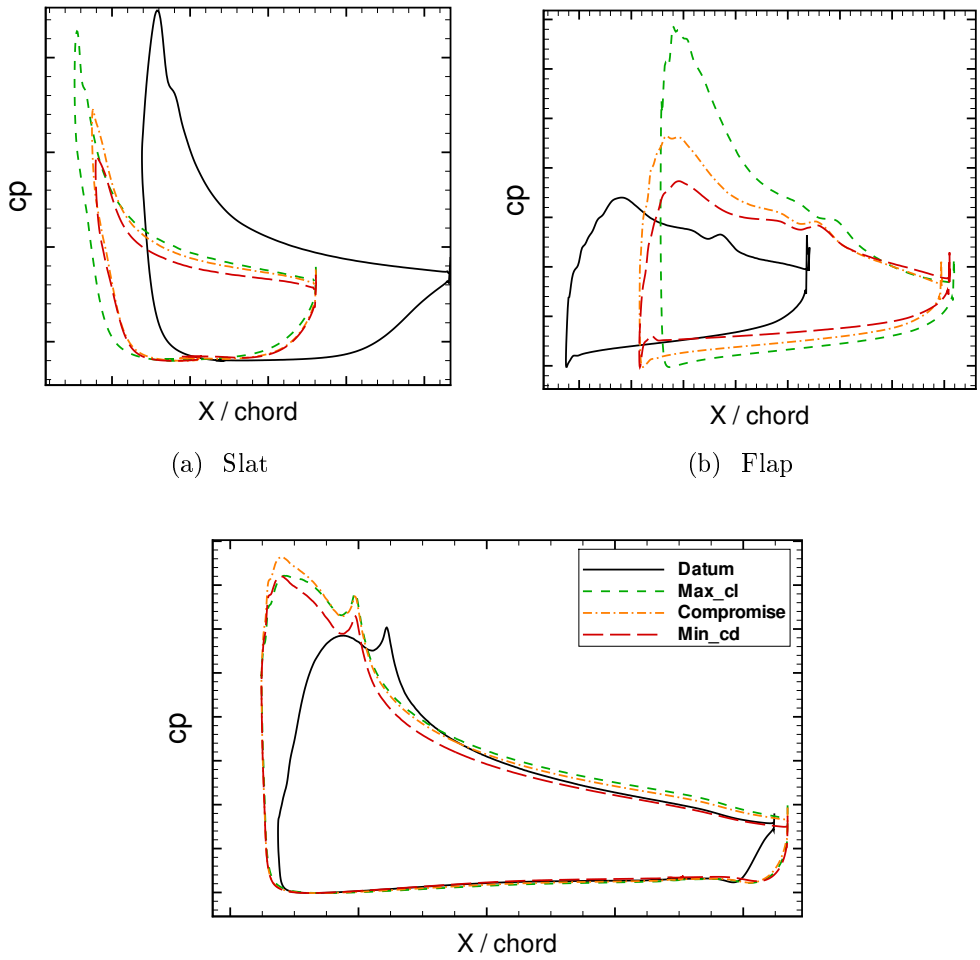

(a) Slat

(b) Flap

(c) Main

Figure 4.8: Pressure coefficient distribution for datum (black solid line), max_cl (green dotted line), compromise (orange dash-dot line) and min_cd design (red dashed line), single-point optimisation.

showing values higher than the datum ones in the whole range of angle of attack considered.

Finally, the compromise solution presents performance levels that lie between the two extreme designs. The deployment settings are similar to the min_cd design, with the only differences being the increased deflection of the flap element and the slight reduction of the slat deflection. This design outperforms the datum configuration in both lift and drag performance for the whole range of angle of attack considered.

The flow field that develops around the analysed designs is illustrated in Figure

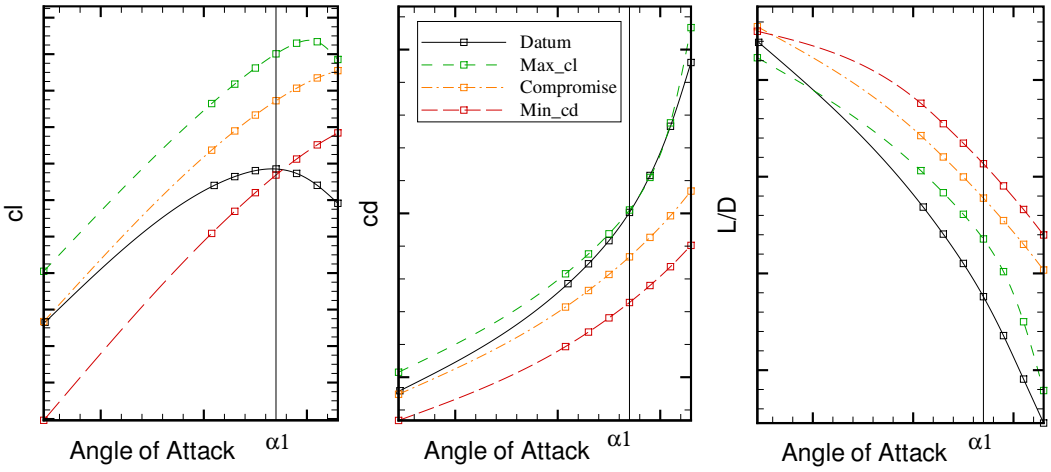

Figure 4.9: Polar comparison for datum (black solid line), max_cl (green dotted line), compromise (orange dash-dot line) and min_cd design (red dashed line), single-point optimisation.

4.10. The contour plots show a wide area of high turbulence intensity for the datum configuration generated by the merging of the main element and the flap wakes, followed further downstream by the merging of the slat wake. This flow characteristic leads to a high value for the drag coefficient and an early breakdown in lift. The increased elements gaps of the optima solutions mitigate the described effect, reducing the drag and allowing the aerofoil to achieve a greater lift and a higher maximum angle of attack. Nevertheless, the max_cl design shows an increase in the turbulence intensity at the flap trailing edge (as a result of the increased load), indicating an incipient flow separation. This feature limits the angle of attack of maximum lift for this design to a value close to the datum configuration one. Such behaviour is not visible in the min_cd and compromise designs, which present a considerably greater angle of attack of maximum lift.

4.3.2 Optimisation Algorithms Comparison

The results of the single-point optimisation presented earlier are compared with an identical set-up performed using the NSGA-II optimisation algorithm and the Solar-

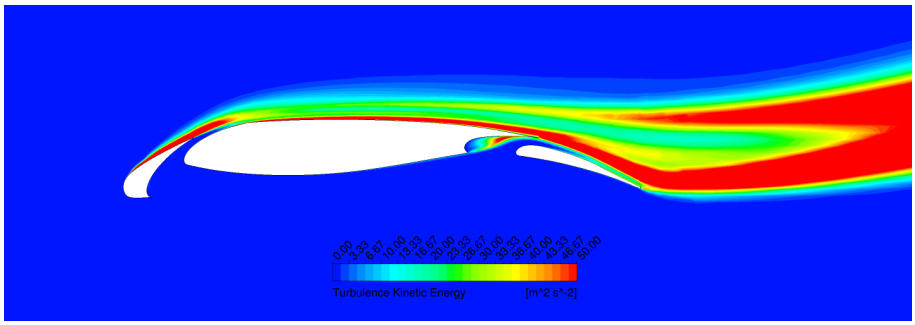

(a) Datum

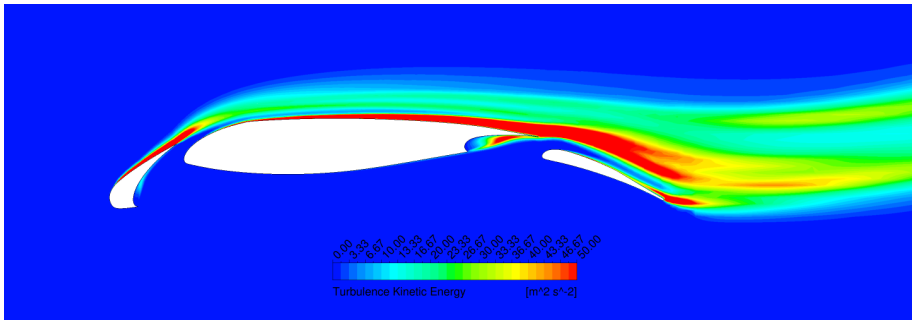

(b) Max_cl

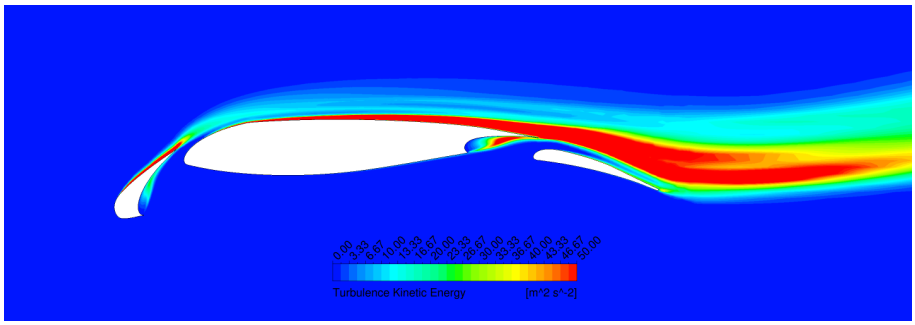

(c) Compromise

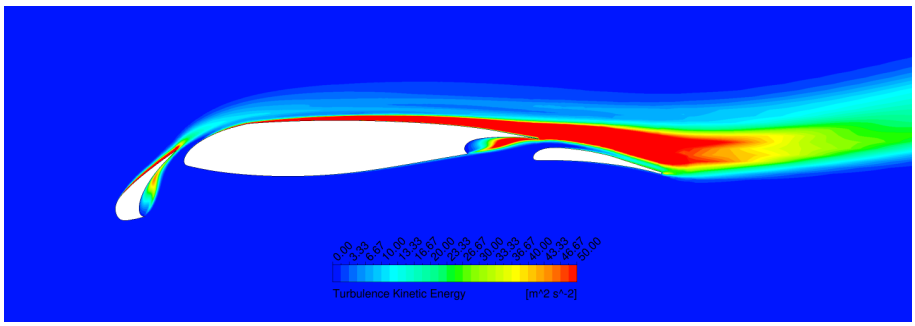

(d) Min_cd

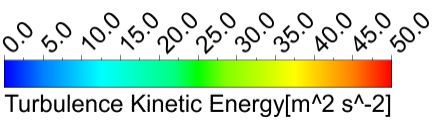

Figure 4.10: Wake visualization for datum and optimum designs, single-point optimisation.

Table 4.5: NSGA-II optimization algorithm settings for the single-point optimisation of the GARTEUR A310 aerofoil.

Parameter	**Value**	**Description**
init_pop	48	Initial Population size
sbx_prob	0.7	Crossover Probability
mut_prob	0.2	Mutation Probability
max_gen	40	Maximum number of generations
conv_gen	3	Convergence Generation
con_thrs	0.001	Convergence Threshold
η_c	15	Distribution index for crossover
η_m	20	Distribution index for mutation
seed	0.1	Initial population seed for random start

TAU chain. In order to guarantee a meaningful comparison, the data analysed are extracted from the two optimisation runs at a similar stage of the optimisation process (equal number of objective functions evaluations). The settings for the NSGA-II algorithm are summarised in Table 4.5, whereas Figure 4.11 and Figure 4.12 illustrate a comparison of the two Search Patterns and Pareto fronts revealed. It is evident that the optimum solutions identified by MOTS fully dominate the NSGA-II ones, apart from a few optima located at the extreme minimum obj2 region. Moreover, the MOTS revealed Pareto front presents a much better spread of the solutions and is also more populated. Indeed, the richness of the Pareto front is one of the limitations of evolution based algorithm, since a maximum size is implicitly set once the number of individuals is fixed [75].

A cross validation of the three optima so far analysed and three respective ones from the NSGA-II Pareto front, is performed to eliminate CFD solver dependencies. The results, illustrated in Figure 4.13, show a higher dependency of the MOTS Pareto from the CFD suite selected. Nonetheless, MOTS solutions continue to dominate NSGA-II ones except in the case of the min_cd design. Finally, the compromise solution for both MOTS and NSGA-II presents identical objective function values when evaluated with the TAU solver, although the configurations present different deployment settings. This characteristic is an indication of the complexity

and richness of the design space in the tackled aerodynamic design problem.

The analysis of the results obtained from the execution of the single-point optimisation has shown a considerable increase in the performance of the datum GARTEUR A310 aerofoil. However, the identified optima usually show also an increased sensitivity to changes in operating conditions. For example, the lift coefficient of the max_cl optima earlier analysed, varies considerably in the range of angles of attack close to the prescribed α_1, as illustrated in Figure 4.9. Therefore, a different optimisation set-up is proposed that directly takes into account such sensitivity and aims at reducing it.

4.4 Uncertainties and Interval Analysis

The use of numerical optimisation techniques in aerodynamic design can provide notable increase in performance for the specified design conditions. However, the identified optima are often very sensitive to small variations in manufacturing tolerances and/or operating conditions [76]. As a result, the optimized design could present inferior performance under actual operating conditions, limiting its application in real-world problems [77]. Uncertainty quantification is, therefore, becoming an increasingly important aspect of the numerical optimisation assisted design [78].

Real-world system design has to face different kinds of uncertainties which are usually beyond the (direct) control of the designer. Chen et al. [79] identify four types of uncertainties:

1. **Changing environmental and operating conditions.** Typical examples are operating pressure, temperature, Mach number or angle of attack.

2. **Production tolerances and actuator imprecision.** This type of uncertainty is related to the manufacturing of a product, which can be performed only to a certain degree of accuracy.

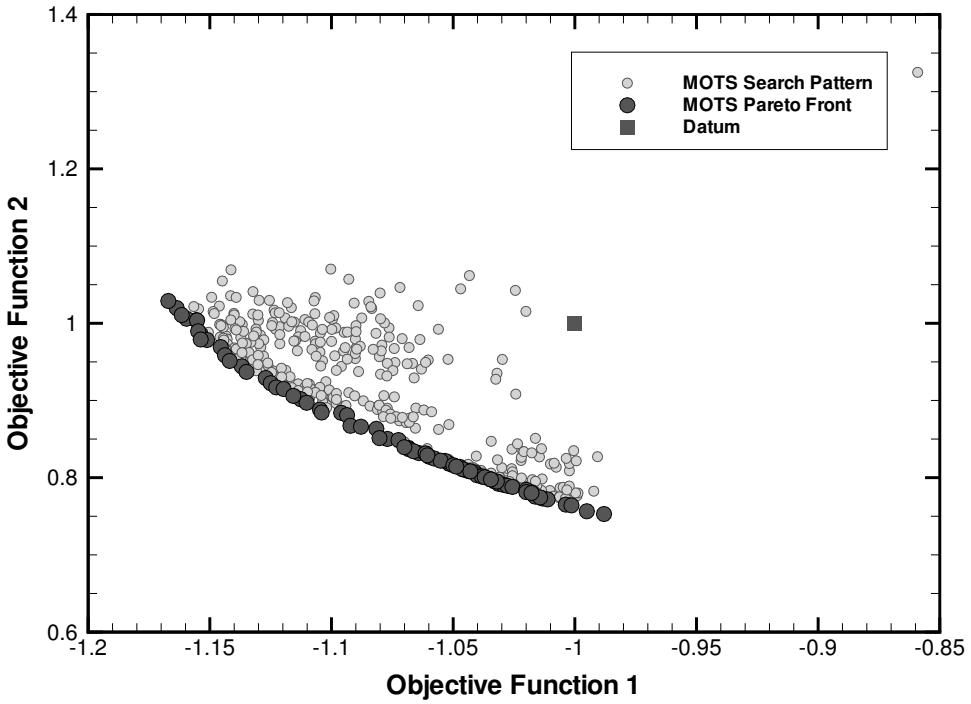

(a) MOTS algorithm + CFX

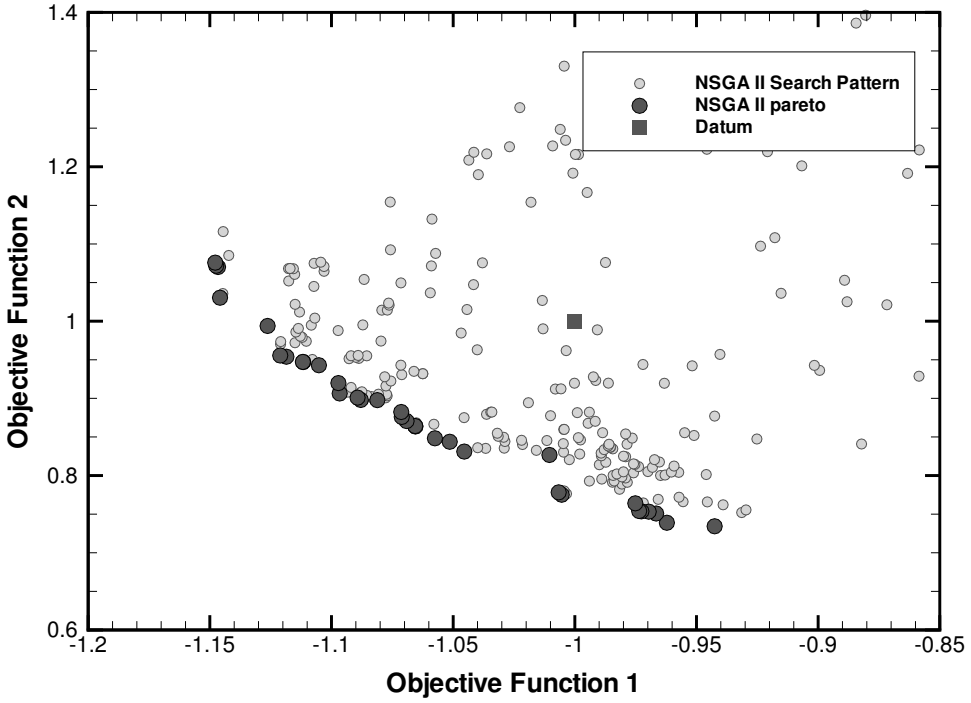

(b) NSGA-II algorithm + Tau

Figure 4.11: Comparison of Search Pattern for MOTS (a) and NSGA-II (b), single-point optimisation.

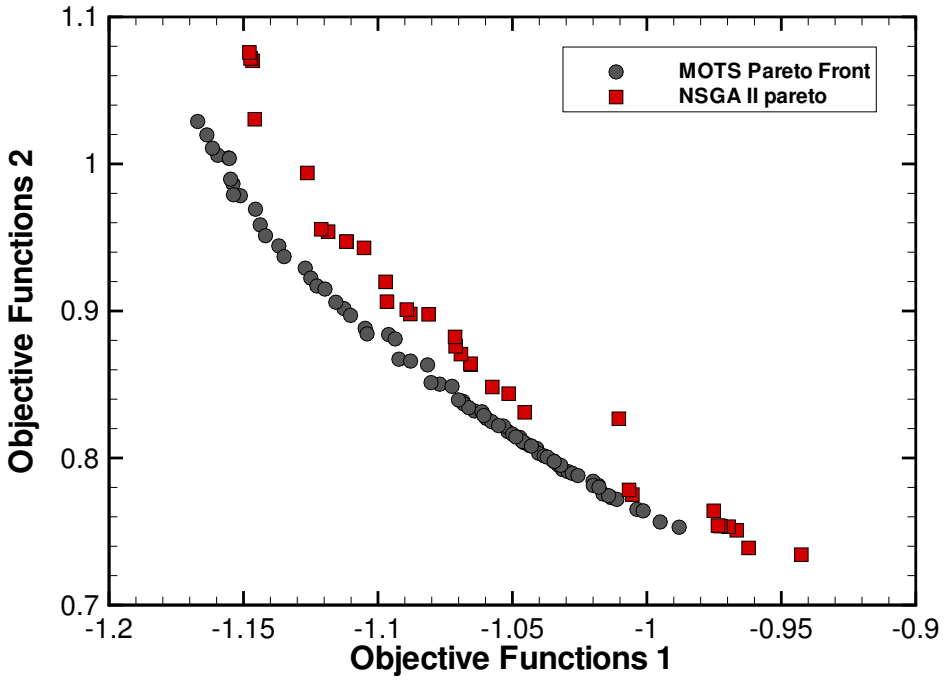

Figure 4.12: Comparison of Pareto front for MOTS and NSGA-II, single-point optimisation.

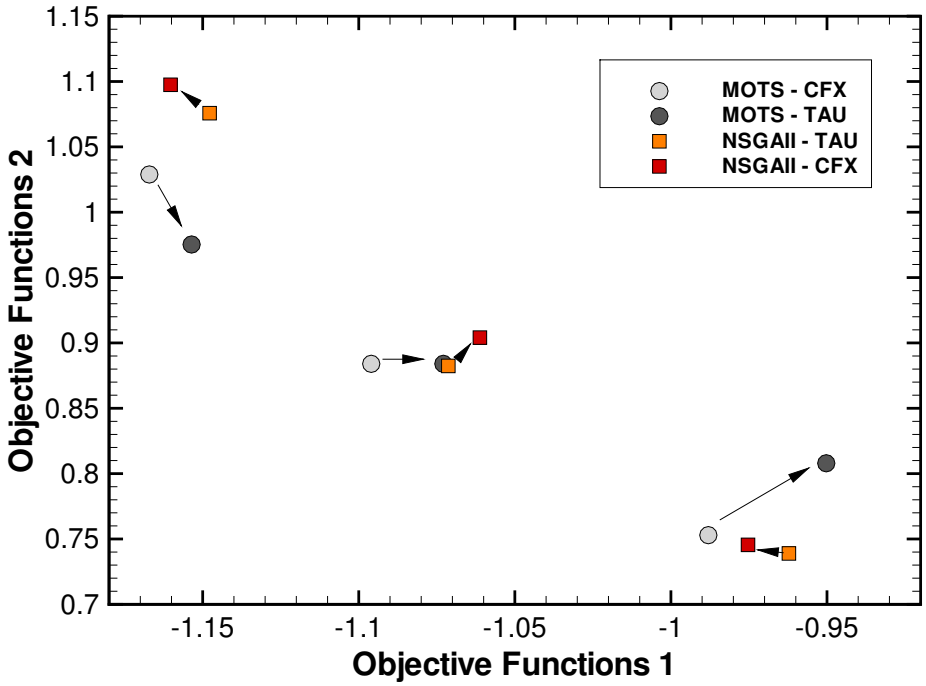

Figure 4.13: Cross validation of MOTS and NSGA-II Pareto fronts, single-point optimisation. Three points from the respective Pareto fronts are evaluated using a different CFD suite.

3. **Uncertainties in the system output.** Uncertainties related to the imprecision in the evaluation of the system output. It includes measuring errors as well as approximations errors (linked to the use of models instead of physical objects).

4. **Feasibility uncertainties.** Related to the fulfilment of constraints the design variables must satisfy. This class of uncertainties considers the uncertainty effects on the design space rather than on the objective function.

In this work only the first type of uncertainties is considered, with an optimisation setup (presented in the next Section) which considers aerofoil's performance over a range of angles of attack.

The Interval Analysis (IA) method [80] is used to evaluate the sensitivity of the analysed design to variation of α. The basic idea in IA is to identify an appropriate interval for the input parameters of interest and to evaluate the output interval consisting of all possible values of the result of the operations performed on the input. This method is especially effective for problems such as the one here tackled, where only the bounds of the uncertain parameters are needed rather than their precise probabilistic distributions. Moreover, it can be implemented in a systematic way on modern computing systems, therefore taking advantage of existing simulation tool such as a CFD code.

4.5 Multi-point Optimisation

The second optimisation set-up here presented, namely *"multi-point"*, uses the interval analysis method to account for changes in operating conditions. In particular, the input angle of attack value of the CFD simulation is varied within a specific range to evaluate the variation of the aerofoil aerodynamic performance. A similar approach is used by Srinath in [81] for the optimisation of a single element aerofoil. Three values of α are chosen within the range $[\alpha_1 - 1°; \alpha_1 + 1°]$ to define the two

objective functions expressed in Equation (4.2). The first objective function relates to the overall performance of the configuration in the range of angle of attack considered, leading the optimizer to explore designs that increase the cl value of the three operating points $\alpha_1 - 1°$, α_1, and $\alpha_1 + 1°$. The second objective function aims at minimising the variation of the lift coefficient with angle of attack. A constraint on the drag coefficient is applied through the penalty function P. Such a penalty is active only when the sum of the drag coefficient at the three operating points is higher than the datum value.

$$\begin{aligned} \text{obj1} &= -\frac{cl|_{\alpha_1-1} + cl|_{\alpha_1} + cl|_{\alpha_1+1}}{(cl|_{\alpha_1-1} + cl|_{\alpha_1} + cl|_{\alpha_1+1})|_0} + P \\ \text{obj2} &= \frac{\|cl|_{\alpha_1} - cl|_{\alpha_1-1}\| + \|cl|_{\alpha_1+1} - cl|_{\alpha_1}\|}{(\|cl|_{\alpha_1} - cl|_{\alpha_1-1}\| + \|cl|_{\alpha_1+1} - cl|_{\alpha_1}\|)|_0} + P \\ P &= \max\left[0, \frac{1}{2}\left(\frac{cd|_{\alpha_1-1} + cd|_{\alpha_1} + cd|_{\alpha_1+1}}{(cd|_{\alpha_1-1} + cd|_{\alpha_1} + cd|_{\alpha_1+1})|_0} - 1\right)\right] \end{aligned} \tag{4.2}$$

The aim of the optimisation setup here proposed is the identification of high-lift configurations with a reduced sensitivity of the maximum lift coefficient to the variation in α. This characteristic is important for the satisfaction of the landing and take-off requirements of the high-lift system, since the evaluated cl_{max} value can be guaranteed even if the angle of attack deviates from its prescribed value. It is not here suggested that the cl_{max} condition is a robust operating point and that the aircraft should operate at this condition.

Indeed, this multi-point optimisation set-up represents a much more challenging task compared with the single-point. First of all, in order to achieve the desired response, the stall characteristic of the aerofoil has to be modified. Element deployment settings can only partially influence the behaviour of the aerofoil near the maximum lift region. As a consequence, flap shape modification is included within the optimisation process, using the Free Form Deformation parametrisation technique described in Chapter 3. Finally, the increase of both the number of design

point evaluations and design variables leads to a considerable rise in computational cost.

The generated FFD control grid around the datum flap element is illustrated in Figure 4.14. A total of 16 control points are used all around the flap geometry in order to be able to accurately define a local region where deformation occurs. In fact, it is an essential requirement in high-lift design not to modify the shape of the stowed configuration in order to retain cruise performance. In the current study, flap shape changes are confined to the area between the flap leading edge and the suction side kink. Therefore, only the control points close to the specified region are allowed to move, as shown in Figure 4.14, where an example new shape is obtained prescribing deformations to the points 1-5. This parametrisation set-up introduces six additional design variables, defined in Table 4.6 together with their initial step size and range of variation.

Table 4.6: Range of variation for the additional shape parameters, multi-point optimisation set-up.

Parameter	Description	Step	Range
CP1_x	translation of control point 1 along x	0.05	$[-0.2; 0.2]$
CP2_x	translation of control point 2 along x	0.05	$[-0.2; 0.2]$
CP3_x	translation of control point 3 along x	0.05	$[-0.2; 0.2]$
CP3_z	translation of control point 3 along z	0.05	$[-0.2; 0.2]$
CP4_z	translation of control point 4 along z	0.05	$[-0.2; 0.2]$
CP5_z	translation of control point 5 along z	0.05	$[-0.2; 0.2]$

Finally, the MOTS algorithm is used in conjunction with Ansys®CFX to obtain the results presented next.

4.5.1 Results and Discussion

The results here presented are extracted from the optimisation process after 72 iterations, corresponding to 467 objective functions evaluations. Three times the number of CFD simulations has to be executed to evaluate the objective functions

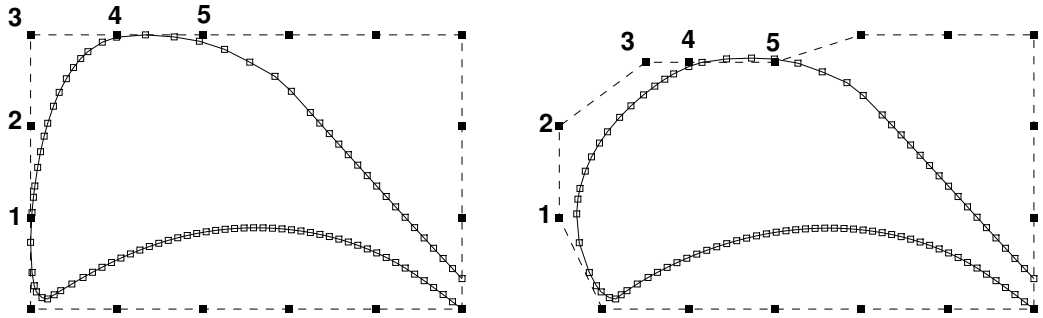

(a) Datum FFD Grid and Flap Geometry (b) Deformed FFD Grid and Flap Geometry

Figure 4.14: Example application of the Free Form Deformation algorithm to the flap element of the GARTEUR A310 aerofoil.

value compared to the single-point case. The increased computational cost combined with the increase in the number of design variables have pushed the turn around time of the complete optimisation to around 800 hours, just over 1 month. Evaluation time is selected as the halting criteria for this optimisation set-up. The tool is run on a twelve-node parallel PC cluster of 3.0 GHz Intel 5160 Xeon dual-core machines. The time required for a single candidate CFD simulation is around 120 minutes, and an average of 14 objective functions evaluations (up to 28) for iteration are required.

The revealed search pattern and the correspondent Pareto front are illustrated in Figure 4.15. It can be seen that this specific optimisation set-up produces a non-smooth Pareto front, with a discontinuity located in the region of minimum obj1 values. Furthermore, a much higher scatter is found in the Pareto front in comparison with the single-point results. These characteristics reflect the increased complexity introduced in both the design space and objective functions definition. Nonetheless, the MOTS optimisation algorithms is able to identify several optimum designs that improve both objective functions values.

The two extreme optimum solutions from the revealed Pareto front, indicated as min_obj1 and min_obj2, are analysed in detail. The values of the deployment settings for the two optima are reported in Table 4.7, together with the percentage

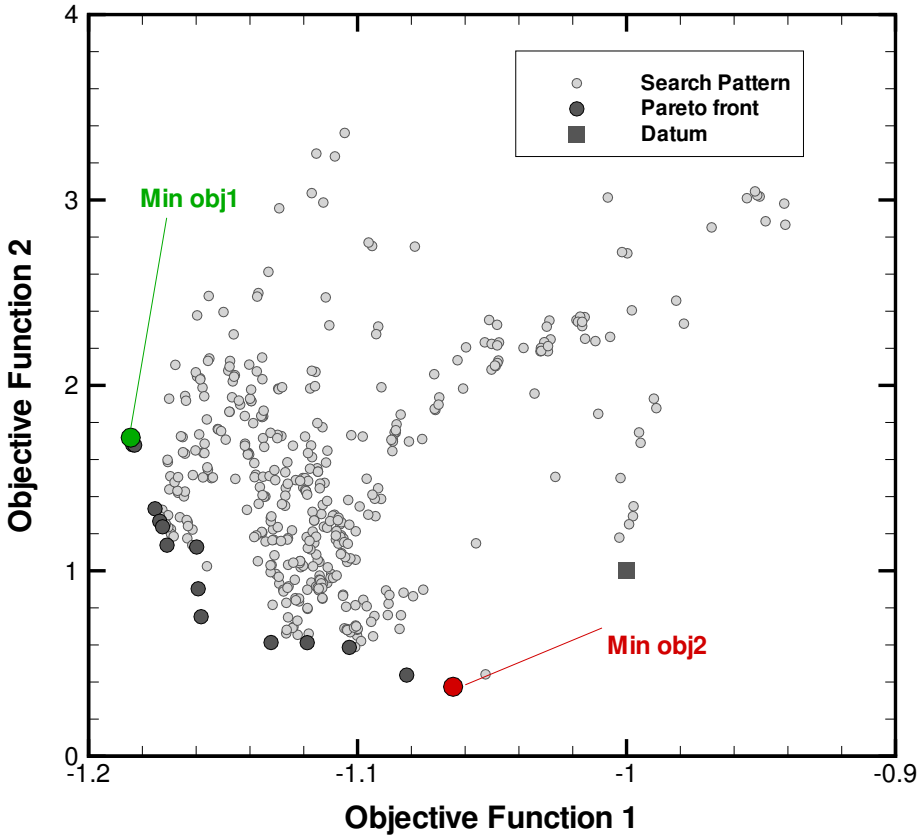

Figure 4.15: Pareto front and Search Pattern revealed by MOTS after 72 iterations, multi-point optimisation. The min_obj1 (green) and min_obj2 (red) are highlighted.

increase in the objective functions. An 18% increase in lift performance is achieved by the min_obj1 design, with a negligible increase in aerodynamic drag (only a 2% value for the penalty function P). However, for the same design, the value of the second objective function is 71.2% higher than the datum configuration. This behaviour can be explained considering the evaluated $cl - \alpha$ polars illustrated in Figure 4.16. As it can be seen from the plot, the min_obj1 design presents a higher α_{clmax}, which falls beyond the angle of attack range defined for the optimisation process. Therefore, the monotonically increasing segment of the lift curve is used for the evaluation of the objective functions, leading to very different values for the three lift coefficients at $\alpha_1 - 1°$, α_1, and $\alpha_1 + 1°$.

The min_obj2 design, instead, shows an improvement in both objective functions

Table 4.7: Design variables (deployments and shape) and objective functions improvement for the optimum designs, multi-point optimisation.

	Min_obj1	**Min_obj2**
Δobj1	-18.4%	-6.5%
Δobj2	71.2%	-62.6%
Penalty function P	2%	0%
Δx_S	-0.025	-0.005
Δz_S	-0.026	-0.036
Θ_S	7°	2°
Δx_F	0.007	-0.013
Δz_F	0.021	0.021
Θ_F	8°	2°
CP1_x	0.05	0.05
CP2_x	0.00	-0.1
CP3_x	0.00	0.1
CP3_z	0.2	0.15
CP4_z	0.05	0.10
CP5_z	0.15	0.05

(see Table 4.7). The $cl-\alpha$ polar illustrated in Figure 4.16 reflects the 6.5% increase in lift, showing an upward shift compared with the datum one. No increase in drag is, however, associated with the augmented lift performance, as shown by the null value of the penalty function P. Moreover, the cl_{max} region of this design falls within the angle of attack range defined for the optimisation process. The polar close-up (also shown in Figure 4.16) illustrates the reduced sensitivity of the optimum solution to variations in angle of attack values. In particular, a 63% reduction in the second objective function is achieved by the specific design.

Finally, Table 4.8 presents an assessment of sensitivity of the three optimum designs identified in the single-point optimisation set-up (evaluated using Equation (4.2)). The results show a much lower performance of all the optima compared with the datum design, emphasizing the importance of including sensitivity to changes in operating conditions within the design process.

The geometrical characteristics that lead to the performance increase are illustrated in Figure 4.17. Both the deployments settings and the flap shapes of the two

Table 4.8: Assessment of sensitivity to operational conditions for the single-point optima.

	Min_cd	**Compromise**	**Max_cl**
Δobj1	-0.3%	-11.2%	-18.0%
Δobj2	200%	139%	122%

optimum solutions are compared to the datum aerofoil. The improvement in lift performance is achieved increasing Δx for both the slat and flap elements, in agreement with the results obtained in the single-point optimisation. On the contrary, a reduction of the variable Δz_F is observed for both the optima. This translates, for the min_obj2 design, to the positioning of the flap near the trailing edge of the main element. Furthermore, the flap geometries of the two optima show common features: an increase in the element thickness at around 25% chord location and a reduction in the leading edge radius. It is important to point out that these shape changes do not affect the stowed configuration of the aerofoil, which retains its cruise shape.

Figure 4.18 illustrates the flow-field that develops around the two optimum configurations revealed, at the angle of attack α_1. For both the designs, the reduction in the flap lap reflects in a higher interaction of the main element wake with the flap upper surface. The airflow leaving the main element trailing edge presents a much higher curvature compared to the datum configuration (see Figure 4.18(b)). Such characteristic is emphasized by the shape of the flap element, which promotes the air to flow from the main element pressure side to the flap suction side. However, as a result of this, the main element recirculation bubble is also increased. It is evident that the stall behaviour of the configuration is dependent on the interaction between the main element wake and the flap walls. In particular, reduced flap gap settings, characteristic of the min_obj2 design, minimise the variation of lift with angle of attack in the near-stall region. With regard to the changes in slat settings, the same figure shows a much greater influence on the flow-field of the min_obj1

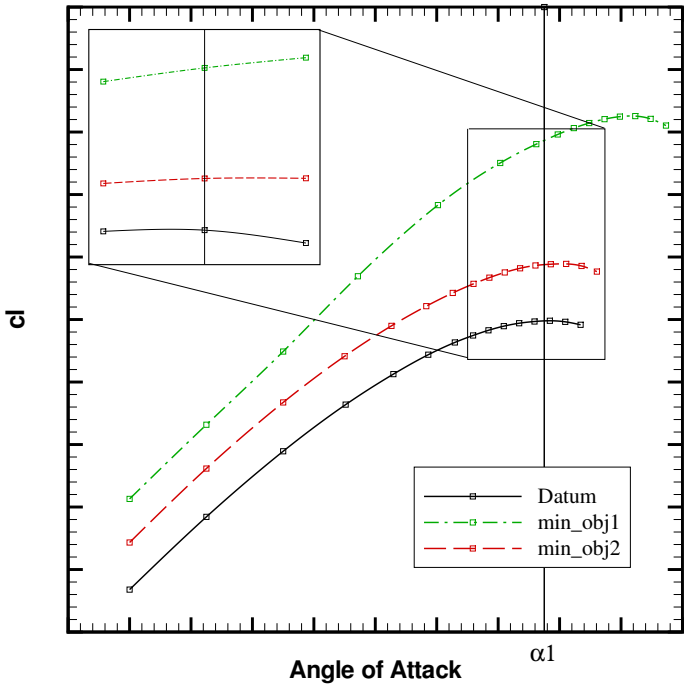

Figure 4.16: Datum (black solid line), min_obj1 (green dot-dashed line) and min_obj2 (red dashed line) $cl - \alpha$ polars comparison, multi-point optimisation. The close-up shows the considered range of angle of attack centred in α_1.

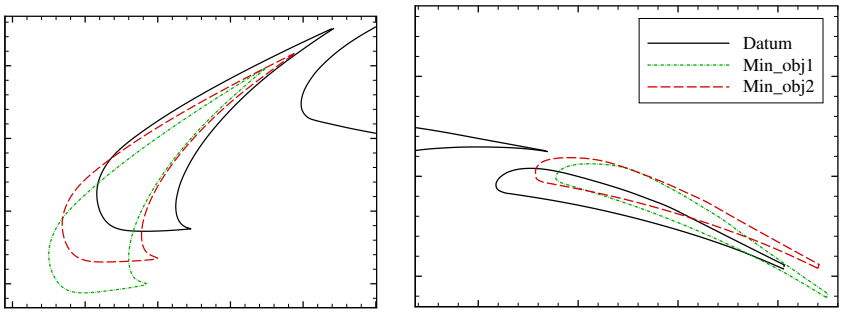

(a) slat deployments

(b) flap shape + deployments

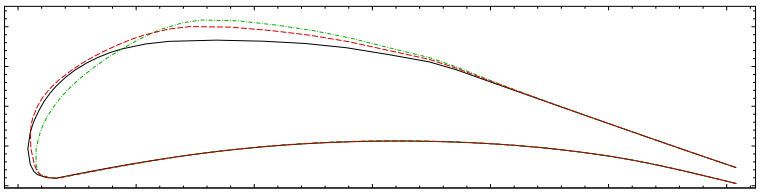

(c) close-up flap shape

Figure 4.17: Geometry comparison of Datum (black solid line), min_obj1 (green dot-dashed line) and min_obj2 (red dashed line), multi-point optimisation.

design. The stagnation point in the main wing is shifted aft, and the recirculation bubble in the slat cove region increases. This characteristics are reflected in the lift polar of the specific design, that presents a higher α_{clmax} value.

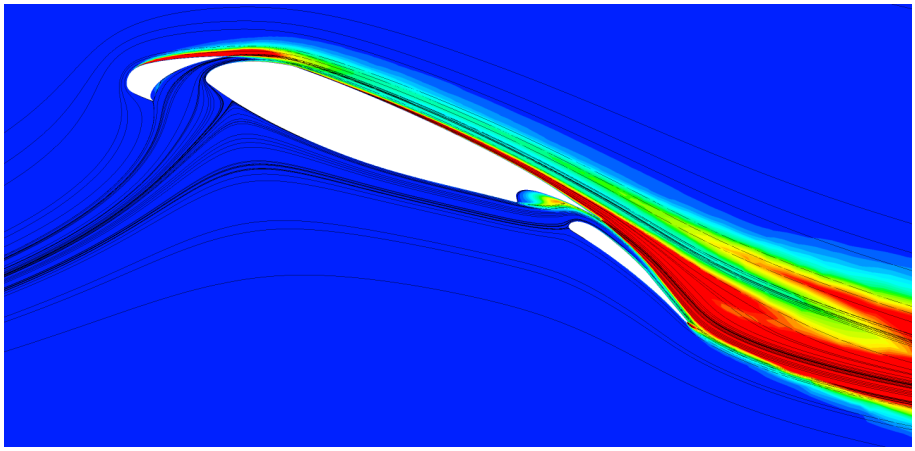

(a) Datum

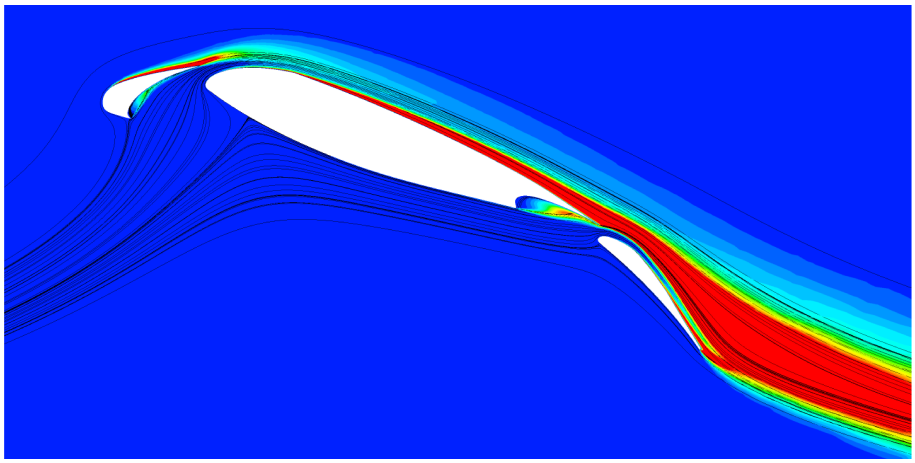

(b) Min_obj1

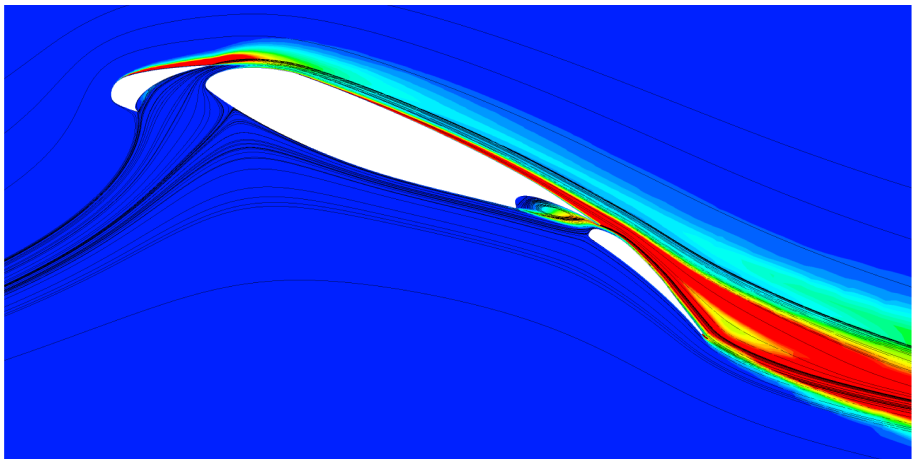

(c) Min_obj2

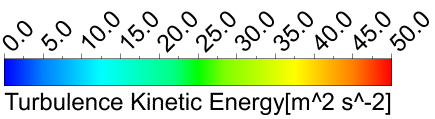

Figure 4.18: Wake visualization for datum and optimum designs at α_1, multi-point optimisation.

Chapter 5

The APODO Project

5.1 Introduction

The Engineering Doctorate programme differs in many aspects from a conventional PhD research. Firstly, the research project is always industrially focused, the problem being of direct relevance to the Industrial Sponsor. Secondly, the EngD researcher has to address not only the technical issues of the research work, but also *"management issues"* related to it, such as its business and commercial implications.

However, instead of focusing on the overall impact of the EngD research, the author in collaboration with the academic and industrial supervisors has decided to direct the above mentioned business analysis on a smaller project, namely APODO (Aerofoil POD Optimisation). Having a more limited scope compared to the overall EngD research, the APODO project is better suited to perform an analysis of the techniques used during its implementation as well as the challenges faced. Moreover, it is also an activity which is conducted at a higher Technology Readiness Level (TRL), meaning that it's impact on the Industrial Sponsor's business is more quantifiable and focused on a short-term period.

The APODO project represents an industrial application of the findings of the author's research. The project aims at implementing aerofoil optimisation capabil-

ities within a designer tool currently under development at the Industrial Sponsor. It is, therefore, a branch of a wider development programme. The analysis performed and presented in this chapter focuses on the project management skills and techniques required by the author to lead the project. The *"Agile"* development concept, described in more details in Section 5.3.1, is used to carry out the APODO project with the aim of minimising cost and maximising the quality of the delivered tool. Furthermore, the feedback and comments received by the designers during the testing and validation phase are also reported and discussed. But before entering the more managerial analysis, a technical description of APODO is presented.

5.2 Technical Description

The main goal of APODO is to enable shape optimisation for single element aerofoil at cruise, and deployment settings optimisation for multi-element aerofoils at take-off and landing. A Proper Orthogonal Decomposition (POD) Reduced Order Model (ROM), generated using RANS flow-field simulations, is selected as evaluation tool for the aerofoils' aerodynamic performance (a detail description follows in section 5.2.1) . The newly developed design tool is used to set-up the tradestudy and generate a set of different aerofoil shapes or deployment settings. These input files are then transferred to the High Performance Computing (HPC) cluster, and RANS simulations are performed for each design point. At completion of all the simulations, the POD approximation is generated using the available *"snapshots"*. The reduced order model is, then, downloaded to the local machine and the optimisation process can be set-up within the design tool, and executed locally.

Learning from the experience of previous ad-hoc optimisation implementations within the Industrial Sponsor environment, this architecture is preferred to a RANS-in-the-loop one. In fact, this optimisation strategy presents several advantages. First of all, the optimisation process is de-coupled from the RANS execution, reducing

the risk of failure during the process. Secondly, the generated POD model can be re-used to tackle different optimisation problems, as long as the same set (or a reduced set from the original one) of design variables is used. Furthermore, the workflow mimics the typical designer task, where a set of data is generated for the *"manual"* investigation of the design space. Finally, the use of POD model eliminates some of the disadvantages of reduced order model optimisations, where only integral quantities (e.g. aerodynamic coefficients) are used. In particular, since the POD is here used to represents an approximation of the entire flow-field, the user can perform the same post-processing tasks as with a full RANS simulation, like for instance, visualise pressure and mach contours or velocity streamlines.

However, the selected approach presents also some drawbacks. The model is not guaranteed to be accurate over the whole design space, especially if the problem tackled is highly non-linear. Besides, the number of snapshots required to construct an accurate POD model increases rapidly with the number of design variables. Finally, the mesh used within the CFD process for the generation of a POD model has to retain its topology which implies the use of either a structured mesh or mesh deformation techniques. The latter approach is used in the industrial implementation here presented, introducing some limitations on the range of variation of the deployment variables. In fact, while variations in deflection angle of the element can easily be accommodate by mesh deformation techniques, the variation in overlap and especially in gap is a much harder task. This is mainly due to the fine resolution of the baseline mesh in the slot region between two consecutive elements and the consequent deformation induces on the small surface and volume elements. If too big a difference between the baseline and the newly specified gap is imposed it is likely that the mesh deformation will generate negative volume cells. This behaviour is highly reduced with a proper definition of the baseline mesh for the mesh deformation process (baseline that presents variable value at the centre of the variation range) and appropriately define the range of variation of the gap variable.

5.2.1 Background Literature

The Proper Orthogonal Decomposition has its roots in statistical analysis, and is a powerful and elegant method to obtain approximate descriptions of a high-dimensional process [82]. It is a specific type of reduced basis technique, which provides a basis for the modal decomposition of an ensemble of functions. In literature the POD has usually been associated with the Karhunen-Loeve expansion and principal component analysis. However, a study presented by Liang et al. [82] shows that the POD actually consists of three closely connected and equivalent methods: the Karhunen-Loeve Decomposition (KLD), the Principal Component Analysis (PCA), and the Singular Value Decomposition (SVD). Independently from its mathematical implementation, the POD represents the most efficient method of capturing the dominant components of a given system using a finite number of *"empirical eigenfunctions"* or *"modes"*. Its optimality derives from the fact that the obtained basis functions minimise the average error of the approximation with respect to the full system.

A detailed description of the theory and the mathematical determination of the POD is presented by Holmes et al. in [83], and only a brief review is here given. Firstly, it is important to recognize that, although the POD can, and it usually is, applied to non linear problems, the basis functions provided by the methods are linear: *"Linearity is the source of the [POD] method's strengths as well as its limitations ..."* [83]. Nevertheless, the source of data used to generate the POD modes can be, indeed, non-linear.

Let's consider an ensemble $\{u^k\}$ of scalar fields, each being a function $u = u(x)$. The aim of the decomposition is to find an optimal basis $\{\varphi_j(x)\}_{j=1}^{\infty}$ for the ensemble, so that the finite dimensional representation of the form

$$u_N(x) = \sum_{j=1}^{N} a_j \varphi_j(x), \tag{5.1}$$

describes a typical member of the dataset better than representation of the same dimension in any other basis.

The optimality is expressed in mathematical terms as the minimisation of the average error between u and its projection onto φ. The same condition can be expressed as the maximisation of the average projection of u onto φ, suitably normalised:

$$\max_{\varphi} \frac{\left\langle |(u,\varphi)|^2 \right\rangle}{\|\varphi\|^2} \tag{5.2}$$

where $|\cdot|$ denotes the modulus and $\|\cdot\|$ is the L^2-norm, given by

$$\|f\| = (f,f)^{\frac{1}{2}},$$

and the notation $(\cdot,\cdot)$ expresses the inner product of two functions over a pre-defined interval. The solution of Equation (5.2) has multiple roots which constitute the basis functions in the linear decomposition in Equation (5.1). This problem is equivalent to a calculus of variations in which the quantity $\langle |(u,\varphi)| \rangle^2$ has to be maximised subject to the constraint that $\|\varphi\|^2 = 1$. It can be shown (see Holmes et al. [83]) that the solution to this problem requires the basis functions to satisfy

$$\int_{\Omega} \langle u(x)\, u(x') \rangle \, \varphi(x')\, \mathrm{d}x' = \lambda \varphi(x) \tag{5.3}$$

Therefore, the eigenfunctions $\{\varphi_j\}$ of the integral Equation (5.3) constitute the POD basis. When considering discrete cases, such as when dealing with computational results, the ensemble of functions u^k are a group of N-dimensional vectors. In this case, the kernel in Equation (5.3) becomes the autocorrelation tensor

$$\mathbf{R} = \langle u \otimes u \rangle,$$

and the integral eigenvalue problem becomes

$$\mathbf{R}\varphi = \lambda\varphi,$$

The evaluation of the basis functions allows the decomposition of any member of the ensemble u^k as

$$u(x) = \sum_{j=1}^{\infty} a_j \varphi_j(x) \tag{5.4}$$

The computational cost of the decomposition is proportional to the dimension N of u, since the $N \times N$ eigenvalue problem has to be solved to evaluate the basis functions. Consequently, the representation of a large system with a relatively small number of modes may be substantially expensive. However, the problem may be reduced to an $M \times M$ one, where M is the number of ensemble functions, through the application of the method of snapshots, due to Sirovich [84]. In this procedure a series of snapshots is generated, which typically correspond to state vector realizations of the system (solutions) at various times, frequencies, or configurations. The resultant autocorrelation matrix is given by

$$R_{ij} = \frac{1}{M} \int_{\Omega} u_i u_j \mathrm{d}\Omega \tag{5.5}$$

where u_i is the i-th snapshot and $i, j = 1, 2, ..., M$, and M is the total number of snapshots. The eigenvectors of R are computed as an intermediate step

$$Ra = \lambda a,$$

from which the POD basis functions can be calculated as

$$\varphi^K = \sum_{i=1}^{M} a_i^k u_i \,(x, y) \quad K = 1, 2, \ldots, M \tag{5.6}$$

where a_i^K is the i-th element of eigenvector a corresponding to the eigenvalue λ_K.

The eigenvectors of R are used to construct the POD basis functions as per Equation (5.6), while the eigenvalues can be interpreted as a measure of the "energy" captured by each eigenvector. In other words, they represent the amount of the variation associated with a particular mode. Typically, the modes are then sorted in descending eigenvalue order, and only p modes are included in the POD model, so that the energy captured is greater than some threshold (usually set to 99% or higher). It must be emphasised that the energy measure indicates how accurately a snapshot from the initial set can be reproduced, it is not related to the accuracy of reconstructing a new snapshot.

Figure 5.1 illustrates an example of the first four modes of a POD reduction on a single aerofoil RANS simulation, as presented by LeGresley and Alonso [5]. In the example reported the obtained modes are used to project the full incompressible RANS equations and the obtained reduced equation system is used to evaluated the flow field of different airfoil shapes.

Thanks to its optimality property, the POD basis reduction technique has gained a widespread attention in several fields, such as image processing, data compression, and oceanography [85]. Most recently, the POD has been used in aerodynamic applications for various purposes. Ruana et al. [86] use a variation of POD, Normalised POD, to compress fluctuating building pressure data in wind-engineering area. In CFD applications, POD is generally used for the construction of a reduced order aerodynamic model, projecting the governing equations onto the reduced space of the basis functions. Such method is used by LeGresley and Alonso [5] for the development of a ROM evaluator for inviscid subsonic aerodynamic flows around 2-D aerofoils. In a follow on work Alonso et al. [87] exploit a mixed approach for the use of the POD reduction technique, using RANS snapshots to extract the basis functions and Euler equations for the projection phase. Also, a special treatment for shockwaves is added to the POD model in order to increase its accuracy. Epureanu [88] applies the POD decomposition in the frequency domain to the viscous flow in

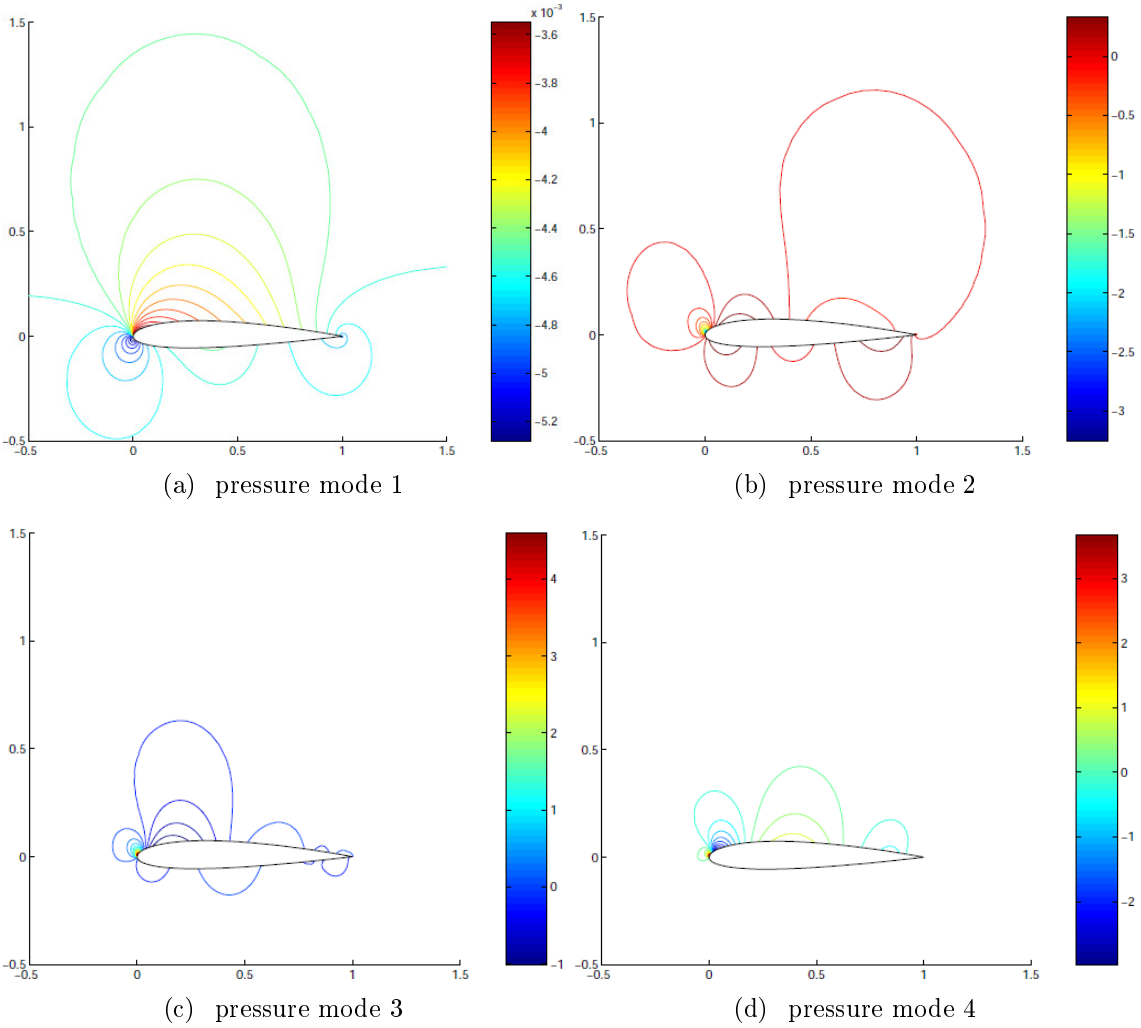

(a) pressure mode 1

(b) pressure mode 2

(c) pressure mode 3

(d) pressure mode 4

Figure 5.1: POD pressure coefficient modes example for a Naca1413 aerofoil. Source [5]

a turbomachinery cascade. An unsteady perturbation is imposed to the flowfield about its evaluated non-linear steady state, and the POD decomposition is then applied to the model. A similar approach is used by Lieu et al. [89] to construct an aerodynamic ROM which, coupled with a modal structural representation, is used for the flutter analysis of a complete F-16 aircraft.

A different application of the method is the *"Gappy POD"*, which allows the reconstruction of incomplete data independent of the governing equations of the described problems. The method is based on the procedure developed by Everson and Sirovich [90], whose work focuses on reconstruction of images from partial

data. Bui-Thanh et al. [91] apply the same technique to the reconstruction of full aerodynamic flowfields combining incomplete experimental and computational data. Moreover, the authors use the same methodology, with only slight modifications, for the inverse design of single-element aerofoils. A POD based ROM is also used in a two-step optimisation process for the RAE2822 aerofoil performed by Duan et al. [92]. First, a genetic algorithm is used in conjunction with a POD-ROM to extensively search the design space. Then, a steepest descent algorithm refines the optimum employing a RANS solver.

In addition, recent works [93, 94] have applied POD as a geometric-filtration technique, using the reduction process to generate new geometries as a combination of the initial snapshots. Finally, a more detailed review on the basic aspects and use of reduced order modelling is provided by Lucia et al. [95].

The specific POD decomposition used in this work falls within the Gappy POD category. As described in the previous paragraphs, the main idea of gappy POD is the use of the POD basis (evaluated from a set of initial snapshots) to reconstruct additional gappy flow vector, i.e. flow vectors that present missing data. The same technique can be extended to the approximation of completely missing flow vectors, effectively utilising the POD model as an interpolation between known data points. However, in order to achieve this goal firstly the initial set of snapshots must be redefined. Rather than containing only flow variables, each snapshot is augmented to also contain airfoil coordinates and a set of design variables (e.g. angle of attack, Mach number, parameterisation variables, element's deployment settings). For example, consider the augmented snapshot set $\{V_i\}_{i=1}^{m}$, where each snapshot contains a surface-pressure distribution P_i and a corresponding set of airfoil coordinates C_i and design parameters D_i:

$$V_i = \begin{bmatrix} C_i \\ D_i \\ P_i \end{bmatrix} \tag{5.7}$$

The target vector $V_* = [C_*^T \, D_*^T \, P_*^T]^T$ can then be considered as an incomplete data vector, where D_* is known and C_* and P_* must be determined. Thus, the gappy POD procedure can be used to determine the geometry and flowfield of a newly generated airfoil shape (obtained changing the value of the design parameters), effectively transforming the solution of the RANS equations into a problem of reconstructing missing data.

The application of the gappy POD technique starts with the definition of a "mask" vector n^k, which indicates for a flow vector snapshot where the data are missing and where are available:

$$\begin{aligned} n_i^k &= 0 \quad \text{if } U_i^k \text{ is missing or incorrect} \\ n_i^k &= 1 \qquad\quad \text{if } U_i^k \text{ is known} \end{aligned}$$

where U_i^k denotes the i-th element of the flow solution vector U^k. Let's then consider a set of completely known snapshots $\{U^i\}_{i=1}^m$ with POD basis $\{\phi^i\}_{i=1}^m$, and a solution vector g that has some elements missing. In order to reconstruct the full vector it is possible to define an intermediate repaired vector $\tilde{g}$, expressed as an expansion of the form Eq. 5.1:

$$\tilde{g} \approx \sum_{i=1}^{p} b_i \phi^i \tag{5.8}$$

The POD coefficients b_i are computed imposing the minimisation of the error between the original and repaired vectors, defined as:

$$E = \|g - \tilde{g}\|_n^2 \tag{5.9}$$

using the gappy norm so that only the original existing data elements in g are compared. Differentiating Eq. 5.9 with respect to each of the b_i in turn, the linear system of equations is obtained

$$Mb = f \tag{5.10}$$

where $M_{ij} = (\phi_i, \phi_j)_n$ and $f_i = (g, \phi_i)_n$. Finally, the complete g is reconstructed by replacing the missing elements in g by the corresponding repaired elements in $\tilde{g}$.

5.2.2 Work-flow Description

The POD-ROM model is here exploited within an optimisation process using the approach that Carlberg and Farhaty [96] define as the *"offline-online strategy"*. It consists of two different stages: firstly the design space is sampled for the evaluation of the snapshots and the ROM is generated (offline phase); then the optimisation process is performed (online phase) using the ROM as the objective functions evaluator. The advantages and drawbacks of the above described strategy have already been highlighted in Section 5.2. Additionally, when applying this strategy it is important to consider the existence of a *"break-even"* point, which expresses the number of online evaluations needed before overall cost savings are obtained using the offline-online procedure. Kipouros et al. [97] present an alternative way of exploiting ROM within an optimisation process, which assists, rather than replace, the full fidelity evaluator. In their work the ROM is used in real-time as a substitute of the costly RANS evaluation when a predefined criterion is met. Moreover, the full fidelity evaluations made during the optimisation process are used to train the ROM, increasing its accuracy and reliability.

Figure 5.2 introduces the workflow of the optimisation strategy used within

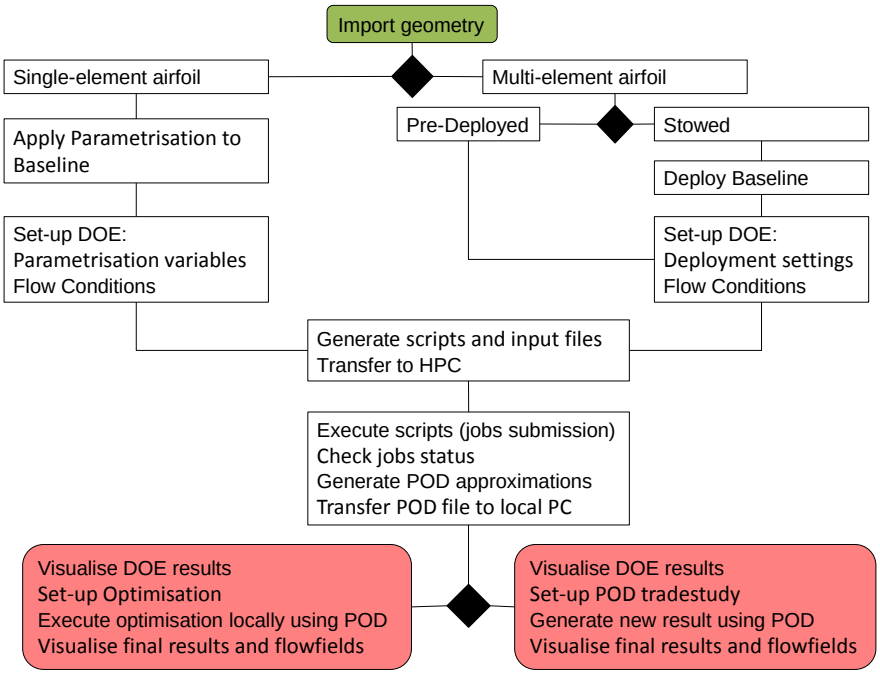

Figure 5.2: Worflow of the offline-online optimisation strategy used in the APODO project.

APODO. First of all, the baseline geometry is imported into the tool. To facilitate the data exchange with other design tools in use at the Industrial Sponsor, several file formats can be read in as well as exported. Moreover, when considering multi-element aerofoils, the geometry can be imported in either the stowed or pre-deployed configuration, as shown in Figure 5.3. In the first case, the absolute deployments parameters will be used for the positioning of the high-lift devices, while an incremental approach is used in the latter case. Pre-deployed geometries are generally used when the difference between the 2D and 3D deployments are relevant, and a non negligible deviation in element's geometries is observed when using one or the other deployment laws (e.g. krüeger slat for swept wings, where the deployment angle can be as high as 130°). In this eventuality, the high-lift devices are deployed in a specific external CAD package using the full 3D geometry and a deployed section at the desired span location is exported for the 2D study.

Following the single-element aerofoil analysis branch in Figure 5.2, the next step is to choose a parametrisation algorithm to represent the shape of the aerofoil. Sev-

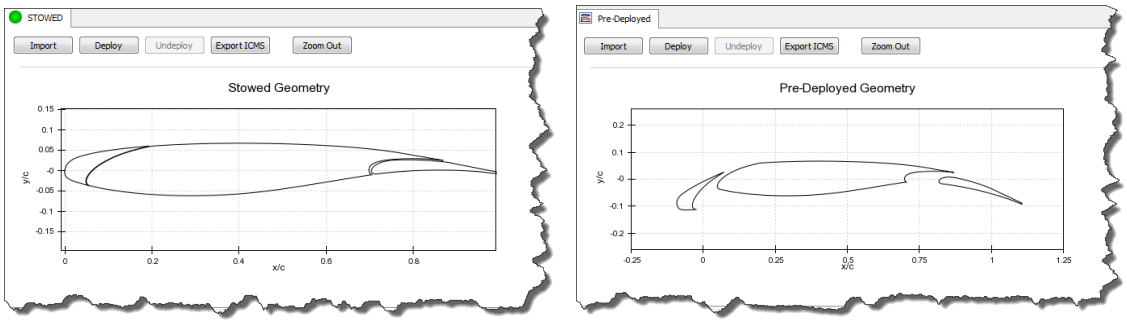

(a) Multi-element stowed

(b) Multi-element pre-deployed

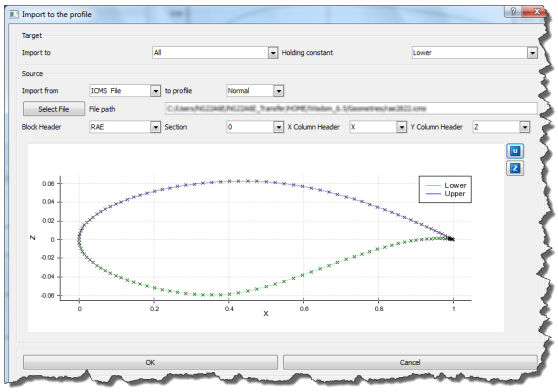

(c) Single-element

Figure 5.3: Imported baseline geometry for multi-element aerofoils in stowed (a) and pre-deployed (b) configuration, and for single-element aerofoils (c).

eral techniques, including PARSEC [43] and CST [46], are available to the user, who can then select the most appropriate one for the specific case. Next, the parameters that define the baseline aerofoil are evaluated performing a least square fit of the geometry. The quality of the fitting can be assessed, prior to the execution of further analysis, comparing the imported geometry with the parametrised one.

Next, the user sets up a tradestudy, specifying the flow conditions, i.e. Mach, Reynolds Number and angle of attack range, and the RANS solver settings. A suitable set of design variables, i.e. shape parameters for single aerofoils and deployment settings for multi-element ones, will be presented to the user (see Figure 5.4 and Figure 5.5), who will have to choose an appropriate subset and define the range of variation of each variable. Finally, the offline stage of the process is terminated with the selection of a method for the generation of the Design Of Experiment

(DOE) and the evaluation of the tradestudy. A background process is then started, which launches the meshing process of the baseline configuration on the HPC cluster, performs the mesh deformation for each design point of the tradestudy (once the baseline mesh is available) and submits the RANS solver simulations to the cluster scheduling system. An additional job is submitted for the POD reduction process, which will execute only after the completion of all the RANS simulations.

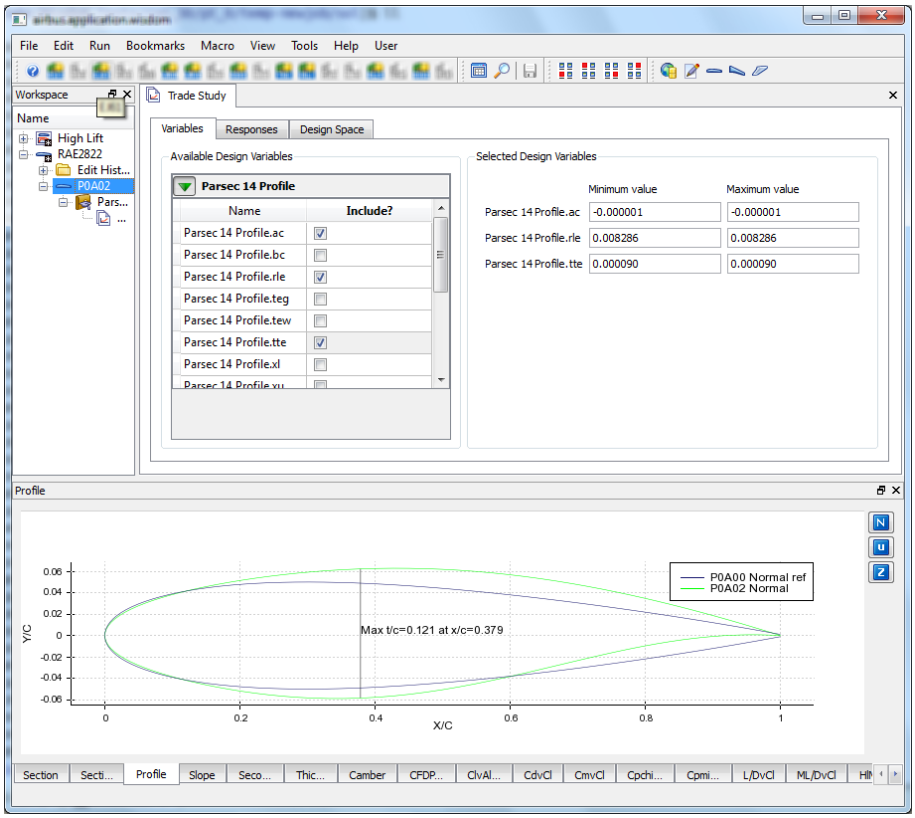

Figure 5.4: Design variables set available to the user for the setup of the tradestudy. Single-element shape.

The user can monitor the status of the tradestudy evaluation and download in real-time the data of the completed design points. When all the simulations have completed, the user will be able to add a POD tradestudy on the analysis tree. The POD model will, then, be copied to the local machine and used in substitution of the RANS solver to perform further tradestudies, for example include intermediate alphas or design variables values, or to run numerical optimisations. In the latter case, the user has to choose the responses to include in the optimisation run, select

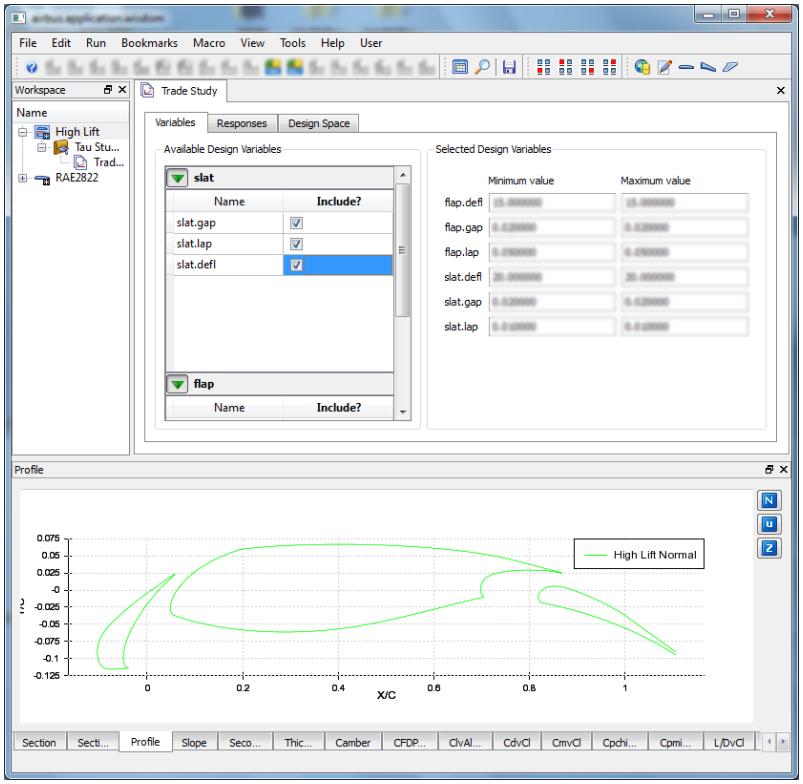

Figure 5.5: Design variables set available to the user for the setup of the tradestudy. Multi-element positioning case.

the objective (minimise, maximise, target, inclusive and exclusive) and a weighting factor, as shown in Figure 5.6. The weighting factors are used to construct a weighted averaged formulation of the multi-objective problem when single objective algorithms are selected, whereas they are ignored when selecting multi-objective techniques. Finally, an appropriate optimisation algorithm is selected and set up for the specific case (number of maximum iterations, convergence criteria, initial population, etc...), and the optimisation process is executed on the local machine.

At completion of the optimisation process, the results can be post-processed within the same environment. Several design space visualisation techniques are available, including contour plots, hat plots, self-organising maps, and parallel coordinates. Moreover, the pressure coefficient distribution and the flowfield of each design point can be visualised and compared with the baseline, to better understand the physics that lead to the performance gains. Also, a RANS simulation can be

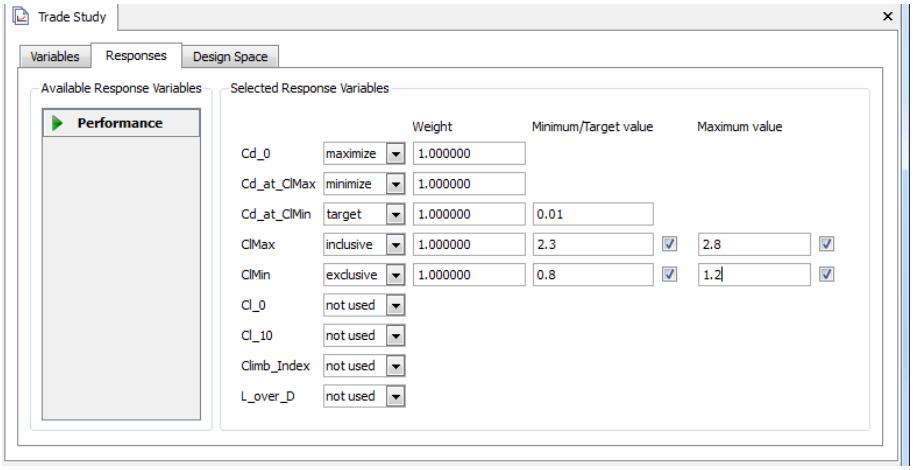

Figure 5.6: Selection of responses and objectives for the setup of a POD optimisation.

easily executed on the most promising configurations, thus performing a validation of the achieved improvements. Finally, additional design points (evaluated using the full RANS simulation) can be added to the existing POD model at discretion of the user, increasing the ROM model accuracy in particular regions of the design space.

5.2.3 Optimisations Results

Two optimisation cases are here presented in order to demonstrate the application of the developed tool within an industrial environment. The first test is a single element supercritical aerofoil, namely RAE2822, illustrated in Figure 5.7.

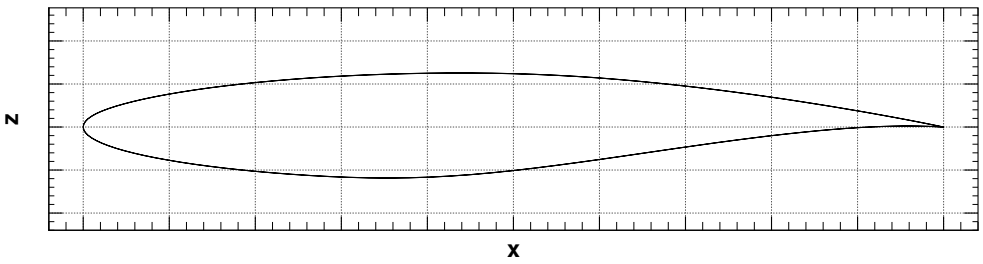

Figure 5.7: RAE2822 aerofoil geometry.

The baseline geometry is imported into the tool and parametrised using a modified PARSEC technique, which requires the specification of 14 parameters. As specified in the previous section, a least square fit is performed, leading to the deter-

Table 5.1: Description of the identified design variables, their datum value and range of variation for the RAE2822 shape optimisation.

Design Variable	**Min Value**	**Datum**	**Max Value**	**DP341**
ac - camber parameter 1	-1×10^{-2}	-1×10^{-4}	1×10^{-2}	-8.59×10^{-3}
bc - camber parameter 2	-1×10^{-2}	-1×10^{-4}	1×10^{-2}	-4.35×10^{-3}
ytc - camber parameter 3	-1×10^{-2}	0.000	1×10^{-2}	4.37×10^{-3}
rle - leading edge radius	4×10^{-3}	8.8×10^{-3}	1.2×10^{-2}	8.85×10^{-3}
teg - trailing edge angle	-9.728	-6.728	-3.728	-8.44

mination of the parameters values that best represent the datum aerofoil. After this first step, only 5 amongst the 14 parameters are selected as design variables. These parameters are the ones that represent the most critical changes, from a designer point of view, on the aerofoil geometry. Their link to the geometrical characteristic of the aerofoil, their datum values and their range of variation are summarised in Table 5.1.

Next, a DOE of 60 design points is generated, using the Latin Hypercube method [98], and evaluated using a RANS solver. A single angle of attack of alpha= 2.3°is considered at a Mach number of 0.75 and Reynolds number of 6.5 million. The POD model constructed using the 60 snapshots is then used to minimise the aerofoil drag at a constant lift coefficient, chosen equal to the datum value of $cl = 0.69$. The latest condition is implemented as a quadratic penalty function, so that for the specific case the the objective function is defined by:

$$\text{obj} = \frac{1}{11} cd + \frac{10}{11} \left(cl - cl_{target}\right)^2 \tag{5.11}$$

where $cl_{target} = 0.69$.

Although several optimisations were performed using different algorithms, both deterministic and stochastic, the results here presented are obtained using a Genetic Algorithm (GA). The initial population is formed by 40 candidates and the optimisation is halted after 10 generations. The crossover probability is set to 0.7, while the mutation probability is 0.1. The search pattern of the optimisation is illustrated in

Figure 5.8, where the optimum design identified in each generation (vertical separation lines) is highlighted. It can be seen from the figure that the algorithm reaches a minimum value for the objective function after 341 POD evaluations. The objective function value for this specific design is 0.989211×10^{-3}, and the horizontal line in the figure indicates this lower limit. Also, it is clear that the optimisation process has identified a similar optimum design at iteration 163. A more detailed analysis of the geometry of the designs shows that the only difference between the two aerofoils is the slightly lower value of the variable *ytc* for the DP163.

The datum pressure distribution and geometry are compared with the optimum one in Figure 5.9. A reduction in the shock intensity is achieved increasing the *ytc* parameter, which, effectively, results in a reduction of the angle of attack of the aerofoil. The consequent loss in lift is compensated by slightly increasing the leading edge radius and camber at the rear of the aerofoil. The optimum design achieves a reduction in the drag level of 9.13%, with a lift coefficient only 0.24% higher than the target value, as summarised in Table 5.2. However, a higher nose-down pitching moment is also obtained, which should then be compensated by an higher tail load, reducing the drag benefit at the overall aircraft level.

The identified optimum design, DP341, is validated using the full RANS simulation. The resultant pressure distribution is compared with the one predicted by the POD model in Figure 5.9. Clearly, the POD model closely matches the RANS results, with only minimal differences on the near-shock region of the aerofoil's suction side. The accuracy of the ROM prediction is reflected in the value of the aerodynamic coefficients, which are compared to the RANS simulation ones in Table 5.2. Indeed, the accurate prediction of the shock pattern shown by the POD model indicates a good exploration of the design space by the initial RANS DOE. In fact, as stated by Lorente et al. [99], in order to derive a POD-ROM able to deal with moving shock waves (as a result of the change in design variables) a large number of snapshots and POD modes is necessary.

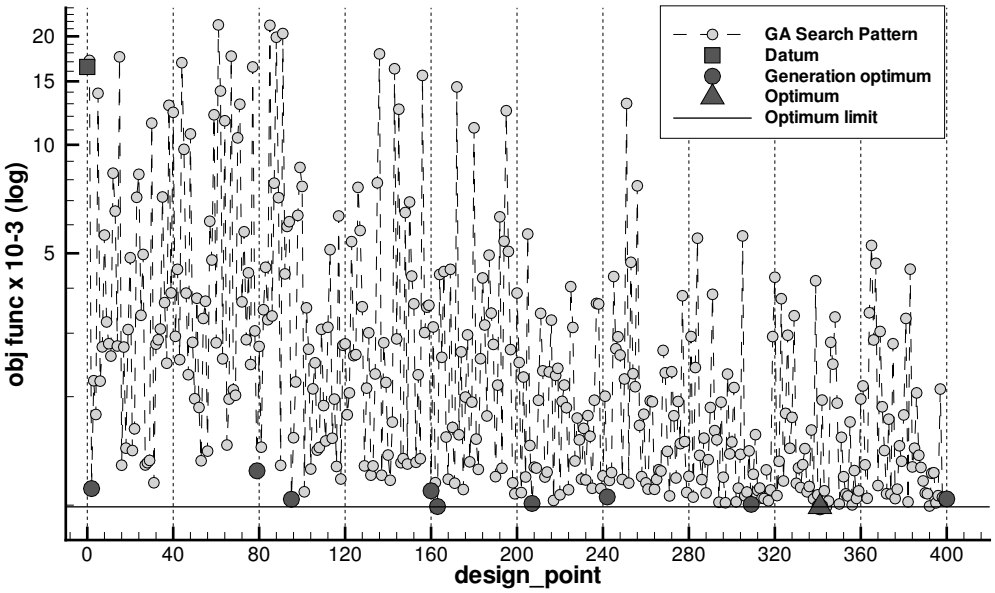

Figure 5.8: Optimisation search patter revealed by GA, showing the datum RAE2822 aerofoil (square) and the identified optimum, DP341 (triangle).

Table 5.2: Comparison of the aerodynamic coefficient for the datum and optimum design, RAE2822 optimisation.

	Datum	**POD**	**RANS**	**POD-Datum %**	**POD-RANS %**
cl	0.68980	0.69146	0.69741	0.24%	0.86%
cd	0.01203	0.01086	0.01084	−9.73%	−0.18%
cm	−0.25643	−0.26925	−0.27147	5.00%	0.82%

The second test case presented is the GARTEUR A310 multi-element aerofoil, already introduced in Chapter 4. The stowed configuration is imported into the tool, so that the direct deployment parameters are used to control the placement of the high-lift devices. The gap, lap and deflection angle of each element are used as design variables, adding up to a total of 6 parameters. As for the RAE2822 case, the Latin Hypercube method is selected to generate the initial DOE, which consists of a total of 250 design points. The same optimisation problem specified in the single-point section of Chapter 4, here briefly reported, is executed using the POD-ROM approach:

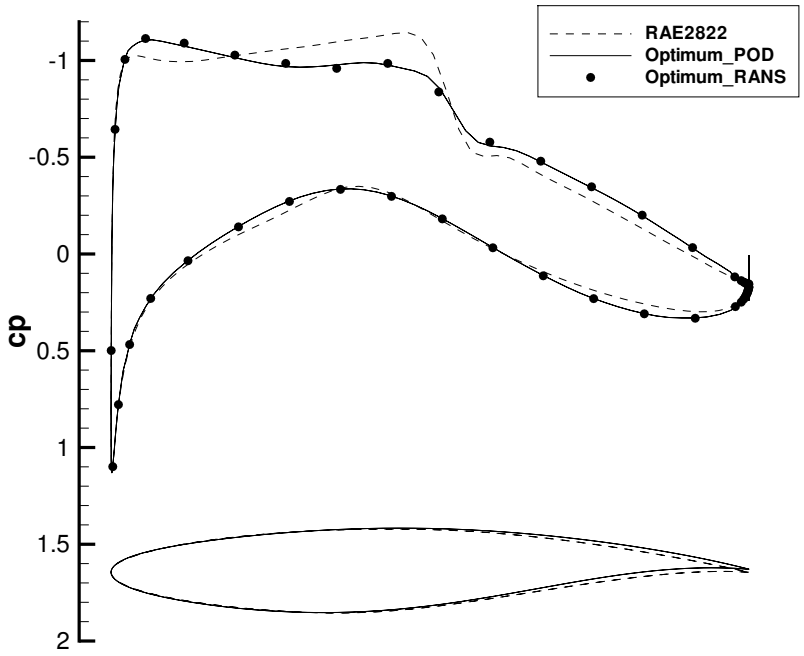

Figure 5.9: Comparison of geometries and pressure coefficient distribution for the datum RAE2822 (dashed line) and the selected optimum, evaluated using POD (solid line) and full RANS (dots).

$$\text{obj1} = -\frac{cl}{cl_0} \quad ; \quad \text{obj2} = \frac{cd}{cd_0} \tag{5.12}$$

where the subscript 0 indicates datum design values, and the aerodynamic coefficients are evaluated at a fixed angle of attack α_1.

In order to tackle the defined multi-objective problem and, concurrently, fully explore the design space, a Multi-Objective Genetic Algorithm is selected as optimisation technique. An initial population of 48 candidates is evolved for 10 generations to obtain the results in Figure 5.10, where the MOGA search pattern and the revealed Pareto front are shown. From the figure it is possible to observe that, not only the trade-off between the conflicting requirements is well captured, but also several designs are identified that increase both objective functions values. From this latter set of designs, a *"compromise"* solution which presents notable improvements for

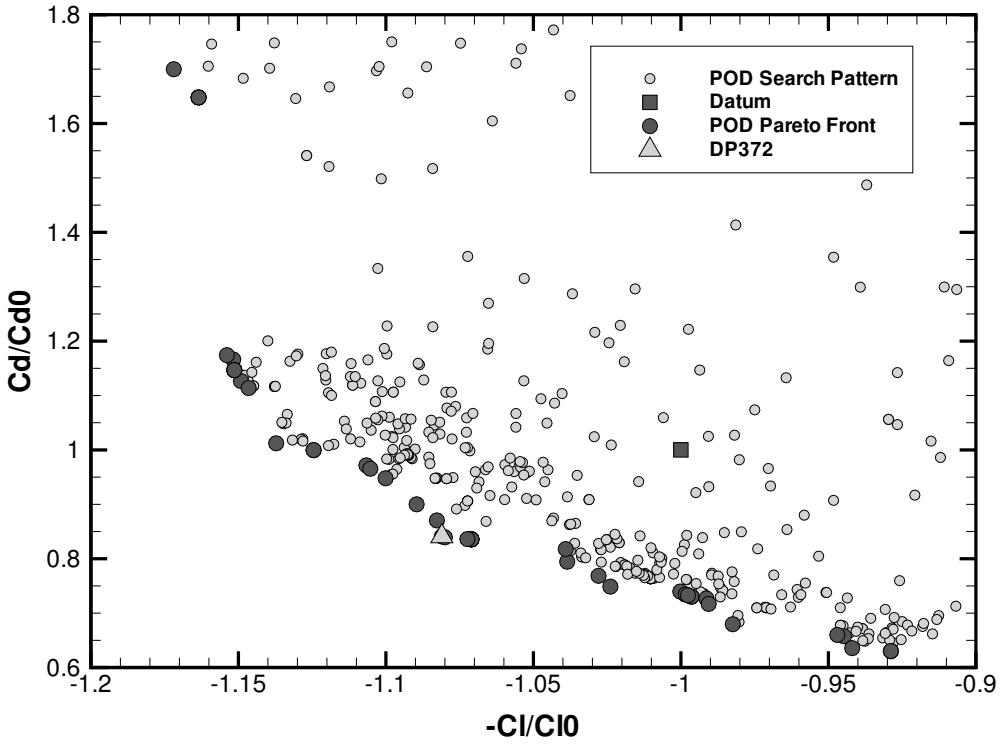

Figure 5.10: MOGA Search Pattern revealed after 10 iterations, correspondent to 480 POD evaluations for the GARTEUR A310 optimisation.

both the considered metrics, namely DP372, is selected for further analysis.

The percentage variation of the design variables for the optimum DP372 over the datum values are presented in the first column of Table 5.3. The table also shows the 6 points from the initial DOE which present the minimum distance from the DP372 optimum in terms of each design variable, evaluated as $|\text{DP372}_{value} - \text{DOE Point}_{value}|/\text{Datum}_{value}$. The results show that a different DOE point is identified for each of the design variable, indicating that the identified optimum is located in a region of the design space not covered by the initial DOE. Furthermore, an *"average distance"* is evaluated using the individual design variables value for the entire initial DOE (values shown in the last row of Table 5.3 for the 6 identified points), which presents a minimum value for the DOE point 144. The latter is, hence, considered the closest DOE point to the identified optimum DP372.

The geometry and pressure distribution of the datum aerofoil and the DP372 de-

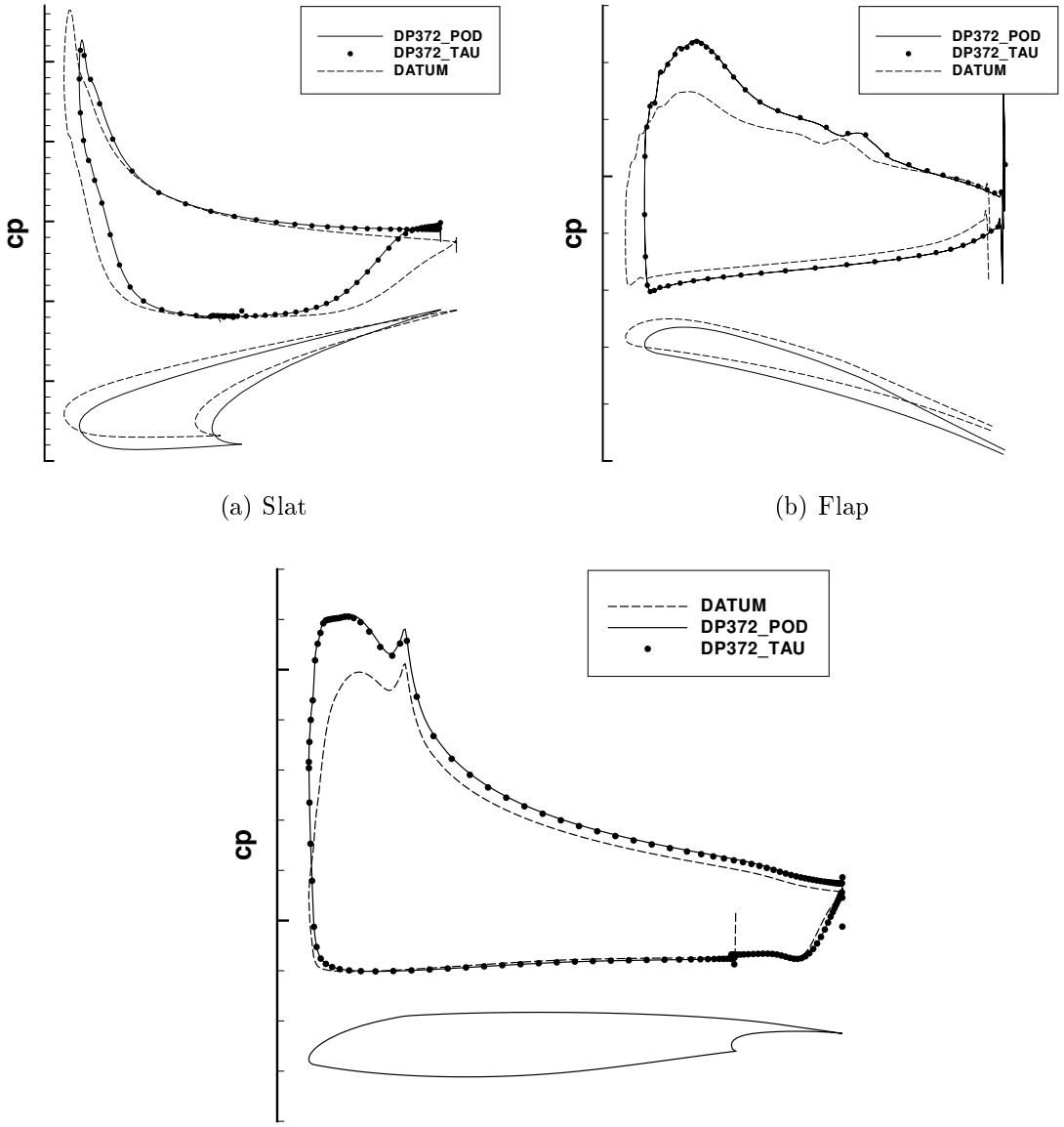

(a) Slat

(b) Flap

(c) Main

Figure 5.11: Comparison of pressure coefficient distribution for the the datum GARTEUR A310 (dashed line) and the selected optimum, evaluated using POD (solid line) and full RANS (dots).

sign are compared in Figure 5.11. The increased flap deflection (Figure 5.11(b)) leads to an increase of both flap and, principally, main element load. On the contrary, the load on the slat is decreased compared with the datum, despite the increased deflection of the element. The improvements on the objective functions are summarised in Table 5.4.

Figure 5.11 also illustrates the comparison of *cp* distribution evaluated using the

Table 5.3: Design variables values for the DP372 optimum and distance from the initial DOE points.

		DOE Points					
	DP372	**7**	**228**	**23**	**144**	**117**	**194**
Slat.gap	-17.76%	**0.05%**	26.46%	9.86%	4.51%	12.54%	4.06%
Slat.lap	+30.53%	36.02%	**0.12%**	25.31%	2.82%	21.29%	14.33%
Slat.defl	+30.94%	20.70%	45.20%	**0.19%**	3.83%	13.04%	40.78%
Flap.gap	+8.83%	5.49%	6.56%	1.47%	**0.13%**	13.78%	20.48%
Flap.lap	-16.01%	15.78%	31.64%	29.20%	5.72%	**0.07%**	1.91%
Flap.defl	+81.77%	98.84%	38.51%	69.12%	30.48%	32.17%	**0.04%**
Average	-	29.48%	24.75%	22.52%	**7.91%**	15.48%	13.60%

Table 5.4: Objective functions improvements for the compromise design DP372, evaluated using the POD model and full RANS.

	POD	**RANS**	**POD-Datum %**	**POD-RANS %**
obj1= $-\frac{cl}{cl_0}$	−1.08104	−1.07345	8.104%	0.759%
obj2= $\frac{cd}{cd_0}$	0.8411	0.88143	15.890%	−4.034%

POD model and RANS simulation. The agreement is more than satisfactory for all the aerofoil's elements. Nonetheless, a slight over-estimation of the slat pressure peak is present, due to an higher predicted velocity at the stagnation point. This effect is clearly shown in Figure 5.12, where the POD flowfield of the DP372 is compared to the RANS and to the datum ones. Apart from this small discrepancy, the two illustrated Mach contours for the DP372 design are, practically, identical.

Moreover, the effects of the different deployment settings on the wakes of each element is highlighted in Figure 5.13, which illustrates the Turbulent Kinetic Energy contours. In particular, the figure clearly shows that the slat wake is considerably reduced in the DP372 design with comparison to the datum. Also, no mixing of the slat and main wakes is visible in the identified optimum, while these wakes are confluent in the datum design. This effect leads to a smaller aerofoil wake and, consequently, a decrease in the drag coefficient. Conversely, both the main and flap

wakes of the DP372 design present a slightly increased Turbulence Kinetic Energy levels.

The search pattern and Pareto front revealed with the above described POD optimisation strategies are compared with the results obtained in Chapter 4. In particular, the previous analysis presented the optimisation of the same GARTEUR configuration using the NSGA-II optimisation algorithm coupled with the identical RANS solver here used to produce the POD snapshots. The comparison, presented in Figure 5.14, shows the two different search patterns, with the RANS one appearing more constrained in the high cl region. In addition, a discontinuity is present in the POD search pattern at $cl/cl0 \approx 1.16$, which is not present in the RANS search pattern. This behaviour might be linked to an over-prediction of the lift coefficient by the POD model in this specific region of the design space. Moreover, the comparison of the Pareto front in Figure 5.15 shows that the Pareto front of the POD approach closely resembles the RANS one, and even dominate the latter in the lower cd region. This behaviour can be attributed, mainly, to the difference in the performance evaluator, since both optimisations exploit a genetic algorithm for the exploration of the design space. In fact, as shown by the comparison in Table 5.4, the POD model tends to under-predict the drag coefficient and, hence, the Pareto front is further developed in the low cd region. This behaviour of the POD model may be related to a lower estimation of the friction coefficient, since the pressure distribution is clearly well reproduced by POD (as shown in Figure 5.11).

Finally, to further analyse the validity of the POD predictions, the revealed POD Pareto front is evaluated using RANS simulations. The results, presented in Figure 5.15, confirm the tendency of the POD model to under-predict the drag values, though this does not affect the shape of the final Pareto front. More important instead is the over-prediction of the physical limit on cl. In fact, although the POD model predicts increase in cl values of up to 15%, the RANS simulations show that a physical limit is reached and the lift performance cannot be increased by

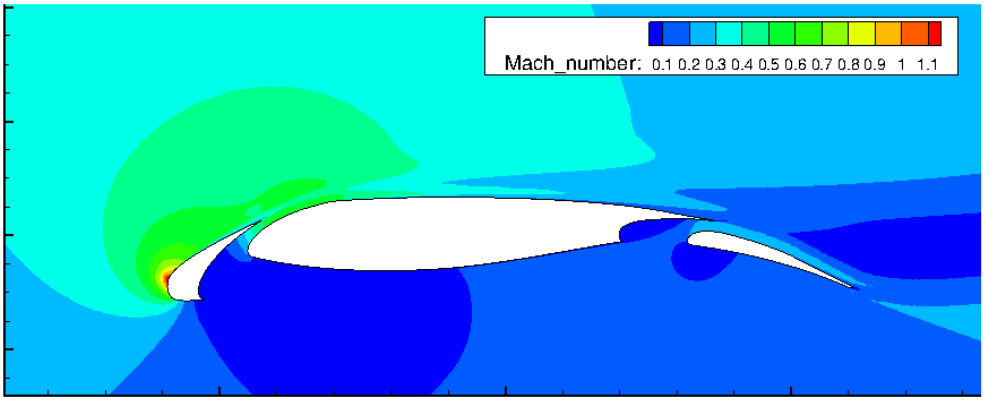

(a) Datum (RANS)

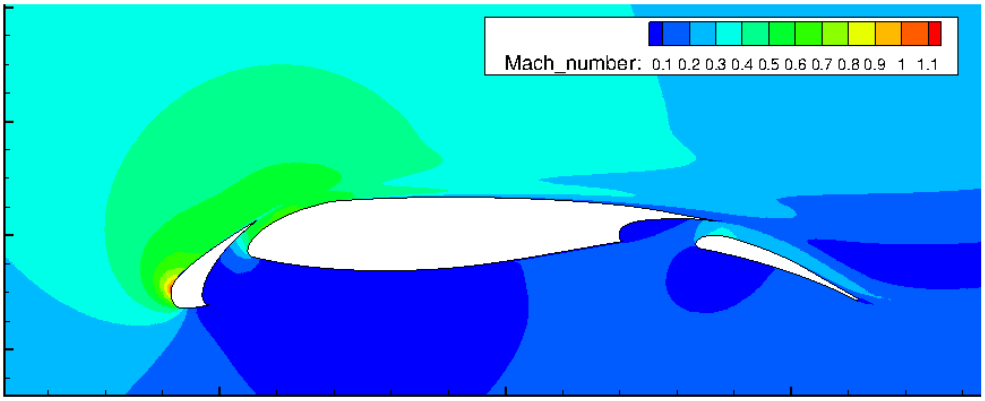

(b) DP372 (POD)

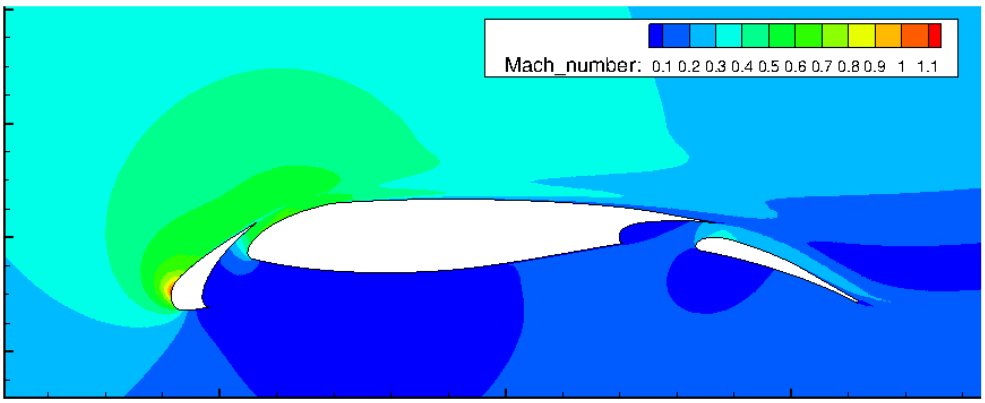

(c) DP372 (RANS)

Figure 5.12: Comparison of flowfield Mach distribution for the Datum (a) and the DP372 optimum, evaluated using POD (b) and full RANS (c).

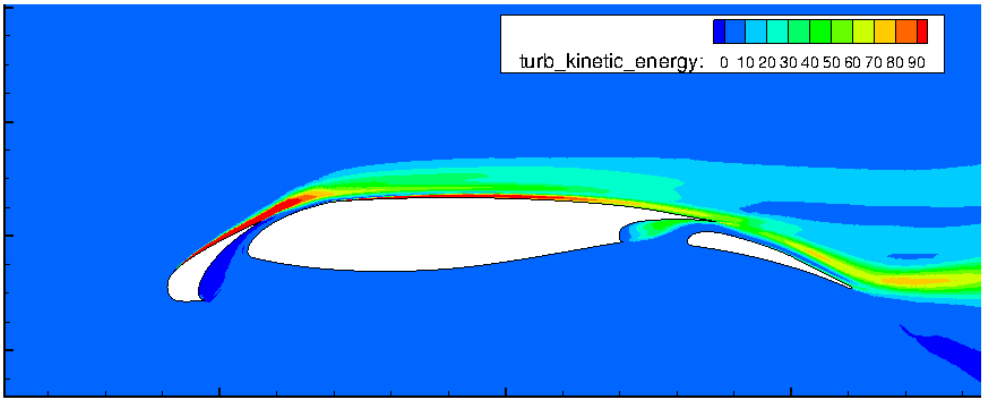

(a) Datum (RANS)

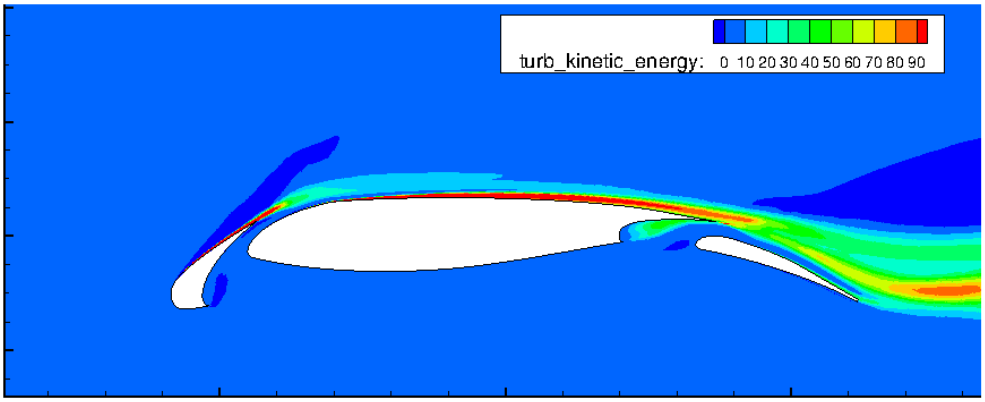

(b) DP372 (POD)

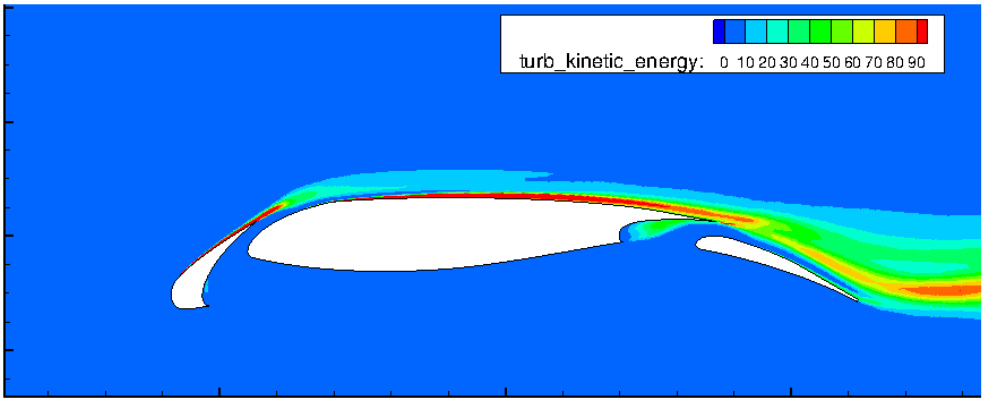

(c) DP372 (RANS)

Figure 5.13: Comparison of flowfield Turbulent Kinetic Knergy distribution (0-10% maximum value) for the Datum (a) and the DP372 optimum, evaluated using POD (b) and full RANS (c).

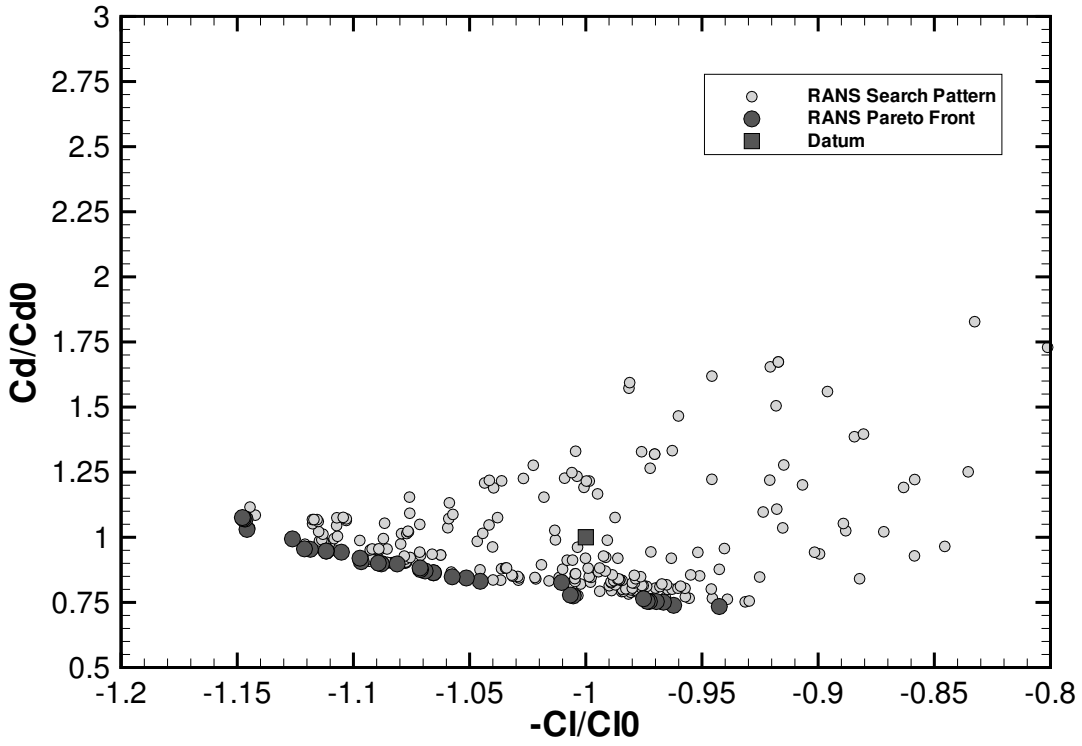

(a) NSGA-II / RANS

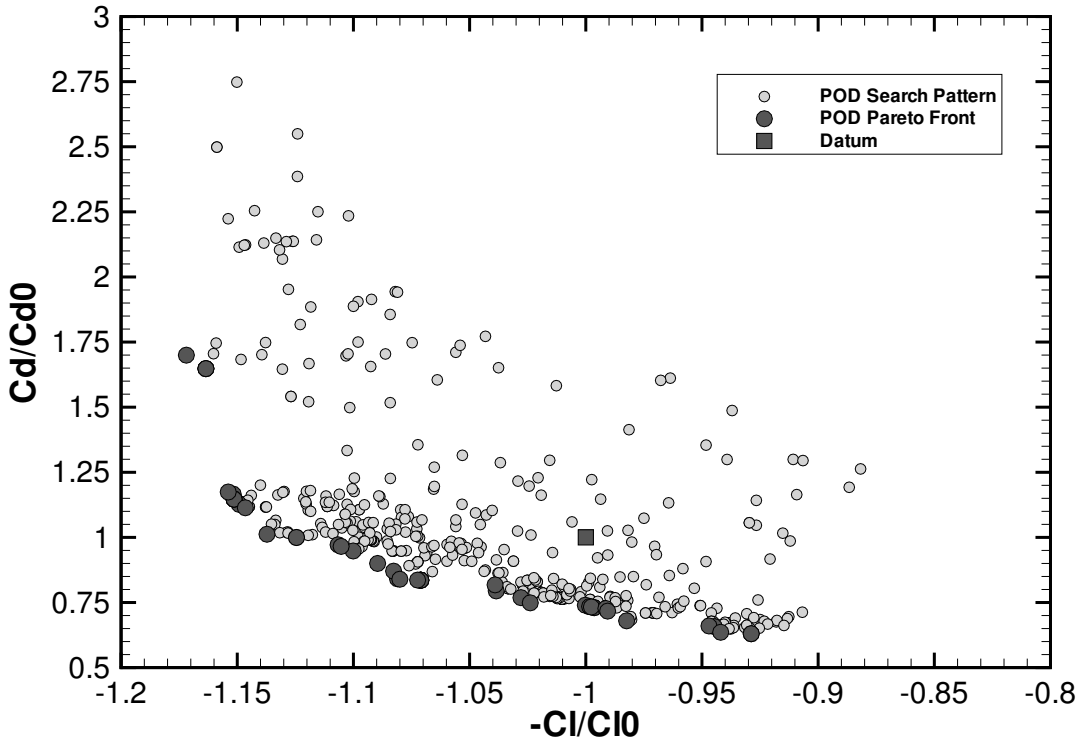

(b) MOGA / POD

Figure 5.14: Search pattern and Pareto front obtained with the NSGA-II coupled RANS (a), and MOGA coupled POD optimisation strategies (b).

more than 13% of the datum value. Therefore, more designs that present this cliff in the lift coefficient should be included into the POD model to better capture the physical limitation in cl. Nevertheless, the presented POD-ROM approach is, clearly, producing satisfactory results, especially in view of the reduction in computational cost and the re-usability of the POD model for further studies.

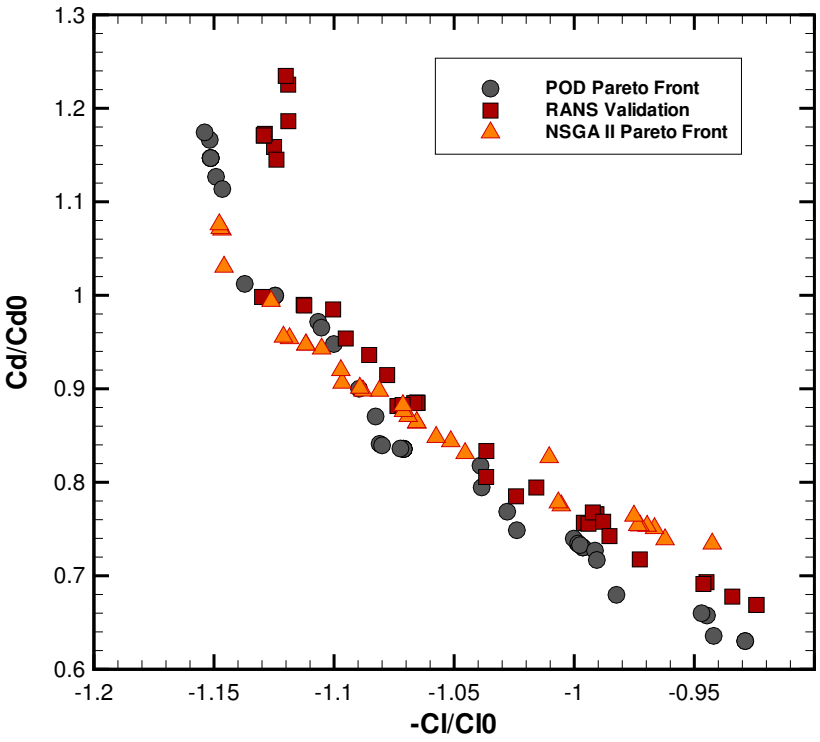

Figure 5.15: Validation of the Pareto front revealed by the MOGA coupled POD optimisation strategy using RANS simulations. Comparison with NSGA-II coupled RANS results.

5.3 Project Management Analysis

The previous section has described the technical aspects of the APODO project, together with the application of the developed tool to two relevant test cases. The next sections will focus on the methodologies and challenges faced during the execution of the project from a management point of view. Firstly, a background literature review is presented in order to introduce some basic concepts and terminology that

will be used throughout the rest of the chapter.

5.3.1 Concurrent Engineering and Agile Development

The concept of Concurrent Engineering (CE) was first introduced in manufacturing [100], and, since then, it has been defined in several ways by different authors. It is primarily an approach to the design of products that considers the different phases concurrently, moving away from the traditional sequential philosophy. Undoubtedly, CE is a powerful principle, which allows the inclusion of downstream issues into the upstream phases of a development process [101]. The main goal of CE is the reduction of lead-time with a concurrent improvement of quality and cost.

Three basic elements constitute the CE approach, namely *"early involvement of participants"*, *"the team approach"*, and *"concurrent workflow"* [102]. Early involvement of many participants is paramount to obtain the desired lead-time reduction. The main benefits come from fewer mismatches between the product characteristics and the existing process capabilities. Such mismatches are, usually, exacerbated by the lack of communication between end-users and designers. In fact, while the users have broad knowledge about the product to be developed and limited knowledge about the process, the opposite is true for the designers. Therefore, cross-functional teams are vital if a complex process, such as the new product development, wants to be completed successfully. Finally, thanks to early availability of information, designers can work at the same time on different phases of the development, receiving prompt feedback from the users.

Although initially developed for manufactured products (physical products), the method can easily be applied to computer software development. Clearly, both hardware and software manufacturing are facing nowadays similar issues [103] and can hence benefit from the same methodologies. It was inevitable that software development practitioners would then turn to manufacturing and adapt its lean approach to the development of software [104]. In early 2001 seventeen of the Agile

proponents came together and drafted the Agile Software Development Manifesto, which reads as follows:

" We are uncovering better ways of developing software by doing it and helping others do it. Through this work we have come to value

- **Individuals and interaction** over process and tools
- **Working software** over comprehensive documentation
- **Customer collaboration** over contract negotiation
- **Responding to change** over following a plan

That is, while there is a value in the items on the right, we value the items on the left more" [105].

The Agile Methods were established.

Before going into the details of the Agile development mantra and the implementation of a particular Agile method, namely Extreme Programming (XP), the four stages of the software life cycle [106] are here presented:

- **Requirement analysis:** the purpose and intended use of the software are specified by the customer through the draft of a set of "requirements". Those generally include a description of what is to be done, together with the specification of any constraint imposed by an environment or resources.
- **Design:** represents the translation of what into how, and is the main technical step of the development. It is usually split in two aspects: the identification of algorithms to accomplish the specified tasks, and the division of the software into parts which interact with each other. Design helps in specifying hardware and system requirements and also helps in defining overall system architecture.
- **Implementation:** is a synonymous with programming, where the abstract "how" identified during the design is transformed into actual steps executed

on computer hardware. It is the main focus of the developers, which will be assigned as many programming tasks as the number of identified software parts.

- **Testing:** the intent of this phase is to find and correct the defects of the developed code and to verify that it is solving the needs addressed. The testing can be performed at various levels, starting from software parts (unit) testing, all the way up to full system and acceptance testing.

The traditional approach to software development, known as the *"Waterfall Approach"*, excludes any interaction between the development stages just presented. Each phase must be completed before the next one can start, in a strictly sequential approach. Its strength resides in the detailed information derived in each phase and, especially, in the requirements analysis. Heavy documents are produced that capture all the users' requirements, which are then passed on to the following phases. A carefully designed programming phase can then be performed, with all the developers contributing toward the delivery of the final product. However, as a consequence of this approach the users are excluded from the development process at the end of stage one! Obviously, traditional approaches to software development assume that the complete set of requirements for a project can be anticipated at early stages and, thus, cost reduction can be achieved by eliminating change and uncertainty [107]. This approach, however, results in a stiff and unresponsive process management, which cannot adapt to the external environment changes.

The Agile approach, instead, embraces changes and strives to minimise the cost of responding to them. As stated by Becks et al. [105] it represents *"an alternative to documentation driven, heavyweight software development processes"* [105]. In particular, an Agile process has to be both light and sufficient [108]: light, meaning that it must be manoeuvrable; sufficient because it has to stay in the game, i.e. has to deliver a final product. Clearly, the focus is on the communication between developers and users. The developers have to bring out part of a customer's needs,

develop and deliver a software that might fulfil those needs and accept customer feedback about its deficiencies. The identified corrections are then carried out, and the process continues with another part, and so on until the entire final product is developed. The advantage of having working code all along the development process, even if only limited to specific capabilities, is immense. Users can try the functionality as soon as it becomes available and, concurrently, the developers can highlight any flaw in its implementation. Even if the working code is then scrapped, it is a far better way of steering the development toward useful coding than a discussion over future *"intangible"* delivery of an entire system.

Once the Waterfall model is abandoned in favour of an Agile approach, a new set of requirements is needed to drive the development cycle. Nevertheless, it is the customer that must start the process, and in this it is helped by the definition of *"User Stories"*. A user story is a sample of what the customer expects to do with the software. It is composed of three aspects, as described by Cohn [109]:

1. a written description of the story used for planning, and as a reminder;
2. conversations about the story that serve to flesh out the details of the story;
3. tests that convey and document details, and that can be used to determine when a story is completed.

The power of the user stories resides in their simplicity. They provide inputs for the developers to design and implement software that behaves as the customer expects, but are not dragged down by the detailed description of a tasking document. In fact, since the customer involvement continues throughout the development, new information and correction of assumptions can be supplied if needed. In addition, the user stories represent the preliminary test cases for a piece of Agile development, the ones that the developers will, for example, use in a capabilities demonstration. Obviously, additional testing will be performed by the end-users on similar cases, providing essential feedback to the developers.

5.3.2 Extreme Programming

Several Agile approaches are available in literature, including Extreme Programming (XP), Crystal methodologies, SCRUM, Adaptive Software Development, Feature-Driven Development (FDD), Dynamic Systems Development and Agile Modelling (AM) [110]. Among them, Extreme Programming is one of the most extensively used and it is the method selected to run the APODO project. XP prizes four values: communication, simplicity, testing, and courage [108]. The *"courage"* value is here intended as the determination of the developers to continuously make improvements to the system. The 12 rules of Extreme Programming are concise and to the point [104].

1. **The Planning Game:** At the start of each iteration customers, managers, and developers meet to flesh out, estimate, and prioritise requirements for the next release. The requirements are called *"User Stories"*.

2. **Small Releases:** An initial version of the system is put into production after the first few iterations. Subsequently, working versions are put into production anywhere from every few days to every few weeks.

3. **Metaphor:** Customers, managers, and developers construct a metaphor, or set of metaphors after which to model the system.

4. **Simple Design:** Developers are urged to keep design as simple as possible.

5. **Tests:** Developers work test-first; that is, they write acceptance tests for their code before they write the code itself. Customers write functional tests for each iteration and, at the end of each iteration, all tests should run.

6. **Refactoring:** As developers work, the design should be evolved to keep it as simple as possible.

7. **Pair Programming:** Two developers sitting at the same machine write all code.

8. **Continuous Integration:** Developers integrate new code into the system as often as possible. All functional tests must still pass after integration or the new code is discarded.

9. **Collective ownership:** The code is owned by all developers, and they may make changes anywhere in the code at anytime they feel necessary.

10. **On-site customer:** A customer works with the development team at all times to answer questions, perform acceptance tests, and ensure that development is progressing as expected.

11. **40-hour Weeks:** Requirements should be selected for each iteration such that developers do not need to put in overtime.

12. **Open Workspace:** Developers work in a common workspace set up with individual workstations around the periphery and common development machines in the centre.

In order for XP to work, the development team has to frequently receive feedback and inputs from the customers. Short iterations, in the two- to six-week range are, therefore, strongly recommended. Features, not tasks, are used as first priority in planning the development, since they represent a more understandable language for the customer. Additionally, at the end of an iteration, the customer can re-prioritise the features desired in the next cycle, adding new ones or discarding originally planned ones. That is what XP practitioners define *"dynamic prioritisation"*. This includes also the definition of *"MoSCoW"* rules for features: Must have, Should have, Could have, Want to have sometime.

However, an Agile approach to software development is not always the correct answer. Agile can be especially beneficial in situations where a lean process wants to be used to solve the specific problem tackled, and when the requirements are not exact and likely to gradually clarify as the project progresses. Whereas, when

precise and unchanging requirements are available and each part of the system must be documented and verified (e.g. when the software is only part of a wider solution), the Waterfall approach will work better.

5.3.3 Development Team and Users Stories

The development team for the APODO project was made up of 3 members: the author and 2 professional developers from an external specialist software-development company. The author had multiple roles within the project, being concurrently the project leader, the customers-developers link, as well as a developer. A Preliminary meeting with all the involved parties was held on the 5th of May 2012 with the aim to collect and analyse the customer needs. In addition, the scope of the project was clearly defined, together with an identification of the major risks and the definition of correspondent mitigation plans. Particularly, the external development of the POD reduction method (performed in a concurrent R&T programme) was recognised as a high risk blocker for the successful completion of the APODO project, so that several alternative solutions were identified. Nevertheless, none of these alternatives had to be considered since the project did not incur in any particular issues related to the POD implementation.

The APODO project officially started on the 29th of May 2012, with a planned final release for the end of January 2013. In accordance to the XP software development approach, the first task performed by the author, as project leader, was the identification of the number and lengths of the project's iterations. Firstly, a total of 4 weeks were subtracted from the 36-week duration of the project to account for holidays (Summer and Christmas breaks). The remaining 32 weeks were organised in 4-week long iterations, totalling 8 iterations. The reduced size of the development team was a factor in the definition of the iteration's length, since no substantial changes to the code could have been delivered by the team in less than the identified 4 week period.

The next step in the progression of the project was the definition of user stories that would convey the customer needs to the developers. After consultation with the customers, 6 main user stories were defined, which included comments and preliminary unit tests:

- User Story 1: Evaluate a single RANS run
- User Story 2: Create a RANS Tradestudy
- User Story 3: Create a POD model
- User Story 4: Create a POD Tradestudy
- User Story 5: Optimise using POD model
- User Story 6: Visualise the Design Space

To illustrate the structure and content of the above listed user stories, an example is reported in Figure 5.16.

Next, user points were associated to each story, corresponding to the predicted time required to complete it. The stories that were found to be too demanding were divided into shorter ones, increasing in this way the flexibility of the overall planning. At the beginning of each iteration the author specified the functionalities to be included, prioritising and/or modifying the initial user stories. Moreover, the 12 rules of XP development introduced in the previous section were observed as closely as possible.

The first release of the tool, in a preliminary or *"beta"* version, was performed after 5 iterations, on the 2nd of November 2012. The release included RANS tradestudy capabilities for both single and multi-element aerofoils, but did not cover the generation or use of POD models. Nonetheless, an introductory WeBeX® session with the customers was held on the 12th of November 2012. The goal of the session was the demonstration of the implemented features, as well as the collection of feedback

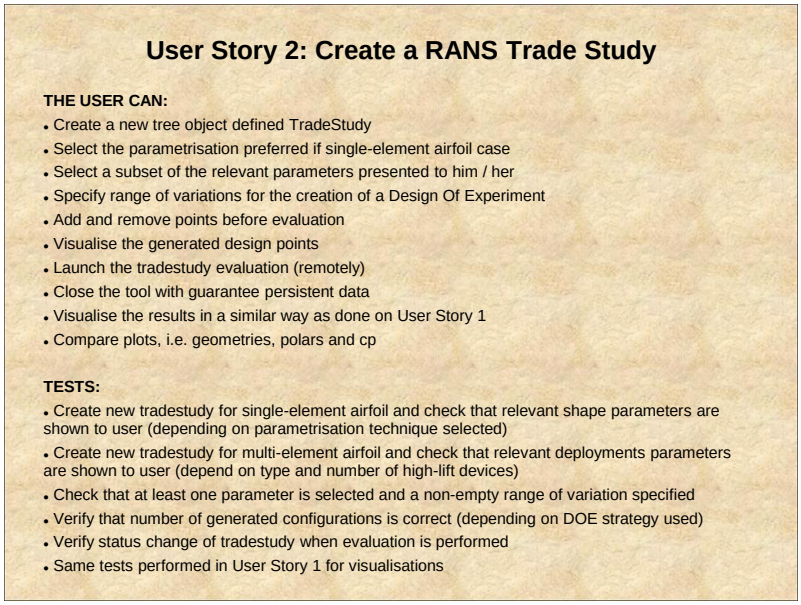

Figure 5.16: Example of a User Story used during the software development project APODO. The card presents the description of the story and part of the identified tests.

to steer the next iterations. The beta version was really well received, although changes were proposed to some of the design space visualisation techniques. An additional outcome of the session was the possibility of satisfying further customers, not initially considered at the start of the project. In particular, interest in the tool arose for the analysis of the effect of leading edge ice roughness on single element aerofoil at low speed. This study could have been performed implementing slight modifications to the already integrated RANS simulation setup environment. A cost/benefit analysis was carried out and, in accordance with the original customers, the decision was taken to include the extra developments into the project, postponing by 4 weeks the final release date.

Following the beta version in November 2012, an updated version was released for each subsequent iteration, allowing an extensive testing of the tool. The POD model generation was introduced at the sixth iteration, in early December 2012, whereas the main optimisation capabilities were enabled in early January 2013, corresponding to the seventh iteration. In order to identify the most relevant objective functions to include within the optimisation setup environment, several online meetings were

held with the customers just before the start of the seventh iteration. Finally, at the end of February 2013 the latest release was handed to the identified users for testing, together with a complete user guide and tutorials documentation.

The open source project management web application Redmine was used to support the planning and tracking of the APODO project. A virtual project was set-up into Redmine and, for each iteration, the chosen user stories were uploaded and broken up into *"issues"*. Then, every developer logged the time spent on each issue, in the effort to progress it and bring it to completion. Therefore, the updated status of the project, as shown in Figure 5.17, was always available to the author who could then dynamically react to any stopper. An example of the information provided by Redmine is illustrated in Figure 5.18, where the logged hours of each user are shown on a timeline. The plot shows that further time is logged to the project after its completion. This time corresponds to the further modifications to the tool made during a *"Pilot Study"* conducted with the low-speed aerodynamics design team, and discussed in more detail in the next section.

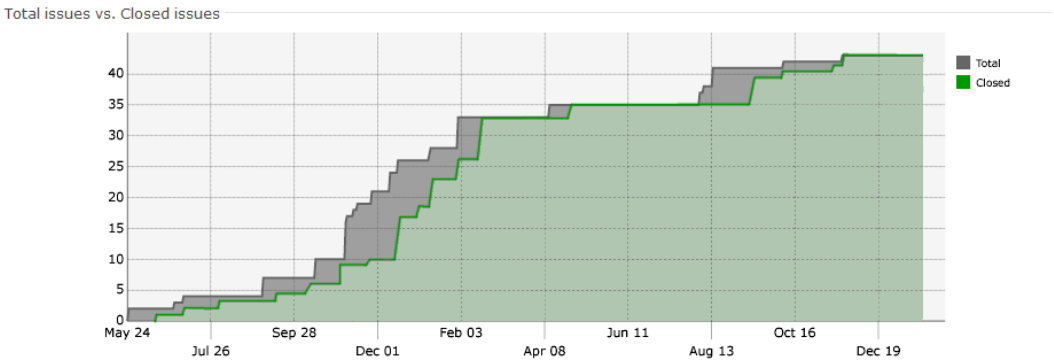

Figure 5.17: APODO project Roadmap. The progress of the project is tracked by plotting the total number of issues versus the closed ones.

5.3.4 Pilot Study and Users Feedback

The *"Pilot Study"*, conducted in collaboration with the low-speed aerodynamics design team, aimed at bridging any eventual gap identified in the tool in order to

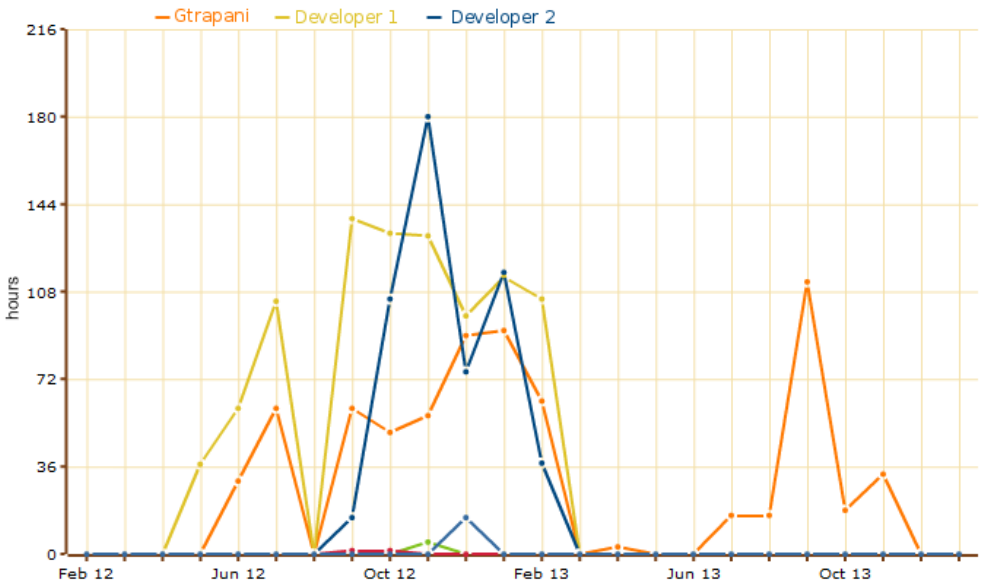

Figure 5.18: Timeline of the logged hours to the APODO project coloured by user.

push its use in full production. Initially, the tool was provided to two designers and several demo sessions were performed during the month of April 2013 to introduce all the capabilities. The proper testing tasks of the study spanned from June to November 2013, with regular reviews to check on progress and collect any feedback. During the study, the role of the author was to provide a guidance in the efficient use of the tool as well as provide responsive support to the designers. The latter task involved the inclusion of both light-weight and substantial additional capabilities, not envisaged during the running of the APODO project. The major modification to the tool was the inclusion of the incremental positioning of pre-deployed high-lift configurations, and the consequent optimisation of such configurations. This activity was mainly responsible for the peak in logged hours occurred in September 2013 (Figure 5.18). Nonetheless, such modification has greatly enhanced the usability and accuracy of the obtained results, increasing the potential of making it an everyday design tool. The *"Pilot Study"* was concluded in November 2013 with encouraging positive feedback, and further enhancements to the tool will probably be performed in the next years under further R&T programmes.

Chapter 6

Quasi-three-dimensional Approach

6.1 Description of the Method

The 2D optimisation framework introduced in Chapter 3 is further developed and extended to enable the optimisation of 3D high lift geometries. For this purpose a *"quasi-three-dimensional"* evaluation tool is included into the framework, and used to simulate the aerodynamic performance of high-lift configurations. The quasi-three-dimensional method obtains the three-dimensional aerodynamic performance of the wing combining a series of two-dimensional viscous evaluations at specified wing spanwise locations with an inviscid calculation of the wing planform. Since it accounts for the non-linear variation in lift with angle of attack (within the two-dimensional evaluations), the resulting method is non-linear. Therefore, it allows the evaluation of the aerodynamic characteristics over the entire angle-of-attack range, including maximum lift condition and partly separated flow. The attractiveness of this approach over full 3D RANS methods is the steep reduction in the geometrical complexity and computational cost, while maintaining satisfactory levels of accuracy.

The method was first introduced by Brune and McMasters [111]. More recently, a complete dissertation on the method is presented by Jacob [112], together with the application of the method to both a single and a multi-element test case. In his work

the comparison of the obtained results with wind tunnel data shows more than satisfactory agreement. The method described by Jacob forms the basis of the specific quasi-three-dimensional approach used in this work, which will be described later in the Chapter. Further developments on the approach are presented by Van Dam et al. [36], where two-dimensional data, obtained using an incompressible RANS solver, are coupled with a non-planar wake model lifting surface. The method is compared against experimental data on a part-flapped wing, showing good agreement in the spanwise lift distribution, including the steep drop present at the flap break.

Generally, the accuracy of the quasi-three-dimensional method is highly dependent on the accuracy of the input sectional data. Therefore, the use of two-dimensional RANS solvers for the evaluation of the sectional characteristic (as presented by Van Dam et al. [36]) will, on the one hand, provide accurate representation of the two-dimensional flow. On the other hand, however, the computational cost of performing a RANS simulation for each defined wing section can be prohibitive. This is especially true when a high number of sections is considered in order to accurately capture the spanwise geometry variation of the wing (e.g. wing where the high-lift system differs along the span), or when a study on different deployment settings is to be performed. Indeed, this is the goal of the work presented here, where the quasi-three-dimensional method is used within an optimisation environment to identify optimal deployment settings. In such applications, the minimisation of the computational overhead is a priority. Consequently, an inviscid-viscous coupled approach is preferred to the RANS method.

Inviscid-viscous coupled methods have been around for some time, since 1940s when first studied by Preston [113]. His work focuses on the displacement effects of laminar boundary layers near the trailing edge of aerofoils, and was later expanded to include turbulent boundary layers by Spence [114]. Already at this early stage, a high influence of the viscous flow over the aerodynamic performance of the aerofoils

is identified (reduction of lift from 5% to 15% depending on the value of the Reynolds number). However, neither Preston nor Spence were able to calculate the effect of viscosity over the whole aerofoil surface. In fact, no closed form solutions exists for the boundary layer equations on curved surfaces (such as aerofoils). Numerical methods are, thus, needed to solve the problem in an iterative process, as proposed by Powell in 1965 [115].

Advancing computing capabilities meant that more complicated methods could be explored. In 1981, Le Balleur and Nieron [116] introduced a formulation that combines a panel method for the simulation of the outer flow and an integral method for the solution of the boundary layer equations. In this way, it is possible to solve both laminar and turbulent boundary layers, as well as calculate partially separated flows. In fact, a semi-inverse algorithm with relaxation method is used to couple the viscous and inviscid regions, allowing the computation of small separation regions near the trailing edge. Moreover, the authors use a direct solution methodology for the boundary layer equations when the flow is attached, while an inverse methodology is applied when flow separation is detected.

The above described method, called VIS18, is extensively used for the analysis and design of high-lift devices for general aviation and transport aircraft [9]. The results obtained have shown that the method can provide accurate predictions for a wide range of angle-of-attack, also being able to handle complex configurations and partially separated flow. Furthermore, the accuracy of several viscous-inviscid methods is assessed by Klausmeyer [117], comparing the obtained results with both RANS solutions and experimental data, during a workshop held in 1997 at NASA Langley Research Center. The investigation of a McDonnell Douglas Aerospace (MDA) two-dimensional, single flap, three-element aerofoil revealed that *"the RANS methods showed less variability than did potential/Euler solvers coupled with boundary-layer solution techniques. However, some of the coupled methods still provided excellent predictions."* [117]

When dealing with viscous-inviscid methods it is impossible not to mention the contributions of Drela [118], developer of the XFOIL [119] and MSES [120, 121] codes. The first one, XFOIL, is used for the analysis of isolated aerofoils, and exploits a linear vorticity panel method coupled with a two equations model for the solution of the boundary layer. MSES, instead, solves the inviscid flow using a streamline-based discretisation of the Euler equations. Nevertheless, in both codes a strong viscous-inviscid interaction is obtained, and the entire system of equations is solved using a Newton method.

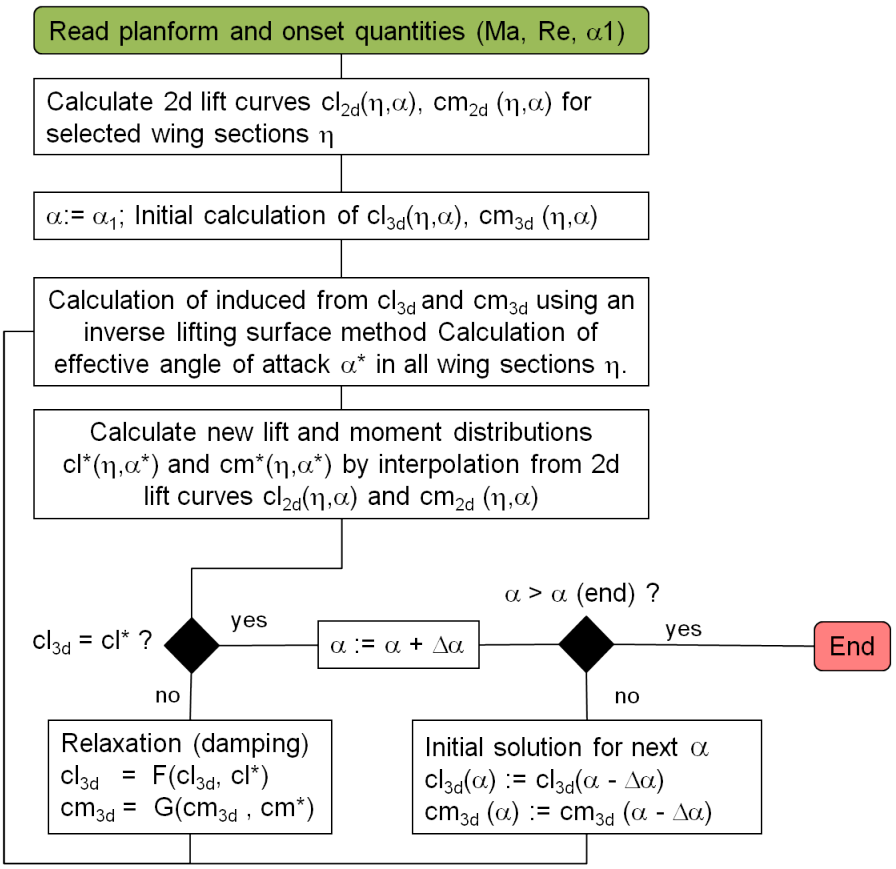

Figure 6.1: The iterative process of the quasi-three-dimensional method

In the work here presented the two-dimensional aerodynamic performance are evaluated using a panel method coupled with an integral formulation for the solution of the boundary layer. Furthermore, a lifting surface technique is used to evaluate spanwise lift and induced angle-of-attack distributions. The iterative process used to obtain the three-dimensional aerodynamic performance is described in Figure 6.1.

First of all, an entire polar is evaluated for each spanwise section (capturing the maximum angle-of-attack), and the evaluated aerodynamic coefficients are stored in a common database. Secondly, a wing angle of attack is selected and a reasonable initial spanwise distribution of lift and moments is assumed. This distribution forms the input of the reverse application of the lifting surface method, which evaluates the effective basic flow at each spanwise section. Then, the two-dimensional characteristics of the sections are extracted from the generated common database using the effective angle-of-attack distribution as input. This information is used to produce new lift and moment distributions, which are then compared to the one obtained in the previous iteration. If the two distributions do not match, the procedure is repeated until convergence is reached. Finally, the drag characteristic of the wing is evaluated adding the viscous contribution, obtained from the two-dimensional data, and the induced drag, evaluated at the Trefftz plane. The described process is performed for each specified wing angle-of-attack.

The quasi-three-dimensional approach can be an efficient methodology for the conceptual and preliminary design of high-lift systems. In the literature, its application in an industrial context is presented by Reckzeh [122]. In his paper, Reckzeh describes both the challenges faced and the methodologies used in the design of the Airbus A380. In particular, the author emphasises how the use of quasi-three-dimensional approaches has led to a reduction in number of wind tunnel tests. In fact, several high-lift wing concepts and variations were evaluated before starting the testing campaign, providing an already pre-optimised design. As a result, a reduction in wind tunnel costs was achieved, as well as a deeper and more targeted optimisation.

6.2 Background Literature

The next sections present the background literature on the foundation of the quasi-three-dimensional approach. Firstly, the potential flow theory is discussed together with a description of the panel method for the evaluation of inviscid flows around an object of arbitrary shape. Secondly, the concept of boundary layer is introduced, and the integral form of the describing equations derived. Next, the lifting line theory is outlined, together with the Trefftz plane method for the evaluation of the induced drag.

6.2.1 Panel Method

Panel methods have been extensively used in the aerospace industry since the late 1960s [123]. They have been introduced in order to numerically analyse the potential flow around both non-lifting and lifting bodies. The main concept at the core of such methods is the *"principle of superimposition"*, which allows the construction of solutions to complex problems by summing simpler elementary flows. The validity of this principle is guaranteed by the linearity of the equations that describe the potential flow, as will be shown later. A flow is defined as potential if it is incompressible, inviscid and irrotational. When those conditions are satisfied it is possible to express the velocity as the gradient of a scalar function called the velocity *"potential"*, denoted by ϕ.

$$\vec{V} = \nabla\phi \tag{6.1}$$

Moreover, from the continuity equation for irrotational incompressible (constant density, i.e. $\rho = \text{constant}$) flows

$$\nabla \cdot \vec{V} = 0 \tag{6.2}$$

Combining 6.1 and 6.2, the governing equation of potential flow is obtained

$$\nabla^2 \phi = 0 \tag{6.3}$$

Equation 6.3 is a second-order linear partial differential equation, commonly know as Laplace's equation. It is one of the most famous and extensively studied equations in mathematical physics. As anticipated earlier in the section, the main characteristic of Laplace's equation is its linearity, which allows the sum of any number of particular solutions to obtain a complex one.

In order to solve the governing equation in 6.3 for different geometric shapes appropriate boundary conditions must be specified. In particular, when considering the external aerodynamic flow over a stationary body, two different type of conditions are considered:

1. the flow must approach the uniform freestream conditions as the distance from it tends to infinity;

2. the velocity vector must be tangent to the surface.

The first boundary conditions states that the disturbance introduced by the body on the flow must decay far away from the body itself. The second one, instead, states that the flow cannot penetrate the body if it has a solid surface. Those conditions are mathematically expressed as:

$$\begin{aligned} \nabla\phi &\to V_\infty \quad \text{for } r \to \infty \\ \nabla\phi \cdot \hat{n} &= 0 \quad \text{on body surface} \end{aligned} \tag{6.4}$$

where V_∞ is the freestream velocity.

Applying the above specified boundary conditions to 6.3 it is possible to find a solution to the elementary flows that constitute the building blocks of the panel method. Those basic flows are:

- Uniform flow

- Source and Sink
- Doublet
- Vortex

Source and Sink, Double and Vortex are usually refer to as singularities, since the solution to this flow produces a singular point for the velocity, i.e. $V \to \infty$, at the origin. That is why, usually, panel method are also know as singularities methods. The detailed determination of the solutions to the elementary flows, discussed in [124], is here neglected.

The process to solve an arbitrary potential flow problem is now described. Firstly, the expression of the potential function for each of the basic flows, obtained as a solution to the Laplace's equation, is used to create a complex flow where the body surface represents a streamline. Then, the velocity field is evaluated using 6.1 and, consequently, the pressure distribution around the body using Bernoulli's equation:

$$p_\infty + \frac{1}{2}\rho V_\infty^2 = p + \frac{1}{2}\rho V^2 \tag{6.5}$$

which, in the case of incompressible inviscid flows, is valid throughout the entire field. A more convenient way of expressing the pressure is using the a-dimensional coefficient cp, defined as

$$cp = \frac{p - p_\infty}{\frac{1}{2}\rho V^2} = 1 - \left(\frac{V}{V_\infty}\right)^2 \tag{6.6}$$

Once the pressure field is evaluated, the coefficients for the normal and tangent force acting on the body can be obtained from the integral of the cp over the body's surface (indicating with l the lower surface of the aerofoil, and with u the upper):

$$
\begin{aligned}
c_n &= \frac{1}{c}\int_0^c (cp_l - cp_u)\, dx \\
c_a &= \frac{1}{c}\int_0^c \left(cp_u \frac{dy_u}{dx} - cp_l \frac{dy_l}{dx}\right) dx
\end{aligned}
\tag{6.7}
$$

Finally, the aerodynamic performance of the body in terms of lift and drag is obtained considering the angle of attack α

$$
\begin{aligned}
cl &= c_n\, cos\alpha - c_a\, sin\alpha \\
cd &= c_n\, sin\alpha + c_a\, cos\alpha
\end{aligned}
\tag{6.8}
$$

Using the described procedure the flow over a circular cylinder can be simulated through the sum of a uniform and a doublet. Therefore, the surface of the cylinder becomes a streamline of the flow, so that the boundary condition at the body surface is satisfied (see 6.4). However, the symmetric characteristic of the resultant flow (along the axis aligned to the uniform flow's velocity) results in a zero value for the lift force. The lifting case is achieved superimposing to the obtained flowfield a vortex of strength Γ, which produces a non symmetric flow. Due to the addition of the vortex, the circulation of the cylinder is now not zero, but equal to the vortex's strength Γ.

The lifting flow over a cylinder is found to be dependant on the value of the vortex strength [124], or circulation. In fact, there is not a single value that solves the flow, but a different solution is found for any value of the circulation. This result is not limited to flow over cylinder but it extends to any smooth body, including aerofoils. However, the indetermination of the solution is solved imposing the *"Kutta condition"*: the circulation on the body is equal to that particular value which results in the flow leaving smoothly at the trailing edge. So, the lifting flow over a cylinder is completely determined.

The procedure so far described allows the solution of the potential flow problem in a direct way, that is specifying a composition of elementary flows such that the

body surface becomes a streamline of the flow (satisfying, at the same time, the Kutta condition). It does not allow, however, the solution of the inverse problem: to specify a body shape and obtain the resulting flow. Indeed, this is a much more interesting problem, and it is at this stage that the numerical solution comes to play.

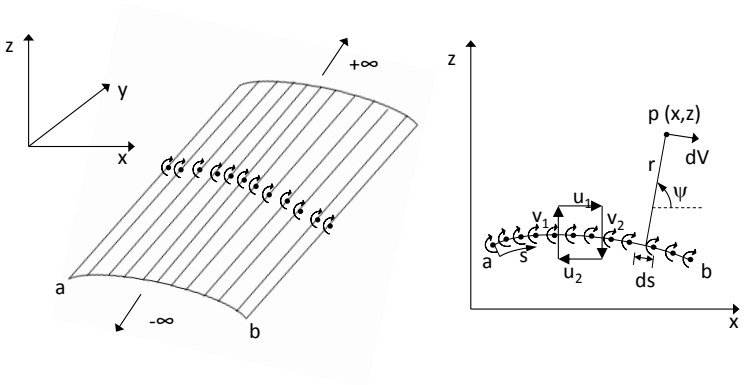

Figure 6.2: Representation of a vortex sheet.

First of all, the concept of a *"vortex-sheet"* must be introduced. As illustrated in Figure 6.2, a vortex sheet is an ensemble of infinitesimally small (in term of strength) vortex filaments, which are placed side by side along a smooth line. The strength per unit length along s is defined as $\gamma = \gamma(s)$, with s being the distance measured along the vortex sheet. It is, therefore, possible to consider an infinitesimal portion ds of the sheet as a distinct vortex of strength γds. This small section of the sheet induces an increment in the velocity vector dV, or equivalently in the potential $d\phi$, anywhere in the flow field given by

$$dV = -\frac{\gamma ds}{2\pi r} \quad ; d\phi = -\frac{\gamma ds}{2\pi}\psi \tag{6.9}$$

where r and ψ are cylindrical coordinates of a point P in the flow. Consequently, the effect of the entire vortex sheet is the sum of these infinitesimal contributions over the sheet length

$$\phi(x,y) = -\frac{1}{2\pi}\int_a^b \psi\,\gamma\,ds \tag{6.10}$$

Moreover, it is possible to demonstrate [124] that the tangential velocity experiences a local jump across the vortex which is equal to the local sheet strength. Referring to Figure 6.2, the just stated property can be mathematically expressed as $\gamma = u_1 - u_2$.

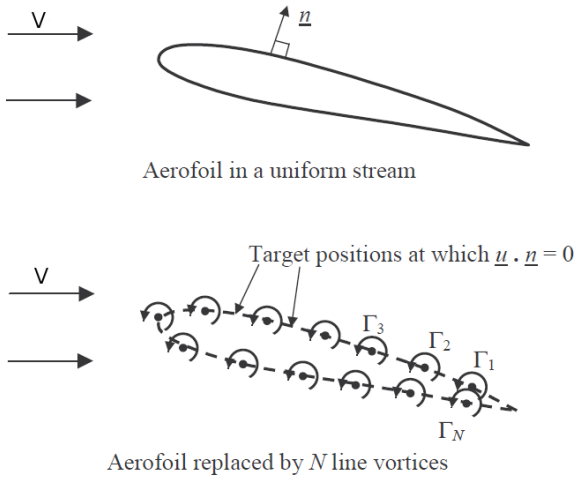

Figure 6.3: Distribution of vortex sheet over the surface of an arbitrary aerofoil.

The inverse problem to the solution of the potential flow can now be formulated. Let consider an aerofoil in a freestream with velocity V_∞, and let replace the surface of the body with a vortex sheet, as illustrated in Figure 6.3. Now, let calculate the variation of $\gamma(s)$ such that the aerofoil becomes a streamline of the flow and such that the Kutta condition is satisfied. Such problem does not admit a closed-form analytical solution, so that numerical techniques must be used instead. For this purpose, let discretise the vortex sheet approximating it by a series of straight panels. Moreover, let assume the vortex strength $\gamma(s)$ per unit length to be constant over a given panel. Thus for the n panels shown in Figure 6.3 this will results in a series of unknown vortex strength $\gamma_1, \gamma_2, \gamma_i, \ldots, \gamma_n$. Finally, let consider the midpoint of each panel as a control point where to apply the boundary condition of non permeability. It is now possible to calculate the potential at the generic control point of coordinates

(x_i, y_i)

$$\phi\left(x_i, y_i\right) = -\sum_{j=1}^{n} \frac{\gamma_i}{2\pi} \int_j \psi_{ij}\, ds_j \tag{6.11}$$

where $\psi_{ij} = tan^{-1}\left(y_i - y_j\right)/(x_i - x_j)$

Let now apply the boundary condition at the control point of the i-th panel. In particular, in order to have no flow penetrating the aerofoil's surface, the velocity vector must be tangent to the i-th panel. As a result, the superimposition of the freestream flow velocity and the velocity induced by the vortex panels must have no normal component at the panel's control points. This condition is mathematically expressed as

$$V_n = V_\infty\, cos\beta_i - \sum_{j=1}^{n} \frac{\gamma_i}{2\pi} \int_j \frac{\partial \psi_{ij}}{\partial n_i}\, ds_j = 0 \tag{6.12}$$

where $V_\infty\, cos\beta_i$ is the normal component of the freestream velocity, as shown in Figure 6.3.

Equation 6.12 is a linear algebraic equation, where the values of the integrals depend only on the geometry of the panels. Therefore, it is possible to numerically solve the equation and obtain the n unknowns $\gamma_1, \gamma_2 \ldots, \gamma_n$. This is the essence of the vortex panel method. The set of velocities expressed by the equation is commonly defined *"matrix of influence"* [123], and it is the coefficient matrix of the set of linear algebraic equations in the unknown values of source strength that expresses the zero velocity boundary condition. Although the system in 6.12 presents n equations in n variables, a further condition must be satisfied by the solution, namely the Kutta condition. For a vortex sheet distribution it is possible to demonstrate [124] that the Kutta condition reduces to the cancellation of the circulation at the trailing edge, i.e. $\gamma(te) = 0$. Within the numerical implementation of the vortex panel, the Kutta condition can be applied considering two control points nearby the trailing edge, i and $i - 1$, and imposing

$$\gamma_i = -\gamma_{i-1} \tag{6.13}$$

resulting in a cancellation of the strength of the two vortex at the intersection point (the trailing edge). The addition of the Kutta condition makes the system overdetermined, with $n+1$ equations and n unknowns. So, one of the control points is ignored in order to reduce the system to a determined one. Once the vortex strength distribution $\gamma(s)$ is calculated, the velocity on the aerofoil's surface can be obtained considering the velocity u_2 internal to the aerofoil equal to zero

$$\gamma = u_1 - u_2 = u_1 - 0 = u_1 \tag{6.14}$$

From the velocity field the pressure coefficient is evaluated from 6.6 and, finally, the aerodynamic coefficients from 6.8. At this stage the inverse problem of potential flows is solved.

The described vortex panel method considers a constant value of γ over a panel, resulting in a *"first-order"* accuracy. Indeed, higher-order panel methods have been developed and applied to relevant test cases [125, 126], with notable increase in the accuracy of the solution. Moreover, the method can be extended to higher subsonic regimes introducing compressibility effects correction, such as the Prandtl-Glauert formula. Finally, the panel method can be coupled with a boundary layer method to solve the viscous flowfield around single and multi-element aerofoils, as presented in the next section.

6.2.2 Boundary Layer Theory

In 1904 the mathematician and aerodynamicist Ludwig Prandtl reasoned from experiment that, for sufficiently high Reynolds numbers, a thin region exists near the wall where the viscosity to the flow is dominant. It is so that the concept of *"Boundary Layer"* was first introduced. Despite the reduced geometrical extension of this

region, Prandtl had realised the massive influence that it has on the aerodynamic performance of the body. Within the boundary layer the flow is retarded by the influence of friction, reducing its magnitude from the freestream value to zero at the body surface. The height of the boundary layer, indicated as δ, is defined as the distance above the wall, along the y direction, where $u = 0.99\,U_e$ (see Figure 6.4), with U_e equal to the velocity at the outer edge. Obviously, δ varies along the body surface, and so does the velocity profile $u = u(y)$. This latter is defined as the variation of u between $y = 0$ and $y = \delta$.

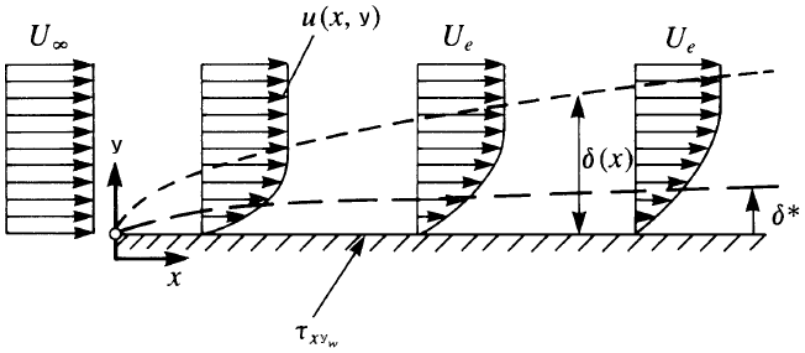

Figure 6.4: Boundary layer [6].

In addition to the velocity boundary layer thickness δ defined earlier, other two important properties of the boundary layer are frequently used. The first one is the *"displacement thickness"*, indicated as δ^*, and defined mathematically as

$$\delta^* = \int_0^{y_1} \left(1 - \frac{\rho u}{\rho_e u_e}\right) dy \quad dy \leq y_1 \to \infty \tag{6.15}$$

The displacement thickness can be interpreted as the physical displacement of the external inviscid flow due to the presence of the boundary layer. It is strictly linked to the concept of effective body, i.e. the concept by which the viscous flow that develops around an aerofoil can be replaced by an inviscid flow around a body whose surface consists of the outer edge of the boundary layer. As a consequence, δ^* is the relevant parameter to consider when coupling boundary layer method with inviscid external flows.

The second property is the momentum thickness, ψ. It is related to the reduction in the momentum caused by the presence of the boundary layer, and its mathematical definition is

$$\theta = \int_0^{y_1} \frac{\rho u}{\rho_e u_e}\left(1 - \frac{u}{u_e}\right) dy \quad dy \leq y_1 \to \infty \tag{6.16}$$

Both the displacement and the momentum thickness will be used for the derivation of the integral solution of the boundary layer equations later on in this section. Firstly, lets consider the Navier-Stokes equations and the continuity equation for a two-dimensional, steady flow [124]:

$$\begin{aligned}
&\text{Continuity:} && \frac{\partial(\rho u)}{\partial x} + \frac{\partial(\rho v)}{\partial y} = 0 \\
&\text{x momentum:} && \rho u \frac{\partial(u)}{\partial x} + \rho v \frac{\partial(u)}{\partial y} = -\frac{\partial p}{\partial x} + \mu\left(\frac{\partial^2 u}{\partial x^2} + \frac{\partial^2 u}{\partial y^2}\right) \\
&\text{y momentum:} && \rho u \frac{\partial(v)}{\partial x} + \rho v \frac{\partial(v)}{\partial y} = -\frac{\partial p}{\partial y} + \mu\left(\frac{\partial^2 v}{\partial x^2} + \frac{\partial^2 v}{\partial y^2}\right)
\end{aligned} \tag{6.17}$$

This set of second order differential equations can be simplified when considering the flow within a boundary layer. In particular, a normalised form of the equations is obtained introducing the values of the freestream velocity U_∞ and using the definition of Reynolds Number, i.e. $\mathrm{Re} = (\rho V L)/\mu$. Then, the order of magnitude analysis is performed on such normalised equations, to neglect terms which are not significant for the specified flow. The basic assumption of boundary layer theory is that $\delta \ll c$ and $\mathrm{Re} \geq 1/\delta^2$, that is small thickness of the boundary layer and relatively high Reynolds numbers. Moreover, it is clear that within the thin layer the gradient $\partial u/\partial x$ is of an order of magnitude smaller than the normal variation of the velocity, $\partial u/\partial y$. Those assumptions allow the complete Navier-Stokes equations in 6.17 to be reduced to the simpler parabolic boundary layer equations, which in their dimensional form are expressed as:

$$\begin{aligned} &\text{Continuity:} && \frac{\partial(\rho u)}{\partial x} + \frac{\partial(\rho v)}{\partial y} = 0 \\ &\text{x momentum:} && \rho u\frac{\partial u}{\partial x} + \rho v\frac{\partial u}{\partial y} = -\frac{dp_e}{dx} + \frac{\partial}{\partial y}\left(\mu\frac{\partial u}{\partial y}\right) \\ &\text{y momentum:} && \frac{\partial p}{\partial y} = 0 \end{aligned} \tag{6.18}$$

The y momentum equation in 6.18 is particularly important, since it states that the pressure in the boundary layer region is dependent only on the downstream location x. Thus, the outer pressure of the inviscid flow is impressed directly to the surface without changes. In addition, the boundary conditions for the above equations are $y = 0$, $u = 0$, $v = 0$ at the wall, and $y \to \infty$, $u \to U_e$ at the boundary edge.

Despite the reduction in complexity in comparison with the complete Navier-Stokes equations, only a limited number of closed form solutions to the boundary layer problem exist. The first to obtain a mathematical solution of the equations in 6.18 was Blasius in 1908. He considered the flow over a thin flat plate, and assumed that the same dimensionless shape could be used to represent the local velocity profile along the surface. In doing so, he transformed the continuity and momentum equations in a single ordinary differential equation. This *"similarity method"* was later extended by Falkner and Skan [127] to include cases where both favourable and adverse pressure gradients are present. The obtained family of similarity solutions, which represents the flow over a wedge of angle $\beta\pi$, provides different velocity profiles depending on the value of the parameter β. The Falkner and Skan equations include velocity profiles for the stagnation point, $\beta = 1$, as well as for the separation point (point where the boundary layer separates from the body surface), $\beta = -0.199$.

However, for most engineering design analyses the detailed variations of the flow variables within the boundary layer is not of paramount importance. In fact, in such applications, the main relevant quantities are the wall shear stress and the displacement thickness. The first is needed to calculate the viscous drag of the body, while the second is required for the coupling with inviscid external flows. The

von Karman *"integral momentum method"* for the boundary layer equation provides exactly these variables. The derivation of the equation is based on the integration of the x-momentum equation in 6.18, with respect to y, across the boundary layer.

$$\int_0^\delta \rho u \frac{\partial (u)}{\partial x}\, dy + \int_0^\delta \rho v \frac{\partial (u)}{\partial y}\, dy = -\int_0^\delta \frac{dp_e}{dx}\, dy + \int_0^\delta \frac{\partial}{\partial y}\left(\mu \frac{\partial u}{\partial y}\right)\, dy \tag{6.19}$$

A further simplification of the above equation can be achieved eliminating the pressure term using the momentum equation on the outer edge of the boundary layer, as by

$$U_e(x)\, \frac{\partial U_e(x)}{\partial x} = -\frac{1}{\rho}\frac{dp_e}{dx} \tag{6.20}$$

Therefore, the substitution of these results into 6.20 and the use of the continuity equation to replace the derivatives of v with those of u lead to the following equation

$$\frac{d}{dx}\int_0^\delta (U_e - u)\, u dy + \frac{dU_e}{dx}\int_0^\delta (U_e - u)\, dy = \frac{\tau_w}{\rho} \tag{6.21}$$

where τ_w is the wall shear stress.

Finally, the expression can be rearranged in function of the displacement and momentum thickness, recalling their definition in 6.15 and 6.16

$$\frac{d}{dx}\left(U_e^2\, \theta\right) + U_e\, \delta^* \frac{dU_e}{dx} = \frac{\tau_w}{\rho} \tag{6.22}$$

or in a-dimensional form

$$\frac{d\theta}{dx} + (H+2)\frac{\theta}{U_e}\frac{dU_e}{dx} = \frac{cf}{2} \tag{6.23}$$

where

$$\begin{aligned} C_f &= \frac{\tau_w}{\frac{1}{2}\rho U_e^2} && \text{friction coefficient} \\ H &= \frac{\delta^*}{\theta} && \text{shape factor} \end{aligned} \tag{6.24}$$

The von Karman integral equation is valid for both laminar and turbulent boundary layers. However, it cannot be solved without additional information, since it contains three unknowns δ^*, θ and τ_w. Consequently, a family of velocity profiles (such as the Falkner and Skan presented earlier) has to be specified, which completely defines the velocity fields within the boundary layer. Even so, singularities arise when attempting to integrate the equation in regions near the trailing edge or beyond a point of flow separation. In these regions, the flow exhibits stronger inviscid-viscous interaction and the boundary layer must be solved in *"inverse mode"*, rather than the traditional mode. Therefore, the external velocity is not specified, but the boundary layer adjusts through the displacement effect. However, one-equation integral methods, such as the one produced by equation 6.23, are not suited for flows with strong interaction [6]. Two-equation boundary layer methods must, then, be considered.

Two-equation methods eliminate the direct link between the profile shape and the pressure gradient by specifying an additional equation, the integral kinetic energy equation. The latter is obtained by a suitable manipulation of the integral continuity and momentum equations (see White [128]) and is expressed in dimensionless forms as

$$\frac{d\theta^*}{dx} + 3\frac{\theta^*}{U_e}\frac{dU_e}{dx} = 2c_\Delta \tag{6.25}$$

where

$$\begin{aligned} c_\Delta &= \frac{\int_0^{y_1} \mu \left(\frac{\partial u}{\partial z}\right)^2 dz}{\frac{1}{2}\rho U_e^3} && \text{dissipation coefficient} \\ \theta^* &= \int_0^{y_1} \left(1 - \frac{u^2}{U_e^2}\right)\frac{u}{U_e} dz && \text{kinetic energy thickness} \end{aligned} \tag{6.26}$$

By combining the just obtained kinetic energy equation and the integral momentum one (Eqs. 6.25 and 6.24), and rearrenging the terms, the kinetic energy shape parameter equation is obtained:

$$\frac{\theta}{H^*}\frac{dH^*}{dx} = \frac{2c_\Delta}{H^*} - \frac{c_f}{2} + (H-1)\frac{\theta}{U_e}\frac{dU_e}{dx} \tag{6.27}$$

where the kinetic energy shape parameter is defined as $H^* = \theta^*/\theta$. As a result, there is no explicit link between H and the local external velocity in either of the equations. However, three closure relations for H^*, c_f , and c_Δ are now required to integrate the momentum and kinetic energy shape parameter equations simultaneously. Those closures may be written as

$$\begin{aligned} H^* &= f_1(H) \\ Re_\theta \frac{c_f}{2} &= f_2(H) \\ Re_\theta \frac{2c_\Delta}{H^*} &= f_3(H) \end{aligned} \tag{6.28}$$

where $Re_\theta = U_e\theta/\nu$ is the momentum thickness Reynolds number. These three functions can be determined if some profile family is assumed, as presented by Drela and Giles [118] for both laminar and turbulent flows.

Now that the methods for the evaluation of the inviscid outer flow and for the solution of the boundary layer equations have been derived, the focus is shifted to the coupling process. In the literature three basic approaches to solve the viscous-inviscid interaction problem (with limited separation) can be found. The first one is the quasi-simultaneous method of Veldman [129], which solves simultaneously the boundary layer equations and an approximation of the outer flows (modelled through an interaction law). The second is the semi-inverse method developed by Carter [130] and Le Balleur [116]. In this approach the inner and outer flows are coupled through a relaxation formula which successively updates the displacement thickness distribution. Both the direct and inverse techniques for the solution of the boundary layer equations are used accordingly to the status of the flow (attached

or separated). Clearly, this method involves sequential solution of the viscous and inviscid flow equations. Finally, the third method is the fully simultaneous approach of Drela and Giles [118]. In their work the authors eliminate the sequential solution of the inviscid and viscid equations using a Newton method for the solution of the entire non-linear equation. In this work, the semi-inverse technique of Carter is preferred to the other two for the inviscid-viscous coupling process.

6.2.3 Lifting Line Theory

The determination of the aerodynamic characteristics of finite wings is the focus of this section. The lift generated by a wing is the result of a generally lower pressure acting on its upper surface compared with the pressure acting on the lower surface. This pressure difference is the cause of a spanwise flow (from the lower surface to the upper one) which, combined with the freestream velocity, generates the wing's trailing vortex system. This swirling motion of the air travels downstream of the wing causing two main effects: a change in the effective angle of attack along the wing, and an induced curvature of the flow. The first effect is due to the downward induced flow, or *"downwash"*, which added to the freestream generates an *"induced angle of attack"*. The second effect is due to the chordwise variation in value of the downwash, small far ahead of the wing and higher far behind it.

The presence of the downwash modifies the flow at the local aerofoil sections along the span. First of all, the changes in the local relative wind alter the angle of attack actually seen by the local aerofoil section. As a result, the effective angle of attack for the section is smaller than the geometrical one (see Figure 6.5), and it is defined as $\alpha_{eff} = \alpha - \alpha_i$. Secondly, the inclination of the local lift vector is modified as well, so that an *"induced drag"* force is created.

The first theory that attempted to predict the above described phenomena was developed in the early 1900s by Ludwig Prandtl. The main idea on which the theory is based is the replacement of the finite wing with a *"bound vortex"*, i.e. a vortex that

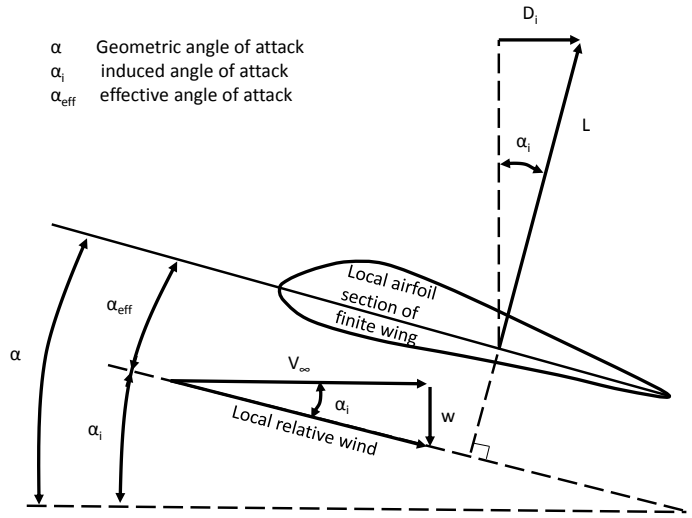

Figure 6.5: Effective angle of attack and induced drag generated by the downwash on the local aerofoil section of a finite wing

is fixed at some location in the flow. In particular, the vortex is usually placed at the wing quarter chord line. However, a vortex line cannot start or finish abruptly (Helmhotz's theorem), so that the vortex is shed into the flow and creates a wake. This configuration results in a horseshoe shaped vortex system, with the bounded vortex continuing into two vortices trailing downstream. These trailing vortices produce a downwash distribution w over the bound vortex itself which approaches infinity at the wing tips.

It was clear to Prandtl that such a downwash distribution did not represent realistically the flow of a finite wing. Therefore, a more refined model was proposed, which uses a large number of horseshoe vortices, each of different length, distributed spanwise along a single line, as illustrated in Figure 6.6. As a consequence, the wing representation now presents a series of trailing vortices, which strength is equal to the jump in circulation along the lifting line. Extrapolating this concept to an infinite number of vortices with strength $d\gamma$, it is possible to express the induced angle of attack at the arbitrary location y_0 along the lifting line as

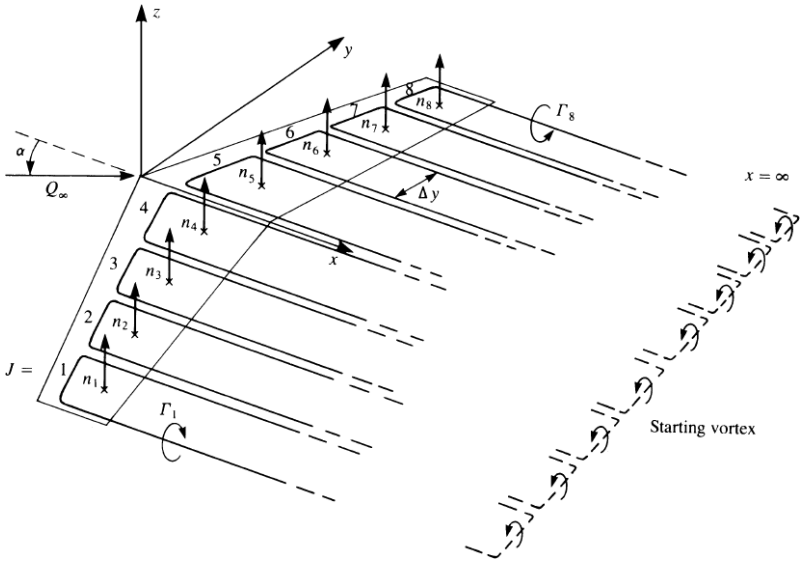

Figure 6.6: Lifting-line model consisting of a finite number of horseshoe vortices along the y-axis [6].

$$\alpha_i\left(y_0\right) = \frac{1}{4\pi V_\infty} \int_{-b/2}^{b/2} \left(\frac{d\gamma/dy}{y_0 - y}\right) dy \tag{6.29}$$

where $\alpha_i(y_0)$ is approximated by the ratio $w(y_0)/V_\infty$.

Let now introduce the Kutta-Jukowsky relation which links the strength of the bound vortex to the lift distribution

$$\frac{dL(y)}{dy} = \rho\, V_\infty\, \frac{1}{2}\, c(y)\, c_l(y)\, V_\infty = \rho V_\infty \Gamma(y) \tag{6.30}$$

Moreover, considering the sectional lift coefficient $c_l = c_{l\alpha}\left(\alpha - \alpha_i - \alpha_{L=0}\right)$, it is possible to express the geometric angle of attack as

$$\alpha = \frac{c_l\left(y\right)}{c_{l\alpha}} + \alpha_i + \alpha_{L=0} \tag{6.31}$$

Finally, substituting in 6.31 the expression of the induced angle of attack found in 6.29 and using the Kutta-Jakowsky relation 6.30 to express the sectional c_l as a function of the circulation Γ, the fundamental equation of Prandtl' s lifting-line theory is obtained

$$\alpha\left(y_0\right) = \frac{2\Gamma\left(y_0\right)}{c_{l\alpha} V_\infty c\left(y_0\right)} + \alpha_{L=0}\left(y_0\right) + \frac{1}{4\pi V_\infty} \int_{-b/2}^{b/2} \left(\frac{d\gamma/dy}{y_0 - y}\right) dy \tag{6.32}$$

Equation 6.32 is an integro-differential equation in a single variable Γ. All the other quantities are defined by the geometry of the wing and the design point conditions.

The predictions obtained using the lifting line theory are reasonably accurate when high-aspect ratio, unswept wings are considered. However, the classical method lacks any chordwise information, since the vortex are concentrated in a line. An extension to the lifting line theory, suitable for wing with sweep or low aspect ratio, is the *"lifting surface"* or Weissinger method. In this case, the bound vortex segments are still positioned along the quarter-point line, while the flow tangency condition is, instead, applied to different collocation points. These points are, usually, positioned at the three-quarter chord location. This extended method computes good results for the spanwise lift distribution and the induced drag [124].

6.2.4 Trefftz Plane Method

The Trefftz Plane method is a far-field integration method used to evaluate the induced drag of three-dimensional incompressible, inviscid flowfield over a lifting surface. As introduced in the previous section, the induced drag arise as a consequence of the inclination of the force vector relative to the freestream caused by the trailing vortex system. The method uses the integral form of the momentum equation to write the forces in terms of the quantities on the outer boundaries. In particular, under the conditions of inviscid and incompressible flow, the vorticity of the flow is confined to a thin sheet, and the momentum equation reduces to

$$F = \iint_S \rho\, \vec{V}\left(\vec{V}\cdot\hat{n}\right)\, dS + \iint_S \frac{\rho}{2}\, \vec{V}^2 \hat{n}\, dS \tag{6.33}$$

The control volume is taken large enough so as to assume that the flow escapes the control volume almost entirely from the downstream outflow face. The integral in 6.33 is performed on a plane positioned aft of the wing, and oriented perpendicular to the freestream (as shown in Figure 6.7). Such plane, defined *"Trefftz plane"*, has to be far downstream so that, apart from the freestream throughflow, all the motion is in the crossflow plane $(y-z)$ and no velocity is induced in the x-direction. Expressing the velocity vector in terms of freestream and perturbation values, $\vec{V} = (U_\infty + \acute{u}, \acute{v}, \acute{w})$, the induced drag can be evaluated from the integral

$$D_i = \frac{\rho}{2} \iint_{S_T} \left(\acute{v}^2 + \acute{w}^2 - \acute{u}^2 \right) \, dS \tag{6.34}$$

Therefore, the induced drag is dependent only on the perturbation velocities. In addition, if the flow is inviscid, the wake at the Trefftz plane is parallel to the local freestream and, hence, the x velocity perturbation must die away, i.e. $\acute{u} \ll \acute{v}, \acute{w}$. Consequently, the drag can be obtained by integrating the $\acute{v}$ and $\acute{w}$ component on this plane only:

$$\frac{\rho}{2} \iint_{S_T} \left(\acute{v}^2 + \acute{w}^2 \right) \, dS = -\frac{\rho}{2} \iint_{wake} \Gamma(y) V_n \, dl \tag{6.35}$$

where $\Gamma(y)$ is the circulation on the wing at a specific location and V_n is the wake-induced velocity normal to the wake trace.

In conclusion, equation 6.35 expresses the relation between the wing circulation and the resultant induced drag. It is a powerful equation, since it allows to accurately estimate the induced drag avoiding the expensive integration of the pressure coefficients over the wing surface [131].

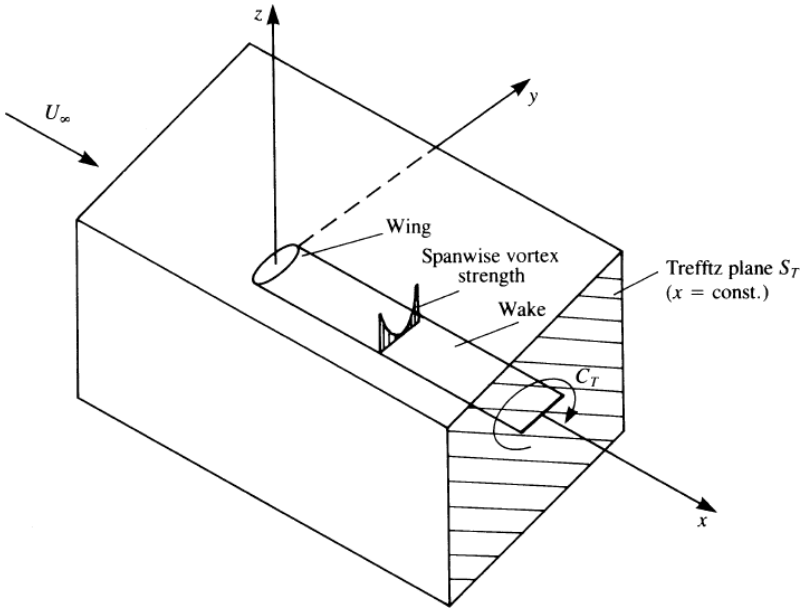

Figure 6.7: Control Volume and Trefftz Plane [6]

6.3 Validation and Verification

The validation and verification study of the quasi-three-dimensional code used in this work is presented in this section. The code itself is a propietary sofware of the Industrial Sponsor, developed internally by the department of methods and simulation in the late 90s. The NASA *"Trapezoidal Wing"* [132], illustrated in Figure 6.8, is selected as test case configuration. An extensive set of experimental, as well as numerical (RANS) data is available for the selected test case, as a result of the study performed by several partners during the AIAA CFD High Lift Prediction Workshop [32] (held during the 28th AIAA Applied Aerodynamics Conference June 26-27, 2010, Chicago, IL).

The Trapezoidal Wing is a back-swept untwisted wing, with no dihedral and a comparatively low aspect ratio. The main geometrical characteristics of the test case are summarised in Table 6.1. In particular, the wing presents a span of 2.16$[m]$, an aerodynamic mean chord of 1.0067$[m]$ and a reference area (full span wing) of 4.0929$[m^2]$. The trapezoidal wing is equipped with full-span slat and flap elements. The latter, can be positioned at two different rigging settings: *"configuration 1"*,

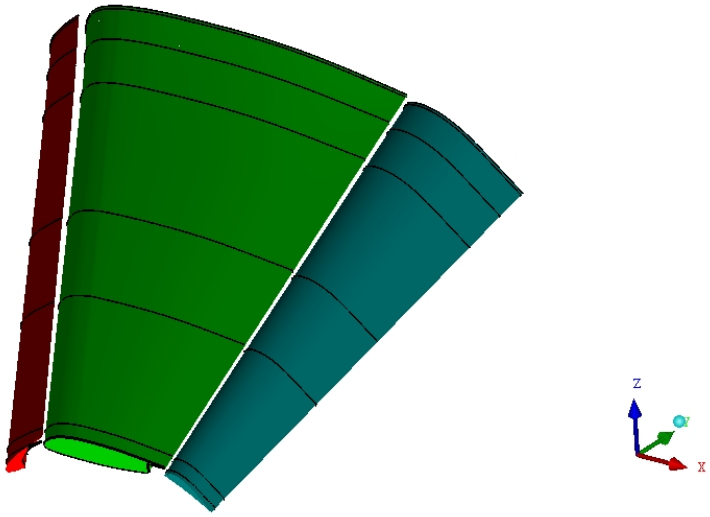

Figure 6.8: The NASA Trapezoidal Wing

with a flap deployment angle of 25° and *"configuration 8"*, with a lower flap deployment settings at 20° angle. The first configuration is chosen for the validation study here presented. Nonetheless, the lower flap settings configuration is used to assess the accuracy of the quasi-three-dimensional method in predicting the effects of flap increments. Finally, the supports that connect the slat and flap to the main element, or *"brackets"*, are here neglected, since they are not modelled in the approach adopted.

Table 6.1: Trapezoidal Wing geometrical characteristics.

Aerodynamic Mean Chord	c_{ref}	1.0067	$[m]$
Geometric Mean Chord	c_{geom}	0.9473	$[m]$
Moment Reference:		x = 0.87229	$[m]$
		y = 0	$[m]$
		z = 0	$[m]$
Semi Span	$b/2$	2.16	$[m]$
Reference Area	A	4.0929	$[m^2]$
Aspect Ratio	Λ	4.561	[-]
Quarter Chord Sweep	φ_{25}	29.97°	[-]

The quasi-three-dimensional representation of the test case consists of seven two-dimensional profiles, extracted from the deployed 3D geometry (see Figure 6.8) at the spanwise positions specified by Table 6.2. The first section, indicated as s0153,

is the wing root section, just after the wing-fuselage junction. The fuselage is here modelled as an *"auxiliary wing"*, which spans from the symmetry plane to the wing root section. This modelling strategy allows the method to capture the reduction in spanwise lift distribution in the near-fuselage region, so increasing the accuracy of the simulation.

After the extraction of the two-dimensional geometries, each 2D section is normalised by the local chord, and the entire polar (up to two angles of attack beyond the maximum lift condition) is evaluated using a viscous-inviscid coupled method. The obtained data are, then, collated into a sectional database and used as input for the lifting surface iterative procedure.

Table 6.2: Spanwise location of the 2D sections for the quasi-three-dimensional representation of the Trapezoidal Wing.

Section	**Span location** $[m]$	**Adimensional location** η
s0153	0.153	0.07
s0300	0.300	0.14
s0500	0.500	0.23
s1100	1.100	0.51
s1500	1.500	0.69
s2100	2.100	0.97
s2160	2.160	1.00

The results obtained using the quasi-three-dimensional approach are compared with experimental data in Figure 6.9. The lift-alpha polar shows a satisfactory matching of the two datasets, although the quasi-three-dimensional method slightly under-predicts the linear region of the lift curve. This is probably due to the approximate modelling of the fuselage effects, which are here simulated using the definition of an auxiliary wing. Nonetheless, the maximum lift coefficient of $cl_{max} = 2.9955$ achieved in the wind tunnel is closely matched by the used approach, which predicts a $cl_{max} = 3.0057$. However, the correspondent angle of attack at which it occurs is over-predicted, being 3 degrees higher than the experimental value of $\alpha = 33°$. The deviation is deemed to be acceptable for trend analyses or for the use within

an optimisation process.

In addition, the comparison of the drag polar shows the correct trend, once again with some discrepancies at higher angle of attack. This behaviour is, mainly, a consequence of the under-prediction of lift at these conditions, which results in a lower total drag value. In fact, an examination of the $cd-cl$ polar clearly illustrates a more than satisfactory accuracy of the quasi-three-dimensional method in predicting the drag for a given lift condition. Also, the constant delta between wind tunnel data and simulation in the drag polar can be attributed to the presence of the brackets, which effect is not considered by the used numerical approach.

Moreover, pressure coefficient distributions are compared at three different stations along the span. Figure 6.10 illustrates the comparison for the moderate angle of attack $\alpha = 10°$. The results obtained agree well with the experimental data for the inboard stations ($\eta = 0.17$ and $\eta = 0.65$), whereas the tip section ($\eta = 0.95$) reveals considerable deviations. This behaviour is, to some extent, expected. In fact, the flow around the tip region is dominated by highly three-dimensional features, which are not captured by the quasi-three-dimensional approach.

Finally, a flap deflection study is performed to assess the accuracy of the used tool in capturing variations in aerodynamic performance due to changes in the deployment settings. For this purpose, the relative reduction of lift ($\Delta cl/cl$) associated with the decreased flap deflection of configuration 8 (compared with configuration 1) is evaluated. The results, plotted against wind tunnel data in Figure 6.11, show a fair agreement on the trend, thought the quasi-three-dimensional approach does not quite match the absolute experimental values. This is particularly true in the lower angle of attack range, while the match is satisfactory at high alphas.

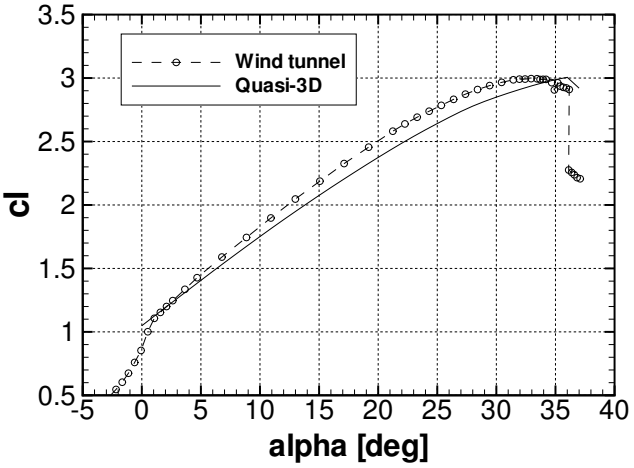

(a) $cl - \alpha$

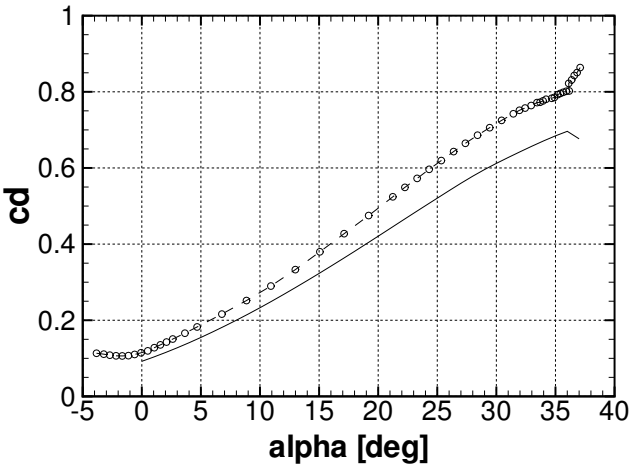

(b) $cd - \alpha$

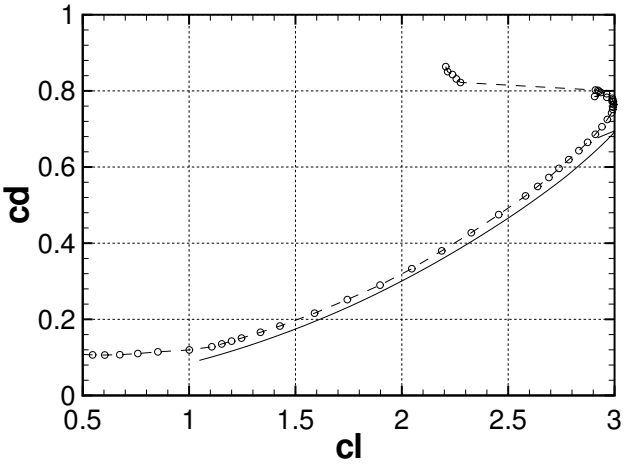

(c) $cd - cl$

Figure 6.9: Polars comparison for the Trapezoidal Wing configuration. The quasi-three-dimensional method (solid line) is compared against wind tunnel data (line with dots).

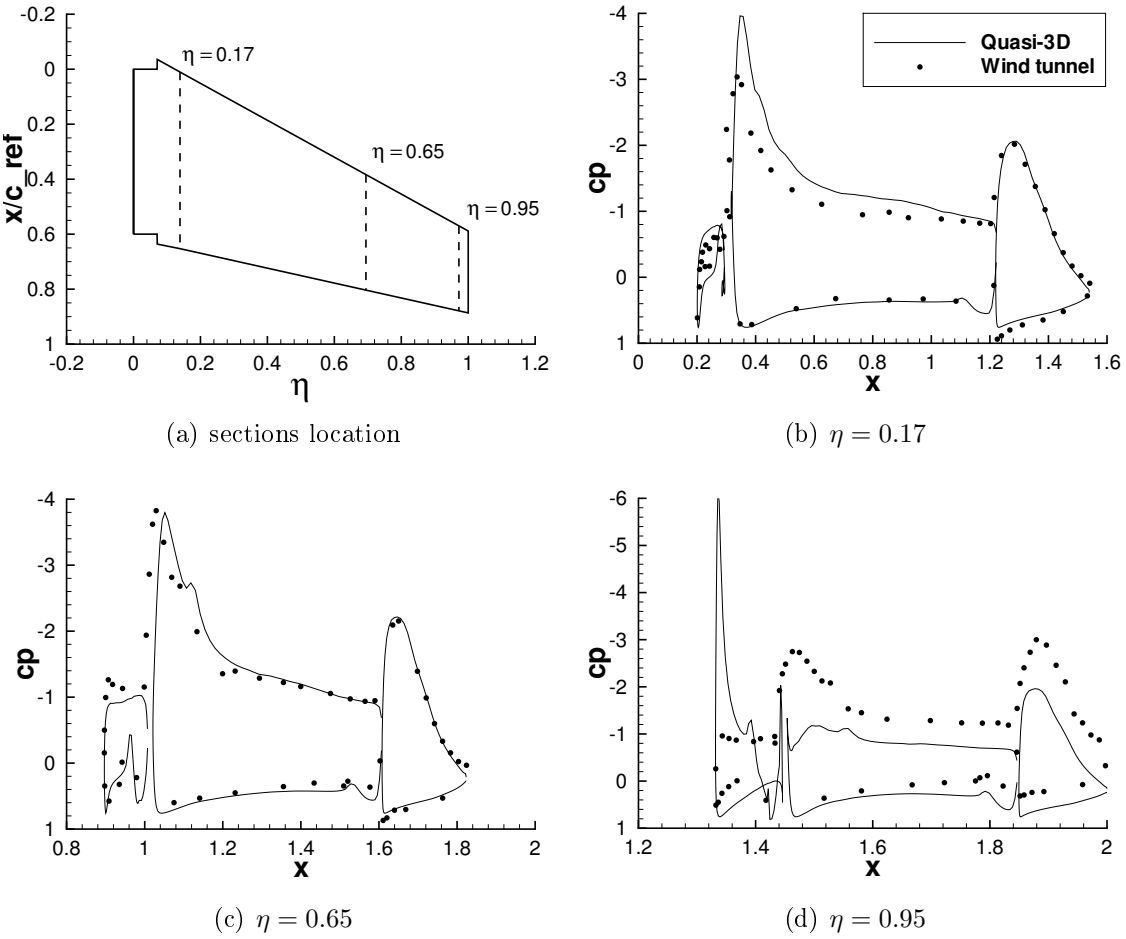

(a) sections location

(b) $\eta = 0.17$

(c) $\eta = 0.65$

(d) $\eta = 0.95$

Figure 6.10: Trapezoidal Wing pressure coefficient comparison at $\alpha = 10°$ for three different stations along the span. The quasi-three-dimensional results (solid line) is compared against wind tunnel data (line with dots).

6.4 The Extended Optimisation Framework

The validation study presented in the previous section has shown that the quasi-three-dimensional method can satisfactorily predict the aerodynamic performance of complex high-lift configurations. Therefore, the approach is used to extend the optimisation framework previously used for the design of multi-element 2D sections. As illustrated in Figure 6.12, the analysis starts with the specification of the new deployment settings and the generation of the input files for the two-dimensional sectional simulations. After the parallel execution of the 2D polars and of the inverse lifting line method, the aerodynamic performance of the configuration is obtained.

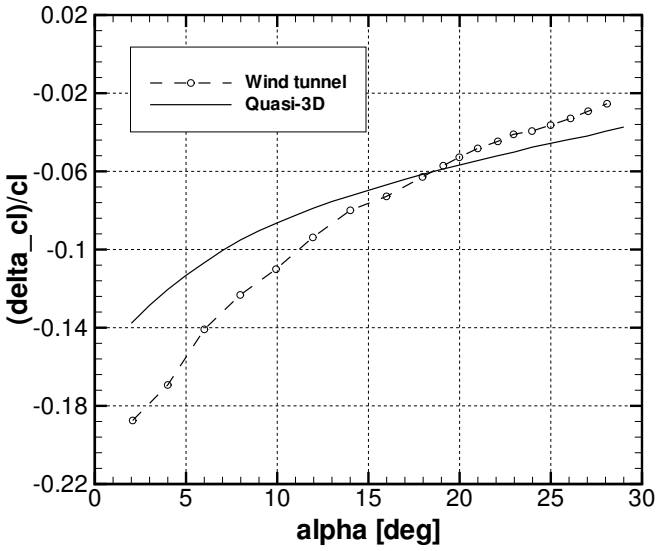

Figure 6.11: Effect of reduced flap deflection on lift polar. Comparison of quasi-three-dimensional prediction (solid line) against wind tunnel data (line with dots).

Then, this data are used to evaluate the objective functions specified within the design problem. As a final step, the optimisation algorithm collates the information regarding design variables and corresponding objective function values, and produces a new candidate for the next evaluation. The described loop is performed until a halting criteria is met, and the final results are output for the subsequent analysis.

6.4.1 Test Case Description

The 3D test case used throughout this work is the KH3Y (DLR-F11) geometry, illustrated in Figure 6.13. The geometry is representative for a wide-body twin-jet high lift configuration, and it includes a detailed model of the wing and fuselage components. Unlike the Trapezoidal Wing used in the validation study, the KH3Y configuration presents a 4°dihedral angle, a twist distribution along the span and a cranked planform. In addition, it is a higher aspect ratio wing than the Trapezoidal test case, with its main geometrical characteristics summarised in Table 6.3.

The wing is equipped with a full-span slat and single-slotted Fowler flap elements. The high-lift system can be deployed in two take-off and one landing settings [133].

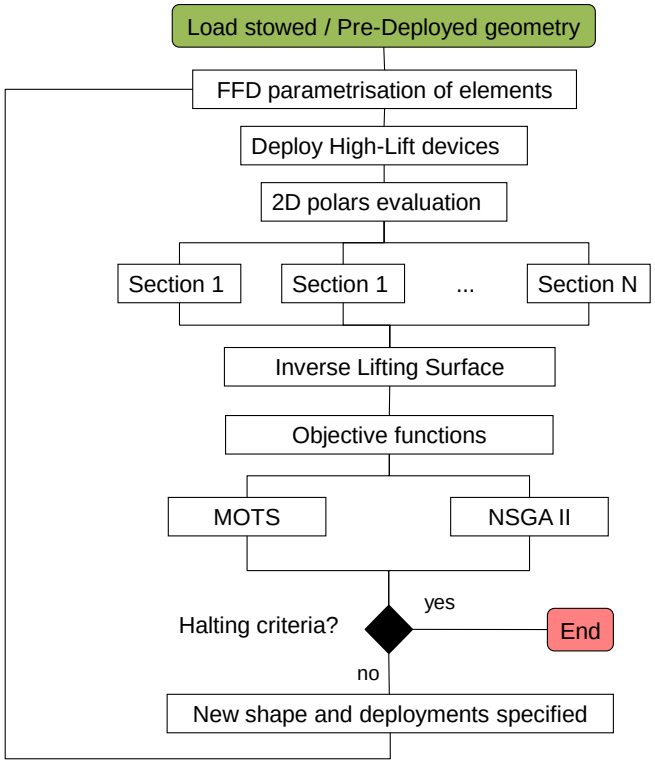

Figure 6.12: The high-lift configuration optimisation framework, extended with the implementation of the quasi-three-dimensional analysis.

In this study only the landing configuration is analysed, with the deployment settings specified in Table 6.4.

Wind tunnel data are available from the EUROLIFT2 framework program [134], for both low and high Reynolds numbers. In particular, the latter have been generated in the European Transonic Wind tunnel (ETW), where the total temperature and pressure can be adjusted to cover a wide range of Reynolds and Mach numbers. From these sets of data, the one indicated as *"run238"* is here used for comparison against RANS and quasi-three-dimensional simulations. Table 6.5 lists the onset conditions for the specific experimental setup. In order to achieve the Reynolds number value of 15.1×10^6 the total temperature in the tunnel is reduced to 114 [K], while the total pressure is increased to three times the atmospheric conditions. In contrast, the Mach number ($Ma = 0.176$) is at the lower limit of the tunnel operational boundaries.

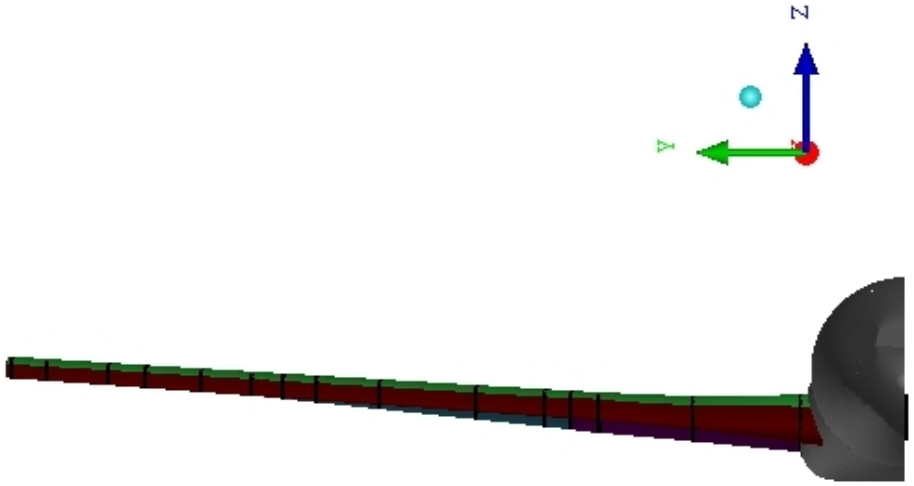

(a) Front view

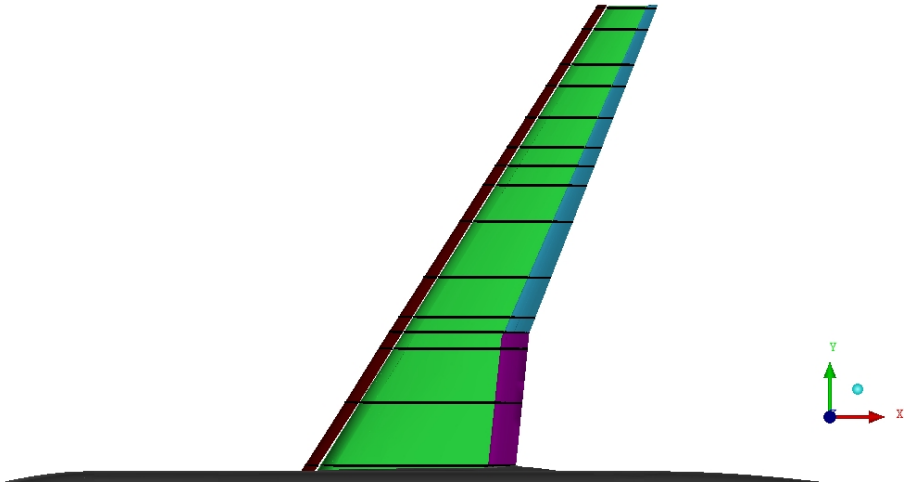

(b) Top view

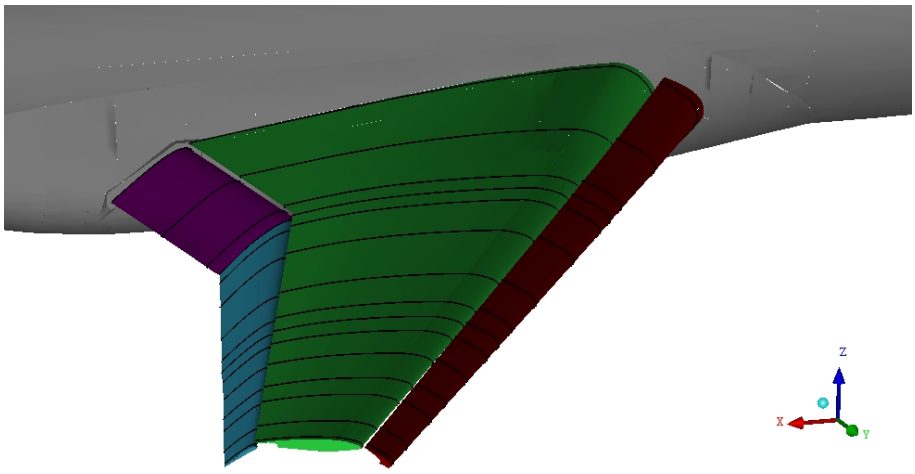

(c) Perspective view

Figure 6.13: CAD model of the KH3Y test case in landing configuration, with highlighted spanwise locations selected for the quasi-three-dimensional analysis.

Table 6.3: KH3Y (DLR-F11) high-lift configuration geometrical characteristics.

Aerodynamic Mean Chord	c_{ref}	0.34709	$[m]$
Geometric Mean Chord	c_{geom}	0.29938	$[m]$
Moment Reference:		x = 1.4289	$[m]$
		y = 0.0	$[m]$
		z = -0.04161	$[m]$
Semi span	$b/2$	1.4	$[m]$
Reference Area	A	0.83826	$[m^2]$
Aspect ratio	Λ	9.353	[-]
Quarter chord sweep	φ_{25}	30°	[-]
Wing Dihedral	Γ	4°	[-]

Table 6.4: KH3Y (DLR-F11) deployment settings for landing configuration.

slat deflection angle	Θ_s	26.5°
slat gap	gap_s/c_{ref}	0.014
slat overlap	ovl_s/c_{ref}	-0.008
flap deflection angle	Θ_f	32.0°
flap gap	gap_f/c_{ref}	0.010
flap overlap	ovl_f/c_{ref}	0.006

Table 6.5: ETW wind tunnel onset conditions, low Reynolds number.

Mach number	Ma	0.176	[-]
Reynolds number	Re	15.1×10^6	[-]
Total pressure	Ptot	301.56×10^3	[Pa]
Total temperature	Ttot	114.7	[K]

The increased complexity of the test case, in comparison to the Trapezoidal Wing, has led to the identification of 16 sections (including 1 section for the auxiliary wing definition) for the quasi-three-dimensional representation, as illustrated in Figure 6.13. Also, the sections are not uniformly distributed along the span, but tend to concentrate in areas where variations in either the wing planform or the high-lift system are substantial. The so defined model is, then, used to compute the polars of the baseline KH3Y configuration.

The obtained results are compared against wind tunnel data in Figure 6.14. The plots show that, for the KH3Y test case, the overall accuracy of the used

approach is even higher than for the validation test case presented in the previous section. This behaviour might be related to the higher aspect ratio of the KH3Y wing in comparison with the Trapezoidal case, which reduces, to some extend, the highly three-dimensional flow features along the wing span. Still, the quasi-three-dimensional approach under-estimates the lift slope in the linear region of the lift-alpha polar (Figure 6.14(a)). The predicted maximum lift coefficient is also under-estimated, with a value of $cl_{max} = 2.812$, whereas the experimental value is close to $cl_{max} = 2.87$. Nevertheless, the predicted angle at which it occurs is only 1° lower than the experimental value of $\alpha = 20°$. On the contrary, the method over-predicts the lift for low angle of attack, where the occurrence of substantial separation in the slat lower surface is not captured.

With regard to the prediction of drag, the quasi-three-dimensional simulation accurately captures the variation of cd with angle of attack. In fact, the $cd - \alpha$ curve (Figure 6.14(b)) closely resemble the experimental data, with an almost constant delta of 0.02% between the two sets throughout the alpha range (excluding the lower alpha values). Furthermore, the same behaviour is shown in the $cd - cl$ curve (Figure 6.14(c)), with the used approach satisfactorily predicting the drag variation with lift, especially at moderate and high cl values.

In addition, a RANS simulation of the same configuration is performed using the commercial CFD Suite Ansys®CFX V15 on the medium grid available from the AIAA High Lift Prediction Workshop [32]. The $k - w$ SST turbulence model is used, in conjunction with an upwind first order scheme for the turbulence numerics and the *"High Resolution"* scheme for the remaining state variables. The results, presented in Figure 6.14, show an over-prediction of the lift curve slope as well as of the maximum lift coefficient, with the RANS simulation predicting a $cl = 2.91$ at $\alpha = 18.5°$. Similarly, higher drag values per given lift condition are predicted by the RANS solutions, as shown in Figure 6.14(c). Consequently, the $cd - \alpha$ curve is steeper than the experimental one, and the drag at high angle of attack is over-

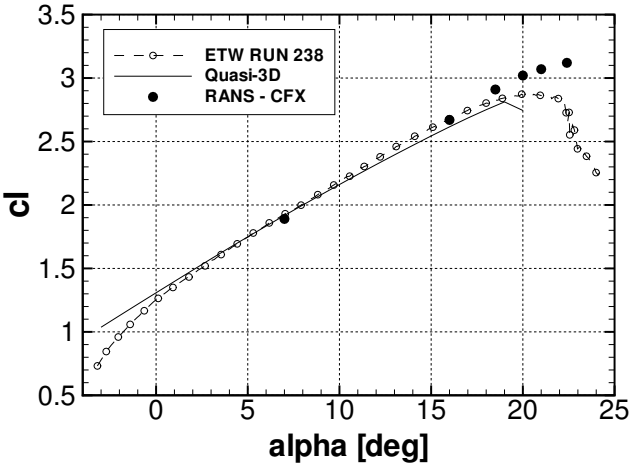

(a) $cl - \alpha$

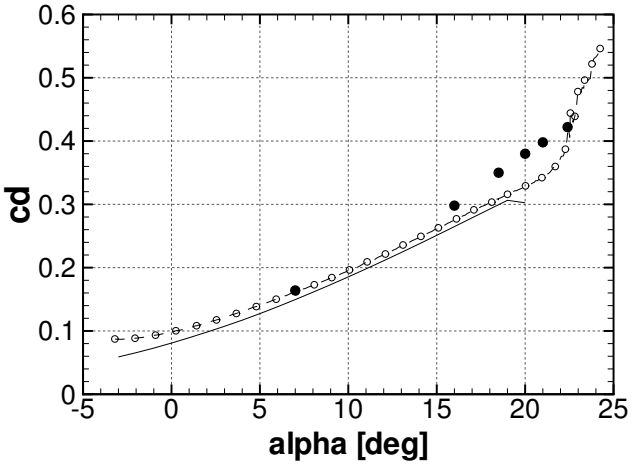

(b) $cd - \alpha$

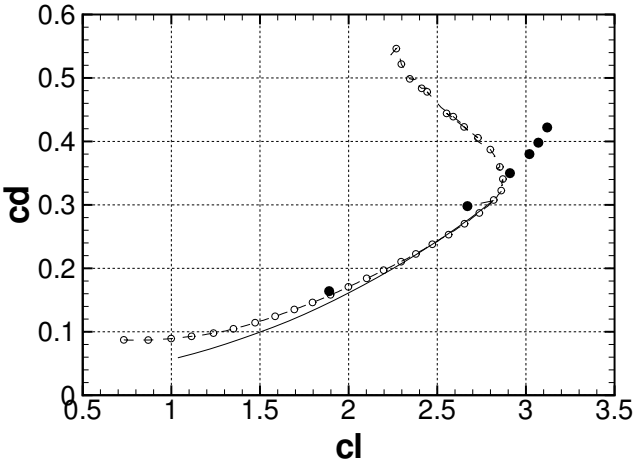

(c) $cd - cl$

Figure 6.14: Polars comparison for the KH3Y configuration. The quasi-three-dimensional method (solid line) is compared against wind tunnel data (line with dots) and RANS simulations (dots).

estimated.

6.4.2 Optimisation Set-Up and Results

The challenges of designing an efficient high-lift system have been already introduced in Chapter 2, where the conflicting requirements of the take-off and landing cases have been discussed in details. In particular, it is highlighted the importance of minimising the aircraft approach speed during the landing phase for both safety and performance reasons.

The optimisation set-up here proposed aims at improving the landing performance of the KH3Y, varying the deployment settings of both the slat and flap elements. For this purpose, a continuous spanwise slat is considered (constituting a single segment), while the flap element is split into an inboard and an outboard segment. As a result, a total of 9 design variables are identified, 3 per each high-lift segment, which control the high-lift system settings. In particular, the design variables represent incremental changes with respect to the datum deployment parameters, in terms of gap, overlap and deflection angle. Therefore, the range of variation for each design variable is defined between 80% and 120% of the datum configuration value.

The aim of minimising the approach speed directly translates into the maximisation of the lift coefficient at the stall angle of attack (recalling that $V_{appr} \propto V_{stall}$ and that $cl_{appr} = cl_{max}/1.54$, see). Thus, the first objective function used in this study is defined as $obj_1 = -cl_{max}$. The minus sign present in the formulation is needed to transform a minimisation problem, which is the default assumed by the optimisation algorithms used in the study, into a maximisation one. Concurrently to the increase in cl_{max}, it is also important to minimise the lift over drag ratio at the approach angle of attack, indicated as L/D_{appr}. This requirement guarantees the desired glide slope at the approach phase, and, thus, it is used to define the second objective function of the optimisation, i.e. $obj_2 = L/D_{appr}$. Indeed, this is in conflict

with the go-around requirements of a high L/D_{appr}, as introduced in Section 2.3.2. Table 6.6 summarises the settings for the KH3Y optimisation problem presented, where the subscript 0 indicates datum configuration values.

Table 6.6: KH3Y optimisation problem set-up.

Design Variable Definition		**Min Value**	**Max Value**
Slat	$(\text{gap}_s)/(\lvert\text{gap}_s\rvert_0)$	0.8	1.2
	$(\text{lap}_s)/(\lvert\text{lap}_s\rvert_0)$	0.8	1.2
	$(\Theta_s)/(\lvert\Theta_s\rvert_0)$	0.8	1.2
Flap Inb	$(\text{gap}_f)/(\lvert\text{gap}_f\rvert_0)$	0.8	1.2
	$(\text{lap}_f)/(\lvert\text{lap}_f\rvert_0)$	0.8	1.2
	$(\Theta_f)/(\lvert\Theta_f\rvert_0)$	0.8	1.2
Flap Out	$(\text{gap}_f)/(\lvert\text{gap}_f\rvert_0)$	0.8	1.2
	$(\text{lap}_f)/(\lvert\text{lap}_f\rvert_0)$	0.8	1.2
	$(\Theta_f)/(\lvert\Theta_f\rvert_0)$	0.8	1.2

Objective Function Definition	
obj1	$(\text{-cl}_{max})/(\lvert\text{cl}_{max}\rvert_0)$
obj2	$(\text{L/D}_{appr})/(\lvert\text{L/D}_{appr}\rvert_0)$

Also, it must be highlighted that the definition of the two objective functions here reported implies the evaluation of the entire aircraft polar. In fact, not only the maximum lift coefficient must be determined for each design, but also the approach angle at which the lift to drag ratio has to be evaluated will vary (recalling from 6.4.2 that $cl_{appr} = cl_{max}/1.54$). Hence, this design problem would represent a real computational challenge if full 3D RANS were to be used.

The first set of results here presented are obtained using the MOTS (Multi-Objective Tabu Search) algorithm introduced in Chapter 3, with the settings listed in Table 4.3. The initial step size is set equal to 0.05 for all the design variables indistinctly, since they express increments over the datum values. Moreover, a maximum number of 1000 objective functions evaluations is imposed as halting criteria.

At completion the optimisation algorithm has performed around 150 iterations, and an average of 7 objective functions evaluations per iteration is evaluated. Furthermore, 63 out of the 1014 designs evaluated are found geometrically infeasible,

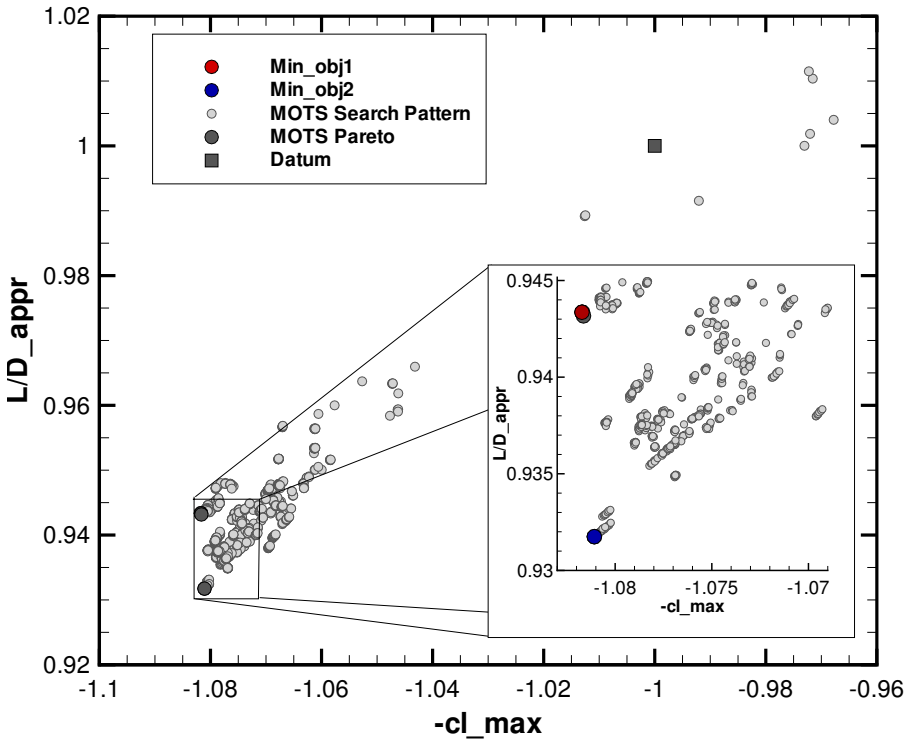

Figure 6.15: Search pattern and Pareto front revealed by MOTS after 150 iterations.

i.e. the specified deployment settings lead to intersecting elements, whereas 54 lead to failure in the quasi-three-dimensional simulation. The latter type of infeasibility carries a time penalty for the whole optimisation process, since it cannot be detected until the execution of the evaluation step. On the contrary, geometrically infeasible designs are rejected before the performance evaluation starts, and, hence, present only a reduced time penalty. In total, the infeasible solutions represent 12% of the explored designs.

In order to reduce the wall-clock time needed for each objective function evaluation, the sectional polars are evaluated in parallel. In particular, a 8 node high performance cluster is used, so that the 16 sections constituting the quasi-three-dimensional representation can be evaluated in 2 batches of 8 sections each. Consequently, the wall-clock time associated with each aircraft polar is reduced to 30 minutes, and the full optimisation run is completed in around 20 days.

The search pattern and the revealed Pareto Front are illustrated in Figure 6.15. In the plots presented, the objective functions are normalised by the datum value, so that the initial configuration is indicated by the values $obj_1 = -1$ and $obj_2 = 1$. It is evident from the figure that the design space is highly constrained in the high *cl* region. In fact, the identified pareto front is almost vertical, with all the pareto points featuring a substantial increase, of about 8%, in maximum lift capabilities compared to the datum design. Nonetheless, two extreme designs are identified, which differ mainly in the lift to drag ratio at approach conditions. The changes in design variables and the improvements in the objective functions for both the optima considered are summarised in Table 6.7. In particular, the L/D_{appr} is reduced to 93.2% of the datum value for the bottom right extreme of the pareto front, or *Min_ obj2* design. Instead, the top left extreme, or *Min_ obj1*, presents an $L/D_{appr} =$ 94.4%, once again compared to the datum value.

Table 6.7: KH3Y optimisation, design variables and objective functions improvement for the two optimum designs Min_obj1, and Min_obj2.

		Min_obj1	**Min_obj2**
	Δobj1	-8.172%	-8.108%
	Δobj2	-5.664%	-6.825%
Slat	$(\text{gap}_s)/(\lvert\text{gap}_s\rvert_0)$	1.00	1.00
	$(\text{lap}_s)/(\lvert\text{lap}_s\rvert_0)$	1.00	1.00
	$(\Theta_s)/(\lvert\Theta_s\rvert_0)$	0.85	0.90
Flap Inb	$(\text{gap}_f)/(\lvert\text{gap}_f\rvert_0)$	0.90	1.10
	$(\text{lap}_f)/(\lvert\text{lap}_f\rvert_0)$	0.85	0.85
	$(\Theta_f)/(\lvert\Theta_f\rvert_0)$	1.00	1.05
Flap Out	$(\text{gap}_f)/(\lvert\text{gap}_f\rvert_0)$	1.20	1.20
	$(\text{lap}_f)/(\lvert\text{lap}_f\rvert_0)$	0.85	0.85
	$(\Theta_f)/(\lvert\Theta_f\rvert_0)$	0.85	0.85

The identified optimised geometries at the extremes of the pareto front are presented in Figure 6.16. Both the optima differ considerably from the datum configuration, especially in the settings of the outer flap element. In particular, both designs present an increase in the gap setting of the outboard flap that reaches the

higher boundary set for this variable, i.e. 1.2, whereas the overlap and deflection settings are reduced to 0.85 times the datum value. Conversely, the slat settings are only slightly modified, with the optima featuring a decreased slat deflection angle. However, despite presenting similar characteristics, the two pareto front extremes differ in the inboard flap settings. In fact, the lower L/D_{appr} design increases both the gap and deflection angle of the inboard flap, whereas the opposite is true for the higher L/D_{appr} design.

Figure 6.17 illustrates the $cl - \alpha$ and $L/D - \alpha$ polars for the datum and the optimum designs identified. The increased maximum lift is clearly visible from the plots, with the two optima achieving a close value of $cl_{max} \approx 3$. Finally, the L/D polars of the two optima closely resemble the datum one for moderate to high angle of attacks. This indicates that the optimisation is able to identify designs which present a better maximum lift performance without changing the wing efficiency. Therefore, the reduction in L/D_{appr} obtained during the optimisation is, mainly, linked to the increased maximum angle of attack, since the approach angle is a function of the maximum lift coefficient.

The history of the optimisation progress for the considered study is now analysed. As shown in Figure 6.18, the MOTS algorithm manages to find solutions that improve both objective functions at the early stages of the optimisation. Moreover, the local search is continued along the discovered optimal path, as illustrated by the evolution of the pareto front up to iteration 12. At this point the optimiser has identified the maximum lift constraint in the design space and tries to widen the pareto front exploring regions of lower L/D_{appr}. At iteration 64 several pareto points are revealed, though it becomes harder for the optimiser to further advance the pareto front. Finally, after iteration 127 MOTS identifies a new region in the design space that allows a further reduction of the approach lift to drag ratio without penalising the maximum lift capabilities. The final pareto front revealed contains four designs.

A more detailed analysis of the performance of the MOTS algorithm and the

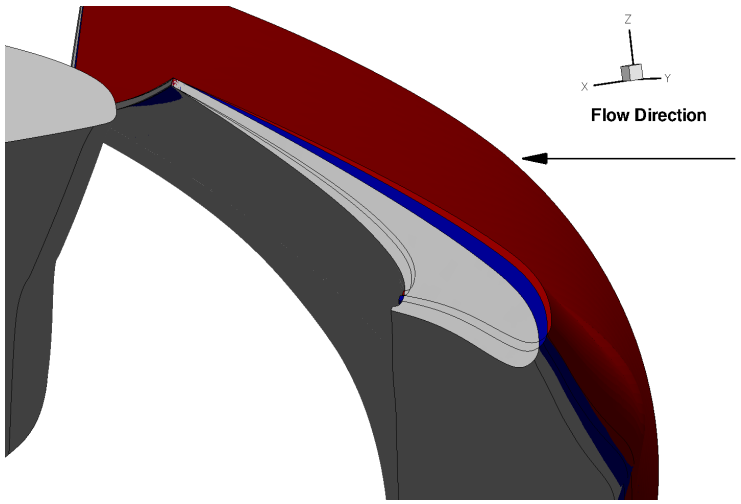

(a) Slat element

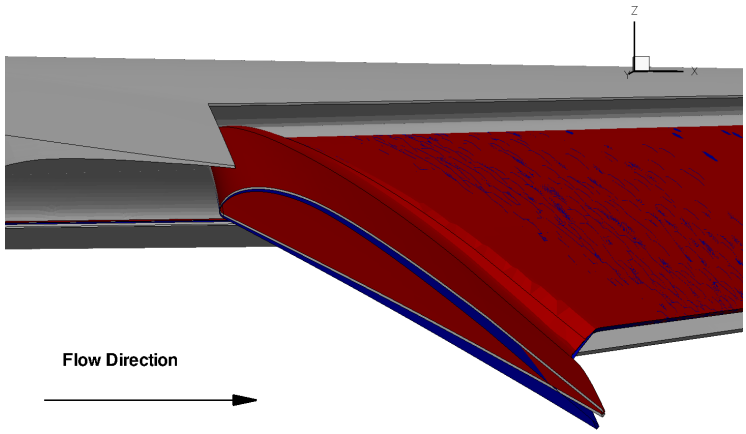

(b) Inboard Flap

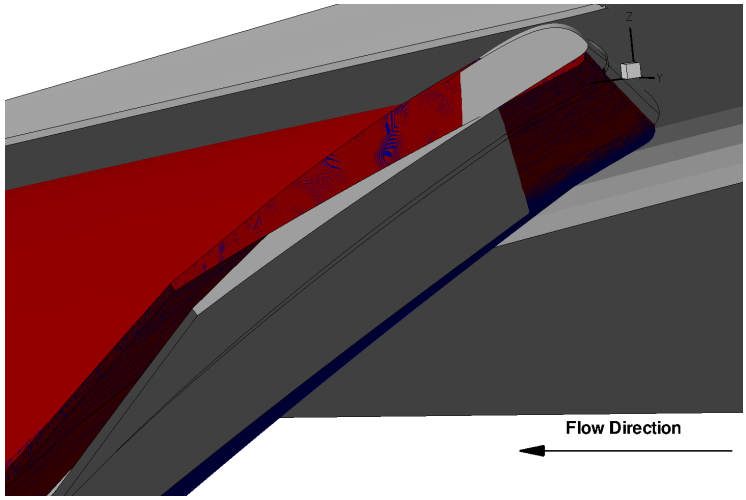

(c) Outboard Flap

Figure 6.16: Geometry comparison of the datum KH3Y (grey), the Min_obj1 design (red) and the Min_obj2 one (blue).

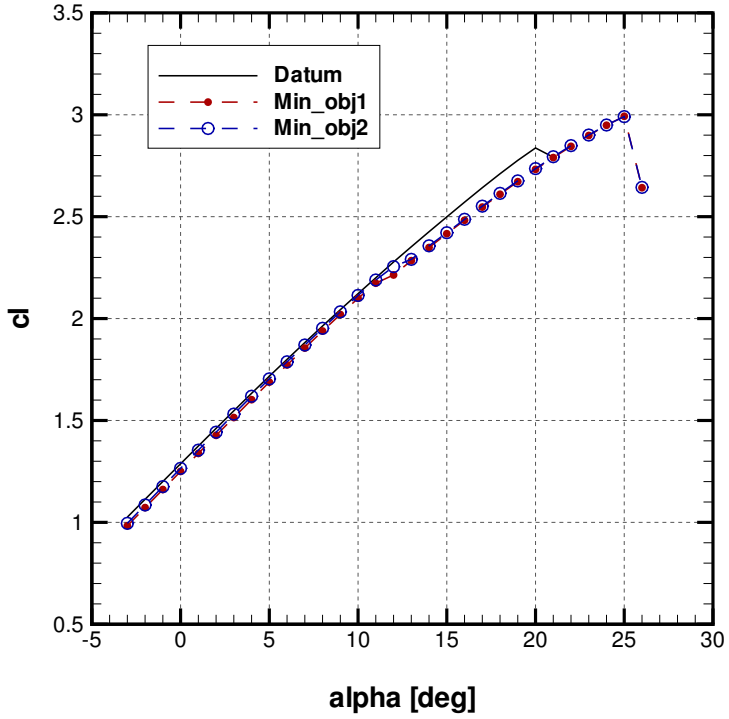

(a) $cl - \alpha$

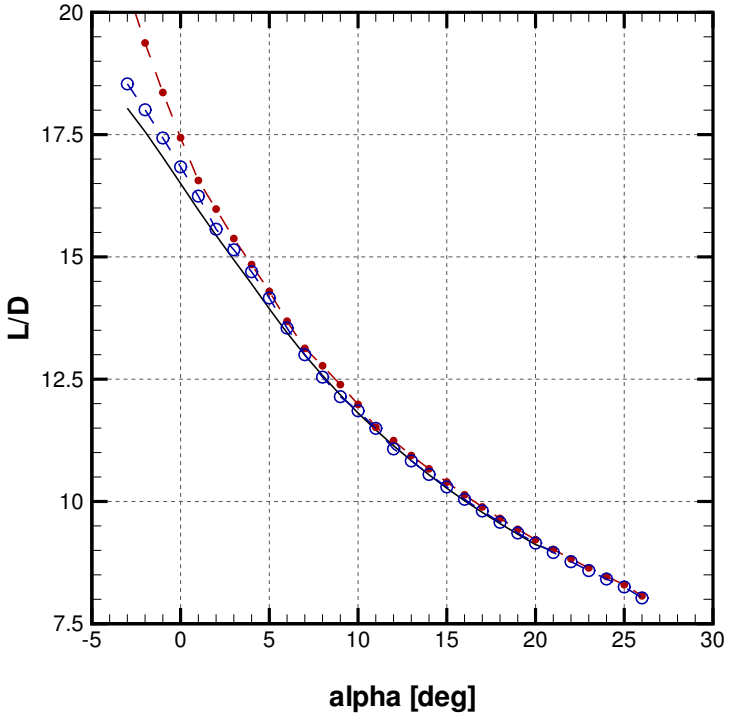

(b) $L/D - \alpha$

Figure 6.17: Polars comparison for the datum KH3Y configuration (solid line) and the identified optima Min_obj1 (red line with dots) and Min_obj2 (blue line with circles), rigid optimisation.

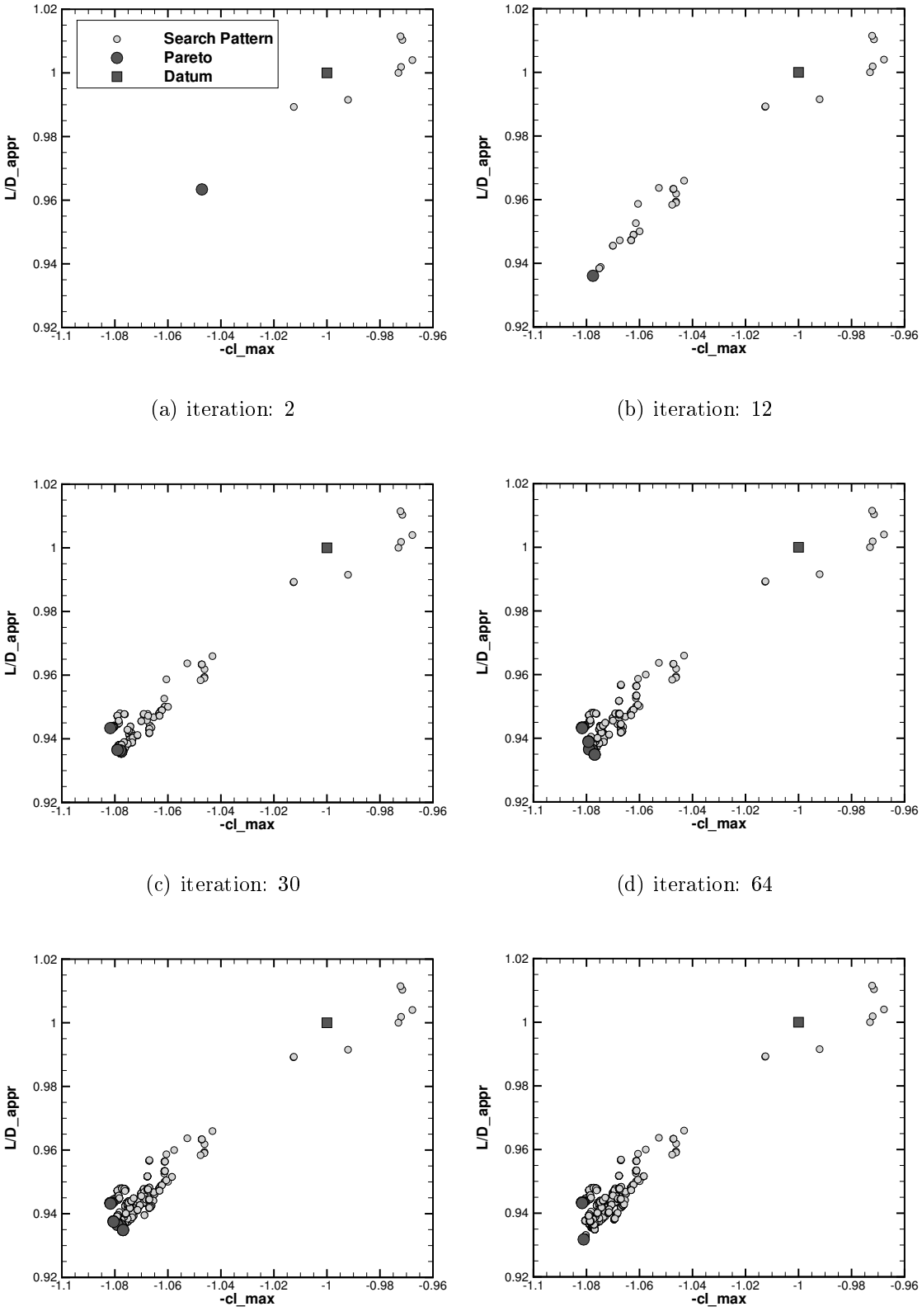

(a) iteration: 2

(b) iteration: 12

(c) iteration: 30

(d) iteration: 64

(e) iteration: 127

(f) iteration: 150

Figure 6.18: Evolution of the search pattern and pareto front during the MOTS optimisation.

strategies used to efficiently and exhaustively explore the design space is presented in Figure 6.19. The number of unsuccessful moves is plotted against the optimisation iteration, together with the defined threshold for the execution of the different strategies implemented in MOTS. Furthermore, the right y-axis shows the increase in the counter of each strategy, after it is executed. Firstly, the graph shows that up to iteration 40 the algorithm is able to identify optimum configurations using the standard local Hooke and Jeeves move. However, the increasing number of unsuccessful moves after that point has led the optimiser to exploit the diversification strategy at iteration 50. This is, however, unsuccessful and the algorithm resorts to an intensification strategy at iteration 55. Still, no pareto solution is found until a second series of intensification and diversification strategy takes place, and non-dominated solutions are found again at iteration 78 and 79. After that the optimisation shows another trend of unsuccessful moves which is interrupted after three series of intensification and diversification strategy and a step size reduction.

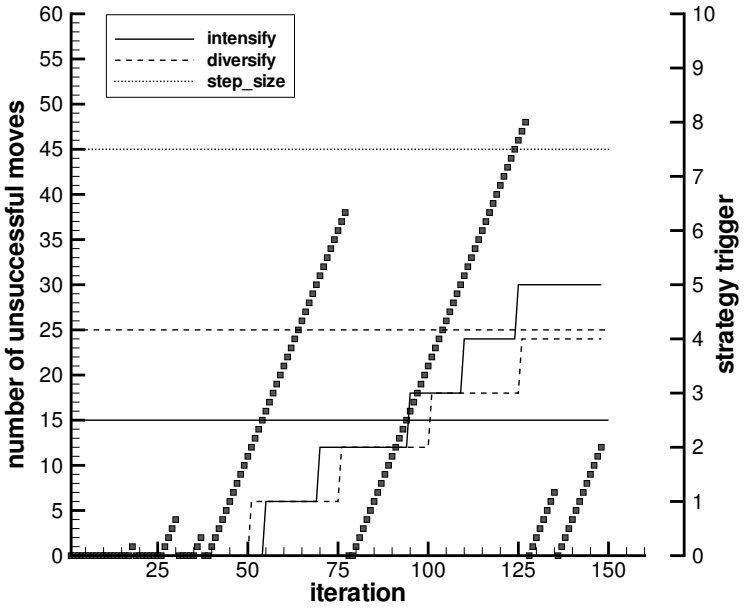

Figure 6.19: Analysis of MOTS strategies for exhaustive exploration of the design space.

The effect of the above described MOTS strategy on the evolution of the pareto front is shown in Figure 6.20. The plot illustrates the revealed pareto front at different stages of the optimisation process. In particular, the chosen iterations present the pareto just after one of the MOTS strategies has taken place. Let consider the pareto front at iteration 40 (red dots) as the starting point for this analysis. From the figure it is clear that the diversification strategy triggered at iteration 77 leads to the addition of a new optimum in the mid region of the pareto front (orange dots). After this step, no more pareto points are identified until the intensification action of iteration 127 and the correspondent extension of the pareto front in the low L/D_{appr} region (green dots). Lastly, the final pareto front (grey dots) is revealed through a standard Hooke and Jeeves move, which involves the increment of the slat deflection angle. This behaviour suggests that too big an initial step size for this design variable has, probably, been specified.

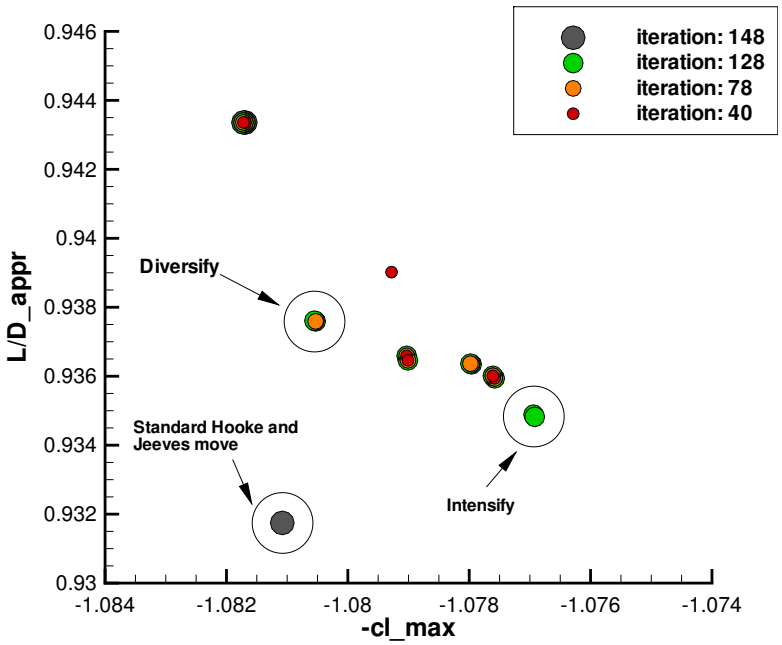

Figure 6.20: Evolution of the MOTS pareto front and impact of the different MOTS strategies.

As it was the case in the two-dimensional single-point optimisation presented

in Chapter 4, the KH3Y optimisation problem is also tackled using the NSGA-II algorithm. Consequently, it is possible to compare the outcomes of the two optimisations, and perform an assessment of the performance of the algorithms on a real-world design case.

For this specific test case, the NSGA-II settings are summarised in Table 4.5, with the only difference that a initial population of 36 individuals is specified instead of the 48 reported in the table. Moreover, the population is evolved for 10 generations or until the convergence criteria (increment in the objective functions values of the newly revealed optima) is met for 3 consecutive generations.

The search pattern and pareto front revealed by the NSGA-II algorithm at completion (after 10 generations) is compared to the MOTS results previously described in Figure 6.21. In order to have a meaningful comparison, the data are extracted from the two optimisation processes after a similar number of evaluations are performed, meaning iteration 30 for the MOTS optimisation. Of the 360 analysed designs during the NSGA-II driven optimisation, 20 present infeasible deployment settings, whereas 13 lead to a failure in the quasi-three-dimensional evaluation. If compared to the MOTS statistics, i.e. 12 geometric infeasibility and 10 simulation failures over 350 designs, the NSGA-II infeasible configurations represent an higher percentage of the explored designs.

The Pareto Front identified by the NSGA-II algorithm is visibly less progressed than the one revealed by MOTS. Moreover, the intrinsic stochastic characteristic of evolutionary approaches leads the NSGA-II algorithm to explore areas of the design space which are not particularly promising. This is clearly shown in Figure 6.21(b), where a high number of analysed designs actually reduce the datum performance levels. The local search of MOTS, instead, allows a faster identification of the region of the design space that results in objective functions improvements. This result is somehow expected for this specific application, since a clear optimum path is present in the design space. Therefore, the local search characteristic of MOTS takes full

advantage od this feature, while the stocastic approach of NSGA-II does not. That is why this result cannot be generalised for cases that show a more complex or multimodal design spaces.

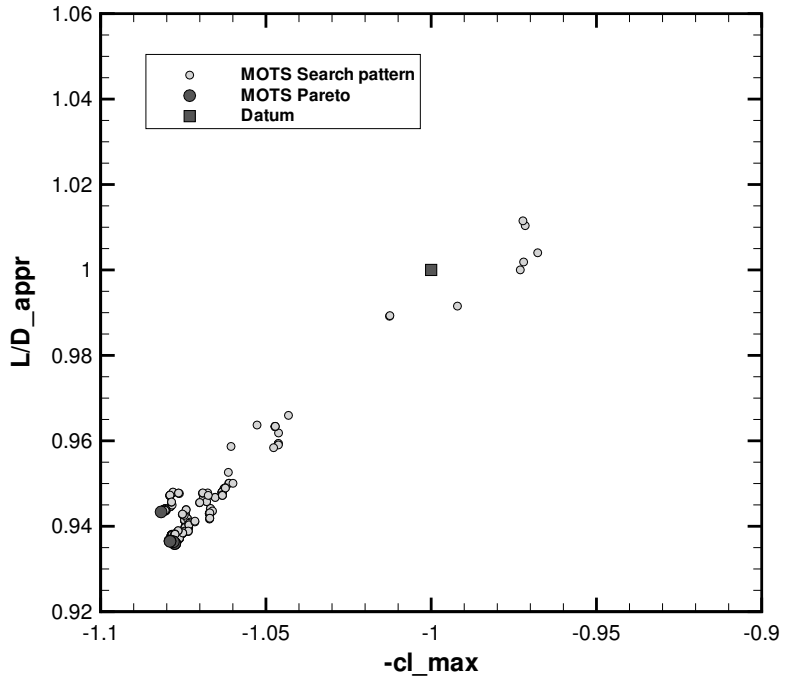

(a) MOTS

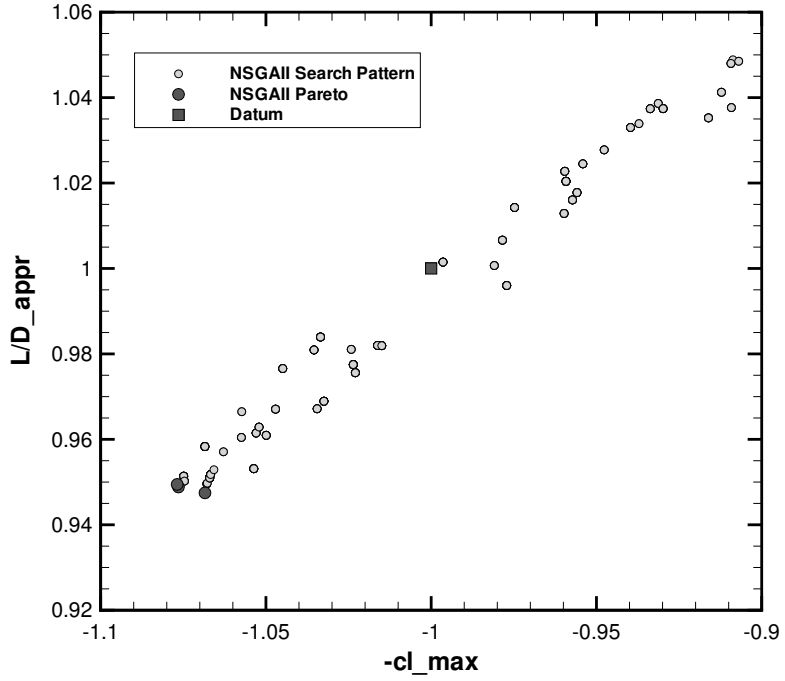

(b) NSGA-II

Figure 6.21: Comparison of the search pattern and pareto front revealed by MOTS and NSGA-II on the same optimisation problem of the KH3Y test case.

Chapter 7

High Lift Rapid Aero-Structural Coupling

7.1 Introduction

It is widely recognised that multidisciplinary simulations have nowadays become key enablers for the development of future, more efficient aircraft concepts [135]. In this context, aero-structural design and optimisations are an attractive area of research, due to the possible performance gains that can be achieved by considering flexible effects early in the design. However, despite the increase in the usage of coupled methods within the industrial design environments, the application of such tools remains focused to specific aeroelastic studies and, usually, it is considered at a later stage of the development. For example, the effects of wing deformations on the performance of the high-lift system are rarely considered during the preliminary design phase.

Indeed, the analysis of flexible high-lift configurations represents an even more challenging problem than the clean wing case (slat and flap retracted), due to the increased complexity of both geometry and flowfield. Still, it is important to estimate the aero-elastic effects due to the impact that they have on the aerodynamic perfor-

mance of the wing at low speed. In particular, the aero-elastic wing twist (due to the aerodynamic loads) can induce significant variations in the spanwise distribution of the local angle of attack. This effect can be particular relevant for swept-back wing, where a bending-induced twist is generated in addition to the torsional deformation of the wing. Tinoco et al. [136] present an example of such effects on a Boeing 737 aircraft. In their work, the authors use a panel method to quantify the effects of aero-elastic twist distribution, comparing the obtained results with flight test data. The outcome of the study illustrates the importance of accurately representing the geometry definition in order to match the flight-measured data.

In addition to the primary effects discussed earlier, the deformation undergone by the wing in high-lift configuration causes also a modification of the gaps between the different elements. This leads to further changes in the aerodynamic performance, although those effects might be of secondary importance. Van der Burg et al. [137] present an assessment of the effects of wing deformation on a high-lift wind tunnel model in take-off settings. Several coupling strategies have been used in combination with different level of fidelity structural models. The outcome showed a reduction of the lift generated by the flexible wing compared with the rigid one, due to the resultant nose down delta twist distribution. These effects, although small at wind tunnel Reynolds number, can be substantial at flight conditions. Consequently, a rapid coupling procedure has been included in the high-lift optimisation framework presented in Chapter 6. The method considers the static interaction between aerodynamic and elastic forces, providing an estimate of the *"flexible"* aerodynamic performance of the wing.

The description of the method is presented in the next sections, following a brief background literature review. The fundamental challenges of performing static aero-elastic simulation using high-fidelity simulations are highlighted. Then, a validation study is conducted prior to the use of the rapid approach for the optimisation of the KH3Y test case.

7.2 Background Literature

7.2.1 Aero-Structural Coupling

The aeroelastic analysis of an aircraft requires the usually separated aerodynamic and structural analysis to be coupled in an efficient and accurate way. In the literature, two approaches may be found which tackle the aeroelastic problem in different ways. These are the *"monolithic"* and the *"partitioned"* approaches. The first one, also referred to as closely coupled, consists in a simultaneous solution of both the aerodynamic and structural equations, allowing communication between the two models at each solution time-step. In the partitioned approach, instead, each discipline is solved using a specific method and a staggered procedure is adopted for the exchange of the boundary conditions. In particular, surface loads and surface deformations are transferred between the structural and the aerodynamic models.

On the one hand, the monolithic approach presents the advantage of obtaining the results with a single solution, as well as allowing exact time synchronisation. On the other, it requires extensive code modification [138], which limits its use to non-commercial packages (source code not available). Therefore, it is not possible to exploit commercially available tools, which are well established for the specific discipline simulation. An example of the development of a monolithic solution is presented by Cizmas et al. [139], where a nonlinear structural model and a nonlinear unsteady aerodynamic model are used in conjunction. Moreover, the successful application of the developed method to two wing test cases is also presented. However, due to the previously mentioned limitations, the use of such approach is gradually declining in favour of the loosely coupled one.

The partitioned approach allows the use of existing aerodynamic and structural codes within the analysis. Also, little or no modification of the code is needed, at the cost of developing an interaction procedure and performing a few iterations between the models to get a converged solution. Thus, the focus of the aero-structural

coupling is shifted to the definition of an accurate and efficient method for the transfer of the interface information. In fact, generally different grids are used for the structural and the aerodynamic analysis, since different resolution requirements and numerics are needed by the two disciplines. Specifically, while the structural analysis is based on finite elements using Lagrangian description, finite volume formulation in Eulerian coordinates is usually used for the aerodynamic analysis. As a result, the grids do not generally coincide at the fluid-structure interface. To overcome the described grid incompatibility issue, several strategies have been developed, see [140, 141, 135, 142]. However, the focus in this work is based on the Radial Basis Functions (RBF) interpolation method presented by Rendall and Allen [143, 144], which represents an elegant and efficient strategy for the solution of the Fluid-Structure Interface (FSI) problem.

7.2.2 Radial Basis Functions

Radial Basis Functions have been extensively used as approximation methods thanks to their ability to construct a global interpolation model from an initial set of scattered data. In addition, the behaviour of the interpolation function in between points can be controlled by selecting different type of bases (the most commonly used are reported in Table 7.1). Indeed, those peculiar characteristics make RBF an efficient approach to the FSI problem introduced in the previous section.

Node information only is required for the interpolation process, so that any arbitrary set of point clouds can be used [135]. These include single and multi-block structured grids , as well as unstructured ones. In fact, no connectivity requirements are needed by the method, simplifying considerably the interpolation operation. Moreover, the same technique can be applied to the aerodynamic volume mesh motion, which can be directly linked to the structural displacement or, alternatively, to the aerodynamic surface mesh motion [143, 145]. Finally, the approach is also computational efficient, since only simple matrix multiplications have to be performed,

and once the interpolation matrix is evaluated at the start of the simulation, it is unchanged throughout the duration of the computation.

Table 7.1: List of commonly used basis functions.

Name	Definition
Gaussian	$\Phi(\|x\|) = e^{-\|x\|^2}$
Thin plate spline	$\Phi(\|x\|) = \|x\|^2 \ln\|x\|$
Hardy's multiquadric	$\Phi(\|x\|) = (c^2 + \|x\|^2)^{1/2}$
Hardy's inverse multiquadric	$\Phi(\|x\|) = 1/(c^2 + \|x\|^2)^{1/2}$
Wendland's C0	$\Phi(\|x\|) = (1 - \|x\|)^2$
Wendland's C2	$\Phi(\|x\|) = (1 - \|x\|)^4(4\|x\| + 1)$
Wendland's C4	$\Phi(\|x\|) = (1 - \|x\|^6)(35\|x\|^2 + 18\|x\| + 3)$
Wendland's C6	$\Phi(\|x\|) = (1 - \|x\|^8)(32\|x\|^3 + 25\|x\|^2 + 8\|x\| + 1)$
Euclid's Hat	$\Phi(\|x\|) = \pi\left(\left(\frac{1}{12}\|x\|^3\right) - r^2\|x\| + \left(\frac{4}{3}r^3\right)\right)$

The first step in the solution of the RBF interpolation problem is the definition of the form of the required interpolation function. Indicating with Φ the adopted basis, with Ω_i a set of RBF coefficients, and with $\mathbf{x}_i$ the location of the R RBFs centres, it is possible to express the interpolation function $s(\mathbf{x})$ as:

$$s(\mathbf{x}) = \sum_{i=1}^{R} \Omega_i \, \Phi\left(\|\mathbf{x} - \mathbf{x}_i\|\right) + p(\mathbf{x}) \tag{7.1}$$

The polynomial term $p(\mathbf{x})$ is added to the standard RBF formulation in order to impose the recovery of the fluid-structure interface in case of a rigid translation or rotation motion. In particular, the requirement for the recovery implies the specification of up to linear polynomials, as presented by Beckert and Wendland [146]. Thus, $p(\mathbf{x})$ is defined as:

$$\begin{aligned} p(\mathbf{x})^x &= \gamma_0^x + \gamma_x^x x + \gamma_y^x y + \gamma_z^x z \\ p(\mathbf{x})^y &= \gamma_0^y + \gamma_x^y x + \gamma_y^y y + \gamma_z^y z \\ p(\mathbf{x})^z &= \gamma_0^z + \gamma_x^z x + \gamma_y^z y + \gamma_z^z z \end{aligned} \tag{7.2}$$

The interpolation problem is now reduced to the determination of the coefficients Ω_i in Equation (7.1). This is done imposing the exact recovery of the original

function, i.e. the positions of the structural nodes in the case of FSI problem. Moreover, when the polynomial term is also included, an additional requirement must be satisfied:

$$\sum_{i=1}^{N} \Omega_i \, q(\mathbf{x}) = 0 \tag{7.3}$$

applied to all polynomials $q(\mathbf{x})$ with degree less than or equal to that of $p(\mathbf{x})$.

Let's now define the coupling matrix, $\mathbf{H}$, that links the aerodynamic nodes displacements to the structural ones. Moreover, let's indicate with the subscript s the properties related to the structure nodes, whereas a indicates the aerodynamic ones. The positions of the aerodynamic surface nodes, here indicated by the vectors $\mathbf{x}_a$, $\mathbf{y}_a$ ans $\mathbf{z}_a$, can be expressed as a function of the extended structural position vectors $\mathbf{X}_s$, $\mathbf{Y}_s$, and $\mathbf{Z}_s$, by Equation (7.4).

$$\begin{aligned} \mathbf{x}_a &= \mathbf{A}_{as}\, \mathbf{a}_x = \mathbf{A}_{as}\mathbf{C}_{ss}^{-1}\mathbf{X}_s = \mathbf{H}\mathbf{X}_s \\ \mathbf{y}_a &= \mathbf{A}_{as}\, \mathbf{a}_y = \mathbf{A}_{as}\mathbf{C}_{ss}^{-1}\mathbf{Y}_s = \mathbf{H}\mathbf{Y}_s \\ \mathbf{z}_a &= \mathbf{A}_{as}\, \mathbf{a}_z = \mathbf{A}_{as}\mathbf{C}_{ss}^{-1}\mathbf{Z}_s = \mathbf{H}\mathbf{Z}_s \end{aligned} \tag{7.4}$$

where the matrices $\mathbf{A}_{as}$ and $\mathbf{C}_{ss}$ are defined as

$$\mathbf{A}_{as} = \begin{pmatrix} 1 & x_{a_1} & y_{a_1} & z_{a_1} & \Phi_{a_1 s_1} & \Phi_{a_1 s_2} & \cdots & \Phi_{a_1 s_N} \\ \vdots & \vdots & \vdots & \vdots & \vdots & \vdots & \ddots & \vdots \\ 1 & x_{a_N} & y_{a_N} & z_{a_N} & \Phi_{a_N s_1} & \Phi_{a_N s_2} & \cdots & \Phi_{a_N s_N} \end{pmatrix} \tag{7.5}$$

$$\mathbf{C}_{ss} = \begin{pmatrix} 0 & 0 & 0 & 0 & 1 & 1 & \cdots & 1 \\ 0 & 0 & 0 & 0 & x_{s_1} & x_{s_2} & \cdots & x_{s_N} \\ 0 & 0 & 0 & 0 & y_{s_1} & y_{s_2} & \cdots & y_{s_N} \\ 0 & 0 & 0 & 0 & z_{s_1} & z_{s_2} & \cdots & z_{s_N} \\ 1 & x_{s_1} & y_{s_1} & z_{s_1} & \Phi_{s_1 s_1} & \Phi_{s_1 s_2} & \cdots & \Phi_{s_1 s_N} \\ \vdots & \vdots & \vdots & \vdots & \vdots & \vdots & \ddots & \vdots \\ 1 & x_{s_N} & y_{s_N} & z_{s_N} & \Phi_{s_N s_1} & \Phi_{s_N s_2} & \cdots & \Phi_{s_N s_N} \end{pmatrix} \tag{7.6}$$

The term $\Phi_{s_1 s_2} = \Phi(\|(x)_{s_1} - (x)_{s_2}\|)$ indicates the basis function evaluated on the distance between points s_1 and s_2. Furthermore, the vectors $\mathbf{X}_s$ and $\mathbf{a}_x$ (analogous definitions hold for $\mathbf{Y}_s$, $\mathbf{a}_y$, $\mathbf{Z}_s$ and $\mathbf{a}_z$) are defined as

$$\mathbf{X}_s = \begin{pmatrix} 0 \\ 0 \\ 0 \\ 0 \\ \mathbf{x}_s \end{pmatrix}, \quad \mathbf{x}_s = \begin{pmatrix} x_{s_1} \\ \vdots \\ x_{s_N} \end{pmatrix}, \quad \mathbf{a}_x = \begin{pmatrix} \gamma_0^x \\ \gamma_x^x \\ \gamma_y^x \\ \gamma_z^x \\ \Omega_{s_1}^x \\ \vdots \\ \Omega_{s_N}^x \end{pmatrix} \tag{7.7}$$

Therefore, the aerodynamic nodes deformations are obtained simply solving the linear system expressed in Equation (7.4).

Computationally, the time required to build the interpolation matrix is proportional to N_s^3, with N_s number of structural nodes (source nodes). The time required to perform the matrix multiplication, instead, varies with $N_s \times N_a$, where N_a represent the number of nodes on the aerodynamic surface mesh.

Finally, the inverse problem of force transfer from the aerodynamic mesh to the structural one is solved evaluating the relative interpolation matrix. For this purpose the energy conservation requirement is used. In particular, considering that

the aerodynamic nodes displacements and the structural ones are related through the coupling matrix $\mathbf{H}$, i.e. $\mathbf{u}_a = \mathbf{H}\,\mathbf{u}_s$, the use of the principle of virtual work leads to

$$\delta W = \delta \mathbf{u}_s^T \cdot \mathbf{f}_s = \delta \mathbf{u}_a^T \cdot \mathbf{f}_a \quad \rightarrow \quad \mathbf{f}_s = \mathbf{H}^T \mathbf{f}_a \tag{7.8}$$

which states that the transpose of the displacement coupling matrix (earlier derived) must be used to transfer forces, if the system energy is to be conserved.

The RBF method, therefore, provides an efficient and compact way of transferring forces and displacements between the aerodynamic and structural simulations. For this reason, it has been chosen for the high-fidelity aero-structural simulation later presented in Sections 7.4.2 and 7.4.3.

In this work Wedland's functions are preferred to other commonly used RBF functions (see Table 7.1) due to their characteristic decay which leads to a more local and physically meaningful displacement and force transfer. In particular, Wedland's C2 functions are adopted (including the linear terms for structure to aerodynamic surface mesh transfer) since they present a better trade-off accuracy/computational cost compared to higher order Wedland's functions, and have been found, in existing literature, to produce good quality results [143, 144].

7.3 Methodology

The static aero-elastic analysis of high-lift configurations is here performed using a simplified, rapid approach. The motivation behind the selection of a lower-fidelity methodology over more detailed ones is twofold: firstly, the usage of the developed method is mainly intended for the preliminary design phase (when fewer details and faster run-times are required); secondly, the method must be rapid and robust to be implemented into a numerical optimisation process. The latter, in particular, is considered to be of crucial importance, since structure flexibility effects are

becoming increasingly important when evaluating the aerodynamic performance of wings in high-lift configurations. Consequently, a modified version of the rapid aero-structural coupling method presented by Agostinelli et al. [147] is used, in conjunction with the quasi-three-dimensional simulation (introduced in Chapter 6) and a condensed structural model (later described).

The presented methodology allows a rapid evaluation of the statically deformed shape of the wing, and its relative aerodynamic performance. The main assumption of the approach is that the distribution of *"twist"*, i.e. the rotation along the axis perpendicular to the aircraft symmetry plane, is mainly responsible for the change in the aerodynamic loads due to structural deformations. Therefore, all the other contributions are neglected.

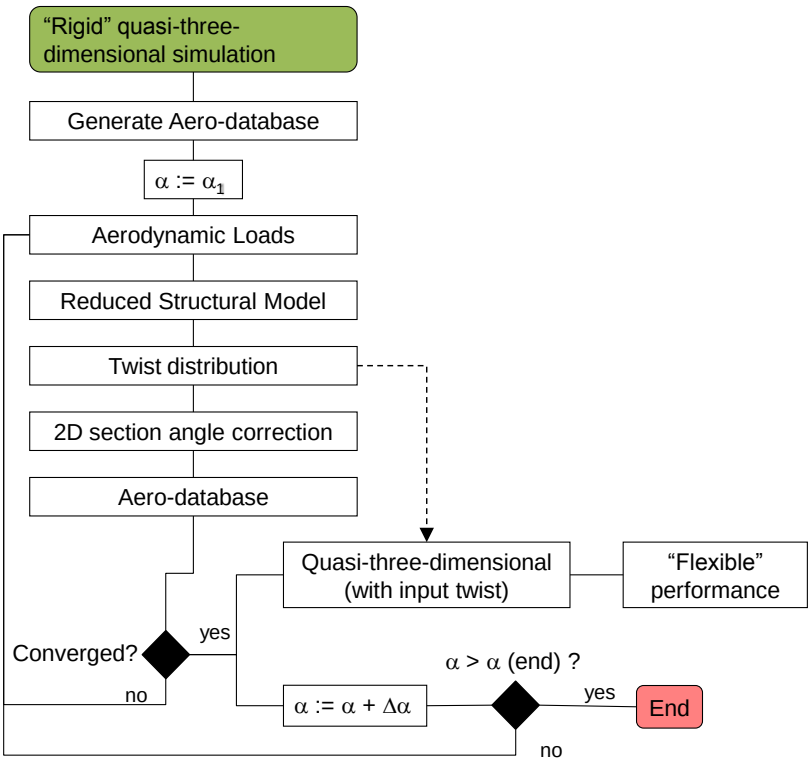

Figure 7.1: Workflow describing the aero-structural coupling loop.

The workflow in Figure 7.1 illustrates the steps needed to perform the rapid coupling procedure. Firstly, a database is generated which contains the aerodynamic loads, evaluated on the rigid configuration, at different angles of attack. The next

step is to consider a specific angle of attack and, using the loads from the database, evaluate the spanwise twist distribution at defined reference locations. Subsequently, this information is used to correct the local angle of attack along the wing span. The applied correction changes the generated aerodynamic loads, and so an updated twist distribution must be calculated. Clearly, an iterative scheme must be used to converge the deformations and the loads that produce them. Finally, once the coupling procedure has converged, the next angle of attack of the 3D polar is selected, and the coupling process is repeated until the entire flexible polar has been evaluated.

However, an underlying assumption is made when performing the local angle of attack correction previously described. In fact, it is assumed that the wing sections are rigid and parallel to the symmetry plane. Hence, changes in the section's geometry are not captured by the method. Moreover, when multi-element airfoils are analysed, like in the case of high-lift configurations, the deployment settings of the elements are also assumed to be fixed. This latter approximation is necessary to guarantee that the 2D polars at the specific spanwise location remain unchanged during the aero-structural coupling process.

A more detailed description of the individual modules that constitute the rapid coupling process is provided in the following sections.

7.3.1 Aerodynamic Model

The quasi-three-dimensional approach described in Chapter 6 is here used to evaluate the aerodynamic loads for the rapid aero-structure coupling. In particular, for every angle of attack included in the 3D polar of the *"rigid"* configuration, the spanwise distributions of the aerodynamic coefficients (cl, cd and cm) is evaluated. These distributions are, later, transformed into forces and moments, and collated into what is here defined the *"forces database"*. It is this database that will be used in the actual coupling process, avoiding the iterative execution of the quasi-three-dimensional simulation at each coupling step. Once the coupling loop has converged

for the considered alpha, the global cl, cd, and cm values of the deformed shape are evaluated more accurately thorough the execution of a quasi-three-dimensional simulation which includes the converged twist distribution.

7.3.2 Reduced Structural Model

The structural model used in the rapid coupling procedure consists of a reduced model [148] obtained from the complete 3D Computational Structure Mechanics (CSM) of the wing. The choice of using a reduced model instead of a full 3D Finite Element Method (FEM) is compatible to the design stage at which the method will be used, i.e. the conceptual or preliminary design phase. In fact, at this stage a detailed structural representation is unlikely to exist. Moreover, the condensed stiffness matrix approach here used presents satisfactory level of accuracy for the proposed analysis (as shown in the validation study later presented), concurrently keeping the computational cost and workflow complexity at a minimum. Therefore, a structural reduction analysis is performed to obtain a compact model for the evaluation of the wing deformations.

The first step in the reduction process is to recognise that, for fairly slender high aspect ratio wings, the structure behaves mainly as an ensemble of beam elements. Consequently, each aircraft component can be represented as a beam lying on along the locus of the shear centres. Furthermore, each beam is divided in several sections or elements, so that a closer representation of the variation of the stiffness properties is possible. Finally, the model is condensed to reduce the number of degrees of freedom, from the original order N to a much smaller set M. The so obtained reduced model is, usually, termed a *"Beam Stick Model"* (BSM).

For the wing component, a set of reference nodes is chosen conveniently along the span and, then, the equivalent stiffness properties are extracted performing a series of static flexibility tests. This is achieved connecting each of the specified reference nodes to the neighbouring CSM mesh points through a multipoint connection

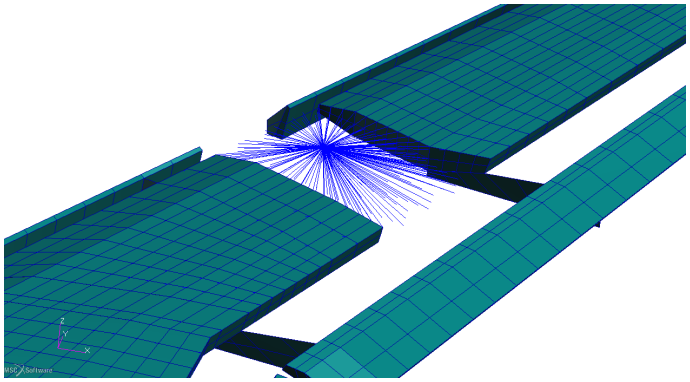

Figure 7.2: Cut-out in a structural mesh to illustrate an example of a multi-connection node in MSC®Patran.

node. Figure 7.2 illustrates an example of an high-lift structural model, where the elements have been hidden to show the multipoint connections. These particular nodes distribute the applied nodal forces to the CSM mesh and, concurrently, link the mesh displacements to those of the reference node. The flexibility matrix of the reduced structural model can now be obtained applying unit loads and moments on each of the reference nodes alternatively, and measuring the displacements of all of them.

The relationship which relates forces and displacements on the reference nodes is illustrated below:

$$\mathbf{u} = \mathbf{K}^{-1}\,\mathbf{Z} = \mathbf{S}\,\mathbf{Z} \tag{7.9}$$

where $\mathbf{S} = \mathbf{K}^{-1}$ represent the flexibility matrix of the reduced structural model and the vectors $\mathbf{u}$ and $\mathbf{Z}$ are expressed as

$$\mathbf{u} = (u_{1,x}\ ,\ u_{1,y}\ ,\ u_{1,z}\ ,\ r_{1,x}\ ,\ r_{1,y}\ ,\ r_{1,z}\ ,\ \ldots\ ,\ r_{M,z})^T \tag{7.10}$$

$$\mathbf{Z} = (F_{1,x}\ ,\ F_{1,y}\ ,\ F_{1,z}\ ,\ M_{1,x}\ ,\ M_{1,y}\ ,\ M_{1,z}\ ,\ \ldots\ ,\ M_{M,z})^T \tag{7.11}$$

Therefore, by applying an unit load on, for instance, the first node in the x

direction, so that $F_{1,x} = 1$, the displacement vector $\mathbf{u}$ measured on all the reference nodes represent the first column of the condensed flexibility matrix. Repeating this procedure for each unit load at each reference node the reduced flexibility matrix can be evaluated. It is, now, possible to evaluate the deformations on the reference nodes due to a generic load case using Equation (7.9).

In the specific case of the KH3Y configuration, 15 reference nodes have been identified along the span of the KH3Y wing. Those nodes have been connected to the corresponding neighbour mesh nodes of the main element only. Hence, the applied loads are transferred to the slat and flap elements through the brackets that connect the different elements. Moreover, clamped boundary conditions have been specified at the root section nodes of both main and flap element for all the structural analyses results here presented.

7.3.3 Aero-Structure Interface

As introduced earlier, the preliminary step of the rapid aero-structural coupling consists in the generation of a database containing the aerodynamic forces acting on the wing. For this purpose, the results of the aerodynamic (quasi-three-dimensional) simulation are interpolated onto the reduced structural model reference nodes. Then, the aerodynamic coefficients are converted into forces and moments using the dynamic pressure q_∞, and the geometrical planform information (see Figure 7.3):

$$\begin{aligned} &\mathrm{F}_x = \tfrac{1}{2}\rho \mathrm{V}^2 \mathrm{S}\, c_x \; ; \qquad \mathrm{F}_y = \tfrac{1}{2}\rho \mathrm{V}^2 \mathrm{S}\, c_y \; ; \qquad \mathrm{F}_z = \tfrac{1}{2}\rho \mathrm{V}^2 \mathrm{S}\, c_z \\ &\mathrm{M}_x = \tfrac{1}{2}\rho \mathrm{V}^2 \mathrm{S}\, cm_x \; ; \quad \mathrm{M}_y = \tfrac{1}{2}\rho \mathrm{V}^2 \mathrm{S}\, cm_y \; ; \quad \mathrm{M}_z = \tfrac{1}{2}\rho \mathrm{V}^2 \mathrm{S}\, cm_z \end{aligned} \tag{7.12}$$

The generated database contains spanwise forces and moments distribution computed for various incidence of the 3D polar, and arranged in the $6M$ dimension array of Equation (7.13). Recalling that M is the number of the reference nodes along

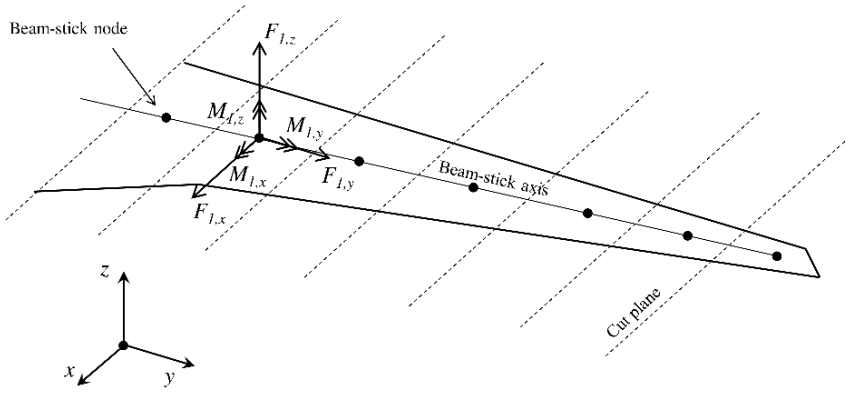

Figure 7.3: Evaluation of forces and moments on the reduced structural model reference nodes.

the span, and indicating with N the number of incidence used during the 3D polar evaluation, the aero-database can be described as in Table 7.2.

$$\mathbf{Z}_m = (\mathbf{F}_m,\ \mathbf{M}_m)^T \tag{7.13}$$

Table 7.2: Example structure of the Aerodynamic Forces database.

	Section 1	Section 2	$\cdots$	Section m	$\cdots$	Section M
α_1	$\mathsf{Z}_{1,1}$	$\mathsf{Z}_{1,2}$	$\cdots$	$\mathsf{Z}_{1,m}$	$\cdots$	$\mathsf{Z}_{1,M}$
α_2	$\mathsf{Z}_{2,1}$	$\mathsf{Z}_{2,2}$	$\cdots$	$\mathsf{Z}_{2,m}$	$\cdots$	$\mathsf{Z}_{2,M}$
$\vdots$	$\vdots$	$\vdots$	$\ddots$	$\cdots$	$\cdots$	$\cdots$
α_l	$\mathsf{Z}_{n,1}$	$\mathsf{Z}_{n,2}$	$\vdots$	$\mathsf{Z}_{n,m}$	$\cdots$	$\mathsf{Z}_{n,M}$
$\vdots$	$\vdots$	$\vdots$	$\vdots$	$\vdots$	$\ddots$	$\cdots$
α_N	$\mathsf{Z}_{N,1}$	$\mathsf{Z}_{N,2}$	$\vdots$	$\mathsf{Z}_{N,m}$	$\vdots$	$\mathsf{Z}_{N,M}$

The coupling loop can now be started. First of all, a flight incidence is considered from the 3D polar simulation, and the correspondent aerodynamic loads are extracted from the aero-database. Secondly, the reduced structural model obtained in the previous section is used to evaluate the displacements of the reference nodes. In particular, the displacement along the z-axis and the rotation along the y-axis

are considered. Last, a correction on the local incidence is made per each spanwise section as follow:

$$\alpha_m = \beta_m + \alpha_{flight} \tag{7.14}$$

where α_m is the absolute incidence for a given section, β_m is the geometric twist (or rotation along the y-axis) and α_{flight} is the flight incidence.

The incidence correction just introduced has a direct effect on the generated wing aerodynamic loads. Therefore, an iterative scheme is used to obtain the converged deformed shape and performance. Indicating with i the iteration number, the iterative process is expressed as:

$$\mathbf{u}^{i+1} = \mathbf{S}\ \mathbf{Z}^i \tag{7.15}$$

where

$$\mathbf{Z}^i = f(\mathbf{u}^{i-1} + \zeta(\mathbf{u}^i - \mathbf{u}^{i-1})) \tag{7.16}$$

with ζ damping coefficient chosen conveniently to guarantee convergence.

The final step of the rapid coupling procedure is the execution of a quasi-three-dimensional analysis on the evaluated flexible wing. For this purpose, the deformation field on the reference nodes is interpolated on the location of the quasi-three-dimensional sections, and the aerodynamic simulation executed. It must be emphasised that no changes in the deployment settings due to the structural deformation are here considered. Hence, the sectional aerodynamic characteristics are unchanged during the rapid coupling process. Consequently, only the inverse lifting surface evaluation of the whole quasi-three-dimensional process must be performed, which represent the least expensive part of the aerodynamic simulation. Finally, this process is executed for every angle of attack of the 3D polar.

The described coupling methodology has recently been successfully applied by Agostinelli et al. for the optimisation of wing twist distribution on a flexible wing in

cruise configuration [147], and for the performance prediction of a propeller powered aircraft including wing flexibility effects [149]. In both those studies, the force database is generated extracting the loads from RANS simulations.

7.4 Validation and Verification

The validation study for the aerodynamic simulations has already been presented in Chapter 6, where the quasi-three-dimensional results are compared to wind tunnel data for two different test cases. Thus, the following sections focus on the validation and verification of the rapid aero-structural coupling procedure. In particular, the deformations obtained with the proposed method are compared against the results of several higher-fidelity simulations, which include coupled RANS-BSM and coupled RANS-CSM analyses, and against wind tunnel measurements. However, firstly a validation of the CSM structural model used as reference for the reduction process is presented.

7.4.1 Computational Structure Mechanics

Two different CSM structural models are used in this work. The first one, created using the commercial software Ansys®APDL, was provided by DLR (see Figure 7.4(a)). Solid elements are used to model the slat, main and flap components, whereas the connection brackets are modelled using shell elements. The slat is attached to the main wing using 7 slat brackets, whereas the flap is mounted with 5 flap brackets. In addition, the inner flap edge is clamped at the fuselage junction. The validation of this specific CSM model has been previously performed during the EUROLIFT II project [137], and it is here re-presented. The second CSM model uses exclusively shell elements, and it has been generated in MSC®Patran (see Figure 7.4(b)).

For the validation of the structural model the available experimental data from

the EUROLIFT-II programme of a concentrated load at the wing tip are used as comparison. The plot in Figure 7.5 shows a good match of the Patran model compared to the experimental data, whereas the APDL model shows a stiffer response. The experimental data show a maximum tip deflection of 25mm, over a 1400mm span wing. This limited deflection ($\approx 2\%$) illustrates the stiff behaviour of the wing model, which has to withstand the high dynamic pressure and low cryogenic temperature of the ETW wind tunnel.

Although some differences are visible between the Ansys®APDL model and the experiment results, this is the CSM model selected for the reduction procedure presented in Section 7.3.2. The generated BSM is used throughout the rest of this work as structural solver for the rapid coupling procedure.

7.4.2 *"One-shot"* Coupling Approach

The validation study for the rapid coupling approach is here divided in two steps. Firstly, a simpler *"one-shot"* approach is used to compare the structural deformations obtained using several level of simulation fidelities. The one-shot approach does not include the iterative process of converging structural deformations and aerodynamic loads. In fact, a single linear static analysis is performed using the interpolated aerodynamic loads from the aero model to the relevant structural nodes.

The increasing level of fidelity simulations include: quasi-three-dimensional coupled BSM; RANS coupled BSM; and RANS coupled CSM. The first approach exploits the already described rapid coupling process, with the imposed condition of a single step in the iterative scheme. For the other approaches more details are given below.

The RANS solution which provides the input loads is obtained using the commercial CFD suite Ansys®CFX V15 on the medium grid available from the AIAA High Lift Prediction Workshop [32]. The k-ω SST turbulence model is used, in conjunction with an upwind first order scheme for the turbulence numerics and the

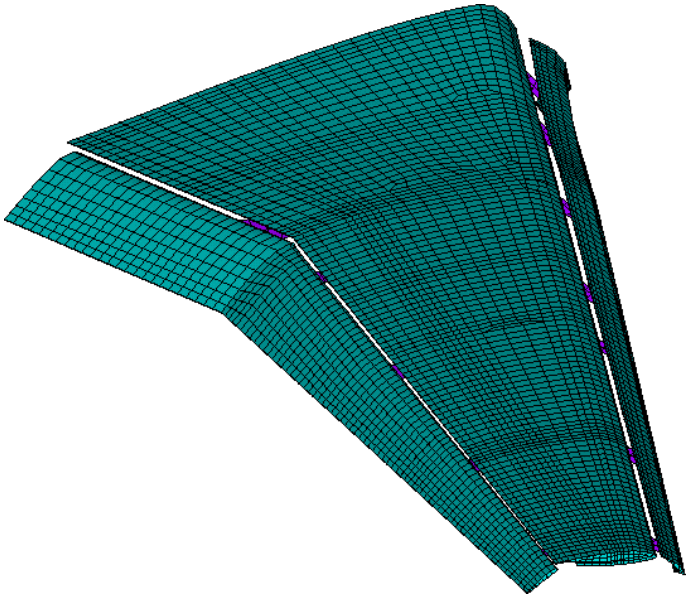

(a) Ansys®APDL solid elements model

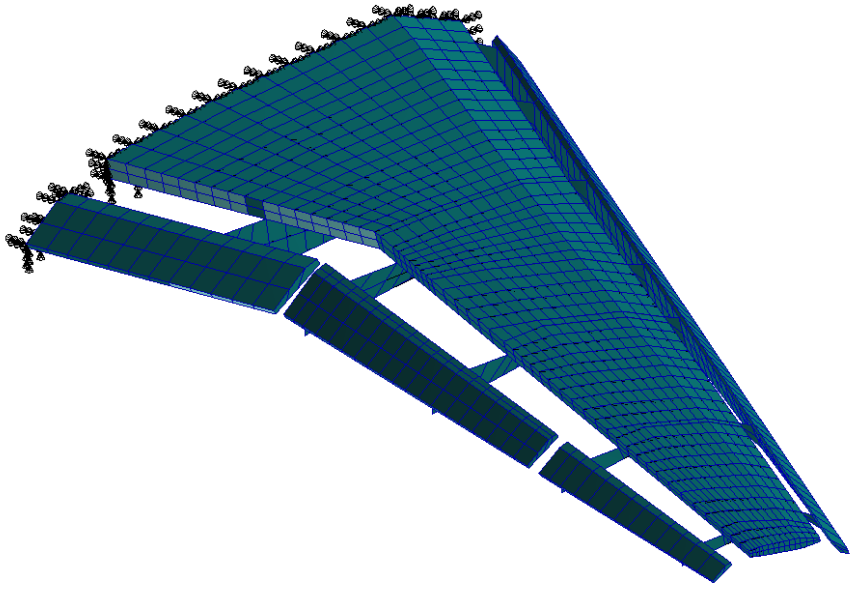

(b) MSC®Patran shell elements model

Figure 7.4: Computational Structural Models of the KH3Y test case in landing configuration generated with Ansys®APDL using solid elements (a), and with MSC®Patran using shell elements (b)

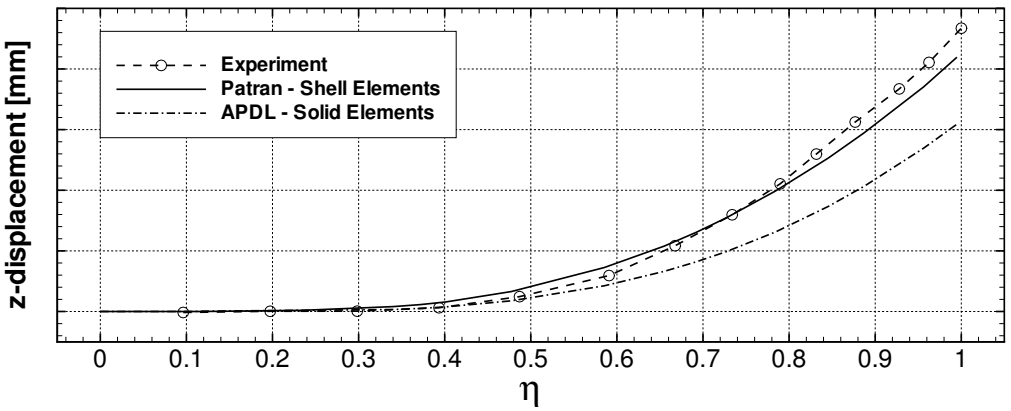

Figure 7.5: Displacement distribution along the $z-$axis for a concentrated load applied at the wing tip. Experimental data (line with dots) are compared with Ansys®APDL simulation (dot-dash line) and MSC®Nastran one (solid line).

"High Resolution" scheme for the remaining state variables. Figure 7.6 illustrates the solution obtained for the hereinafter reference angle of attack, $\alpha = 7°$, at the onset flow condition representative of the ETW experiment (summarised in Table 7.3). The figure shows pressure contours on the aircraft surfaces, together with the visualisation of the mesh on the symmetry plane. Moreover, streamlines are shown to highlight the partial flow separation occurring at the outboard flap, as well as the magnitude of the tip vortex shed.

Table 7.3: ETW wind tunnel flow conditions.

Mach number	Ma	0.2	[-]
Reynolds number	Re	20.0×10^6	[-]
Total pressure	p_{tot}	355.56×10^3	[Pa]
Total temperature	t_{tot}	114.7	[K]
Dynamic pressure	q_∞	9.7	[kPa]

In order to transfer the aerodynamic loads from the RANS solution to the BSM for the execution of the second coupling approach, a lumping process for the forces is performed. Firstly, the wing is divided into strips centred at the location of the BSM reference nodes. Then, for each strip, a numerical integral of the forces is evaluated, and the resultant and equivalent moment are evaluated on the BSM reference node within the considered strip. Subsequently, the displacements of the BSM reference

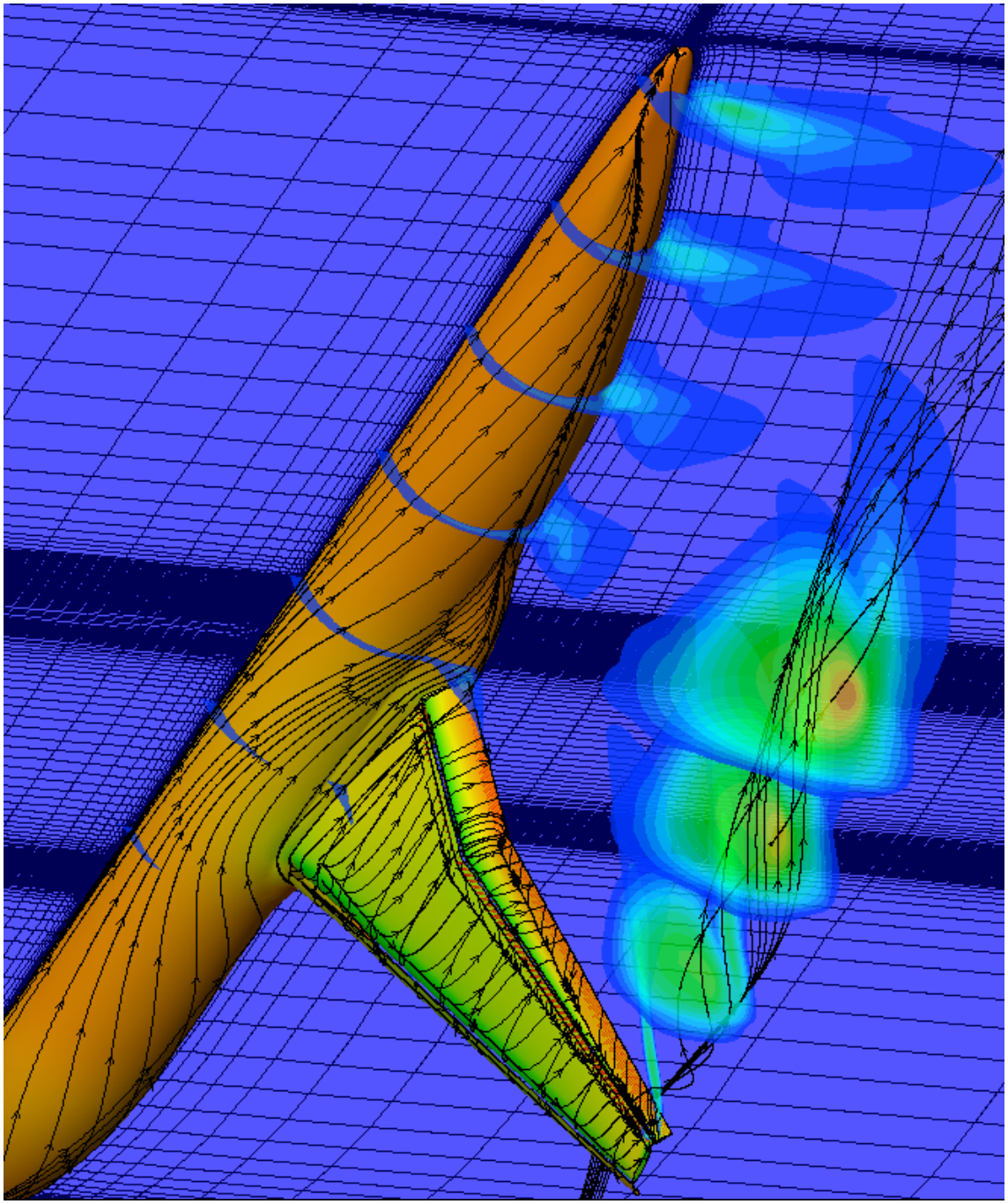

Figure 7.6: Ansys®CFX solution of the KH3Y test case in landing configuration for $\alpha = 7°$. Surface pressure contours are visualised, together with streamlines and turbulent kinetic energy contours on the slices perpendicular to the symmetry plane.

nodes is evaluated from Equation (7.9), with the lumped forces and moments as input loads.

Finally, in the last approach, the aerodynamic loads from the RANS solution are transferred to the Ansys®APDL full 3D structural model. For this purpose, the RBF interpolation strategy [143] described in Section 7.2.2 is used. The two sets of point clouds considered for the generation of the interpolation matrix are the aerodynamic surface mesh for slat, main and flap, and the external nodes of the structural mesh (excluding the supporting brackets). The aerodynamic loads and the transferred structural ones are illustrated in Figure 7.7(a) and 7.7(b) respectively, whereas the corresponding deformations, obtained after a static analysis of the CSM model, are presented in Figure 7.7(c). The figures show that a smooth distribution of forces is achieved throughout the wing span, with the aerodynamic loads well apportioned to the various wing elements (slat, main and flap). The forces present few concentrated spikes, which are a result of the fine structural mesh and the small distance between some of the structural nodes.

A summary of the three different approaches is presented in Table 7.4, while the obtained results are summarised in Figure 7.8. The plot illustrates a comparison of the vertical displacement and the rotation along the y-axis, evaluated at the BSM reference nodes. In addition, experimental measurements from the ETW wind tunnel are also plotted. Note that the wind tunnel data for the twist distribution have been evaluated at a different Reynolds number (and dynamic pressure), namely $\mathrm{Re} = 15.1 \times 10^6$ [133]. Therefore, the RANS and quasi-three-dimensional simulations have been performed also at this condition, in order to obtain meaningful comparisons.

Clearly, the one-shot approach predicts lower deformations than the experimental ones. However, this trend can be associated to the stiffer response of the Ansys APDL structural model compared to the wind tunnel one, as shown by the validation exercise in Figure 7.5. Nonetheless, the three approaches used show a remarkably

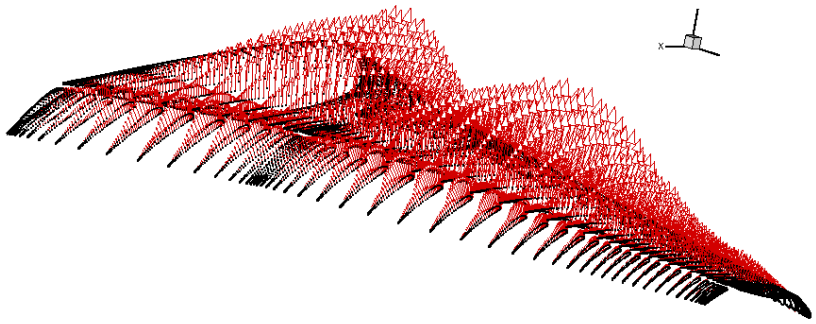

(a) aerodynamic forces

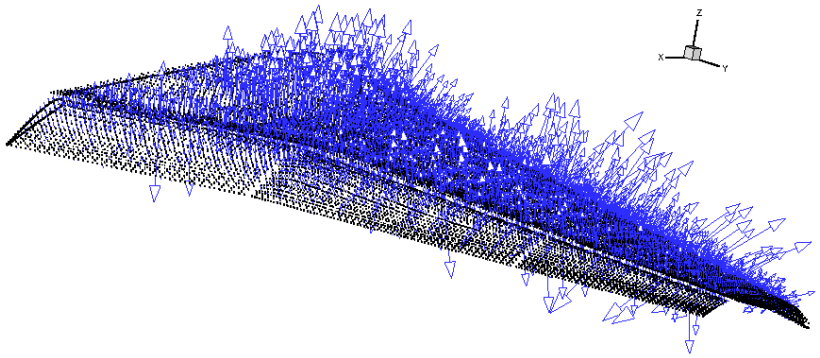

(b) interpolated structural forces

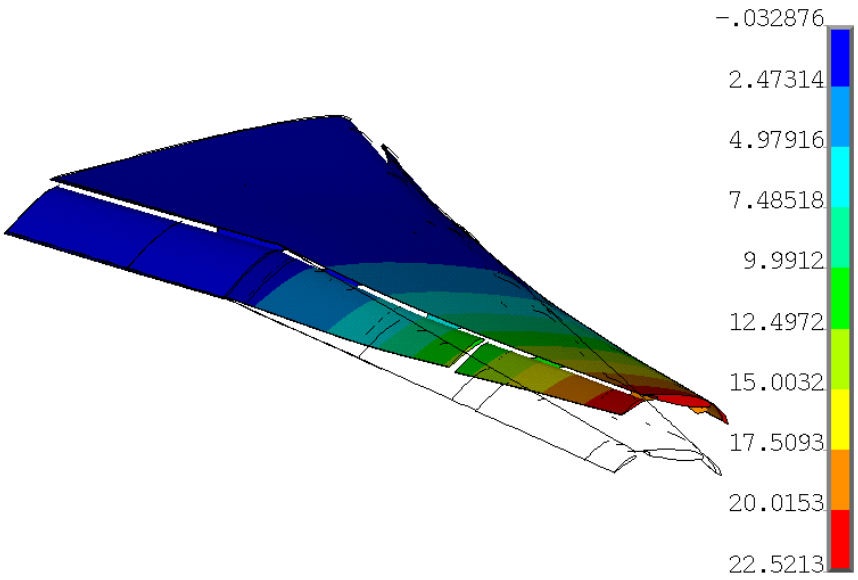

(c) displacement along the z-axis [mm]

Figure 7.7: Aerodynamic loads obtained using a *"one-shot"* RANS-FEM coupling for $\alpha = 7°$. Ansys®CFX suite used for the aerodynamic simulation and Ansys®APDL for the structural deformations.

Table 7.4: Summary of aero-structural coupling approaches.

Aerodynamics	Structure	Coupling Procedure
Rapid approach		
quasi-3D	BSM*	Rapid coupling using aero-database and BSM twist distribution
"One-shot"		
RANS	BSM*	RANS loads are extracted on strips centred at the BSM locations and applied to the BSM
RANS	FEM (ANSYS®APDL)	RBF interpolation strategy is used to map RANS loads into FEM nodes
"Full-coupling"		
RANS	FEM (MSC®Patran)	RBF interpolation strategy is used to map RANS loads into FEM nodes, the FEM displacements are obtained and mapped back to the RANS mesh using the same RBF strategy

*the ANSYS®APDL model is reduced to obtain the BSM

similar trend, with the quasi-three-dimensional coupled BSM estimating the higher deformations. The lowest ones are, instead, predicted by the RANS-BSM approach, while the RANS-CSM lays somewhere in between the two curves. Also, it must be noticed that replacing the BSM with the full CSM influences mainly the torsional response of the structure, as illustrated by the change in shape of the twist curve in Figure 7.8(b).

Generally, a high correlation between the y-axis rotation distribution and the vertical displacement is present, indicating that the bending moment is the major cause of the wing twist. In fact, the bending-twist coupling is a typical behaviour of swept-back wings, which is also highlighted in Figure 7.7(c) by the inclination of the iso-z-displacement curves with respect to the symmetry plane (see Figure 7.7(c)).

In conclusion, a trial closed coupling loop is performed, interpolating the evaluated deformation field of the Ansys®APDL model back to the aerodynamic surface mesh. In order to perform this task, the transpose of the interpolation matrix generated for the force transfer is used. The possibility of exploiting the same matrix

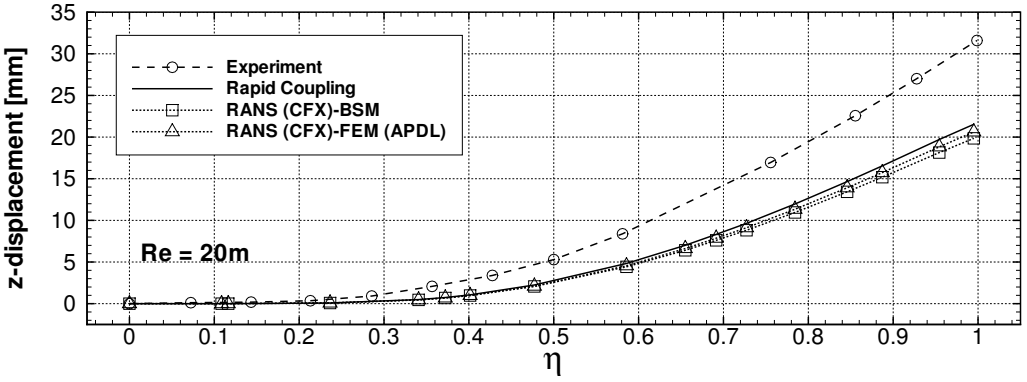

(a) displacement along the z-axis

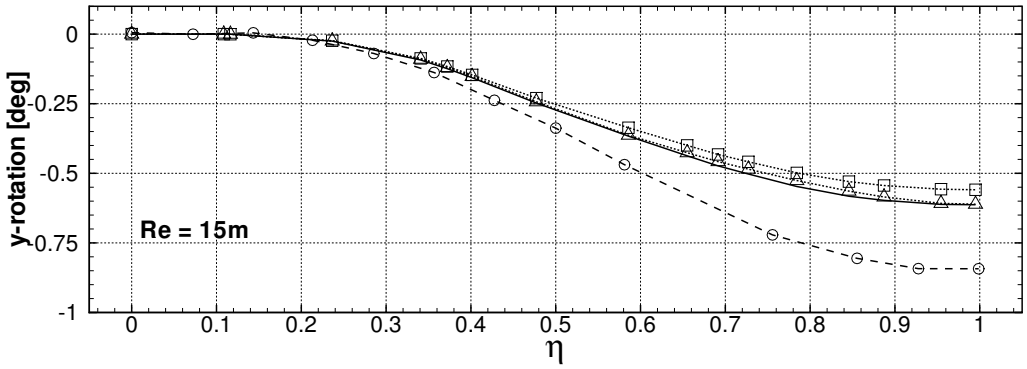

(b) rotation around the y-axis (evaluated at $\mathrm{Re} = 15.1 \times 10^6$)

Figure 7.8: Structural deformation distributions along the span obtained using the *"one-shot"* method. The rapid coupling approach (solid line) is compared against experimental data (line with dots), as well as the results of the CFX-BSM (line with squares) and CFX-APDL approaches (line with triangles).

for both forces and displacements transfer is one of the strength of the RBF formulation, which not only allows computational cost savings, but also guarantees energy conservation during the interpolation process. Figure 7.9 illustrates the deformed aerodynamic surface mesh, obtained scaling the input structural deformations by a factor of 5. The magnified deformations highlight particular areas where special attention must be pai during the interpolation process. In particular, the junctions of the different flap components represent complex regions where singularities can arise in the numerical determination of the interpolation matrix. Those areas must be smoothly resolved if a suitable aerodynamic mesh is to be obtained for further simulations. The obtained results are, however, already showing a good interpolation of the structural deformations, though a small step develops at the outboard flap

junction. Nonetheless, the trial study has demonstrated the feasibility of such complex CFD-CSM interpolation, and has provided promising results for the execution of a static full-loop aero-elastic analysis, described in the next section.

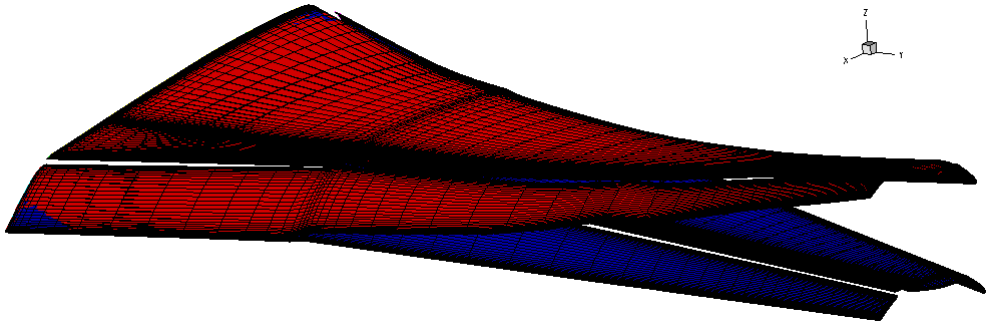

(a) Complete Wing

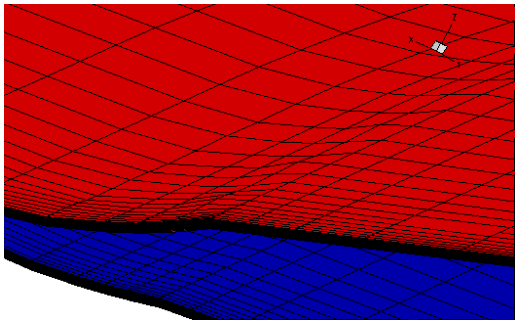

(b) Inboard Flap junction

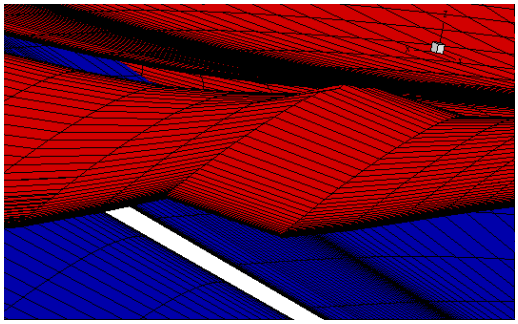

(c) Outboard Flap junction

Figure 7.9: Initial (blue) and deformed (red) aerodynamic surface mesh, obtained using the RBF method to interpolate the structural displacements (multiplied by a factor of 5). Critical areas such as the inboard and outboard flap junctions are emphasised.

7.4.3 *"Full"* Coupling Approach

The one-shot validation study previously presented is here extended to the *"full"* coupling case. The rapid coupling approach, which combines the quasi-three-dimensional simulation with a BSM formulation, is, now, executed in the full iterative mode. Moreover, in order to validate the obtained results, a higher-fidelity static aero-elastic analysis is performed, using the MSC®Patran structural model and the DLR TAU RANS solver. A modified version of the RBF interpolation method earlier described is used to transfer forces and displacements between the aerodynamic and

structural grids. In this specific implementation of the RBF method [150], different interpolation groups are defined for each wing element (slat, main and flap), and special treatments are implemented for the flap junction regions. In addition, a similar RBF formulation as the one used for the CFD-CSM coupling is used to transfer the deformations of the aerodynamic surface mesh to the volume, as presented by Rendall [143]. Finally, the aero-elastic loop is repeated until the deformed shape is sufficiently converged.

The above described analysis is performed to obtain the final deformed configuration illustrated in Figure 7.10. The same onset flow conditions as the one specified in Table 7.3 are used. From the comparison with the initial rigid geometry it is clear that, despite the high rigidity of the model, a considerable deformation is achieved at the wing tip. As a result, the lift and drag coefficients are reduced in comparison to the rigid case. This is illustrated in Figure 7.11, where the convergence history of the simulation is presented for both the flexible and rigid case simulations. In particular, at the prescribed incidence angle of 7°, the results show a reduction in lift of about 1.4% and a 2.5% decrease in drag.

For this specific case, a total of 5 loops, clearly indicated in Figure 7.11 with vertical dotted lines, are needed to converge the simulation. The absolute difference in maximum deformation between two consecutive iterations is used as convergence criteria, and a value of 1×10^{-4} is here prescribed. Also, the convergence history shows that some oscillation is introduced in the CFD simulation by the coupling loops, with the solution stabilising after the third coupling loop, and converging after 27000 CFD iterations.

The interpolated aerodynamic loads on the structure and the relative deformations, in term of displacement along the z-axis, are illustrated in Figure 7.13. The force vectors show a similar distribution as the one-shot case, though the reduced number of nodes in the structural grid (linked to the use of shell elements instead of solid ones) leads to a somewhat more uniform interpolation. In fact, the force

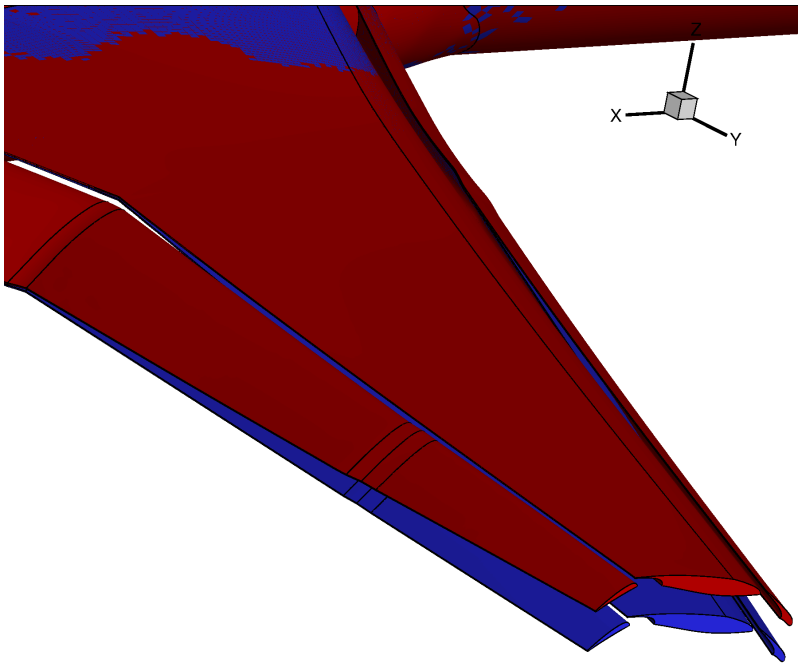

Figure 7.10: Initial rigid (blue) and deformed (red) wing after a *"full"* aero-structural coupling analysis (5 loops) at $\alpha = 7°$. The DLR TAU code is coupled with the MSC®Patran model

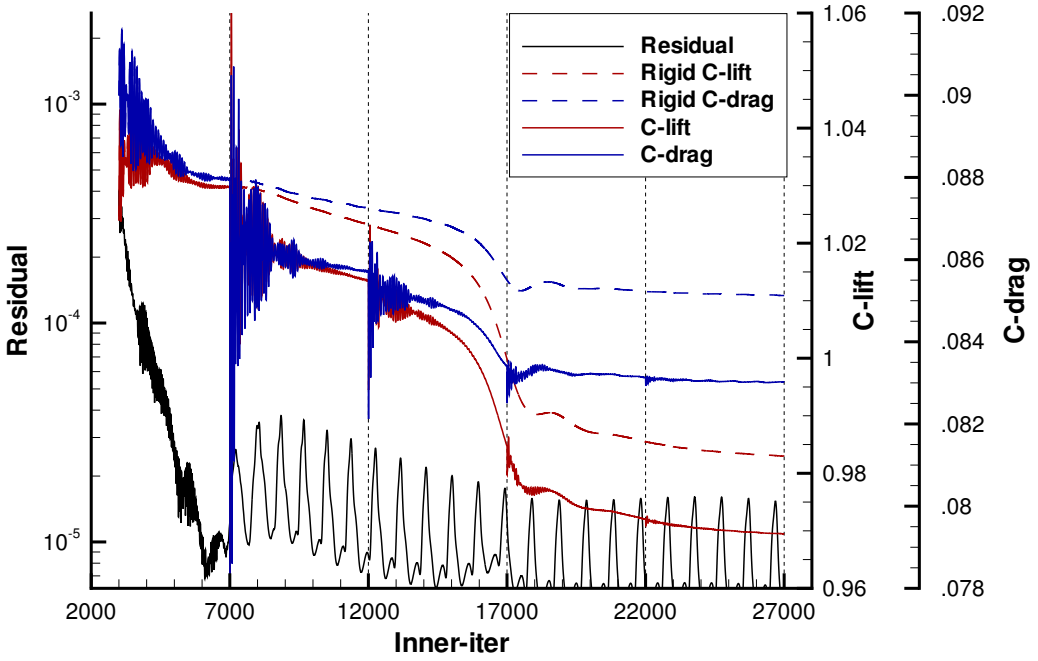

Figure 7.11: Convergence history of the static aero-elastic simulation TAU coupled MSC®Nastran. The 5 coupling steps are marked by dotted vertical lines in the plot.

spikes present in the previous case are here completely eliminated. The deformed shape of the model also closely resembles the one-shot results. However, higher deformations are obtained compared to the previous analysis, with the plots showing a maximum deflection at the tip of about 32 mm, compared to the 22 mm of the one-shot approach.

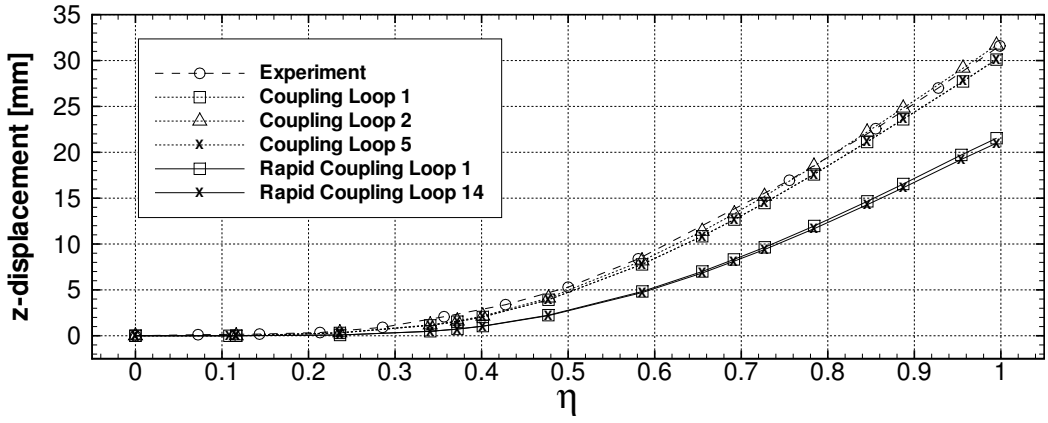

Figure 7.12: Structural deformation distributions along the wing span. The high-fidelity *"full"* method convergence is shown, and compared against the rapid coupling approach (solid line) and experimental data (line with dots).

The vertical displacements obtained with the rapid method and the high-fidelity analysis just presented, are compared against experimental results in Figure 7.12. The converged high-fidelity solution (at iteration 5) closely matches the wind tunnel data, though the results fall slightly short in reaching the maximum deformation value. This improvement compared to the one-shot case is, however, a result of the more compliant CSM model (see Figure 7.5), rather than a consequence of the aero-structure full-loop coupling. In fact, an analysis of the z-displacement plots at various aero-structure coupling loops, also shown in Figure 7.12, indicates that the high-fidelity simulation firstly increases the deformations at loop 2, but then reduces them again and converges to a final equilibrium status almost identical to the first loop. As a result, the simpler one-shot approach should be able to evaluate similar deformation values.

The trend just described indicates that a weak interaction exists between aerody-

namics and structure, since the characteristics of the flow-field are not substantially altered by the structural deformations. This is not the case, for example, for cruise configurations, where the movements in the shock-wave location can lead to complex aero-structure interactions. Therefore, the principal effect of the structural deformations is the modification of the local angle of attack along the span. Indeed, this is the main assumption on which the proposed rapid coupling approach is based.

Finally, the convergence of the rapid approach is also presented in Figure 7.12, where only minor differences are visible between the first and last loop. The under-prediction of the deformation is a consequence of the BSM used within the rapid approach, which has been based on the stiffer Ansys®APDL model.

In conclusion, the results show that the rapid approach can be as accurate as higher-fidelity coupling techniques for the prediction of the structural deformations on an high-lift configuration (see Figure 7.8). Therefore, it represent a powerful tool for the inclusion of flexibility effects within preliminary design analyses.

7.5 Optimisation set-up and Results

The results provided by the extensive validation study performed demonstrate the rapid coupling procedure to be, for the case analysed, as accurate as higher-fidelity methods. Therefore, the method is implemented within the high-lift optimisation framework presented in Chapter 6. Consequently, a further step is added to the workflow, after the completion of the quasi-three-dimensional analysis. In particular, the evaluated rigid 3D polar is used as input to start the rapid coupling analysis, and so obtain the flexible performance of the configuration. This extended framework has been used for the numerical design of the KH3Y configuration. Both the test case and the optimisation set-up are identical to the one presented in Section 6.4.2. The aim of the design problem posed is to optimise the landing performance of the KH3Y configuration, varying the deployment settings of the high-lift elements. A

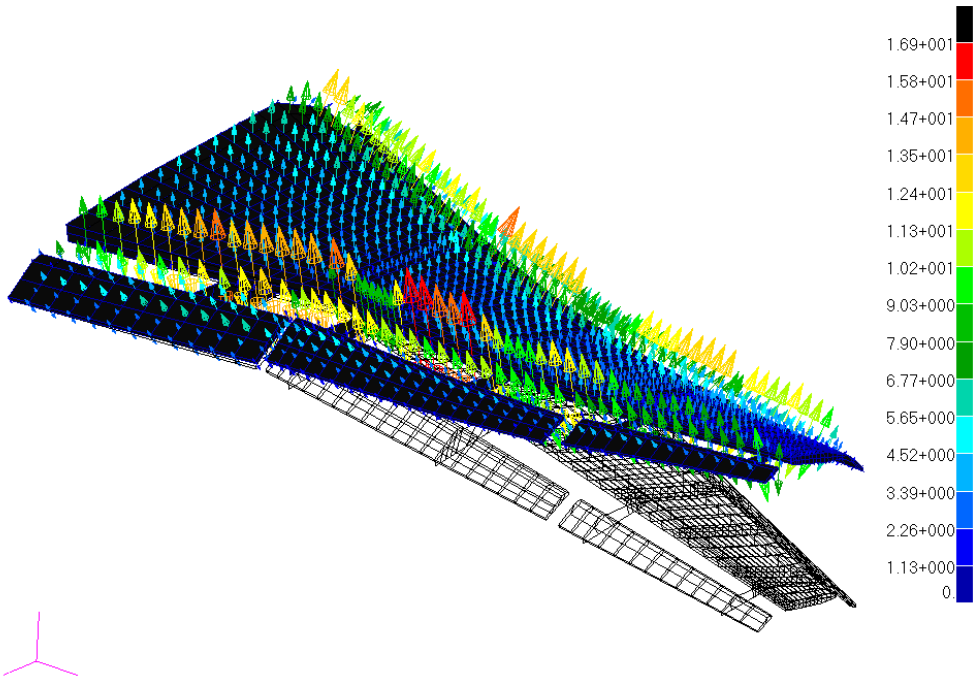

(a) interpolated aerodynamic forces [N]

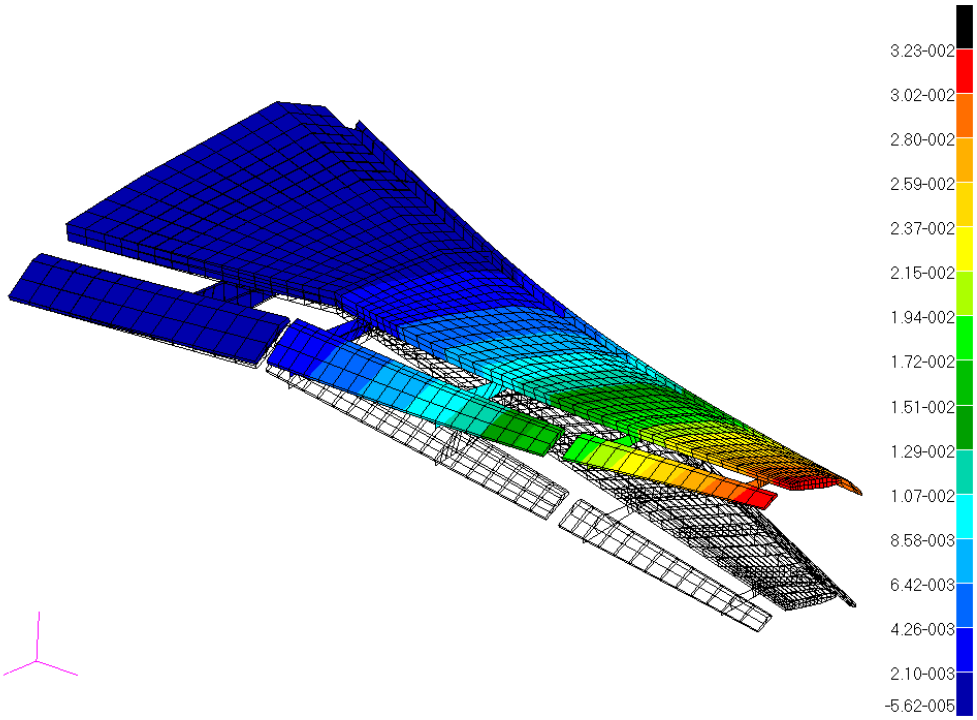

(b) displacement along the z-axis [mm]

Figure 7.13: Structural deformations and aerodynamic loads obtained using a *full* RANS-FEM coupling for $\alpha = 7°$.

summary of the objective functions and design variables definitions is presented in Table 6.6.

Furthermore, the NSGA-II algorithm is selected to drive the optimisation process, with the settings summarised in Table 4.5. However, an initial population of 28 individuals is specified instead of the 48 reported in the table. Moreover, the population is evolved for 50 generations or until the convergence criteria (increment in the objective functions values of the newly revealed optima) is met for 3 consecutive generations.

The optimisation process was successfully executed and the maximum number of generations halting criteria was reached. Of the 1400 candidates produced by the algorithm, 283 were infeasible, with either intersecting elements or failure of the quasi-three-dimensional analysis. When related to the total number of evaluations, the failed designs represent a high percentage, about 20%, of the entire search pattern. This is a drawback of GAs which, in the effort to extensively explore the design space, incur many design failures (especially in the early stage of the optimisation).

Wall-clock time was minimised exploiting the parallel execution of the sectional polars on a 8 node high performance cluster. As a result, the time associated with each quasi-three-dimensional polar is reduced to around 30 minutes. Additionally, the rapid coupling process is executed after the aerodynamic analysis, adding only a small overhead (around 1 minute) to the computation. The overall wall-clock time for completion of the optimisation process was around 30 days.

Figure 7.14 presents the search pattern and the revealed Pareto front at completion. The data is normalised with the values of the initial configuration, so that the datum is identified by the location $obj_1 = -1$ and $obj_2 = 1$. The optimisation algorithm has been able to identify designs which improve both the objective functions, so dominating the datum configuration. Nevertheless, the heuristic features of NSGA-II are visible, with some designs exploring much less promising areas of the design space. Besides, the design space appears more constrained by the cl_{max}

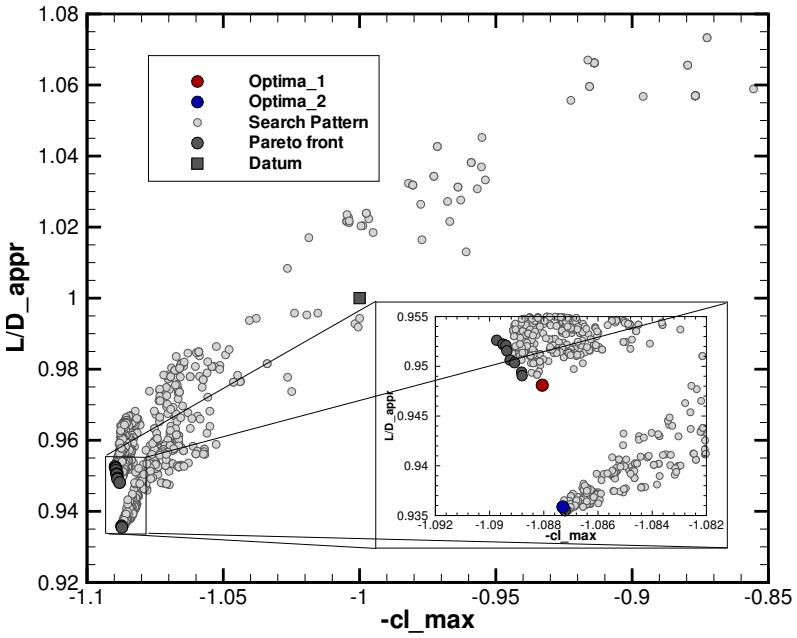

Figure 7.14: Search pattern and Pareto front revealed by NSGA-II after 50 generations for the flexible KH3Y.

criterion, since the Pareto front has an almost vertical trend. A more thorough analysis of the dataset using *"parallel coordinates"* visualisation techniques [151] has been conducted to investigate the peculiar search pattern revealed.

The parallel coordinate visualisation of the design space is presented in Figure 7.15. In the plot each analysed design point is represented by an horizontal line, with the range of variation of the design variables and objective functions shown on the vertical lines. Moreover, the colour scale indicates the design optimality with respect to the posed problem, with blue shadings indicating improved performance. Clearly the plot shows a general trend which characterises the optima configurations, as demonstrated by the clustering of blue lines. In particular, for these designs, all the design variables related to the slat element are reduced with comparison to the datum value. The inboard flap, instead, presents optimal gap settings at values quite close to the datum, whereas a more substantial reduction in the overlap is visible. The deflection angle presents a characteristic split in its optimal value, with a secondary pattern appearing at high values (light blue colour cluster). Finally,

the outboard flap presents an increased value for the gap, and decreased values for both the lap and deflection variables.

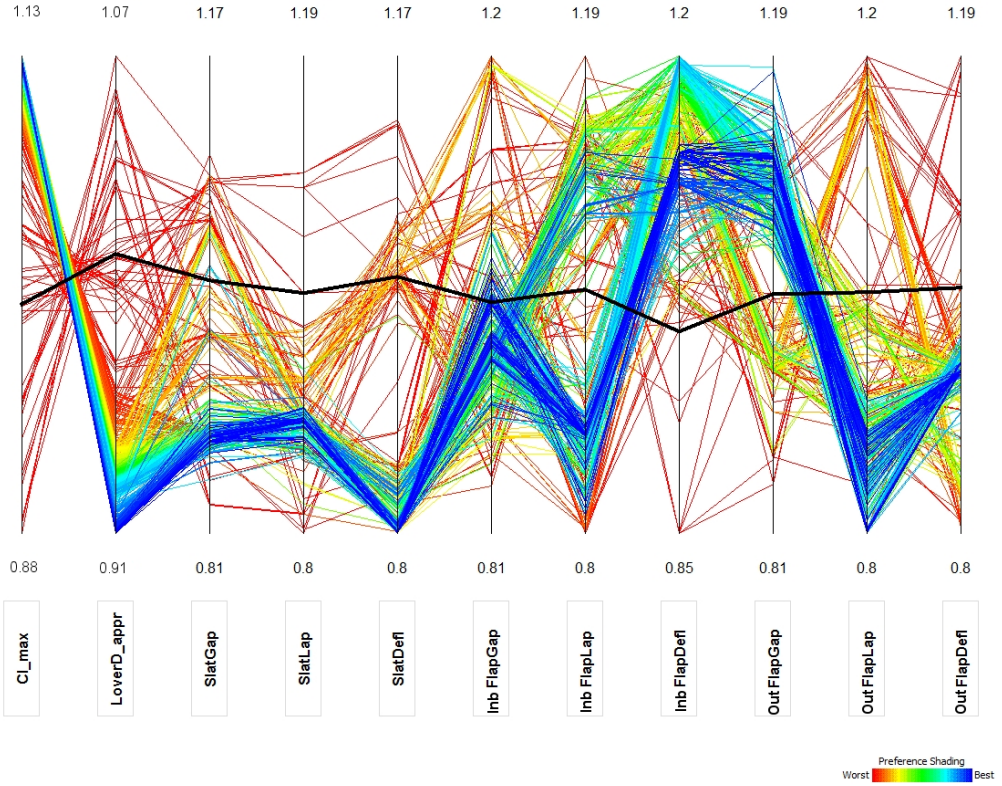

Figure 7.15: Parallel coordinate analysis for the flexible KH3Y optimisation, coloured by optimality of the design. Datum is represented by the central black line.

As in the case of the rigid KH3Y optimisation, a discontinuity is visible in the pareto front (Figure 7.14), nearby the region of compromise designs. This characteristic appears as a feature for the entire search pattern, which tends to split in two distinct point clusters when close to the maximum performance region. Once again parallel coordinates are useful tool to underpin the geometrical variations that lead to this peculiar behaviour. Specifically, the regions of the search pattern that present similar trend are clustered together into two different subsets (see top-left corner of Figure 7.16). Then, the respective parallel coordinate representation of the two subsets are overlaid, as shown in Figure 7.16, illustrating the correlation between the inboard flap deflection and the design point clustering behaviour of the

search pattern previously highlighted. In fact, maximum deflection of the inboard flap is associated with the upper left cluster, whereas somewhat lower deflection values characterise the second cluster.

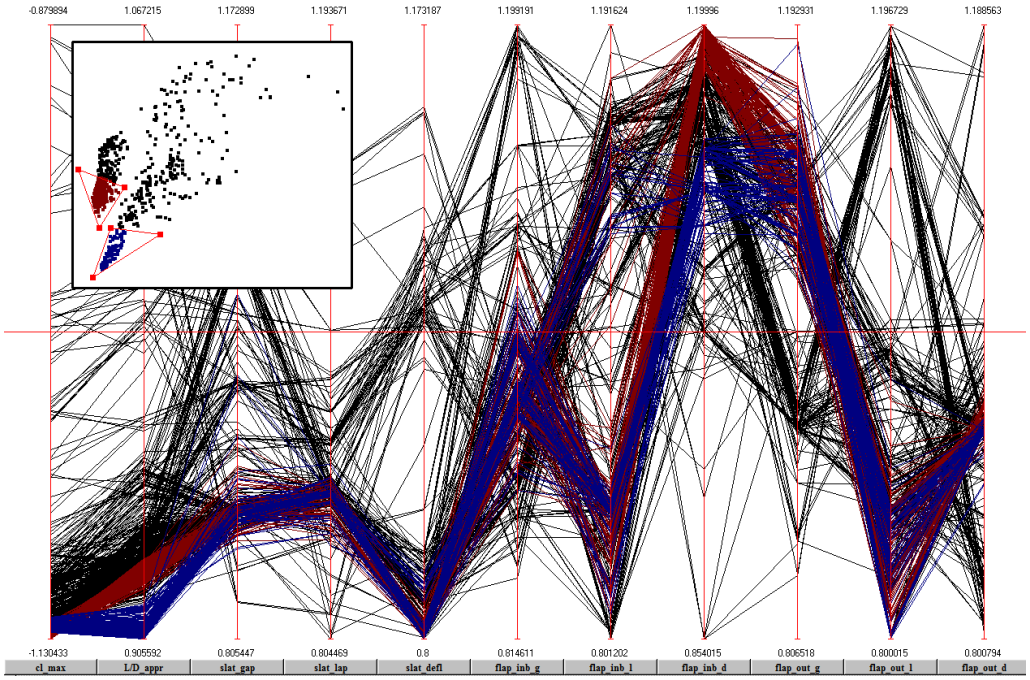

Figure 7.16: Parallel coordinate analysis for the flexible KH3Y optimisation, clustering of search pattern into two sub-sets and identified correlation with inboard flap deflection.

Two optima points, indicated as Optima_1 and Optima_2, are selected from the Pareto front for further analysis. Table 7.5 summarises the improvements in the objective functions as well as the changes in the deployment settings for the two configurations. As previously concluded from the parallel coordinates analysis the main geometrical difference between the optima is the deployment angle of the inboard flap, as illustrated in Figure 7.17. This different setting appears to be affecting more the L/D_{appr} performance of the configuration than the maximum lift value. Confirmation of this trend is given by the $L/D - \alpha$ polar in Figure 7.18(b), which presents lower L/D values for the Optima_1 compared to the other analysed optimum design. The $cl - alpha$ polar, instead, presents a close match between the two optima, with the two curves almost overlapping.

Compared to the rigid optimisation case a higher deflection angle of the inboard flap is achieved, with resultant inboard shift of the load. Also the slat loads are considerably reduced, with a deflection angle that reaches the minimum value of the defined range of variation. The combined effect of these results in a lower twist distribution along the wing, and a slightly higher maximum lift coefficient can be achieved.

Table 7.5: KH3Y flexible case optimisation, design variables and objective functions improvement for the two optimum designs Optima_1, and Optima_2.

		Optima_1	**Optima_2**
	Δobj1	-8.806%	-8.730%
	Δobj2	-5.190%	-6.4135%
Slat	$(\text{gap}_s)/(\lvert\text{gap}_s\rvert_0)$	0.88	0.88
	$(\text{lap}_s)/(\lvert\text{lap}_s\rvert_0)$	0.88	0.90
	$(\Theta_s)/(\lvert\Theta_s\rvert_0)$	0.80	0.80
Flap Inb	$(\text{gap}_f)/(\lvert\text{gap}_f\rvert_0)$	1.00	1.00
	$(\text{lap}_f)/(\lvert\text{lap}_f\rvert_0)$	0.88	0.90
	$(\Theta_f)/(\lvert\Theta_f\rvert_0)$	1.20	1.14
Flap Out	$(\text{gap}_f)/(\lvert\text{gap}_f\rvert_0)$	1.12	1.12
	$(\text{lap}_f)/(\lvert\text{lap}_f\rvert_0)$	0.80	0.80
	$(\Theta_f)/(\lvert\Theta_f\rvert_0)$	0.96	0.93

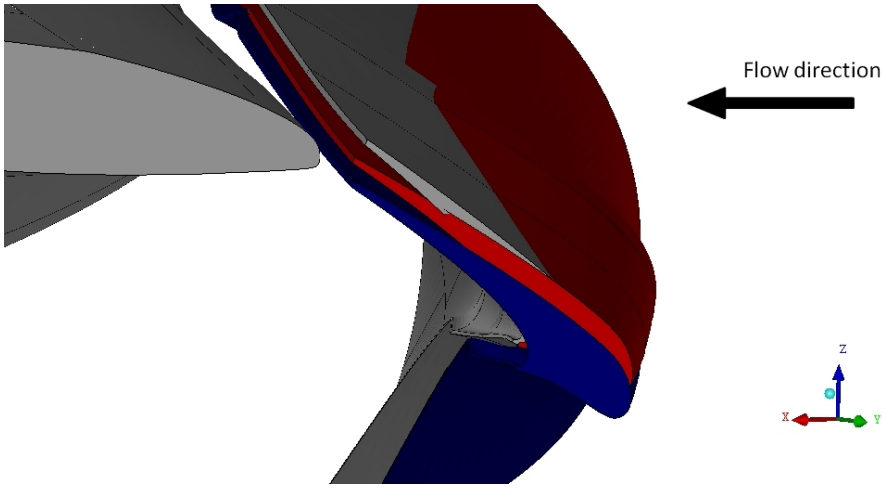

(a) Slat element

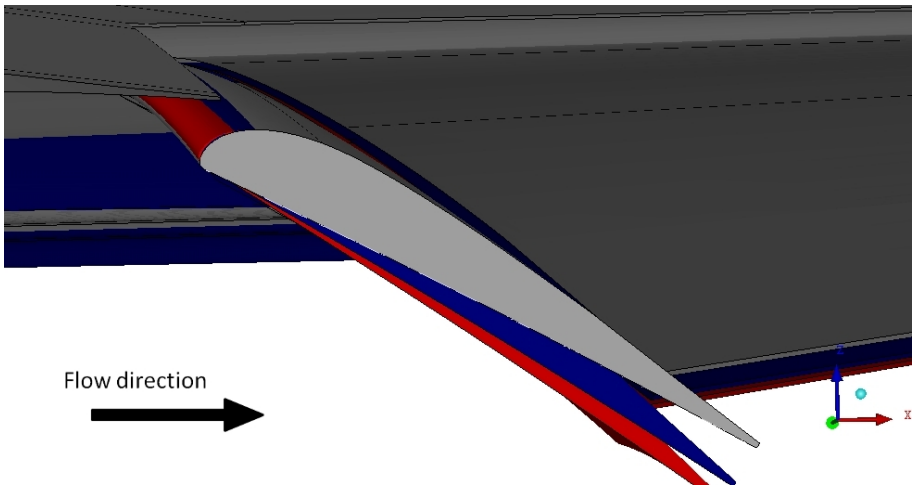

(b) Inboard Flap

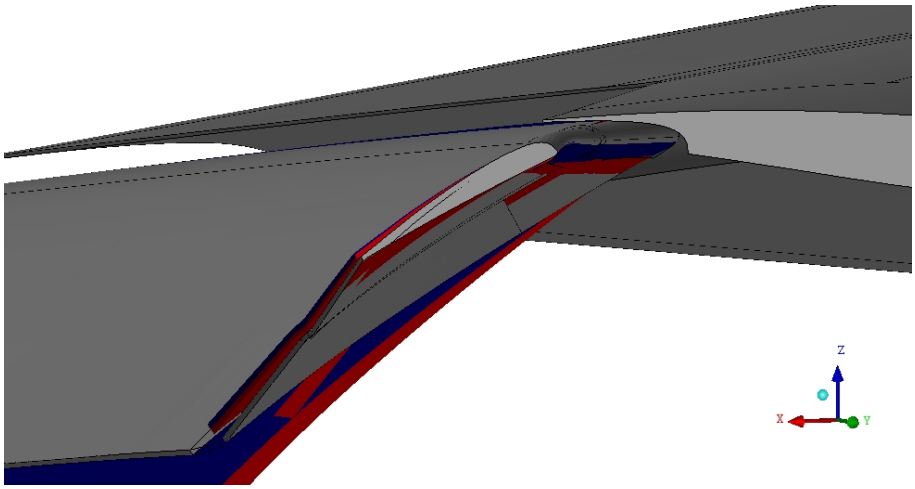

(c) Outboard Flap

Figure 7.17: Geometry comparison of the datum KH3Y (grey), the Optima_1 design (red) and the Optima_2 one (blue), flexible optimisation.

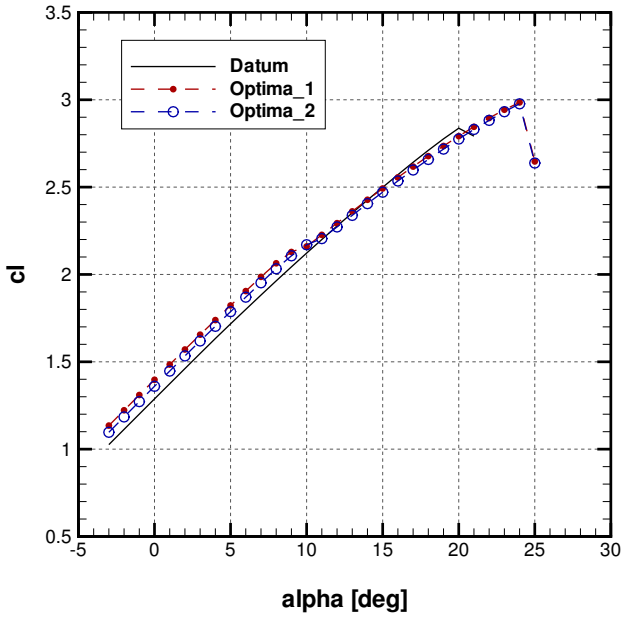

(a) $cl - \alpha$

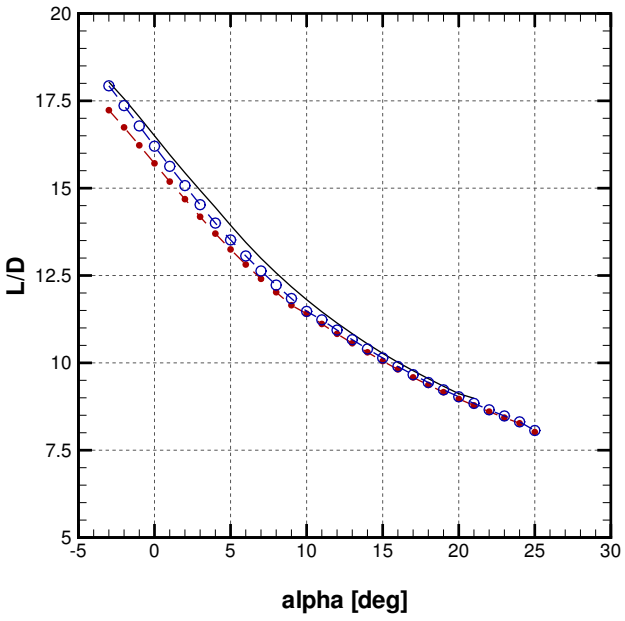

(b) $L/D - \alpha$

Figure 7.18: Polars comparison for the datum KH3Y configuration (solid line) and the identified Optima_1 (red line with dots) and Optima_2 (blue line with circles), flexible optimisation.

Chapter 8

Conclusions

This thesis has presented the development and application of an optimisation framework for the preliminary design of High-Lift aircraft configurations. Specifically, Multi-Objective optimisation techniques are exploited to tackle real-world design problems without imposing any a priori bias into the analysis. In this way, it is possible to present the designer of High-Lift systems with a range of optima, i.e. a Pareto front, which clearly captures the trade-off between conflicting requirements.

The modularity of the presented framework has allowed the application of such techniques to several test cases, starting from 2D multi-element airfoil up to 3D wing-body configurations. The inclusion of different optimisation algorithms as well as several aerodynamic evaluation methods is one of the key innovative aspect of the proposed approach. This feature allows the selection of the appropriate analysis tool for the desired level of fidelity or the specific stage of the design. Moreover, the optimisation framework has been developed keeping in mind that it had to be flexible and easily executed in two greatly different computing environment: the Academic and the Industrial Sponsor's one.

Using such framework the 2D GARTEUR A310 test case has been optimised for take-off conditions. The multi-level parallelisation of the framework has allowed the use of accurate RANS simulations for the flow-field evaluation, with the associated

high-level of fidelity. The presented optimisation case represents one of the few applications found in literature where heuristic multi-objective algorithms have been used in conjunction with RANS simulations. Two identical optimisation set-ups have been executed using the innovative Multi-Objective Tabu Search algorithm and the well-known NSGA-II. The obtained results have successively been compared in order to assess the performance of MOTS in tackling the proposed design study. The analysis identifies the richness of the Pareto front as one of the limitation of the evolution based algorithm (NSGA-II), since a maximum size is implicitly set once the number of individuals is fixed. Furthermore, the enhanced local search characteristic of MOTS results in a much more efficient exploration of the design space, with almost the entire search pattern being located in optimum regions of the design space.

The optimisation study of the GARTEUR A310 airfoil is concluded with a multi-point set-up, in which the maximum lift performance of the test case is maximised concurrently to the minimisation of the its variation within a range of angles of attack. This uncertainties minimisation problem is performed using the interval analysis technique and defining appropriate objective functions. The resulting optimisation set-up is similar to the one proposed by Srinath [81], but the study here presented is the first application of such methods to an high-lift configuration. The obtained results and Pareto Front illustrate the feasibility of such optimisation studies, although both the computational cost and the complexity of the design space increase considerably. A characteristic flap shape with a remarkably small gap to the main wing is identified as a peculiar feature for maintaining the lift performance over a range of angles of attack close to cl_{max}.

The application of the optimisation framework is extended to 3D geometries using a *"quasi-three-dimensional"* method to simulate the aerodynamic performance of high-lift configurations. The method, first introduced by Jacob [112], has been used in literature for the evaluation of the aerodynamic characteristics of high lift wing,

though this is the first work where it is included within an automatic optimisation framework. A realistic high-lift test case, the DLR F11 (KH3Y) wind tunnel model, has been selected as application example. The deployment settings of the full-span slat and of the two single-slotted flap elements (inboard and outboard) are varied to optimise the landing performance of the configuration. The results show that, despite the fact that the datum configuration is already highly optimised, the MOTS optimiser is able to identify regions of improvement in the design space. Once again, the high level of parallelisation of the framework allows the use of heuristic optimisation algorithms in conjunction with more computational expensive simulations, such as the evaluation of the entire aircraft polar needed for the estimation of the case specific objective functions ($-cl_{max}$ and L/D at the approach angle of attack).

Finally, the framework is completed with the addition of a methodology for the estimation of static aero-elastic effects. For this purpose, the rapid coupling approach presented by Agostinelli et al. [149] is here adapted and used in conjunction with the quasi-three-dimensional simulations. This unique aero-structural coupling approach is proved to be, in an in-depth validation study, as accurate as higher fidelity methods for the specific application considered. Therefore, the culmination of this work is the execution of a multi-objective optimisation of the KH3Y wing-body configuration including flexibility effects.

The obtained results present a Pareto front similar to the *"rigid"* optimisation case, although the optima deployment settings are somewhat different. In fact, the inboard shift of the load is more pronounced in the flexible case, with the inboard flap reaching the maximum deflection value within the defined range of variation. This leads to a reduction of the bending-induced twist, and a consequent increase in the local angle of attack of the outboard sections. Also, the slat deployment settings are substantially changed in comparison to the datum design, with the optima featuring a closer slat element, but deployed at a shallower angle. The identified differences between the rigid and flexible cases illustrate the importance of considering aero-

structure influences early on in the design process. This is particularly true when full-size aircraft are analysed, since they present not only a much more flexible structural response than a wind tunnel model, but also experience higher forces due to the higher Reynolds number value.

Although the focus of this work has been the application of multi-objective optimisation techniques to the design of High-Lift systems, much time and effort has been devoted to the development of the optimisation framework itself. Indeed the task is a challenging one, especially considering the number of different methods and algorithms included, as well as the diversity of computing environments the framework had to be executed on. The complexity of the system is reflected not only on the different input/output requirements of each module, but also on the handling of data exchange and location. The author has identified few key points that should be considered when developing such frameworks:

- **Automatic and robust execution of the constitutive blocks.** Each module of the framework should be executed without any intervention of the user (excluding also any intermediate operation on input and output data) and any possible step should be taken in minimising the probability of a module failure;

- **Efficient data handling.** Ability to cope with data stored in different locations (including shared drives in a network), checking availability of data before execution of the module. Differentiated strategy for file usage to reduce wall clock time, copying small files into the execution folder and using links to the original location of bigger files;

- **Remove any temporary file.** Clear up the execution folder from old and temporary data in order to avoid any accidental usage of outdated files. Store and backup only important information/files;

- **Restart capabilities.** It is of paramount importance to be able to monitor,

stop and restart the optimisation process. This is especially true when several servers and clusters are used for the execution of the simulation tools, since a failure in any of these will lead to a loss of data;

- **Robustness to failure.** The framework and the optimisation algorithm (when it is possible to do so) should cope with failures of the evaluated design point, recording the reason for the failure and producing a new design to evaluate;

- **Debugging and post-processing.** It is important to capture and store log files and errors in order to be able to debug and post-process the optimisation results;

- **Single run.** It should be possible to run the analysis chain of the framework outside of the optimisation loop for post-optimisation analysis. Any of the analysed design point can, in this way, be easily re-evaluated to obtain more detailed information on the design features that produced the performance improvements.

These guidelines have been closely followed during the development of the optimisation framework used in the foregoing studies.

Finally, beside the described optimisation framework additional developments have been carried out at the Industrial Sponsor: i.e. the APODO project. This development is aimed at building a bridge within the aerospace industry between the currently used manual design process and an optimisation assisted one. APODO represents an unique example of application of POD surrogate model to the optimisation of high-lift airfoils. The presented results have shown the potential of the proposed approach, but also its intrinsic limitations. In particular, the comparison of the Pareto front revealed using the POD implementation and the one obtained using the RANS-in-the-loop process (see Figure 5.15) highlights the computational cost/accuracy trade-off of the POD method. The produced results are of satisfactory

quality, especially in view of the reduction in computational cost and the re-usability of the POD model for further studies.

8.1 Future Work

The presented framework has enabled the aerodynamic optimisation of High-Lift systems taking into account also static aero-elastic deformations within the analysis process. Indeed this represents an important step toward the development of an integrated system for the Multi-Disciplinary Optimisation (MDO) of such systems. However, further developments are envisaged in order to fully exploit the advantages of MDO and obtain a solution which is optimum at an overall aircraft level.

Firstly the deployment laws for the system's kinematics could be directly included within the performed analysis. This would enable not only a direct specific definition of the constraints which the system must satisfy (rather than a limitation on the range of variability of the design variables as currently implemented), but also the execution of multi-point optimisations, considering concurrently the take-off and landing performance of an high-lift configuration. Furthermore, different linkages concepts and associated weight penalties could be considered within the same optimisation set-up, introducing binary design variables that would switch between one concept and another depending on the element's position with respect to the main wing. It is clear how these developments would be a natural extension of the multi-point optimisation problem presented for the 2D GARTEUR A310 multi-element airfoil.

Secondly, the availability of a structural model (even if a reduced one) could be further exploited in order to include structural limitations on the flap tracks as a constraint within the optimisation process. In fact, better aerodynamic designs generally lead to increased loads on the high-lift devices, with consequently thicker tracks structures. As a result, those designs are associated with weight penalties,

which could also lead to system infeasible solutions. Therefore, it is important to consider such constraints within the optimisation process.

Moreover, in order to further reduce the wall-clock time to completion, the already implemented multi-level parallelisation could be flanked by a multi-fidelity approach. Specifically, CFD methods of different level of accuracy can be combined in order to accelerate the convergence of the optimisation process. Clearly, the proposed optimisation framework offers a strong basis for further development, since several methods have already been implemented and used in isolation. For example, the 2D panel coupled boundary layer used within the quasi-three-dimensional approach could be coupled with RANS simulations for the optimisation of high-lift sections.

With regard to the APODO development, the POD-based optimisation presents some clear strengths when compared to the *"traditional"* approach. In fact, it is the natural bridge from a manual optimisation task, typical of a current design process, to a completely automatic process. However, further development is required on the ROM construction technique in order to increase its accuracy and range of applicability. In particular, the challenges of producing a high quality mesh around a multi-element airfoil which retains its topology (requirement for the POD decomposition) for different deployment settings must be addressed. Clearly, this represents, currently, the limiting factor in the application of POD-based optimisation to design problems that present a wide range of variability of the design variables.

Finally, an interesting application case for the developed framework would be the design of innovative high-lift solutions to enable laminar wing technology. In fact, no well-established solutions are available for such application, and innovative concepts can be explored using automatic optimisation techniques such as the one presented in this thesis. It must be specified that although laminar wings are designed to achieve laminar flow at cruise conditions, fully turbulent flow can be assumed at take-off and landing, so that the presented methods can be applied for the design

of such cases. Several technical challenges have to be overcome before laminar wing technology can deliver the promised step-change. Particularly, natural laminar flow wings (wings designed to achieve laminar flow without any control, either active or passive) require the upper surface of the wing (suction side) to be extremely smooth to avoid boundary layer transition. As a result, no step can be present on the surface, excluding the use of the well established slat elements at the leading edge of the wing. Therefore, non-conventional designs must be assessed and compared to find a feasible solution. In this context, krüger flaps are becoming popular once again, since they retract in the lower side of the wing, and also shield the wing leading edge from bugs at low altitude flights. Several concepts could be optimised using the presented framework and assessed in term of the above mentioned requirements.

References

[1] P. K. C. Rudolph, "High-Lift Systems on Commercial Subsonic Airliners," tech. rep., NASA, 1996.

[2] A. Flaig and R. Hilbig, "High-lift design for large civil aircraft.," Tech. Rep. 31, High-Lift System Aerodynamics, AGARD CP 515, September 1993.

[3] D. M. Jaeggi, G. Parks, T. Kipouros, and P. Clarkson, "The development of a multi-objective Tabu Search algorithm for continuous optimisation problems," *European Journal of Operational Research*, vol. 185, no. 3, pp. 1192–1212, 2008.

[4] T. Kipouros, *Multi-Objective Aerodynamic Design Optimization*. PhD thesis, Cambridge University, 2006.

[5] P. A. LeGresley and J. J. Alonso, "Investigation of Non-Linear Projection for POD Based Reduced Order Models for Aerodynamics," in *39th AIAA Aerospace Sciences Meeting & Exhibit, Reno, NV*, AIAA-2001-0926, January 2001.

[6] J. Katz and A. Plotkin, *Low-Speed Aerodynamics*. Cambridge University Press, 2001.

[7] J. E. Green, "Mitigating the Environmental Impact of Aviation: Opportunities and Priorities," tech. rep., Royal Aeronautical Society, 2005.

[8] Deloitte, "AIAC-Global Aerospace Market Outlook and Forecast," tech. rep., Deloitte & Touche LLP and affiliated entities, 2010.

[9] C. P. van Dam, "The Aerodynamic design of multi-element high-lift systems for transport airplanes," *Progress in Aerospace Sciences*, vol. 38, pp. 101–144, 2002.

[10] M. C. Niu, *Airframe Structural Design. Second Edition.* Hong Kong Conmilit Press LTD, 1999.

[11] A. M. O. Smith, "High-Lift Aerodynamics," *Journal of Aircraft*, vol. 12, pp. 501–530, June 1975.

[12] K. Rudnik, P. Eliasson, and J. Perraud, "Evaluation of CFD methods for transport aircraft high lift systems," *The Aeronautical Journal*, vol. 109, pp. 53–64, 2005.

[13] C. L. Rumsey and S. X. Ying, "Prediction of high lift: review of present CFD capability," *Progress in Aerospace Sciences*, vol. 38, pp. 145–180, 2002.

[14] I. Fejtek, "Summary of Code Validation Results For a Multiple Element Airfoil Test Case," in *Proceedings of the 28th AIAA Fluid Dynamics Conference, Snowmass Village, CO*, pp. 1–15, AIAA-97-1932, 1997.

[15] M. Murayama and K. Yamamoto, "Validation of flows on High-Lift configurations by structured and unstructured mesh method," in *43rd AIAA Aerospace Science Meeting and Exhibit, Reno, Nevada*, pp. 1–15, AIAA-2005-1226, 2005.

[16] E. Besnard, A. Schmitz, E. Boscher, N. Garcia, and T. Cebeci, "Two-Dimensional Aircraft High Lift System Design and Optimization," in *36th Aerospace Sciences Meeting and Exhibit, Reno, Nevada*, AIAA-98-0123, Jan 1998.

[17] G. N. Vanderplaats, *DOT Users Manual, Version 4.10.* Miura and Associates, 1994.

[18] S. Eyi, K. D. Lee, S. E. Rogers, and D. Kwak, "High-Lift Design Optimization Using Navier-Stokes Equations," *Journal of Aircraft*, vol. 33, no. 3, pp. 499–504, 1996.

[19] J. W. Wild, "Direct Optimization of Multi-Element-Airfoil for High-Lift using Navier-Stokes Equations," in *4th European Computational Fluid Dynamics Conference Part1, Athens, Greece*, pp. 383–390, John Wiley and Sons Ltd., 1998.

[20] M. J. Siclari, W. V. Nostrand, and F. Aussim, "The design of transonic airfoil sections for an adaptive wing concept using a stochastic optimization method," in *34th Aerospace Sciences Meeting &Exhibit, Reno, NV*, AIAA-96-0329, 1996.

[21] T. Rowan, *Functional Stability Analysis of Numerical Algorithms.* PhD thesis, Department of Computer Sciences, University of Texas at Austin, 1990.

[22] J. F. Wang and J. Periaux, "Multi-point optimization using GAs and Nash/Stackelberg games for high lift multi-airfoil design in aerodynamics," in *Proceedings of the 2001 Congress on Evolutionary Computation, 2001.*, vol. 1, pp. 552–559 vol. 1, 2001.

[23] S. Kim, J. J. Alonso, and A. Jameson, "Multi-Element High-Lift Configuration Design Optimization Using Viscous Continuous Adjoint Method," *Journal of Aircraft*, vol. 41, no. 5, pp. 1082–1097, 2004.

[24] M. Nemec, D. W. Zingg, and T. H. Pulliam, "Multipoint and Multiobjective Aerodynamic Shape Optimization," *AIAA Journal*, vol. 42, no. 6, pp. 1057–1065, 2004.

[25] M. Kanazaki, K. Tanaka, S. Jeong, and K. Yamamoto, "Multi-Objective Aerodynamic Exploration of Element's Setting for High-Lift Airfoil Using Kriging Model," *Journal of Aircraft*, vol. 44, no. 3, pp. 858–864, 2007.

[26] R. Carrese, H. Winarto, X. Li, A. Sóbester, and S. Ebenezer, "A comprehensive preference-based optimization framework with application to high-lift aerodynamic design," *Engineering Optimization*, vol. 44, no. 10, pp. 1209–1227, 2012.

[27] N. Kroll, N. R. Gauger, J. Brezillon, R. Dwight, A. Fazzolari, D. Vollmer, K. Becker, H. Barnewitz, V. Schulz, and S. Hazra, "Flow simulation and shape optimization for aircraft design," *Journal of Computational and applied mathematics*, vol. 203, pp. 397–411, 2007.

[28] J. W. Wild, "Multi-Objective constrained optimization in Aerodynamic design of High-Lift system," *International Journal of Computational Fluid Dynamics*, vol. 22, no. 3, pp. 153–168, 2008.

[29] J. Wild, J. Brezillion, O. Amoignon, J. Quest, F. Moens, and D. Quagliarella, "Advanced Design by Numerical Methods and Wind-Tunnel Verification Within European High-Lift Program," *Journal of Aircraft*, vol. 46, no. 1, pp. 157–167, 2009.

[30] M. Drela, *A User's Guide to MSES 2.95.* MIT Computational Aerospace Sciences Lab, 1996.

[31] E. Benini, R. Ponza, and A. Massaro, "High-Lift Multi-Element Airfoil Shape and Setting Optimization Using Multi-Objective Evolutionary Algorithms," *Journal of Aircraft*, vol. 48, no. 2, pp. 683–696, 2011.

[32] "AIAA CFD High Lift Prediction Workshop (HiLiftPW) Series, http://hiliftpw.larc.nasa.gov/index.html."

[33] J. Brezillon, R. P. Dwight, and J. Wild, "Numerical Aerodynamic Optimisation of 3D High-Lift Configurations," in *26th Congress of International Council of the Aeronautical Sciences*, 2011.

[34] M. Minervino, D. Quagliarella, and P. Iannelli, *Evolutionary and Deterministic Methods for Design, Optimization and Control: Applications to Industrial and Societal Problems ; [EUROGEN 2007 ... Held in Jyväskylä, 11 - 13 June 2007]*, ch. 3D Flap Design using Navier-Stokes Equations and Evolutionary Optimization Techniques on an Industrial Platform. International Center of Numerical Methods in Engineering, 2011.

[35] A. Bhimani and P. S. Mulder, "Managing processes, quality and costs: a case study.," *Journal of cost management*, vol. 15, no. 2, pp. 28–32, 2001.

[36] C. P. van Dam, J. V. Kam, and J. K. Paris, "Design oriented high-lift methodology for general aviation and civil transport aircraft," *Journal of Aircraft*, vol. 38, no. 6, pp. 1076–84, 2001.

[37] J. A. Samareh, "Survey of Shape Parameterization techniques for high fidelity multidisciplinary shape optimization," *AIAA Journal*, vol. 39, no. 5, pp. 877–889, 2001.

[38] M. I. G. Bloor and M. J. Wilson, "Efficient Parameterization of Generic Aircraft Geometry," *Journal of Aircraft*, vol. 32, no. 6, pp. 1269–1275, 1995.

[39] S. Harvey, W. Dawes, and J. Bolger, "An Automated Design Optimisation System for Axial Compressors Part I: Software Development," in *ASME Turbo Expo 2003: Power for Land, Sea and Air, June 2003, Atlanta, GA*, no. GT2003-38650, 2003.

[40] A. Garnesson, "Development of an unconstraint geometry modelling tool for 3D multi-element airfoil configurations in Formula one," Master's thesis, Cranfield University, 2007.

[41] G. Trapani, "Multi-Objective Optimization of 2D High-Lift Airfoil Configurations using Tabu Search," Master's thesis, Cranfield University, 2009.

[42] A. Diwakar, D. N. Srinath, and S. Mittal, "Aerodynamic Shape Optimization of Airfoils in Unsteady Flow," *CMES: Computer Modeling in Engineering and Sciences*, vol. 69, no. 1, pp. 61–89, 2010.

[43] H. Sobieczky, "Parametric Airfoils and Wings," in *Recent Development of Aerodynamic Design Methodologies. Notes on Numerical Fluid Mechanics* (K. Fujii and G. Dulikravich, eds.), vol. 65, Vieweg+Teubner Verlag, 1999.

[44] Y. S. Lian and M. S. Liou, "Mining of Data from Evolutionary Algorithms for Improving Design Optimization," *CMES: Computer Modeling in Engineering and Sciences*, vol. 8, no. 1, pp. 61–67, 2005.

[45] F. Zhu and N. Qin, "Intuitive Class/Shape Function Parameterization for Airfoils," *AIAA Journal*, vol. 52, no. 1, pp. 17–25, 2014.

[46] B. M. Kulfan and J. E. Bussoletti, ""Fundamental" Parametric Geometry Representations for Aircraft Component Shapes," in *11th AIAA/ISSMO Multidisciplinary Analysis and Optimization Conference, Portsmouth, VA*, AIAA-2006-6948, 2006.

[47] R. Hicks and P. Henne, "Wing Design by Numerical Optimization," *Journal of Aircraft*, vol. 15, no. 7, pp. 407–413, 1978.

[48] T. W. Sederberg and S. R. Parry, "Free-Form Deformation of Solid Geometric Models," *SIGGRAPH*, vol. 20, no. 4, pp. 151–160, 1986.

[49] F. J. Thompson, N. P. Weatherill, and B. K. Soni, *Handbook of Grid Generation*. CRC Press, New York, 1998.

[50] J. E. Bardina, P. G. Huang, and T. J. Coakley, "Turbulence Modeling Validation, Testing and Development," NASA technical memorandum–110446, NASA, 1997.

[51] C. L. Rumsey, T. B. Gatski, S. X. Ying, and A. Bertelrudc, "Prediction of high-lift flows using turbulent closure models," *AIAA Journal*, vol. 36, no. 5, pp. 765–774, 1998.

[52] E. Fares and S. Nolting, "Unsteady Flow Simulation of a High-Lift configuration using a Lattice Boltzmann Approach," in *49th AIAA Aerospace Sciences Meeting including the New Horizons Forum and Aerospace Exposition, 4 - 7 January 2011, Orlando, Florida, AIAA 2011-869*, 2011.

[53] P. Eliasson, S.-H. Peng, and A. Hanifi, "Improving the Prediction for the NASA High-Lift Trap Wing Model," in *49th AIAA Aerospace Sciences Meeting including the New Horizons Forum and Aerospace Exposition, 4 - 7 January 2011, Orlando, Florida, AIAA 2011-867*, 2011.

[54] P. Eliasson, A. Hanifi, and S.-H. Peng, "Influence of Transition on High-Lift Prediction for the NASA Trap Wing Model," in *29th AIAA Applied Aerodynamics Conference, 27 - 30 June 2011, Honolulu, Hawaii, AIAA 2011-3009*, 2011.

[55] A. Krumbein, "Automatic Transition Prediction and Application to High-Lift Multi-Element Configurations," *JOURNAL OF AIRCRAFT*, vol. 42, no. 5, pp. 1150–1164, 2005.

[56] R. G. Steed, "High Lift CFD Simulations with an SST-Based Predictive Laminar to Turbulent Transition Model," in *49th AIAA Aerospace Sciences Meeting including the New Horizons Forum and Aerospace Exposition, 4 - 7 January 2011, Orlando, Florida, AIAA 2011-864*, 2011.

[57] P. Shankara and D. Snyder, "Numerical Simulation of High Lift Trap Wing using STAR-CCM+," in *30th AIAA Applied Aerodynamics Conference, 25 - 28 June 2012, New Orleans, Louisiana, AIAA 2012-2920*, 2012.

[58] A. M. Connor and D. G. Tilley, "A Tabu Search method for the optimisation of fluid power circuits," *IMechE Journal of Systems and Control*, vol. 212, pp. 373–381, 1998.

[59] K. Deb, A. Pratap, S. Agarwal, and T. Meyarivan, "A Fast Elitist Multi-objective Genetic Algorithm: NSGA-II," *IEEE Transactions on Evolutionary Computation*, vol. 6, no. 2, pp. 182–197, 2002.

[60] A. Gaiddon and D. D. Knight, "Multicriteria Design Optimization of Integrated Three-Dimensional Supersonic Inlets," *Journal of Propulsion and Power*, vol. 19, no. 3, pp. 456–463, 2003.

[61] F. Y. Edgeworth, *Mathematical Physics*. London, England: C. Kegan Paul, 1881.

[62] V. Pareto, *Cours D'Economie Politique*, vol. I and II. Lasusanne: F. Rouge, 1896.

[63] T. Kipouros, D. M. Jaeggi, W. N. Dawes, G. T. Parks, A. M. Savill, and P. J. Clarkson, "Biobjective design optimization for axial compressors using tabu search," *AIAA Journal*, vol. 46 (3), pp. 701–711, 2008.

[64] R. Hooke and T. A. Jeeves, "Direct search solution of numerical and statistical problems," *Journal of the ACM*, vol. 8, pp. 212–229, 1961.

[65] F. Glover and M. Laguna, "Tabu Search*," in *Handbook of Combinatorial Optimization* (P. M. Pardalos, D.-Z. Du, and R. L. Graham, eds.), pp. 3261–3362, Springer New York, 2013.

[66] S. A. Harvey, *The design optimisation of turbomachinery blade rows.* PhD thesis, Cambridge University, 2002.

[67] T. Kipouros, D. M. Jaeggi, W. N. Dawes, G. T. Parks, A. M. Savill, and P. J. Clarkson, "Insight into high-quality aerodynamic design spaces through multi-objective optimization," *CMES: Computer Modeling in Engineering and Sciences*, vol. 37, no. 1, pp. 1–44, 2008.

[68] T. Ghisu, G. T. Parks, J. P. Jarrett, and P. J. Clarkson, "An Integrated System for the Aerodynamic Design of Compression Systems: part II: Application," *Journal of Turbomachinery*, vol. 133, no. 1, p. 011012, 2011.

[69] C. M. Fonseca and P. J. Fleming, "An overview of evolutionary algorithms in multiobjective optimization," *Evolutionary Computation*, vol. 3, no. 1, pp. 1–16, 1995.

[70] C. A. C. Coello, "Evolutionary Multi-Objective Optimization: a historical view of the field," *Computational Intelligence Magazine, IEEE*, vol. 1, no. 1, pp. 28–36, 2006.

[71] D. Goldberg, *Genetic Algorithms in Search, Optimization and Machine Learning.* Reading, Massachusetts: Addison-Wesley Publishing Company, 1989.

[72] E. Zitzler and L. Thiele, "Multiobjective evolutionary algorithms: A comparative case study and the strength pareto approach," *IEEE Transactions on Evolutionary Computation*, vol. 3, no. 4, pp. 257–271, 1999.

[73] J. J. Thibert, "The Garteur High Lift Research Programme," Tech. Rep. 31, High-Lift System Aerodynamics, AGARD CP 515, September 1993.

[74] F. Manie, O. Piccini, and J. P. Ray, "Test report of the 2D model M1 in the ONERA F1 wind tunnel," GARTEUR high lift Action Group AD (AG-08) TP041, GARTEUR, October 1989.

[75] T. Kipouros, T. Peachey, D. Abramson, and A. M. Savill, "Enhancing and Developing the Practical Optimisation Capabilities and Intelligence of Automatic Design Software," in *8th AIAA Multi-Disciplinary Design Optimization Specialist Conference, Honolulu, Hawaii*, AIAA-2012-1677, 2012.

[76] L. Huyse, S. L. Padula, M. R. Lewis, and L. Wu, "Probabilistic approach to free-form airfoil shape optimization under uncertainty," *AIAA Journal*, vol. 40, no. 9, pp. 1764–1772, 2002.

[77] F. Li, G. Li, G. Sun, Z. Luo, and Z. Zhang, "Multi-Disciplinary Optimization for Multi-Objective Uncertainty Design of Thin Walled Beams," *CMES: Computer Modeling in Engineering and Sciences*, vol. 19, no. 1, pp. 37–56, 2010.

[78] M. Dodson and G. T. Parks, "Robust Aerodynamic Design Optimization Using Polynomial Chaos," *Journal of Aircraft*, vol. 46, no. 2, pp. 635–646, 2009.

[79] W. Chen, J. Allen, K.-L. Tsui, and F. Mistree, "A procedure for robust design: Minimizing variations caused by noise factors and control factors.," *ASME Journal of Mechanical Design*, vol. 118, no. 4, pp. 479–493, 1996.

[80] R. W. Walters and L. Huyse, "Uncertainty Analysis for Fluid Mechanics with Applications," NASA CR–2002–211449, NASA, Feb. 2002.

[81] D. N. Srinath, S. Mittal, and V. Manek, "Multi-Point Shape Optimization of Airfoils at Low Reynolds Numbers," *CMES: Computer Modeling in Engineering and Sciences*, vol. 51, no. 2, pp. 169–188, 2009.

[82] Y. C. Liang, H. P. Lee, S. P. Lim, W. Z. Lin, K. H. Lee, and C. G. Wu, "Proper Orthogonal Decomposition And Its Applications-part I: Theory," *Journal of Sound and Vibration*, vol. 252, no. 3, pp. 527–544, 2002.

[83] P. Holmes, J. L. Lumley, and G. Berkooz, *Turbulence, Coherent Structures, Dynamical Systems and Symmetry.* Cambridge University Press, 1998.

[84] L. Sirovich, "Turbulence and the Dynamics of Coherent Structures. Part 1: Coherent Structures.," *Quarterly of Applied Mathematics*, vol. 45, no. 3, pp. 561–571, 1987.

[85] G. Berkooz, P. Holmes, and J. L. Lumley, "The proper orthogonal decomposition in the analysis of turbulent flows.," *Ann Rev Fluid Mech*, vol. 25, pp. 539–575, 1993.

[86] D. Ruana, H. Hec, D. A. Castanon, and K. C. Mehtac, "Normalized proper orthogonal decomposition (NPOD) for building pressure data compression," *Journal of Wind Engineering*, vol. 94, pp. 447–461, 2006.

[87] D. Alonso, J. M. Vega, and A. Velazquez, "Reduced-Order Model for Viscous Aerodynamic Flow Past an Airfoil," *AIAA Journal*, vol. 48, pp. 1946–1958, 2010.

[88] B. Epureanu, "A parametric analysis of reduced order models of viscous flows in turbomachinery," *Journal of Fluids and Structures*, vol. 17, pp. 971–982, 2003.

[89] T. Lieu, C. Farhat, and M. Lesoinne, "Reduced-order fluid/structure modeling of a complete aircraft configuration," *Computer Methods in Applied Mechanics and Engineering*, vol. 195, no. 41-43, pp. 5730–5742, 2006. John H. Argyris Memorial Issue. Part II.

[90] R. Everson and L. Sirovich, "Karhunen-Loeve procedure for gappy data," *Journal of the Optical Society of America A: Optics, Image Science, and Vision*, vol. 12, pp. 1657–1664, 1995.

[91] T. Bui-Thanh, M. Damodaran, and K. E. Willcox, "Aerodynamic Data Reconstruction and Inverse Design Using Proper Orthogonal Decomposition," *AIAA Journal*, vol. 42, pp. 1505–1516, 2004.

[92] Y. Duan, J. Cai, and Y. Li, "Gappy Proper Orthogonal Decomposition-Based Two-Step Optimization for Airfoil Design," *AIAA Journal*, vol. 50, pp. 968–971, 2012.

[93] D. J. J. Toal, N. W. Bressloff, A. J. Keane, and C. M. E. Holden, "Geometric Filtration Using Proper Orthogonal Decomposition for Aerodynamic Design Optimization," *AIAA Journal*, vol. 48, pp. 916–928, 2010.

[94] S. S. Ghoman, Z. Wang, P. C. Chen, and R. K. Kapania, "Hybrid Optimization Framework with Proper-Orthogonal-Decomposition-Based Order Reduction and Design-Space Evolution Scheme," *Journal of Aircraft*, vol. 50, no. 6, pp. 1–11, 2013.

[95] D. J. Lucia, P. S. Beranb, and W. A. Silva, "Reduced-order modeling: new approaches for computational physics," *Progress in Aerospace Sciences*, vol. 40, pp. 51–117, 2004.

[96] K. Carlberg and C. Farhaty, "A Compact Proper Orthogonal Decomposition Basis for Optimization-Oriented Reduced-Order Models," in *12th AIAA/ISSMO Multidisciplinary Analysis and Optimization Conference, Victoria, BC, Canada*, AIAA-2008-5964, 2008.

[97] T. Kipouros, M. Molinari, W. N. Dawes, G. T. Parks, M. Savill, and K. W. Jenkins, "An Investigation Of The Potential For Enhancing The Computational Turbomachinery Design Cycle Using Surrogate Models And High Performance Parallelisation," in *ASME Turbo Expo 2007, Montreal, Canada*, pp. 1415–1424, 2007.

[98] M. D. McKay, R. J. Beckman, and W. J. Conover, "Comparison of three methods for selecting values of input variables in the analysis of output from a computer code," *Technometrics*, vol. 21, no. 2, pp. 239–245, 1979.

[99] L. S. Lorente, J. M. Vega, and A. Velazquez, "Generation of Aerodynamic Databases Using High-Order Singular Value Decomposition," *Journal of Aircraft*, vol. 45, no. 5, pp. 1780–1788, 2008.

[100] A. Kusiak, *Concurrent Engineering: Automation, Tools, and Techniques.* Wiley, 1993.

[101] A. M. Belay, P. Helo, J. Takala, and F. M. Kasie, "Effects of Quality Management Practices and Concurrent Engineering in Business Performance," *International Journal of Business and Management*, vol. 6, no. 3, 2011.

[102] X. Koufteros, M. Vonderembse, and W. Doll, "Concurrent engineering and its consequences," *Journal of Operations Management*, vol. 19, pp. 97–115, 2001.

[103] Z. Feng, B. R. Gaines, Q. Tan, and M. C. Zhou, "Concurrent engineering tool in software development," in *Systems, Man, and Cybernetics, 1996., IEEE International Conference on*, vol. 3, pp. 1753–1757 vol.3, 1996.

[104] D. Cohen, M. Lindvall, and P. Costa, "A State of the Art Report: Agile Software Development," tech. rep., Fraunhofer Center for Experimental Software Engineering and The University of Maryland, January 2003.

[105] K. Beck, A. Cockburn, R. Jeffries, and J. Highsmith, "The Agile Manifesto," 2001.

[106] D. Hamlet, *Composing Software Components. A Software-testing Perspective.* Springer Science+Business Media, LLC 2010, 2010.

[107] J. Highsmith and A. Cockburn, "Agile Software Development. The Business of Innovation," *Computer*, vol. 34, no. 9, pp. 120–127, 2001.

[108] A. Cockburn, *Agile Software Development: The Cooperative game (2nd Edition).* Pearson Education, Inc., 2007.

[109] M. Cohn, *User Stories Applied: For Agile Software Development.* Pearson Education, Inc., 2004.

[110] J. Erickson, K. Lyytinen, and K. Siau, "Agile modeling, Agile Software Development, and Extreme Programming. State of research," *Journal of Database Management*, vol. 16, no. 4, pp. 88–100, 2005.

[111] G. W. Brune and J. H. McMasters, "Applied computational aerodynamics, progress in aeronautics and astronautics," vol. 125, ch. Computational aerodynamics applied to high-lift systems, pp. 389–433, AIAA, 1989.

[112] K. Jacob, "A Fast Computing Method for the Flow Over High-Lift Wings," Tech. Rep. 23, High-Lift System Aerodynamics, AGARD CP 515, 1993.

[113] J. H. Preston, "The calculation of lift taking account of the boundary layer," tech. rep., Aeronautical Research Council Reports And Memoranda 2725, 1949.

[114] D. A. Spence, "Prediction of the characteristics of two-dimensional aerofoils," *Journal of the Aeronautical Sciences*, vol. 21, pp. 577–588, 1954.

[115] B. J. Powell, "The calculation of the pressure distribution of a thick cambered aerofoil at subsonic speeds including the effect of the boundary layer," tech. rep., Aeronautical Research Council Reports And Memoranda 1005, 1967.

[116] J. C. Le-Balleur, "Strong matching method for computing transonic viscous flows including wakes and separations," *La Recherche Aerospatiale*, vol. 83, pp. 21–45, 1981.

[117] S. M. Klausmeyer and J. C. Lin, "Comparative Results From a CFD Challenge Over a 2D Three-Element High-Lift Airfoil," tech. rep., National Aeronautics and Space Administration Langley Research Center, 1997.

[118] M. Drela, "Viscous-inviscid analysis of transonic and low Reynolds number airfoils," *AIAA Journal*, vol. 25, no. 10, pp. 1347–1355, 1987.

[119] M. Drela, "Xfoil: an analysis and design system for low Reynolds number airfoils," in *Conference on Low Reynolds Number Aerodynamics*, 1989.

[120] M. Drela, "Newton Solution of Coupled Viscous/Inviscid Multielement Airfoil Flows," in *AIAA 21st Fluid Dynamics, Plasma Dynamics and Laser Conference, Seattle, WA*, AIAA-90-1470, June 1990.

[121] M. Drela, "Design and optimization method for multielement airfoils," in *AIAA/AHS/ASEE Aerospace Design Conference, Irvine, CA*, February 1993.

[122] D. Reckzeh, "Aerodynamic design of the high-lift-wing for a Megaliner aircraft," *Aerospace Science and Technology*, vol. 7, pp. 107–119, 2003.

[123] J. F. Wendt, *Computational Fluid Dynamics. An Introduction.* Springer, 2009.

[124] J. D. Anderson, *Fundamentals of Aerodynamic. Fifth Edition.* McGraw-Hill, 2010.

[125] J. L. Hess, "A Higher Order panel Method for Three-Dimensional Potential Flow," in *7th Australasian Hydraulics and Fluid Mechanics Conference, Brisbane*, 18–22 August 1980.

[126] J. L. Hess, "The Problem Of Three-dimensional Lifting Potential Flow And Its Solution By Means Of Surface Singularity Distribution," *Computer Methods In Applied Mechanics and Engineering*, vol. 4, pp. 283–319, 1974.

[127] V. M. Falkner and S. W. Skan, "Some approximate solutions of the boundary layer equations," *Philosophical Magazine*, vol. 12, pp. 865–896, 1931.

[128] F. M. White, *Viscous Fluid Flow*. McGraw-Hill, 2nd edition, 1991.

[129] A. E. P. Veldman, "New, Quasi-Simultaneous Method to Calculate Interacting Boundary Layers," *AIAA Journal*, vol. 19, no. 1, pp. 79–85, 1981.

[130] J. E. Carter, "A New Boundary-Layer Inviscid Iteration Technique for Separated Flow," tech. rep., NASA Technical Memorandum, 1978.

[131] I. Kroo, "DRAG DUE TO LIFT: Concepts for Prediction and Reduction," *Annual Review Fluid Mechanics*, vol. 33, no. 33, pp. 586–617, 2001.

[132] C. L. Rumsey, J. P. Slotnick, M. Long, R. A. Stuever, and T. R. Wayman, "Summary of the First AIAA CFD High-Lift Prediction Workshop," *Journal of Aircraft*, vol. 48, no. 6, pp. 2068–2079, 2011.

[133] R. Rudnik and E. Germain, "Re-No. Scaling Effects on the EUROLIFT High Lift Configurations," in *45th, AIAA aerospace sciences meeting, Reno, Nevada*, AIAA-2007-752, 2007.

[134] R. Rudnik, K. Huber, and S. Melber-Wilkending, "EUROLIFT Test Case Description for the 2nd High Lift Prediction Workshop," in *30th AIAA Applied Aerodynamics Conference, New Orleans, LA*, AIAA-2012-2924, 2012.

[135] R. Ahrem, A. Beckert, and H. Wendland, "A Meshless Spatial Coupling Scheme for Large-scale Fluid-structure-interaction Problems," *CMES: Computer Modeling in Engineering and Sciences*, vol. 12, no. 2, pp. 121–136, 2006.

[136] E. N. Tinoco, D. N. Ball, and F. A. Rice, "PAN AIR analysis of a transport high-lift configuration," *Journal of Aircraft*, vol. 24, pp. 181–187, 1987.

[137] J. W. van der Burg, H. F. von Geyr, R. Heinrich, P. Eliasson, T. Delille, and J. Krier, "Geometric Installation and Deformation Effects in High-Lift Flows," *AIAA Journal*, vol. 47, no. 1, pp. 60–70, 2009.

[138] K. Chang, H. Chen, T. Tzong, and T. Cebeci, "Aeroelastic Analysis of High Lift Configurations," in *38th Aerospace Sciences Meeting and Exhibit, 10-23 January, Reno, NV*, AIAA-2000-0905, 2000.

[139] P. G. A. Cizmas, J. I. Gargolo, T. W. Strganac, and P. S. Beran, "Parallel Multigrid Algorithm for Aeroelasticity Simulations," *Journal of Aircraft*, vol. 47, no. 1, pp. 53–63, 2010.

[140] J. R. Cebral and R. Lohner, "Conservative Load Projection and Tracking for Fluid-Structure Problems," *AIAA Journal*, vol. 35, no. 4, pp. 687–692, 1997.

[141] C. Farhat, M. Lesoinne, and P. LeTalle, "Load and motion transfer algorithms for fluid/ structure interaction problems with non-matching discrete interfaces: Momentum and energy conservation, optimal discretization and application to aeroelasticity," *Computational Methods in Applied Mechanics and Engineering*, vol. 157, pp. 95–114, 1998.

[142] J. A. Samareh, "Discrete data transfer technique for fluid-structure interaction," in *18th AIAA Computational Fluid Dynamics Conference, Miami, FL*, AIAA-2007-4309, 2007.

[143] T. C. S. Rendall and C. B. Allen, "Unified fluid-structure interpolation and mesh motion using radial basis functions," *International Journal for numerical methods in engineering*, vol. 74, pp. 1519–1559, 2008.

[144] T. C. S. Rendall and C. B. Allen, "Improved radial basis function fluid-structure coupling via efficient localized implementation," *International Journal for Numerical Methods in Engineering*, vol. 78, no. 10, pp. 1188–1208, 2009.

[145] U. Cella and M. E. Biancolini, "Aeroelastic Analysis of Aircraft Wind-Tunnel Model Coupling Structural and Fluid Dynamic Codes," *Journal of Aircraft*, vol. 49, pp. 497–414, 2012.

[146] A. Beckert and H. Wendland, "Multivariate interpolation for fluid-structure interaction problems using radial basis functions," *Aerospace Science and Technology*, vol. 5, no. 2, pp. 125–134, 2001.

[147] C. Agostinelli, C. B. Allen, and A. Rampurawala, "Flexible Wing Twist Optimisation using Rapid Computational Methods," in *AIAA 30th Applied Aerodynamics Conference, New Orleans, LA*, AIAA-2012-2661, 2012.

[148] M. S. A. Elsayed, R. Sedaghati, and M. Abdo, "Accurate Stick Model Development for Static Analysis of Complex Aircraft Wing-Box Structures," *AIAA Journal*, vol. 47, no. 9, pp. 2063–2075, 2009.

[149] C. Agostinelli, C. Liu, C. B. Allen, A. Rampurawala, and G. Ferraro, "Propeller-Flexible wing interaction using rapid computational methods," in *International Forum on Aeroelasticity and Structural Dynamics*, 2013.

[150] B. Stickan, H. Bleecke, and S. Schulze, *Computational Flight Testing. Notes on Numerical Fluid Mechanics and Multidisciplinary Design. Volume 123*, ch. NASTRAN Based Static CFD-CSM Coupling in FlowSimulator, pp. 223–234. Springer-Verlag Berlin Heidelberg, 2013.

[151] A. Inselberg, *Parallel Coordinates. Visual Multidimensional Geometry and Its Applications*. Springer, 2009.

Appendix A

Optimisation Framework

The description of the optimisation framework's implementation is presented in the following sections, which describe the Architectural, Interface and Design characteristics of the framework.

A.1 Architecture

The visual representation of the framework's architecture is presented in Figure A.1. Three main modules can be identified: the *"optimiser"*, the *"interface"* and the *"execution"*. The optimiser is the core of the framework, and is the module responsible for the control of the whole optimisation process. It is here that the problem definition is specified (in terms of design variables, objective functions and optimisation algorithm's specific settings) and where the new designs are generated. The optimiser is then connected to the execution module through an *"interface"*, which translates the design variables provided by the optimiser into geometries. It also generates input and control files for the execution of the simulation methods. Finally, the *"execution"* module is responsible for the actual run of the methods, handling any dependency in terms of IT requirements as well as eventual submission to the scheduling system of the HPC cluster.

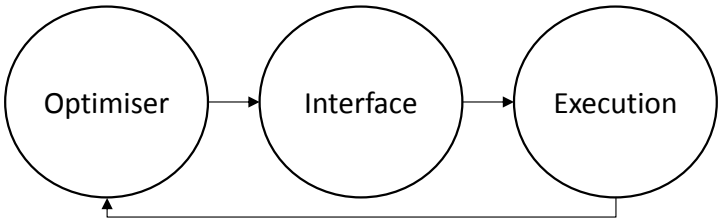

Figure A.1: Architecture description of the optimisation framework.

A.2 Interface Module

The principal function of the *"interface"* module is the translation of the input design variables provided by the optimiser into new geometries, which can then be analysed using one of the available simulation methods within the *"execution"* module.

A process chain is implemented within this module, which starts with the parameterisation of the high-lift elements using the Free Form Deformation technique. In particular, each of the element's shape is in turn modified according to the specified displacement of the FFD control points. These parameters constitute part of the input design variables' set, specified within the optimiser module, which also includes the deployment settings of each element. As illustrated in Figure A.2, after the parameterisation step the modified elements (contained in the Output_geom.dat file) are positioned according to the specified deployment parameters using a specific FORTRAN function, i.e. Deployment.f. Clearly, this step is skipped if a pre-deployed geometry is used. Finally, this newly produced geometry (Deployed_geom.dat) is used as input for the simulation's process chain.

A.3 Framework Design

The actual implementation of the framework has been performed in C++, with C and FORTRAN functions linked trough specific libraries. Executables for both Windows and Linux platforms are then build using GCC compilers, to be run in

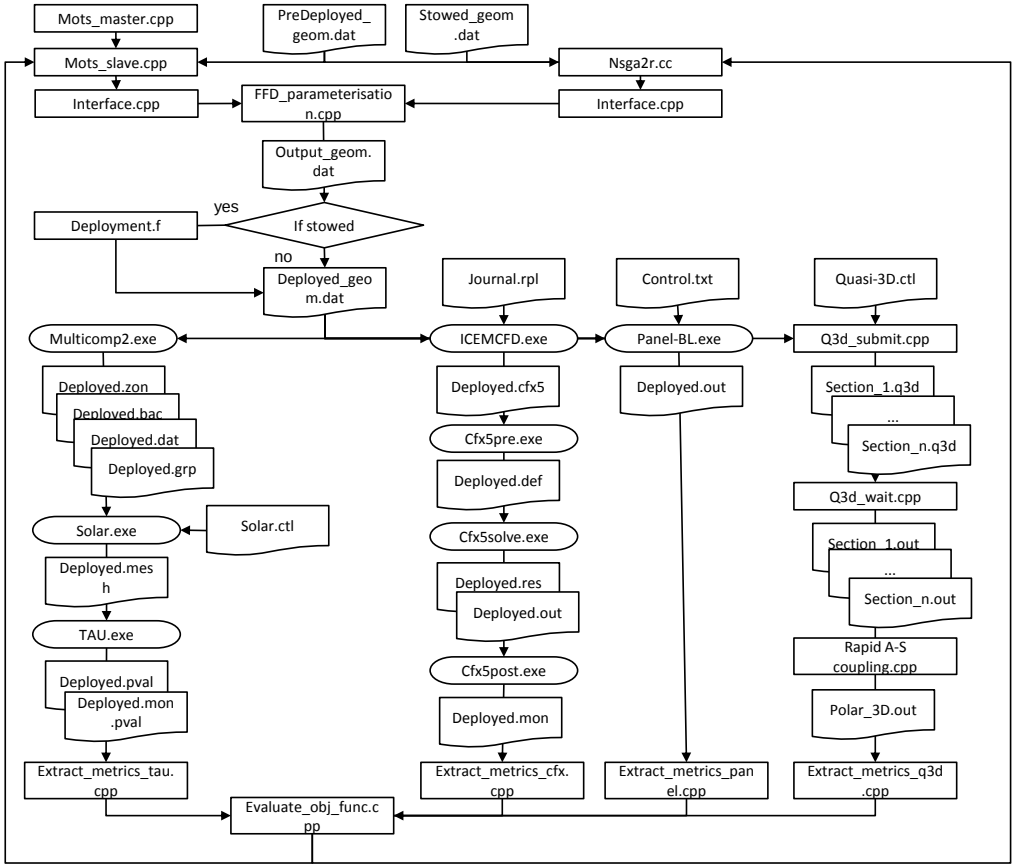

Figure A.2: Workflow representation of the optimisation framework. Main functions, executables and data exchanged are shown.

either the academic or industrial IT environment.

In order to minimise the wall clock time to completion, different parallelisation strategies are exploited. Firstly, a *"master and slave"* architecture is used for the optimisers, in which a master process controls the overall optimisation, while several slaves are executed in parallel on an HPC cluster. Each of the slave process receives a new design from the master, it then performs an evaluation of the design and returns the relative objective functions values back. This parallelisation strategy is defined *"functional decomposition"* and it is implemented using Message Parsing Interface (MPI) techniques. In addition, each slave process can run a parallel execution of the computational expensive analysis methods, such as RANS simulation. This further parallelisation of the process is defined *"domain decomposition"*. An example of such parallelisation strategies is illustrated in Figure A.3.

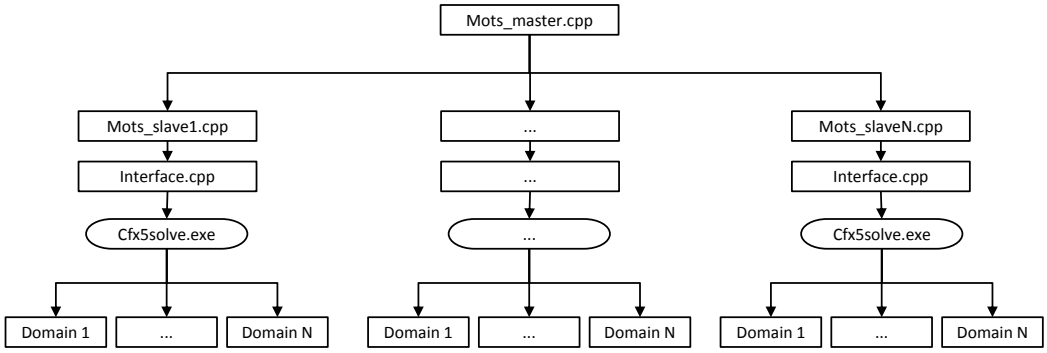

Figure A.3: Parallelisation strategies: "functional" and "domain" decompositions are used concurrently.

The workflow representation of Figure A.2 illustrates how journal files are used for the execution of the commercial software packages. Specifically, a replay file (journal.rpl) containing the command to produce an high quality mesh around a generic multi-element airfoil is used to execute the *"ICEMCFD"* software in batch mode. A similar approach is used for the definition of the RANS simulation using the *"cfx5pre"* software and the extraction of the important metrics trough *"cfx5post"*. A slightly different approach is used for the execution of the *"Solar mesher"* and the *"TAU"* solver, since those software have been designed to be run in batch mode using only a steering file.

The actual execution of the optimisation process differs between the academic and the industrial environments. In the first case, the whole optimisation process is submitted as a single job to the scheduling system of the HPC cluster. The required number of nodes for the job is the product of the nodes required by the RANS simulation (defined by the user) by the number of slave processes specified. Instead, in the industrial HPC environment a new job is submitted every time a RANS simulation (or a quasi-three-dimensional simulation) is executed.

The single job approach is clearly a faster solution, since the job will go through the scheduling system only once (even though the nodes requirement is higher than

a single RANS simulation). However, specific modification or personalisation to the scheduling system must be performed in order to include such types of jobs. Therefore, when such flexibility is not available, as in the case of the industrial environment, the standard scheduling system must be used. In the latter case, specific functions have been implemented in the framework to check the completion of the submitted jobs before starting the metrics extraction procedure. Clearly, this approach is associated with an time penalty, although this is mitigated to a certain extend by the greater HPC capabilities of the industrial sponsor's HPC and the fact that the cluster is dedicated to run only such type of simulations (RANS or quasi-three-dimensional).

Finally, in the case of a quasi-three-dimensional simulation, few specific functions have been implemented in the framework to handle the submission and the execution of the process. In fact, the quasi-three-dimensional simulation differs in many ways from the 2D RANS or Panel ones. Fist of all, several sections are used as input (one for each spanwise section) rather than a single one. Secondly, a maximum of 8 sections can be run concurrently due to specific implementation of the quasi-three-dimensional code and the architecture of the HPC cluster. Therefore, the analysis is executed in batches of 8 sections at a time, until all the defined sections are evaluated. Finally, the rapid aero-structural coupling procedure must also be executed after a complete quasi-three-dimensional simulation.

Appendix B

Publications

- G. Trapani, C. Agostinelli, T. Kipouros, A. Mark Savill and A. Rampurawala, *"A Rapid Approach to the Aerodynamic Design of a Flexible High-Lift Wing"*, 32nd AIAA Applied Aerodynamics Conference, AIAA Aviation, Atlanta, USA, June 2014

- G. Trapani, C. Agostinelli, T. Kipouros, A. Mark Savill and A. Rampurawala, *"Aerodynamic Optimisation of a Flexible High Lift Wing"*, IFASD Conference, Bristol, UK, 24th June 2013

- G. Trapani, T. Kipouros, A. Mark Savill, *"The Design of Multi-element Airfoils Through Multi-Objective Optimization Techniques"*, CMES, Tech Science, vol.88, No 2, 2012

- G. Trapani, T. Kipouros, A. Mark Savill, *"Computational Aerodynamic Design for 2D High Lift Airfoil Configurations"*, Pegasus-AIAA Conference, Seville, Spain, 29th April 2010

B.1 Posters

- G. Trapani, *"Multi-disciplinary Optimisation of Novel Aircraft Configurations"*, Airbus PhD Day, Bristol, UK, October 2013

- G. Trapani, *"Multi-disciplinary Optimisation of Novel Aircraft Configurations"*, DTC poster session, Cranfield University, UK, March 2012

- G. Trapani, *"Multi-disciplinary Optimisation of Novel Aircraft Configurations"*, Airbus PhD Day, Madrid, Spain, October 2012

- G. Trapani, *"Multi-disciplinary Optimisation of Novel Aircraft Configurations"*, Airbus PhD Day, Toulouse, France, October 2011

Airbus PhD day 2013

PhD Title: Multi-Disciplinary Optimization of Novel Aircraft Configurations

Student: Giuseppe Trapani

Supervisors: Prof. A.M. Savill, Dr. Timos Kipouros

Eng. Stefano Tursi

Aims & Objectives

Analysis of high-lift aircraft configurations using parametric geometrical descriptions, sensitivity analysis and different performance simulation capabilities, in the context of the multidisciplinary and multi-objective design optimisation environment. Based on the Airbus tool-chain expanded with several tool-kits developed at Cranfield University.

Contribution to Airbus

The implementation of automated multi-disciplinary optimisation process will lead to a faster, more efficient design process resulting in both a step change increase in aircraft performance and a considerable reduction on time to market.

YEAR 4

POINTS 6462

Next

Quasi-3D approach

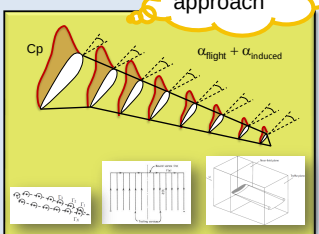

Fig.11 – Quasi-3D method. Aerodynamic coefficients of 2D sections along the span are evaluated and patched together using a lifting surface method.

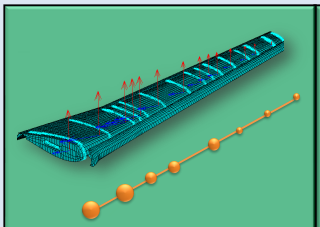

Fig.15 – Reduction of the wing full CSM to a Beam Model. 15 sections along the span have been used.

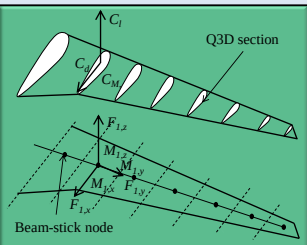

Fig.16 – Generation of the Aerodynamic Database and transfer of forces from aerodynamic to structural model.

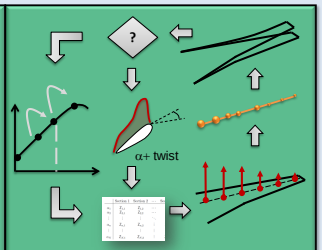

Fig.17 – Rapid coupling loop. The quasi-3D polars are used as inputs of the process, which evaluates the flexible performance.

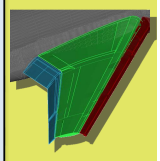

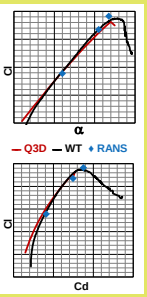

Fig.12 – Validation of the Quasi-3D approach on the DLR F11 geometry. Comparison with RANS and Wind Tunnel Data.

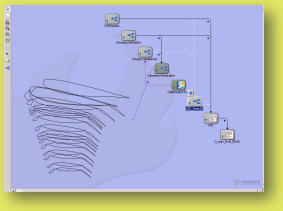

Fig.13 – Implementation of the quasi-3D method within an optimization framework using the commercial software ModelCenter®

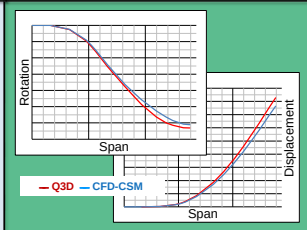

Fig.18 – Validation of the Rapid aero-structural coupling process. Comparison with full CFD-CSM data.

Flexibility Effects

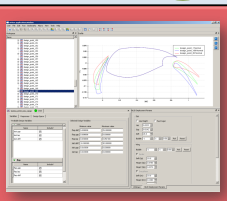

Fig.6 – Design of Experiment setup within Wisdom R&T software. Elements' deployments settings available to use as design variables.

2D multi-objective Optimisation

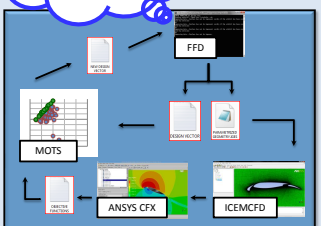

Fig.1 – Optimization framework. The initial geometry is modified by the FFD, meshed and evaluated in ANSYS and finally the objective functions are sent to the Multi Objective Tabu Search optimiser.

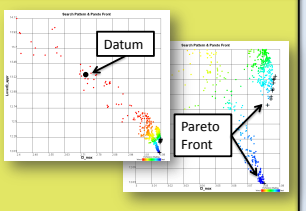

Fig.14 – Pareto Front & Search Pattern. Results of a multi-objective optimisation on the F11 test case in landing configuration.

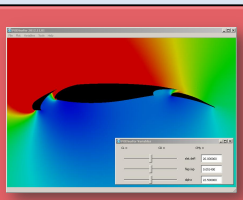

Fig.8 – A Proper Orthogonal Decomposition model is constructed using all the successful RANS simulations. Deployments variables as well as angle of attack can be used as input parameters.

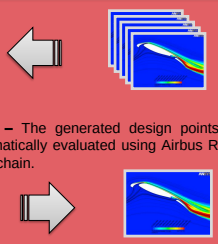

Fig.7 – The generated design points are automatically evaluated using Airbus RANS CFD chain.

Fig.9 – The POD model is used to perform the optimisation studies on the local pc station.

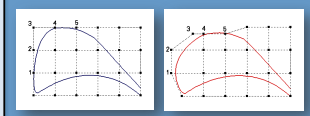

Fig.2 – Free Form Deformation on flap element. The shape of the airfoil is controlled by the movements of the overlapped grid of points.

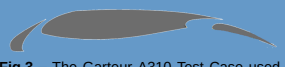

Fig.3 – The Garteur A310 Test Case used in the optimisation applications.

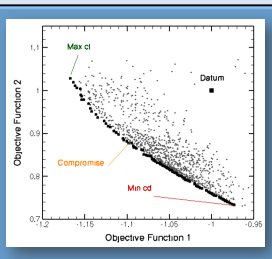

Fig.4 – Pareto Front and Search Pattern. Single-Point maximisation of lift and minimisation of Drag.

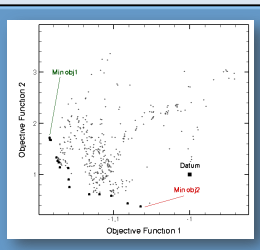

Fig.5 – Pareto Front and Search Pattern. Multi-Point maximisation of lift and robust polar at near stall angle.

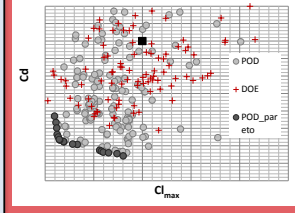

Fig.10 – Pareto Front obtained using a POD model built on 250 RANS design points and the NSGA-II optimisation algorithm.

Industrial application and POD

Cranfield UNIVERSITY

EPSRC Pioneering research and skills

AIRBUS

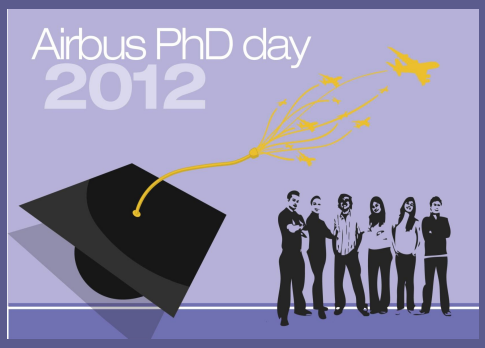

PhD Title: Multi-Disciplinary Optimization of Novel Aircraft Configurations

Student: Giuseppe Trapani
Supervisors: Prof. A.M. Savill, Dr. Timos Kipouros
Eng. Stefano Tursi

Aim of the Research

The aim of the research project is the analysis of novel aircraft configurations using parametric geometrical descriptions, sensitivity analysis and different performance simulation capabilities. Such analysis is to be carried out in the context of the multidisciplinary and multiobjective design optimisation environment based on the Airbus tool-chain expanded with several tool-kits developed at Cranfield University.

Contribution to Airbus

The research project, carried out within the CFMS context, will contribute to the achievement of the challenging goals posed by the ACARE Vision. In particular, the implementation of an automated multidisciplinary optimization framework will lead to a faster, more efficient design process resulting in both a step change increase in aircraft performance and a considerable reduction on time to market.

2D High-Lift Optimization

Initial focus of the research project has been the development of a framework for the automated optimization of multi-element airfoils (fig.1). In particular, a Multi-Objective Tabu Search optimizer has been coupled with a Free Form Deformation tool (fig.2) and the commercial cfd suite Ansys Icemcfd and Cfx5. The different tools have been interfaced through dynamic journals automatically generated by a c++ code. Two optimization processes have been performed at Cranfield University HPC cluster using the Garteur A310 test case (fig.3) as the baseline input.

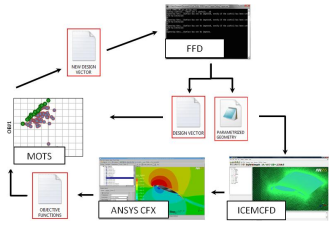

Fig.1 – Optimization framework

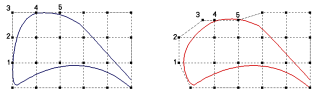

Fig.2 – Free Form Deformation on flap element

Fig.3 – Garteur A310 Test Case

Single-Point

The deployment settings of slat and flap have been selected as design variables (6 in total), with no change in element shape. The lift and drag coefficient at a fixed angle of attack (AoA) represent the two objective functions. The optimization has been halted after 450 hours, corresponding to 164 optimization iterations and 1217 cfd evaluations.

Multi-Point

This set-up has been performed to include operational robustness into the design process. Three angle of attack are considered for the evaluation of the objective functions, which represent the lift performance (obj1) and its variance with AoA (obj2). Flap shape changes have been included, increasing the design variables number to 12.

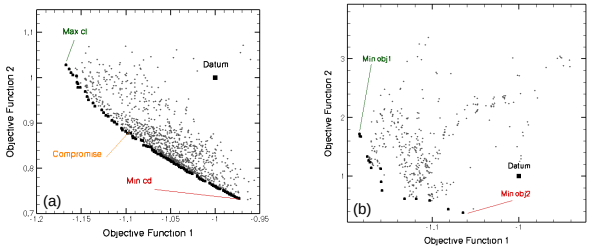

Fig.4 –Pareto Front and Search Pattern: (a) Single-Point; (b) Multi-Point

Quasi 3D High-Lift Optimization

A similar framework for multi-element airfoil optimization has been implemented at Airbus UK (Filton) using the commercial software ModelCenter 10.0 and the Solar-Tau cfd chain. This has been expanded to perform quasi 3D optimization, using a 2D coupled panel method boundary layer and a lifting surface code. The tool allows the rapid evaluation of lift and drag performance of a 3D high-lift wing configurations.

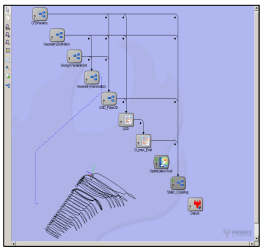

Fig.5 – Quasi 3D ModelCenter Optimization Framework

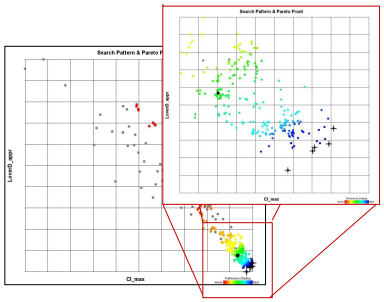

Fig.6 – Q3D Pareto Front & Search Pattern

The framework has been used to perform the optimization of an *"Airbus-like"* wing in landing configuration. The deployment settings of the inboard and outboard high-lift devices have been allowed to change independently. Lift over drag ratio at approach (L/D) and maximum lift coefficient (Cl_max) represent the objective functions.

Flexible Wing

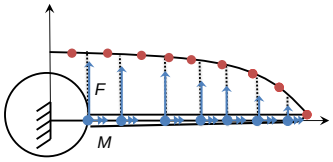

Fig.7 – Rapid static coupling process

As a result of a collaboration with Researcher Engineer Christian Agostinelli a rapid static coupling process has been implemented within the Q3D optimization framework. At each optimization iteration the lift distribution obtained from the quasi 3D tool is used by the tool to evaluate the new wing twist distribution and, therefore, the *"flexible"* performance of the wing. Preliminary results obtained with the described methodology are currently being analysed and validated.

Future work

- Validate the Q3D flexible optimization framework and perform multi-objective and multi-disciplinary optimization of novel wing configuration and/or novel high-lift devices
- Include higher fidelity cfd tools (RANS) into the quasi 3D optimizations.
- Develop and bring into production as an Airbus design tool a Principal Orthogonal Decomposition (POD) optimization framework for high lift airfoils.

Fig.8 – POD approximation of RANS

Acknowledgement

I would like to thank my supervisors, Airbus Operation Ltd and the EPSRC for giving me the opportunity to carry out this challenging research project.

Cranfield UNIVERSITY

EPSRC Pioneering research and skills

AIRBUS

Airbus PhD day 2011

PhD Title: Multi-Disciplinary Optimization of Novel Aircraft Configurations

Student: Giuseppe Trapani
Supervisors: Prof. A.M. Savill – Dr T. Kipouros
Industrial Supervisor: Eng. S. Tursi

Aim of the Research

The aim of the research project is the analysis of novel aircraft configurations using parametric geometrical descriptions, sensitivity analysis and different performance simulation capabilities. Such analysis is to be carried out in the context of the multidisciplinary and multiobjective design optimisation environment based on the Airbus tool-chain expanded with several tool-kits developed at Cranfield University.

Contribution For Airbus

The research project, carried out within the CFMS context, will contribute to the achievement of the challenging goals posed by the ACARE Vision. In particular, the implementation of an automated multidisciplinary optimization framework will lead to a faster, more efficient design process resulting in both a step change increase in aircraft performance and a considerable reduction on time to market.

2D High-Lift Optimization

Initial focus of the research project has been the numerical simulation of the flow-field around 2D High-Lift configurations. The Airbus Test Case A has been selected as case geometry and a validation and verification analysis has been performed.

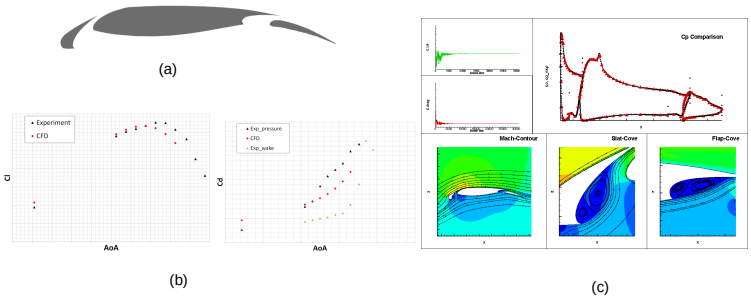

Fig.1 – Test Case A Validation Analysis: (a) Geometry; (b) Drag and Lift polars; (c) Flow-field and Cp

Two different frameworks have been developed for the automated optimization of 2D high-lift airfoils. Using the Cranfield University tools a Multi-Objective Tabu Search optimizer has been coupled with a NURBS parameterization code (PARATOOL) and the commercial CFD suite ANSYS ICEMCFD and CFX5. The different tools have been interfaced through dynamic journals automatically generated by a c++ code.
Implementation at Airbus has been carried out using ModelCenter 10.0 and its built-in optimization toolkit. Two different evaluation tools have been included within the framework: a panel coupled boundary layer code (HILI) and a RANS tool-chain software (Solar-Tau).

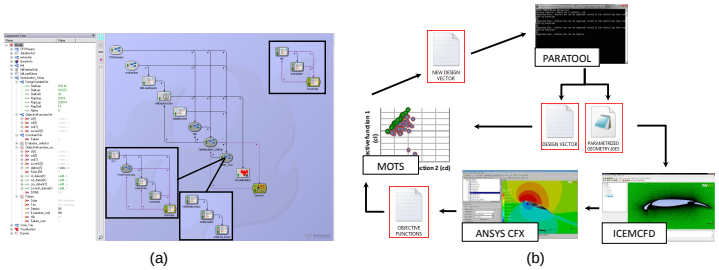

Fig.2 – Optimization frameworks: (a)Airbus; (b)Cranfield University

Results

The optimization framework of fig.2(b) has been used to perform a single point optimization process of the Test Case A. Results of a previous optimization of the same test case can be found in [1], although a different angle of attack was considered. Moreover, a more accurate CFD process has been adopted here, using a different mesh strategy.

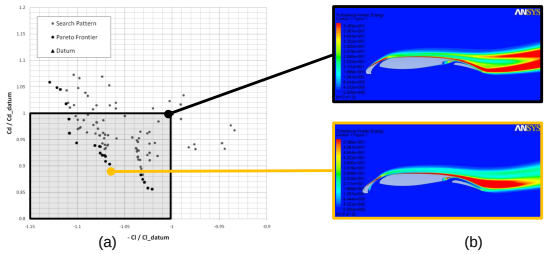

Fig.3 – (a) Pareto Front and Search Pattern; (b) Wake visualization of datum and chosen optimum

The deployment settings of slat and flap have been selected as design variables (6 design variables in total), while the lift and drag coefficient represent the two objective functions. After 27 iterations, corresponding to 215 CFD evaluations, the optimizer has found several solutions that increase both the performance criteria.
A similar optimization process has been performed using a genetic algorithm (Darwin) and the low-fidelity CFD tool implemented in ModelCenter. The faster execution time of the evaluation tool allowed the execution of more than 5000 objective functions evaluations and, hence, an in-depth exploration of the design space. However, only few of the optima increase both the performance criteria. This is probable due to the limitations of the low-fidelity evaluation tool at high angles of attack.

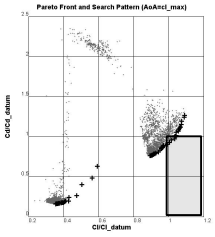

Fig.4 – Pareto Front and Search Pattern

Way forward

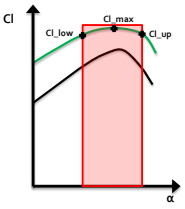

Fig.5 – Multi-Point analysis

In order to introduce operational robustness into the optimization process a multi-point optimization has been set-up. Three angles of attack are considered: the angle at which maximum lift occurs ±1º. The aim of the optimization is to increase the lift performance within the considered range and, concurrently, minimise the off-design performance reduction. The drag performance of the configuration is taken into account using penalty constraints. A simulation is currently running in the HPC cluster of Cranfield University.
Finally, a quasi 3D optimization process has been set-up within the ModelCenter framework. The evaluation tool used comprises the 2D panel method HILI coupled with a lifting surface code. The tool allows the rapid evaluation of lift and drag performance of a 3D high-lift wing configuration. A validation and verification process of the tool is currently being performed.

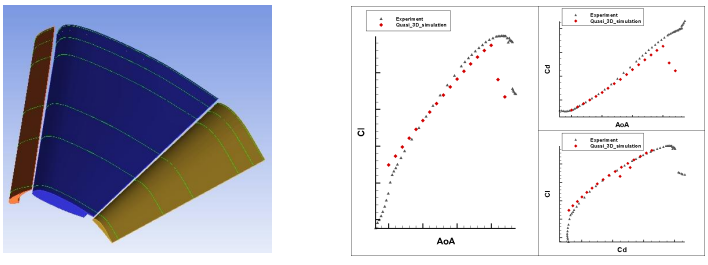

Fig.6 – (a) Trap Wing geometry; (b) Validation results

Acknowledgement

I would like to thank my supervisors and Airbus Operation Ltd for giving me the opportunity to carry out this challenging research project.

[1] Trapani G., Computational Aerodynamic Design for 2D High-Lift Airfoil Configurations. VI Pegasus AIAA Student Conference, Seville, 27th-30th April, 2010

Cranfield UNIVERSITY

AIRBUS

Multi-disciplinary Optimisation of Novel Aircraft Configurations

Giuseppe Trapani

Supervisor: Prof. M. Savill/Dr T. Kipouros

Introduction

The aim of the research project is the analysis of novel aircraft configurations using parametric geometrical descriptions, sensitivity analysis and different performance simulation capabilities. Such analysis is to be carried out in the context of the multi-disciplinary and multi-objective design optimisation environment based on the Airbus tool-chain expanded with several tool-kits developed at Cranfield University.

Contribution to Airbus

The research project, carried out within the CFMS context, will contribute to the achievement of the challenging goals posed by the ACARE Vision. In particular, the implementation of an automated multidisciplinary optimization framework will lead to a faster, more efficient design process resulting in both a step change increase in aircraft performance and a considerable reduction on time to market.

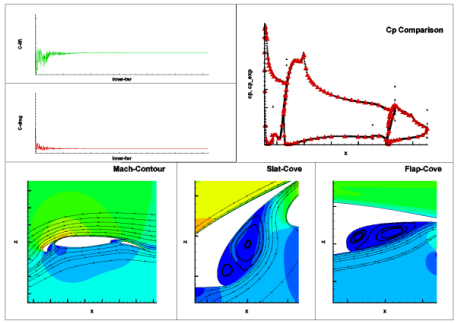

Fig.1 – RANS Simulation of the 2D High Lift Test Case A geometry

Approach To Problem

Initial focus of the research project has been the development of an automated optimization framework for the design of 2D high-lift airfoils (see Figure 2). Two different implementations have been performed:

- @ Cranfield University – A Multi-Objective Tabu Search optimizer has been coupled with a NURBS parameterization code (PARATOOL) and the commercial CFD suite ANSYS ICEMCFD and CFX5 through a c++ interface;
- @ Airbus – ModelCenter 10.0 and its built-in optimisation toolkit have been used to integrate a panel coupled boundary layer code and one of Airbus RANS tool-chain.

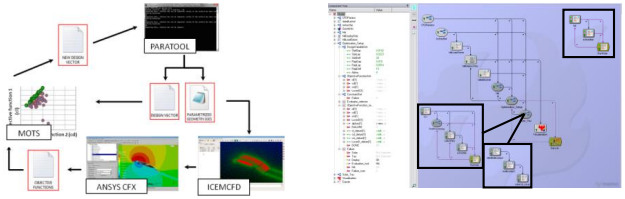

Fig.2 – Optimisation frameworks: (a) Cranfield ; (b) Airbus

The development of a "quasi" 3D optimization process has represented the following step. The evaluation tool used comprises a panel method coupled with a lifting surface code. A rapid evaluation of lift and drag performance of a 3D high-lift wing configuration is possible using 2D airfoil sections and planform definition as input.

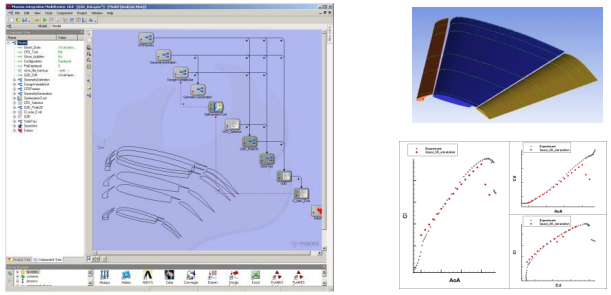

Fig.3 – Quasi 3D Optimisation Framework

Summary of Results

A single point optimisation has been performed using the framework depicted in figure 2a. Slat and flap deployment settings are the design variables (6 in total) while the lift and drag coefficient are the two objective functions. Figure 4 shows the Pareto Front and the Search Pattern found after 93 MOTS iterations, corresponding to 537 CFD evaluations, together with a comparison of the polar curves for datum and optima.

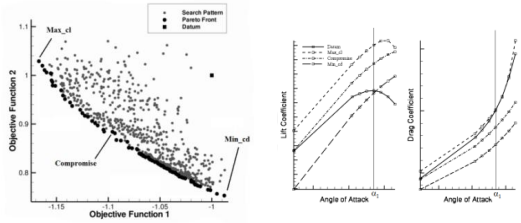

Fig.4 – 2D Single Point Optimisation Results

The multi point optimisation has been set-up to introduce operational robustness within the design process. The outcomes of the optimisation after 78 MOTS iterations (1743 CFD evaluations) are presented in figure 5.

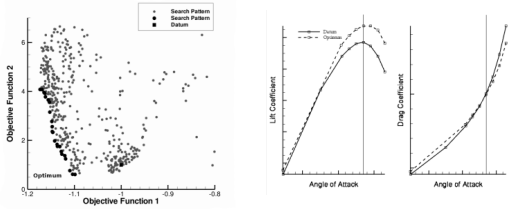

Fig.5– 2D Operational Robust Optimisation Results

Future Work

The next steps of the research encompass:

- Exploit the capabilities of PARATOOL and include element shape modification;
- Perform quasi 3D optimisations driven by the design requirements for high lift systems for both take-off and landing;
- Include a structural model within the framework to perform "Elastic" wing design;
- Consider non-conventional high lift configurations.

March 2012

EngD Studentship - Airbus UK Filton